Starshade Technology Development Activity
Milestone 2:

Optical Model Validation

Anthony Harness, N. Jeremy Kasdin, Michael Galvin

Princeton University

Stuart Shaklan, Phillip Willems, K. Balasubramanian, Philip Dumont,
Victor White, Karl Yee, Richard Muller, Douglas Lisman, Simon Vuong,

Jet Propulsion Laboratory, California Institute of Technology

August 15, 2022

Contents

Executive Summary

We report the results of a suite of high-contrast optical model validation experiments carried out at the Princeton Starshade Testbed in support of Starshade Technology Development Activity Milestone 2. Following the results of the Starshade Milestone 1 demonstration of better than 10^{-10} instrument contrast, we have performed experiments to show that diffraction models accurately predict the contrast due to perturbations representing the building blocks of the instrument error budget. The perturbations include the displacement of petal edge segments, sinusoidal petal edge shape deformations, global petal position errors, and random petal radial placement position errors. We also show that the model accurately predicts the combined effects of two errors. The experiments yield a pair of measured Model Uncertainty Factors (MUFs).

The MUFs are < 1.25 for petal shape perturbations, and <2 for petal position perturbations. The model agreement was primarily limited by the presence of polarization lobes arising from the interaction of light with the edges of the miniature starshade mask. Because of their location within the starshade's inner working angle (IWA), these lobes mainly affected the measurement of individual petal positioning errors. In a full scale starshade, the lobes are negligible with $< 10^{-15}$ contrast. However, they are visible in the testbed with a contrast $< 10^{-9}$, because the mask is 1/1000 scale of the flight starshade.

After detailing the experiment and results, we employ the measured MUFs in two starshade mission concept error budgets and show that the starshades are expected to achieve a total instrument contrast significantly better than 10^{-10} at the IWA.

1 Introduction

The Exoplanet Exploration Program (ExEP) chartered the Starshade Technology Activity, dubbed S5, to bring the starshade to Technology Readiness Level (TRL) 5 for a future space mission. S5 is focused on optical, mechanical, and formation flying technologies culminating in a series of milestones to be completed between 2019 and 2025.[1] The first three milestones focus on the demonstration of optical performance at flight-required levels.

The Princeton Starshade Testbed consisted of an 80-m long, 1-m diameter tube with a fiber-fed point source at one end, a precision etched silicon wafer mask at a distance of 27.5 m, and a camera placed another 50 m downstream. The experiment operated at nominal atmospheric pressure and temperature without a wavefront control system. The testbed is described in the Milestone 1A and 1B reports[2,3] and updates since those reports are described here.

Milestone 1A demonstrated 10^{-10} contrast at the Inner Working Angle (IWA) of a small-scale starshade mask in monochromatic light and verified that we can design a starshade capable of producing scientifically useful contrast levels. Designed with a flight-like Fresnel number, $F = 13$, and with the IWA resolved at 1.7 λ/D by the telescope, these experiments achieved a contrast floor of 2×10^{-11}, with contrast better than 10^{-10} over more than 2/3 of the suppression region between the conventional inner starshade and the inverse outer starshade that was used to support the inner one.

Milestone 1B then expanded the results to cover 4 wavelengths, 641 nm, 660 nm, 699 nm, and 725 nm, to form a broadband shadow covering a 12% bandpass. The noise floor and contrast levels were comparable to those observed in Milestone 1A.

This report and the attached papers detail the experiment and modeling results supporting the completion of Milestone 2. While Milestones 1A and 1B focused on deep contrast, Milestone 2 addresses model validation – the ability to predict the effect of purposely-introduced mask perturbations on the contrast observed in the image. The original wording of Milestone 2 reads:

> *Small-scale starshade masks in the Princeton Testbed validate contrast vs. shape model to within 25% accuracy for induced contrasts between* 10^{-9} *and* 10^{-8}.

Following a set of experiments in which the presence of vector diffraction, solely related to the miniature scale of the starshade mask, limited model accuracy for one class of perturbations, the Milestone was changed with approval of the Exoplanet Exploration Program Technical Advisory Committee (ExoTAC) to read:

> *Small-scale starshade masks in the Princeton Testbed validate contrast vs. shape model to within 25% accuracy for petal shape and 100% for petal position for induced contrasts between* 10^{-9} *and* 10^{-8}.

The required accuracies, 25% and 100%, correspond to model uncertainty factors (MUFs) of 1.25 and 2.0, respectively.

In Shaklan et al 2021,[4] we show that the relaxed requirement on the petal position MUF has only a minor impact on the flight mission concept instrument contrast error budget. Through Milestones 7a[5] (inner disk truss bay stability), 7c[6] (inner disk deployment accuracy), and 8a[7] (petal on-orbit position stability), we demonstrated the ability to initially position and to maintain the position of petals for contrast levels better than 10^{-12} for a range of starshade designs. A factor of 2 MUF makes only a small contribution toward the required

instrument contrast of $< 10^{-10}$.

This report summarizes the experiment and model, and presents the results. Additional details and more thorough descriptions of the experiment and models are included in the set of papers attached to this report:

- S. Shaklan et al, "Completion of model validation experiments at the Princeton starshade testbed" Proc. SPIE 12180 (2022, in press). M2 final results, MUFs, flight mission concept error budgets.
- A. Harness et al, "Optical verification experiments of sub-scale starshades", JATIS 2021. Experiment design, configuration details, summary of experiments, optical model summary, petal-tip experiment, crossed-analyzer measurements, out-of-band experiment.
- A. Harness et al, "Optical experiments and model validation of perturbed starshade designs," Proc. SPIE 2021. Barnett quadrature model, crossed-analyzer results, global petal shift and sine wave perturbations, initial model vs. data results (results are superseded by S. Shaklan 2022).
- A. Harness, "Implementing non-scalar diffraction in Fourier optics via the Braunbek method," Opt. Express 2020. How to combine scalar and vector models, vector modeling details including mask edge shape
- A. Harness et al, "Modeling non-scalar diffraction in the Princeton starshade testbed," Proc. SPIE 2018. An early version of vector model using the innermost radii, with details of the FDTD modeling.
- A. Harness et al, "Demonstration of 1e-10 contrast at the inner working angle of a starshade in broadband light and at a flight-like Fresnel number," Proc. SPIE 2019. Experiment design including comparison to HabEx and SRM mission concepts, deepest observed contrast.
- P. Willems & A. Harness, "Rayleigh scattering in the Princeton starshade testbed," Proc. SPIE 2019. Models the noise floor due to Rayleigh scatter.

2 Experiment Design

The experimental setup and procedures follow similarly from those of Milestones 1A and 1B: a telescope images a light source from within the deep shadow of a starshade and records the extent to which the starshade suppresses the on-axis light. Images of the unocculted light source are used to calibrate the image in units of contrast. The telescope is aligned with the starshade by centering on the diffraction pattern incident on the aperture in light outside of the starshade's design bandpass, much as will be done on-orbit.[8,9]

2.1 Polarization Upgrade

One significant change was made to the testbed since the Milestone 1A/B work. To enable studies of the polarization response, one linear polarizer was added to the light source (fixed in the horizontal position) and another was added on a rotation stage in the optical path of the telescope. Figure 1 shows a cartoon schematic of the laser launching system. As the state of polarization out of the laser's fiber optic varies with external conditions, the power transmitted through the polarizer (and ultimately incident on the starshade) varies with time. To account for this, a beam-splitter after the polarizer sends a fraction of the light to a photometer that records the transmitted power during observations.

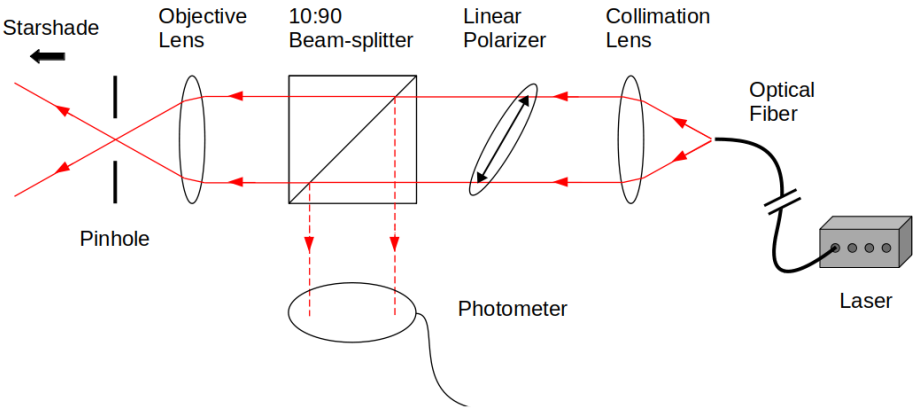

Figure 1: Diagram of laser launching system. The optical fiber enters on the right from the laser outside the testbed. Light is launched from the fiber, collimated, and passes through a linear polarizer before reaching a beam-splitter. 10% of the light is reflected to a photometer to record the throughput. The other 90% continues to an objective lens which sends a diverging beam to the starshade. A pinhole at the focus spatially filters high-order aberrations.

2.2 Perturbed Mask Descriptions

The starshades tested in these experiments start with the same baseline apodization function as the broadband starshades in the Milestone 1B work, except that the number of petals was reduced from 16 to 12. The switch to 12 petals was made to reduce the effects of non-scalar diffraction that were discovered in previous tests to originate from the inner gaps between petals.

An image of a manufactured mask is shown in Figure 2 and parameters common to all the perturbed masks are presented in Table 1. The starshade's Fresnel number ($F = r^2/\lambda Z$, where r is the inner starshade radius, λ is the wavelenth, and Z is the effective distance to the telescope) is 13.8 at the shortest wavelength, 641 nm, and 12.2 at the longest, 725 nm. Table 2 lists the mask serial number and perturbation name.

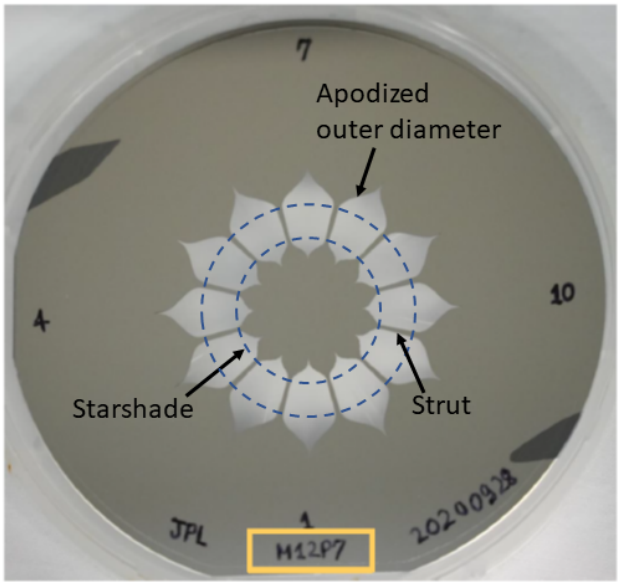

Figure 2: Starshade pattern etched into a silicon-on-insulator (SOI) wafer, manufactured at the Microdevices Lab at JPL. Interior to the inner blue circle is the inner starshade representing a free floating occulter. The inner starshade is supported in the wafer by radial struts. The outer blue circle marks the start of the outer apodization function.

Number of Petals	12
Operating Bandpass	640 to 730 nm
Minimum Radius	8.26 mm
Maximum Radius	12.53 mm
Fresnel No. at $\lambda = 641$ nm	13.8
Fresnel No. at $\lambda = 725$ nm	12.2
Petal Gap Width	21.6 µm
Optical Device Layer*	2 µm Silicon
Metal Coating	0.25 µm Aluminum

*Except M12P2, whose device layer is 1 µm Silicon Nitride.

Table 1: Design and manufacturing parameters common to all masks.

Manufacturing No.	Colloquial Name
M12P2	Displaced Edges
M12P6 & M12P10	Shifted Petals
M12P7	Mixed Perturbations
M12P8	Globally Shifted Petals
M12P9	Sine Waves

Table 2: Key relating mask manufacturing number to colloquial name.

The perturbed starshades start from the baseline apodization function and have at least two perturbations added to the two-dimensional shape. The perturbations are sized to induce contrasts between 10^{-9} and 10^{-8}, which make them faint enough to be informative to models at flight-like contrast levels, but bright enough to not be dominated by the contributions from non-scalar diffraction. Table 3 summarizes the different perturbations and the following sections provide additional details on each. Figure 3 shows the locations of the perturbations on each mask; in describing the locations of the perturbations, the petal number is given by its clock angle on the mask (modulo a 20° rotation to match the orientation in the lab).

Mask	Perturbation	Description	Location
M12P2	Positive Displaced Edge	2.3×414 μm edge displaced out of petal	Inner Petal 5
	Positive Displaced Edge	1.7×532 μm edge displaced out of petal	Outer Petal 11
M12P6 & M12P10	Shifted Petal	7.5 μm outward shift	Petals 1 & 5
	Shifted Petal	10.5 μm outward shift	Petal 9
M12P7	Shifted Petal	8.5 μm outward shift	Petals 1 & 7
	Negative Displaced Edge	10×80 μm edge displaced into petal	Petal 1
	Positive Displaced Edge	10×80 μm edge displaced out of petal	Petal 7
M12P8	Shifted Petal	5 μm outward shift	All Petals
M12P9	Sine Wave	1.75 μm amp., 4 cycles over 2.9 mm	Inner Petal 5
	Sine Wave	1.75 μm amp., 5 cycles over 2.3 mm	Outer Petal 11

Table 3: Summary of shape perturbations and corresponding manufacturing numbers.

2.2.1 M12P2 - Displaced Edges

The displaced edge perturbation simulates the effect of a petal edge segment being displaced from its nominal position during petal assembly on the ground. Figure 4 shows a 2.3 μm tall displaced edge segment built into the design of the manufactured mask M12P2. We call this type of perturbation a positive displaced edge, as the edge is shifted outwards from the petal

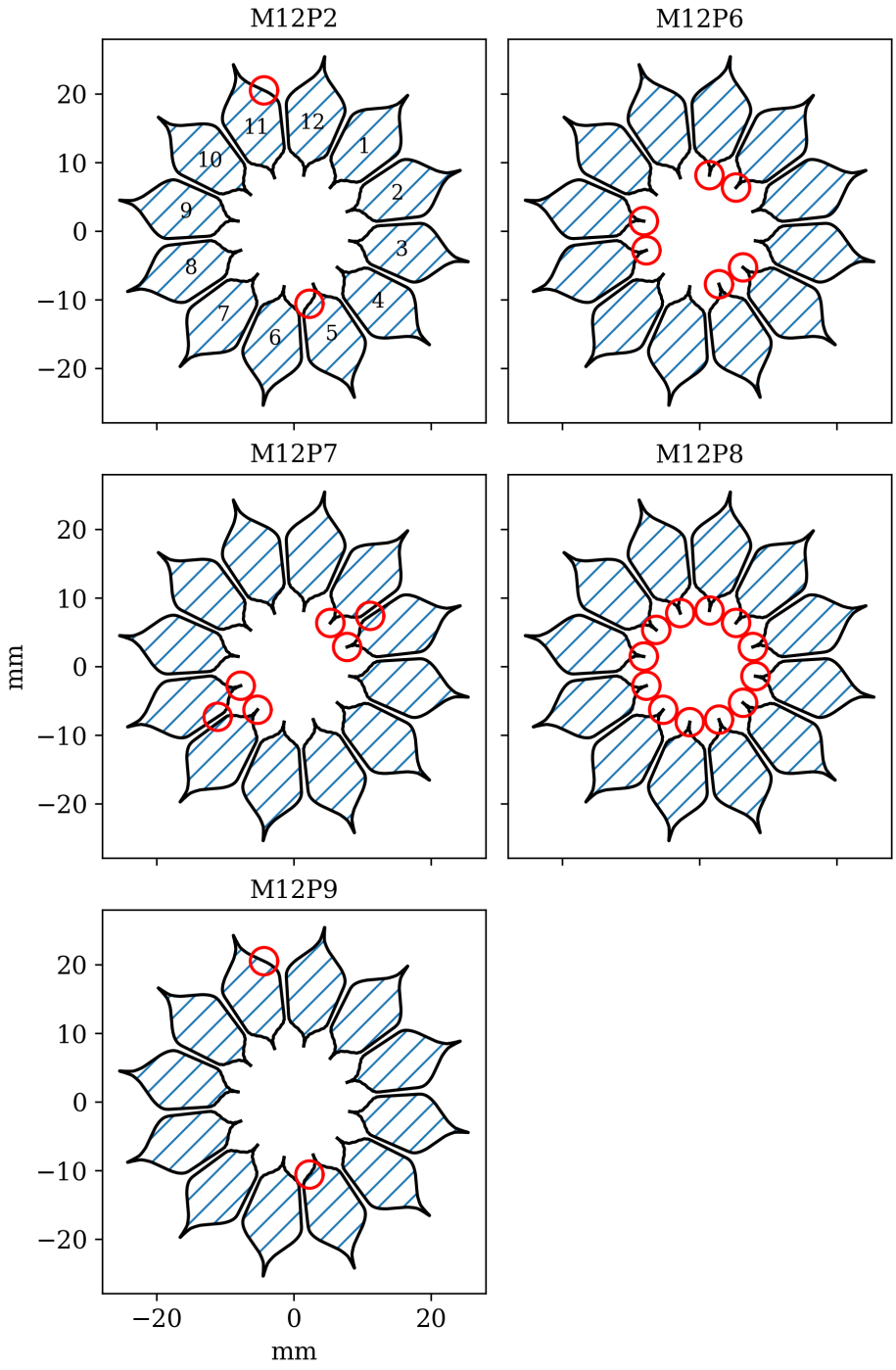

Figure 3: Red circles mark perturbation locations on all masks. The petal number is given by its clock angle on the mask (modulo a 20° rotation to match the orientation in the lab) as shown in the upper left image.

and increases the surface area of the petal. In mask M12P7, one of the perturbations is a negative displaced edge, which means it is shifted inwards and decreases the petal's surface area.

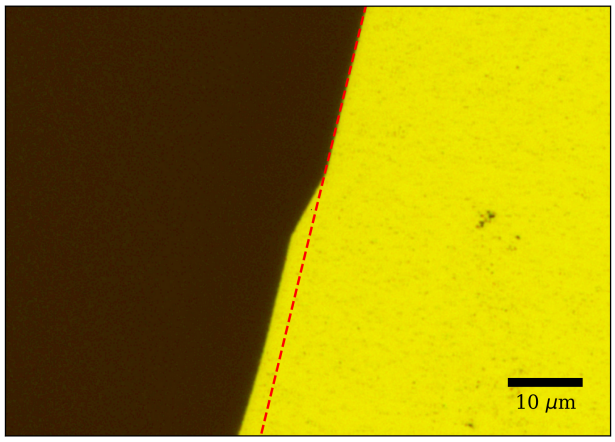

Figure 4: Microscope image of the inner displaced edge perturbation on M12P2. The starshade is gold, and the transparent area is black. The red line denotes the edge of the nominal starshade shape. The 2.3 µm step in the edge simulates a displaced edge segment.

2.2.2 M12P6 - Shifted Petals

In the flight system, petals are semi-kinematically attached to the bays that form the central disk. In mask M12P6, three of its twelve petals are shifted radially outwards by a few microns, the equivalent of a few millimeters on a full-scale starshade; petals 1 & 5 are shifted by 7.5 µm, while petal 9 is shifted by 10.5 µm. Only the petals of the inner starshade are shifted - the struts and the outer apodization function do not change.

Figure 5 shows a scanning electron microscope (SEM) image of how this perturbation is built into M12P6. The SEM image is of the gap between two petals, one of which is shifted radially outwards as a rigid body; the effect of shifting the petal outwards increases the gap spacing between the petals and also creates a small step in the radius at which the petal starts. The step in turn creates a shelf on one side of the gap. Since the petal has a gap on each side, two steps are made for each shifted petal. The steps themselves are of little consequence, resulting in $< 10^{-11}$ contrast. The perturbation lobes are the result of the radially changing apodization function over the full length of the petal.

2.2.3 M12P7 - Mixed Perturbations

Mask M12P7 mixes three different types of perturbations: shifted petals, a positively displaced edge segment, and a negatively displaced edge segment. Petals 1 and 7 are shifted radially outward by 8.5 µm and each have a displaced edge segment located on their radial strut. The edge segment on Petal 1 is a negative displacement, while the one on Petal 7 is a

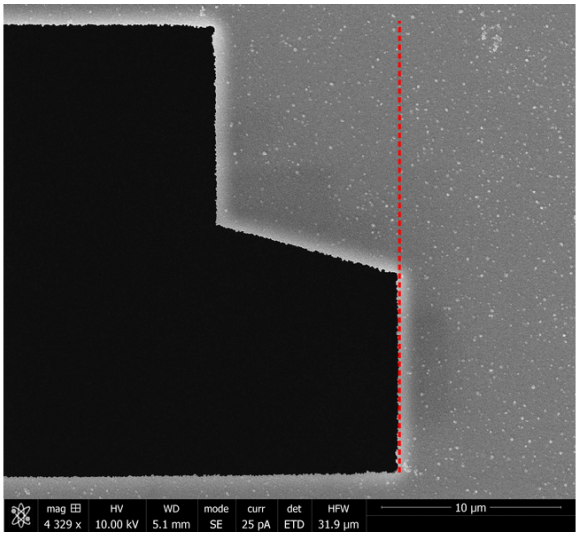

Figure 5: Scanning electron microscope image of the inner gap between an unshifted petal and shifted petal on mask M12P6. The red line marks the petal's original starting position.

positive displacement. The combination of three perturbation types explores the interference between perturbations and results in a strong wavelength dependence.

2.2.4 M12P8 - Global Petal Shift

Mask M12P8 also has shifted petal perturbations, but applied to every petal; each petal is shifted radially outward by 5 µm. Since petals on both sides of the inner gap are shifted, there is no shelf as is seen in M12P6. Shifting all petals outward modifies the apodization function from the ideal case, resulting in a ring of light centered near the inner petal gaps.

2.2.5 M12P9 - Sine Waves

Smooth changes to the edge shape can occur if individual edge segments are misshapen, and with thermal variations due to shadowing and material property variations. These smooth changes can be decomposed into a set of sine waves. The diffraction pattern is particularly sensitive to a sinusoidal petal width change if the sine wave is in sync with the Fresnel half-zones and they constructively interfere. This also places a strong wavelength dependence on the contrast they induce. Due to the small amplitude and long period of the sine wave introduced in these experiments, the change to the shape is imperceptible. As such we do not include a microscope image of this perturbation.

2.3 Summary of Experiments

Table 4 summarizes the different configurations that comprise the full suite of experiments conducted. For the milestone data, each mask is imaged in four wavelengths and at three

mask rotation angles, resulting in twelve images per mask. Additionally, each mask is imaged in four wavelengths with the polarized analyzer orthogonal to the input polarization direction (horizontal in the lab frame). This "crossed analyzer" configuration is used to constrain physical properties of the optical edge, and is detailed in Ref. 10.

Masks	M12P2, M12P6, M12P7, M12P8, M12P9, M12P10
Wavelengths	641, 660, 699, 725 nm
Mask Rotation Angles	0° , 120° , 240°
Analyzer Angles	0° , 90° ("crossed analyzer")

Table 4: Iteration of configurations that comprise the full suite of experiments.

The measurements for each mask were carried out in the following sequence. After installing the mask, the tube was closed and the air was allowed to settle for approximately 3 days. The tube remained closed for the duration of the tests. The mask was positioned in the 0° orientation and a 405 nm laser was used to illuminate the pinhole at the source station. This wavelength was outside the high-contrast design band of the mask, resulting in a bright spot of Arago at the pupil. The pupil lateral position was adjusted until the spot was centered. Then, using a remote switch and without having to touch any fibers, one of the four experiment wavelengths was selected, the camera optics were set to image the point source through the mask, and the analyzer was set to the horizontal position (parallel to the source polarizer). In this configuration, the camera integrated for $\sim$ 5 hours to observe the faint diffraction pattern. Then the mask was rotated to the 120° orientation and the process was repeated, and then again for 240°. Once these three images had been collected, the analyzer was rotated to the vertical position and the 0° orientation measurements were repeated to record the cross-polarization patterns. Then the second wavelength was selected and the full alignment/rotation/analyzer process was repeated, and again for the third and fourth wavelengths. Data for each wavelength typically took about one day to collect, and the full set of data for each mask typically required about one week.

3 Optical Model Summary

The overall modeling flow is shown in Figure 6. At the highest level, the model consists of a scalar propagator that handles the diffraction from the mask to the pupil, and a vector propagator that handles the propagation of light in the vicinity of the edges of the $\sim$ 2 micron thick sidewalls of the mask. The vector model results in two orthogonally polarized fields that are combined with the scalar field as described below. Once the light is propagated to the pupil, a simple Fast Fourier Transform algorithm is used to propagate the light to the image plane.

The optical performance of the flight-scale starshade is well described using the Fresnel approximation[11] and Kirchhoff's boundary conditions in solving the scalar diffraction

problem. This formulation of the diffraction equation is the model we are validating in this work. However, additional physics must be added to the model to account for the non-scalar diffraction effects, dubbed "thick screen effects", that were first observed in Milestone 1A.

Several methods are available for solving the scalar diffraction problem, all of which are shown to be in agreement. Two methods, a boundary diffraction wave method[12] and a similar angular integral method[11,13] convert the two-dimensional diffraction equation into a one-dimensional line integral around the occulter's edge and are well suited to capture the large dynamic range of sizes in the starshade shape.

Recently, Barnett[14] developed a highly-efficient method that utilizes non-uniform Fourier transforms to solve the Fresnel diffraction equation. This method assigns Gaussian quadrature weights to the starshade shape and uses non-uniform FFT algorithms[15] to match the accuracy of edge diffraction algorithms while being orders of magnitude faster.[10] In this work, we use Barnett's areal quadrature method to perform the comparison to experimental results. We modify this approach to handle shape perturbations and to incorporate non-scalar diffraction effects into the scalar diffraction model. The scalar version of this method was cross-checked with the edge algorithms of Refs. 12 and 11. We have further verified the performance of the Barnett algorithm using a "brute force" 2-D grid representation of the mask. The two propagators agree to a contrast level better than 10^{-11}.

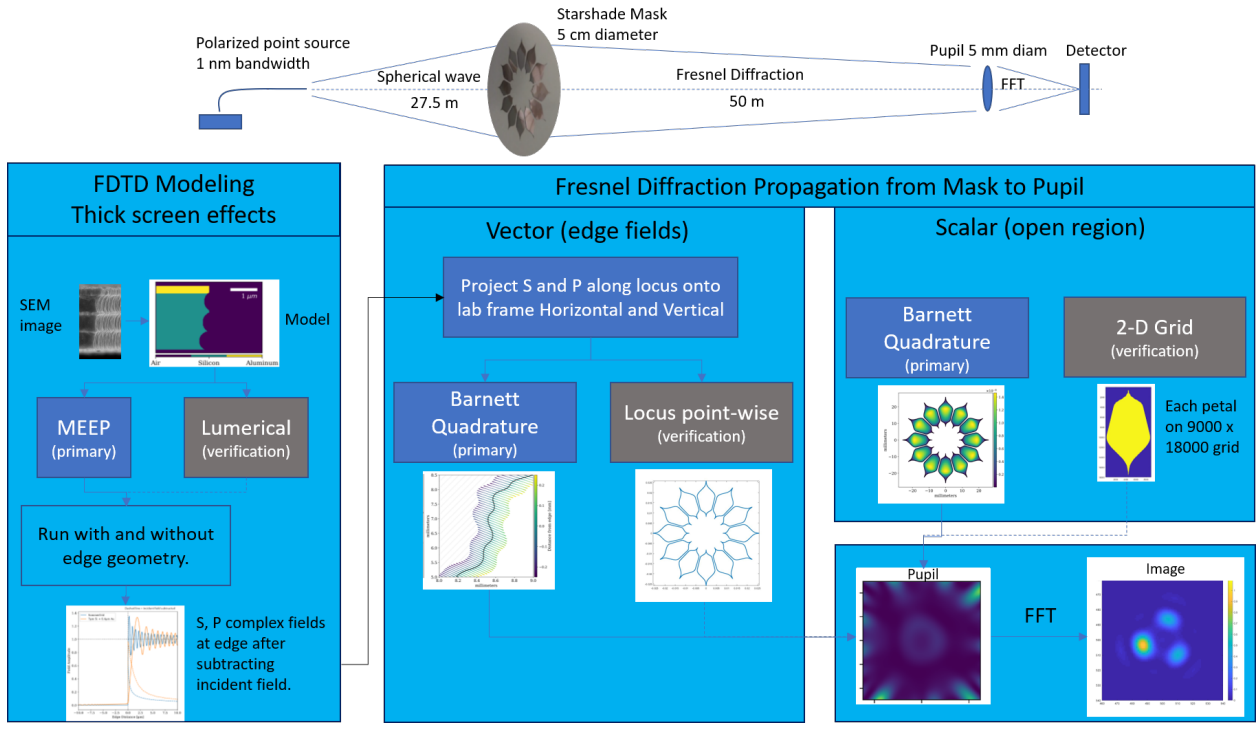

Figure 6: Modeling diagram illustrating the primary models (blue) and backup models (gray).

.

The areal quadrature method is well-suited to model non-scalar diffraction through the Braunbek method developed in Ref. 16. In the Braunbek method, the standard Kirchhoff

boundary conditions (where the incident field is 0 on the diffracting screen and 1 in the aperture) are replaced with the complex field that arises from local diffraction at the edge of the screen. Since the presence of the screen only affects its immediate surrounding, the boundary conditions are changed only in a narrow seam around the edge of the screen. The exact field in the seam around the edge is solved via a Finite Difference Time Domain (FDTD) simulation software package called MEEP[17] of light propagating past the edge of a metal-coated silicon wafer. The model accounts for the cross-sectional profile of the edge including Bosch cycle scalloping and edge taper (Figure 7). We have verified the performance of MEEP using a commercial FDTD package called Lumerical.

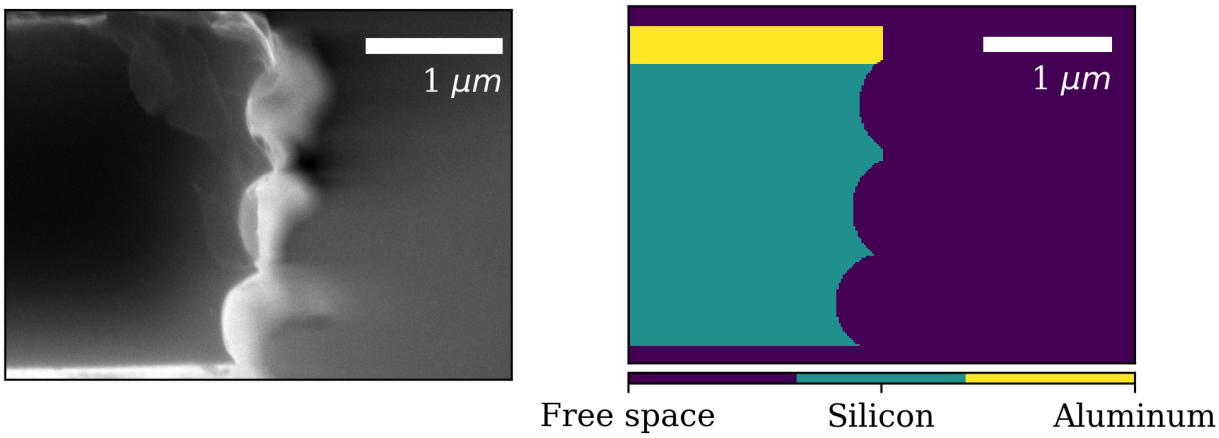

Figure 7: Left: SEM image of the scalloped vertical profile of the wafer edge for a manufactured mask. Right: electric permittivity map of the MEEP[17] FDTD simulation cell displaying the material geometry.

The masks all have slightly different fabrication properties. We used a scanning electron microscope to measure the physical properties of the optical edges (Table 5). The etching error, which is the accuracy of the edge position relative to the design, is used by the scalar diffraction model. The etching error can only be measured at the inner and outer tips. If this error changes as a function of radial position and/or gap width, then the model will not accurately represent this sensitive parameter. The other parameters (edge thickness, taper angle, scallop height, and scallop depth) are used by the vector diffraction model. The accuracy of this model is borne out by the cross-polarization measurements described in Refs 10 and 18. We show several representative mask edge profiles in Appendix B.

4 Milestone Analysis

The milestone is defined by the agreement between the laboratory data and the model. The data consist of images formed by the masks with their particular perturbations. Each perturbation results in a bright localized lobe in the image. In comparisons between experiment and model, we use the average contrast calculated in a photometric aperture of radius 1

Mask	Etching Error	Edge Thickness	Taper Angle	Scallop Height	Scallop Depth
M12P2	+210nm	1 μm	1°	1.2 μm	0.3 μm
M12P6	+40nm	2 μm	1°	0.6 μm	0.1 μm
M12P7	+50nm	2 μm	1°	0.6 μm	0.1 μm
M12P8	+100nm	2 μm	1°	0.6 μm	0.1 μm
M12P9	+140nm	2 μm	1°	0.6 μm	0.1 μm
M12P10	−275nm	2 μm	1°	0.6 μm	0.1 μm

Table 5: Model parameters used to model the thick screen effect via the FDTD method. The etching error is not used in the FDTD, but is used in the scalar model; a positive etching error means the mask is under-etched.

λ/D[†], centered on the perturbation lobe. We form a fractional model error (ME) factor, defined as

$$\mathrm{ME}_j = \frac{\mathrm{Lab}_j \text{ - } \mathrm{Model}_j}{\mathrm{Model}_j} \times 100\% \,, \tag{1}$$

where the measured contrast of the scatter from a particular perturbation at one of the four wavelengths and three orientations is given by Lab_j, and the corresponding model prediction is Model_j. Appendux A show the calibrated experiment images and corresponding models, as well as plots of Lab_j, Model_j, and ME_j for all masks, orientations, and wavelengths.

The values ME_j are compiled below in Figures 8 and 9. We summarize the average agreement between the data and model for each type of perturbation in Table 6. Here we have performed an unweighted average of the ME_j data points for each mask (but have combined the two separate petal shift masks since they represent the same type of perturbation), and report the standard error of the mean for each perturbation. These results include updated mask shape and edge parameters that were not available in Ref. 10.

The model is in excellent agreement with the experiment for the edge notches (M12P2), global petal shift (M12P8), and sine waves (M12P9). For these cases, the model error is $<$ 25% (MUF $<$1.25). But a careful inspection of Figures 15 and 18, and the corresponding model fractional error points in Figures 8 and 9 show that the model underestimates the perturbation contrast for M12P6 and M12P10. The underestimate most likely arises from a still unexplained issue in the combination of the scalar and vector models. The issue is most prominent with the petal shift experiment because the perturbation contrast appears close to the inner petal tips, near the same radius where the polarization lobes are most prominent. The vector model predicts the amplitude of the polarization lobes with sufficient accuracy to estimate the combined lobe and perturbation contrast to ∼20%. It appears that the phase of the model's electric field is off by a factor of $\pi/4$. This leads to destructive interference of the lobe field with the perturbation field which in turn causes an underestimate of the observed

[†]The perturbations of M12P7 are not point-like, so a photometric aperture of radius $1.5 \times \lambda/D$ is used.

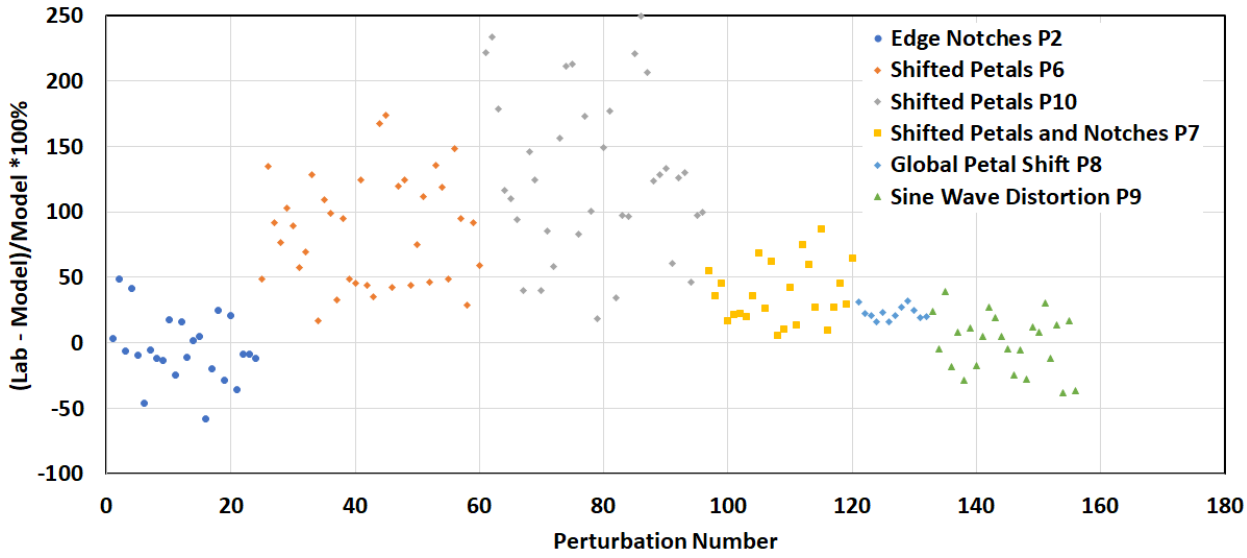

Figure 8: Percent difference between experiment and vector model for all perturbations. For each mask, there are 2 or 3 perturbations, each mask is tested at 4 wavelengths and 3 mask orientations, giving a total of 156 comparison points. The 1-sigma photometric errors relative to the model are less than 6% for all data points.

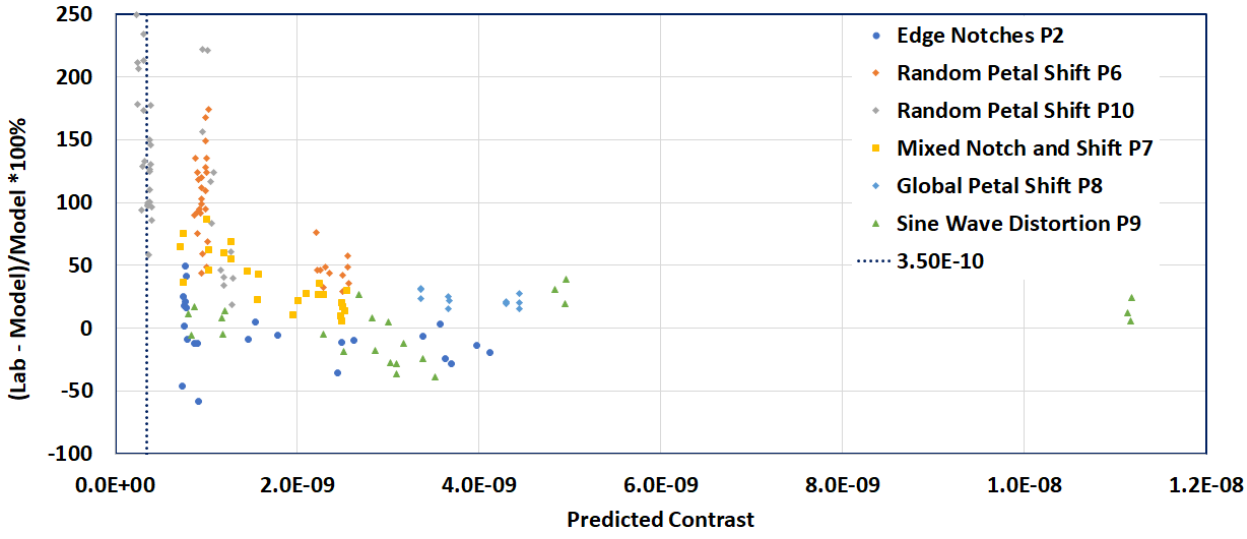

Figure 9: The same data as in Fig. 8 are plotted as a function of the predicted contrast. Data below a predicted contrast level of 3.5×10^{-10} (this includes 9 of 36 points from the M12P10 mask) are excluded from the final analysis.

Mask	Perturbation	Model Error	Crossed Analyzer RMS
M12P2	Edge Notches	-5% ± 5%	33%
M12P6 & M12P10	Shifted Petals	94% ± 6%	15%
M12P7	Shifted Petals + Notches	38% ± 11%	18%
M12P8	Global Shifted Petals	23% ± 2%	49%
M12P9	Sine Waves	0% ± 5%	33%

Table 6: Experiment - Vector Model average agreement for each mask and the weighted average for all Model Errors. The model error is the mean agreement between the experiment and model for all orientations, wavelengths, and perturbations for each mask, and the standard error of the mean.

signal. At the present time, we are unable to explain why the phase of the interference term appears to be incorrect.

Another possibility for the underestimation is that the the model is not informed with the correct petal edge position, i.e. it has been over-etched or under-etched so that the edge is pulled in or pulled back from its ideal in-plane position. We measure the edge position at the inner and outer tips with an accuracy of ∼50 nm, but this is problematic in the wider parts of the petals. If the petal edge etching rate is higher in the outer parts the petal, then the edge may be over-etched without our knowledge; an over-etch of ∼ 150 nm, if included in the model, would compensate for the destructive interference. Mask M12P10, which was manufactured 1 year after M12P6, is known to have a significant under-etch at the inner tips (Table 5); if this is not representative of the rest of the mask, the model would underestimate the contrast.

The same problem arises, but less prominently, in the multi-perturbation mask M12P7. Here, some of the perturbation light comes from the notches which are near the petal tips and at a radius outside the main polarization lobe. This reduces the coherent overlap of the perturbation and polarization fields.

It is important to keep in mind that the major contributing factor to the estimation error is the contrast of the polarization lobes, $\sim 5 \times 10^{-10}$ which is linked to the small scale of the mask. We show that the lobe intensity scales as the inverse square of the mask diameter (Appendix B of Ref. 18). It is also a function of the edge thickness and geometry, but regardless of the edge geometry, the polarization effect is confined to be within a few microns of the edge. The starshade size thus drives the polarization lobe contrast. With a flight-scale starshade 1000x larger than the laboratory starshade (e.g. a diameter of 25 m vs. 25 mm), the lobes will be 1,000,000 times fainter on-orbit, with a contrast of just 5×10^{-16}. Polarization of light by the starshade will be negligible at flight scales.

We submit Table 6 as evidence of satisfying Milestone 2. Petal shape errors are addressed in Masks M12P2 (edge notches) and M12P9 (sine waves). Here the average model agreement is no worse than a a factor of 1.05 ± 0.05, compared to the requirement to be better than a factor of 1.25. Figure 8 shows that the model was off by more than 50% for only one of 48

perturbations spots for these two masks.

Petal position errors are addressed by masks M12P6 and M12P10 (random shift), and M12P8 (global shift). While the average model agreement for the global shift was a factor of 1.23, it jumped to 1.94 ± 0.06 for the random petal position case, for reasons explained above. About half of the measured perturbation spots have model agreement worse than 100%. All of these occurred where the predicted spot contrast was $\sim 10^{-9}$ or less. We recognized before embarking on the milestone work that the presence of polarization lobes and limitations on the ability to characterize the mask would limit the experimental accuracy at contrasts below 10^{-9}, hence the stated lower limit in the text of the milestone, and indeed that has proven to be the case. The largest model errors generally occurred when the predicted contrast was below 3.5×10^{-10}. We have excluded these points from the final analysis contributing to Table 6.

The mixed perturbation mask shows an agreement factor of 1.38 ± 0.11. This is, not surprisingly, about halfway between the agreement for the petal shift (1.94 agreement) and petal shape (1.05 agreement) masks. The model accurately captures both the wavelength and spatial dependencies of the interference between the perturbations.

Finally, the table also lists the RMS agreement between the lobes observed in crossed polarizers. Polarization lobes are shown in Figures 31 - 35 in Appendix A. These lobes arise from the interaction of polarized light along the petal edges. The ability to predict the amplitude and position of the lobes depends on the accuracy of the mask edge description (Figure 7, Table 5, and Appendix B). The lobes are independent of the mask perturbations. The agreement, typically ∼30% or better, proves that the model captures the vector diffraction effects with good accuracy. Note that the polarization lobes have a contrast of just $\sim 10^{-10}$; the absolute model agreement is excellent in an absolute sense.

5 Milestone 2 Model Uncertainty Factors Applied to Flight Mission Concepts

We have developed detailed optical performance error budgets for starshade designs dating back to the Exo-S probe-scale mission concept.[19] We have also studied parametric scaling laws[20] that allow us to estimate the performance of more ambitious missions such as the Astro 2020 recommended mission[21] by considering several factors such as the telescope point-spread function resolution relative to the starshade IWA, the number of petals, and the Fresnel number.

In Figure 10, we show the error budget for the Starshade Rendezvous Mission (SRM),[22] a starshade designed to operate with the Roman Space Telescope and the current reference mission for S5. The error budget is evaluated for a wavelength of 800 nm, at the red end of the 615-800 nm band with the 26 m starshade positioned for an IWA of 104 mas. The error budget is updated to account for completed TRL-5 milestones demonstrating the capability to meet or exceed key performance parameters for petal shape accuracy and stability,[23] petal position accuracy and stability,[24] and most recently, the detailed metrology and assembly process likely to be employed for a flight system (to be published). Each box in the bottom row contains the maximum expected, or 3-sigma, contrast level from assembly

errors, deployment repeatability, instabilities including thermal cycles and thermo-elastic shape errors over the maximum expected temperature range. These ranges are $\sim$ 10-100 microns for petal shape, hundreds of microns for petal position, and a temperature range of -60°C to + 50°C for off-axis solar angles of 83° to 40° respectively.[25]

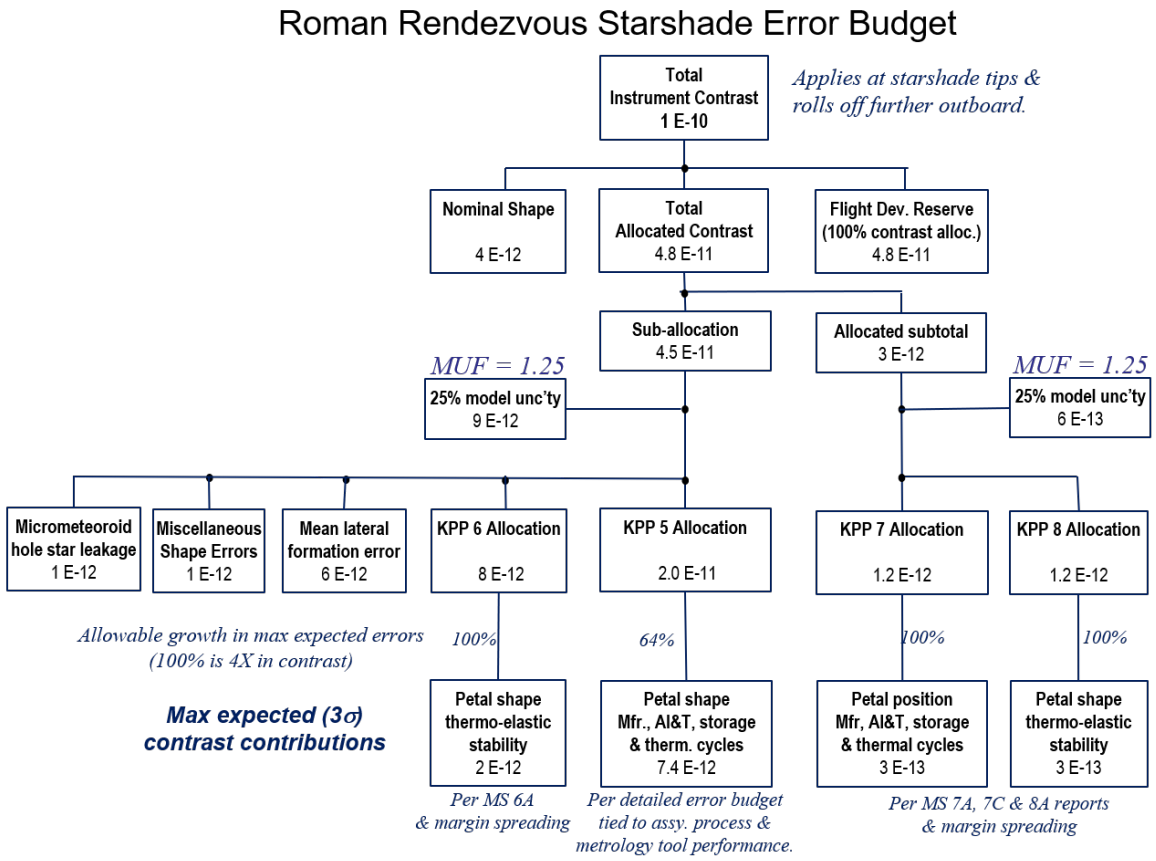

Figure 10: Instrument optical contrast error budget for the 26-m diameter Starshade Rendezvous Mission starshade. The IWA is 104 mas and is at 1.5 λ/D for λ=800 nm.

The error budget includes 100% allowable growth in most key engineering parameters, which in turn leads to a factor of 4 increase in contrast as seen in the second row from the bottom. The SRM budget is shown here with its original MUF of 1.25 applied to both petal shape and petal position contrast. Note that the petal position contributions (lower right of Figure 10) are about 10% as large as petal shape contributions (lower middle). This is the result of the relative sensitivities and relative ease of engineering for these two categories of perturbations. Continuing up the chart, we include a 100% flight development reserve on instrument contrast, leading to a total predicted contrast of 10^{-10}. We note that this contrast is evaluated at the IWA, corresponding to the tips of the starshade. The contrast improves significantly at angles > IWA.

The Astro 2020 report[21] recommends investment in technology development for a 6-m telescope with the ability to image and characterize exoplanets. We have evaluated several

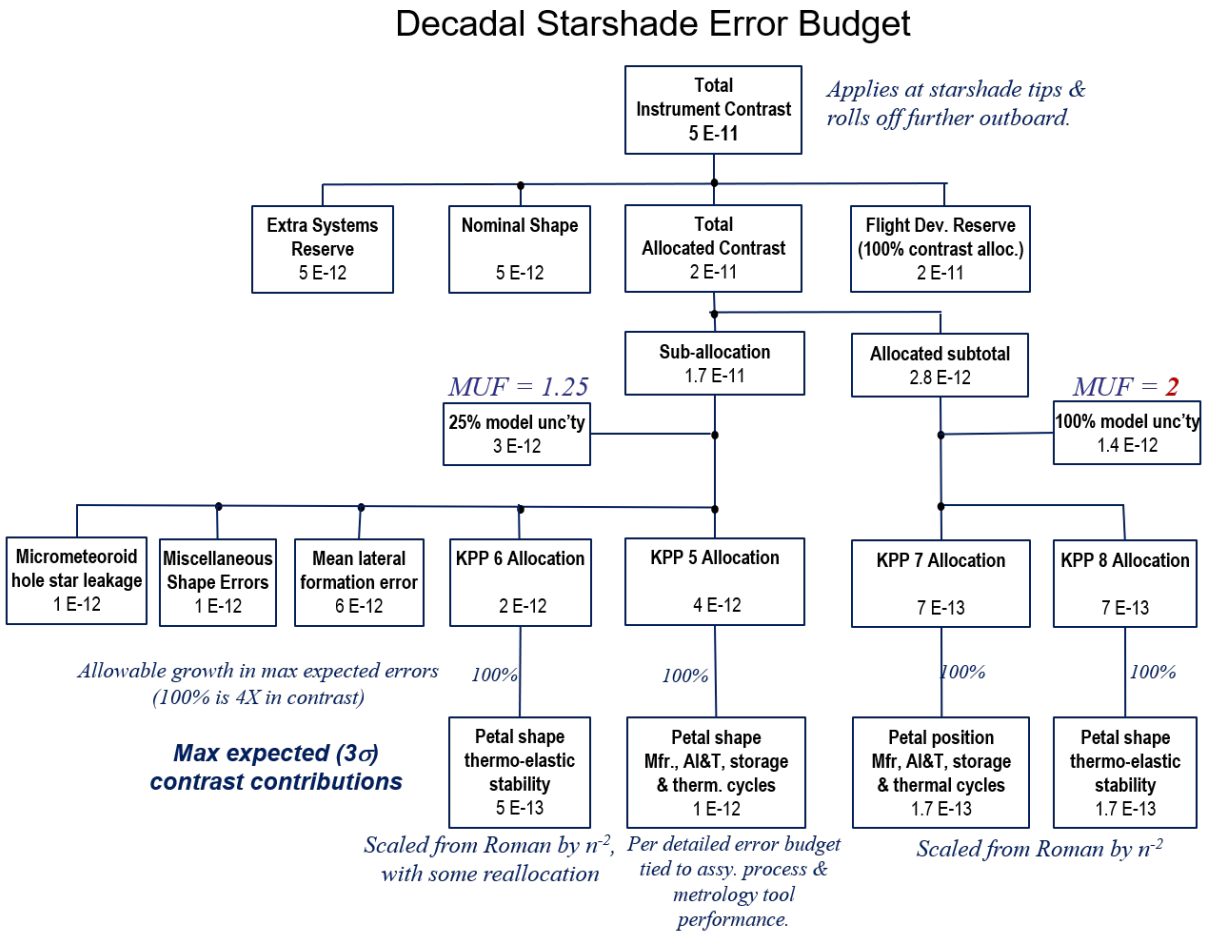

Figure 11: Instrument optical contrast error budget for a 64-m starshade with a 6-m diameter telescope. The wavelength is 1000 nm, and is at 2 λ/D for the λ = 1000 nm.

starshade designs that would enable an on-axis 6-m telescope to do this with high optical efficiency, broad bandwidth, deep contrast, a relatively simple camera, and perhaps most importantly, without imposing extreme wavefront stability requirements on the optical train. One possible design is a 64-m diameter starshade consisting of a 32 m inner disk supporting 24 16-m long petals. The design, which we call the "Decadal" starshade concept, operates simultaneously over a 250-1000 nm bandpass with IWA = 69 mas. Figure 11 shows the error budget, evaluated at 1000 nm and at the IWA. Here we have assumed that the magnitude of the perturbations scales linearly with starshade size. For example, a 100 micron petal position error on SRM becomes a 64/26 = 246 micron error in the Decadal starshade. This is likely to be a worst case scenario because many assembly errors are limited by metrology noise that is independent of distance, and by workmanship such as mechanical shimming precision that is independent of overall diameter.

There are 2 key differences between the Decadal and SRM error budgets. First, the Decadal telescope resolves the starshade at n = 2 λ/D (1000 nm / 6 m = 34.4 mas) while

the 2.4 m Roman telescope resolves the SRM starshade at $n = 1.5$ λ/D. This matters because most of the scattered light from perturbations in the shape of the starshade originates well within the IWA. The telescope partially resolves and localizes the light so that its effect at the IWA is reduced. We have shown[20] that this effect scales approximately as $\sim n^{-3}$, following the radial roll-off of an Airy function. However, for perturbations that are close to the IWA, the roll-off can be less pronounced. We have conservatively assumed that we gain only as n^{-2} in this error budget. Still, that is a decrease in contrast by a factor $(2/1.5)^2 = 1.8$, all else remaining the same.

Second, we have applied a MUF of 2 to the petal position terms. Compared to using MUF=1.25, this adds an additional 10^{-12} to the allocated subtotal for petal position, and another 10^{-12} once the 100% flight development contrast reserve is included. This represents just 4% of the total instrument contrast budget of $5times10^{-11}$. Thus we conclude that the experimentally measured petal position modeling error is easily absorbed into the starshade error budget.

6 Conclusion

Since its "first light" in 2017, the Princeton in-air 80-m starshade testbed successfully demonstrated deep contrast with a floor of 2×10^{-11} over a broad band, at flight-like Fresnel numbers, and successfully validated optical modelling including accurate predictions of diffraction in purposely distorted starshades.

The model validation experiments addressed the key building blocks of the starshade optical shape error budget including petal edge manufacturing, petal shape distortion, and petal position. The experiments also validated the contrast predictions when multiple perturbations are present.

Prediction accuracy was limited by the presence of diffraction lobes that are most pronounced at the inner gaps where petals meet. These lobes arise because polarized light interacts with the edges of the starshade. The lobe shape, position, and amplitude are accurately predicted by models that account for the edge shape parameters. However, we found that the interference of the lobes with the perturbations from shifted petals is not in agreement with the models. The laboratory data is in agreement with the model if we include a $\pi/4$ phase shift in the polarized light, and separately if we incoherently combine the polarized and scalar light. But we do not at this time have a viable justification for either of these possibilities. The polarization effect is negligible in a full-scale starshade because the area of the edge interaction shrinks 1000-fold relative to the area of the starshade when compared to the laboratory scale.

Another possibility is that the polarization model is correct, while our assumption of a uniform over- or under-etch of the petal edge is not. This might be the case because the etch rate, even through our 2 micron thick silicon layer, can be different in the tips and open areas. We can accurately measure the etch with a precision of $\sim$50 nm in the 20 micron wide petal tips. But we have not found a way to make the measurement in the few-mm wide openings that form most of the starshade. This also will not be an issue with a full-scale starshade where we employ 5-micron accurate metrology against petal width requirements of $\sim$ 100 microns.

Nevertheless, the experimental model agreement is better than a factor of two for petal position and better than a factor of 1.25 for petal shape. When the MUFs are applied to assembly and thermal distortion measurements of a 4-m scale prototype petal, and to assembly and repeatability measurements of a 10-m scale prototype inner disk, all appropriately scaled up to full flight scale, the flight starshade error budget yields excellent performance. The error budget predicts that the Decadal starshade will have at least 2x deeper contrast than SRM, and perhaps 4x deeper as warranted by the milestone progress to date. Mainly driven by the telescope resolution relative to the IWA, this dwarfs the effect of the experimentally measured MUF.

Acknowledgments

This work was performed in part at the Jet Propulsion Laboratory, California Institute of Technology under a contract with the National Aeronautics and Space Administration (80NM0018D0004). Starshade masks were manufactured using the facilities at the Microdevices Lab at JPL. A.H. performed all of the experiments and image contrast analysis reported herein. D. McKeithen contributed modeling to verify FDTD results and imaged the mask edges on a scannning electron microscope. This project made use of the resources from the Princeton Institute for Computational Science and Engineering (PICSciE) and the Office of Information Technology's High Performance Computing Center and Visualization Laboratory at Princeton University. The authors acknowledge the use of Princeton's Imaging and Analysis Center, which is partially supported through the Princeton Center for Complex Materials (PCCM), a National Science Foundation (NSF)-MRSEC program (DMR-2011750).

References

[1] P. Willems, "Starshade to TRL5 (S5) Technology Development Plan," *Jet Propulsion Laboratory Publications*, 2018. https://exoplanets.nasa.gov/internal_resources/1033/.

[2] A. Harness, S. Shaklan, N. J. Kasdin, *et al.*, "Starshade technology development activity Milestone 1A: Demonstration of high contrast in monochromatic light at a flight-like Fresnel number," *Jet Propulsion Laboratory Publications*, 2019. https://exoplanets.nasa.gov/internal_resources/1210/.

[3] A. Harness, S. Shaklan, N. J. Kasdin, *et al.*, "Starshade technology development activity Milestone 1B: Demonstration of high contrast in broadband light at a flight-like Fresnel number," *Jet Propulsion Laboratory Publications*, 2019. https://exoplanets.nasa.gov/internal_resources/1211/.

[4] S. Shaklan, A. Harness, N. Kasdin, *et al.*, "Completion of model validation experiments at the princeton starshade testbed," *Proc. SPIE*, vol. 12180, 2022.

[5] M. Aria, D. Webb, F. Mechentel, *et al.*, "Starshade technology development activity Milestone 7C: Demonstration of dimensional stability of perimeter truss bay longeron and node," *Jet Propulsion Laboratory Publications*, 2020. https://exoplanets.nasa.gov/internal_resources/1677/.

[6] M. Aria, D. Webb, J. Steeves, *et al.*, "Starshade technology development activity Milestone 7A: Demonstration of deployment accuracy of the starshade inner disk subsystem," *Jet Propulsion Laboratory Publications*, 2020. https://exoplanets.nasa.gov/internal_resources/1676/.

[7] D. Webb, S. C. Bradford, J. Steeves, *et al.*, "Starshade technology development activity Milestone 8A: Verify petal position on-orbit stability," *Jet Propulsion Laboratory Publications*, 2020. https://exoplanets.nasa.gov/internal_resources/1696/.

[8] S. Martin and T. Flinois, "Simultaneous sensing of telescope pointing and starshade position," *Journal of Astronomical Telescopes, Instruments, and Systems*, vol. 8, no. 1, pp. 014010–1 – 014010–18, 2022.

[9] A. Chen, A. Harness, and P. Melchior, "Lightweight starshade position sensing with convolutional neural networks and simulation-based inference," *arXiv:2204.03853v*, 2022. [doi.org/10.48550/arXiv.2204.03853].

[10] A. Harness, S. Shaklan, P. Willems, N. Kasdin, K. Balasubramanian, *et al.*, "Optical experiments and model validation of perturbed starshade designs," *Proc. SPIE*, vol. 11823, no. 12, pp. 1–9, 2021.

[11] A. Harness, S. Shaklan, W. Cash, and P. Dumont, "Advances in edge diffraction algorithms," *J. Opt. Soc. Am. A*, vol. 35, pp. 275 – 285, Feb. 2018. [doi:10.1364/JOSAA.35.000275].

[12] E. Cady, "Boundary diffraction wave integrals for diffraction modeling of external occulters," *Optics Express*, vol. 20, p. 15196, Jul. 2012. [doi:10.1364/OE.20.015196].

[13] W. Cash, "Analytic modeling of starshades," *The Astrophysical Journal*, vol. 738, p. 76, Aug. 2011. [doi:10.1088/0004-637X/738/1/76].

[14] A. H. Barnett, "Efficient high-order accurate Fresnel diffraction via areal quadrature and the nonuniform fast Fourier transform," *Journal of Astronomical Telescopes, Instruments, and Systems*, vol. 7, no. 2, pp. 1 – 19, 2021.

[15] A. H. Barnett, J. Magland, and L. af Klinteberg, "A parallel nonuniform fast fourier transform library based on an "exponential of semicircle" kernel," *SIAM Journal on Scientific Computing*, vol. 41, no. 5, pp. C479–C504, 2019.

[16] A. Harness, "Implementing non-scalar diffraction in Fourier optics via the Braunbek method," *Optics Express*, vol. 28, 2020.

[17] A. F. Oskooi, D. Roundy, M. Ibanescu, P. Bermel, J. Joannopoulos, and S. G. Johnson, "Meep: A flexible free-software package for electromagnetic simulations by the FDTD method," *Computer Physics Communications*, vol. 181, no. 3, pp. 687 – 702, 2010.

[18] A. Harness, S. Shaklan, P. Willems, N. J. Kasdin, B. K. Balasubramanian, P. Dumont, V. White, K. Yee, R. Muller, and M. Galvin, "Optical verification experiments of sub-scale starshades," *Journal of Astronomical Telescopes, Instruments, and Systems*, vol. 7, no. 2, pp. 1 – 32, 2021.

[19] S. Shaklan, L. Marchen, E. Cady, *et al.*, "Error budgets for exoplanet starshade (exos) probe-class mission study," *Proc. SPIE*, vol. 9605, no. 96050Z, pp. 96050Z–1 – 965050Z–14, 2015.

[20] S. Shaklan, L. Marchen, and E. Cady, "Shape accuracy requirements on starshades for large and small apertures," *Proc. SPIE*, vol. 10400, no. 104001T, pp. 104001T–1 – 104001T–10, 2017.

[21] National Academies of Science, Engineering and Medicine, *Pathways to Discovery in Astronomy and Astrophysics*. Washington DC: The National Academies Press, 2021. [doi.org/10.17226/26141].

[22] A. Romero-Wolf, G. Bryden, S. Seager, N. J. Kasdin, *et al.*, "Starshade rendezvous: exoplanet sensitivity and observing strategy," *Journal of Astronomical Telescopes, Instruments, and Systems*, vol. 7, no. 2, pp. 021210–1 – 021210–28, 2021.

[23] D. Webb, M. Arya, S. Bradford, E. Hilgemann, *et al.*, "Advances in starshade technology readiness for an exoplanet characterizing science mission in the 2020's," *Proc. SPIE*, vol. 11117, p. 0P, 2019.

[24] M. Arya, F. Mechentel, D. Webb, *et al.*, "Demonstration of deployment repeatability of key subsystems of a furled starshade architecture," *Journal of Astronomical Telescopes, Instruments, and Systems*, vol. 7, no. 2, pp. 021202–1 – 021202–29, 2021.

[25] D. Webb, J. Steeves, F. Mechentel, M. Arya, *et al.*, "Starshade technology development activity Milestone 6A: Verify petal shape on-orbit stability," *Jet Propulsion Laboratory Publications*, 2021. https://exoplanets.nasa.gov/internal_resources/2008/.

Appendix A: Experiment Data and Model Comparison

In this section we present the main experimental results and comparisons to the optical model. Experimental and model images are shown for three mask orientations at four wavelengths. In comparisons between experiment and model, we use the average contrast calculated in a photometric aperture of radius 1 λ/D[†], centered on the perturbation. D is the 5 mm diameter of the camera entrance pupil. The full derivation of the contrast calculation is presented in Appendix A of Ref. 18. For M12P8, the perturbations appear as a ring at the base of the petals; the contrast for this mask is calculated as the average contrast in a $2 \times \lambda/D$ wide annulus centered on the base of the petals.

Below we show images in the nominal polarization for M12P2, and M12P7-M12P10. Masks M12P3-5 were defective. We also show crossed-polarization data for M12P2 and M12P6-M12P9. We did not collect crossed-polarization data for M12P10 due to time constraints.

[†]The perturbations of M12P7 are not point-like, so a photometric aperture of radius $1.5 \times \lambda/D$ is used.

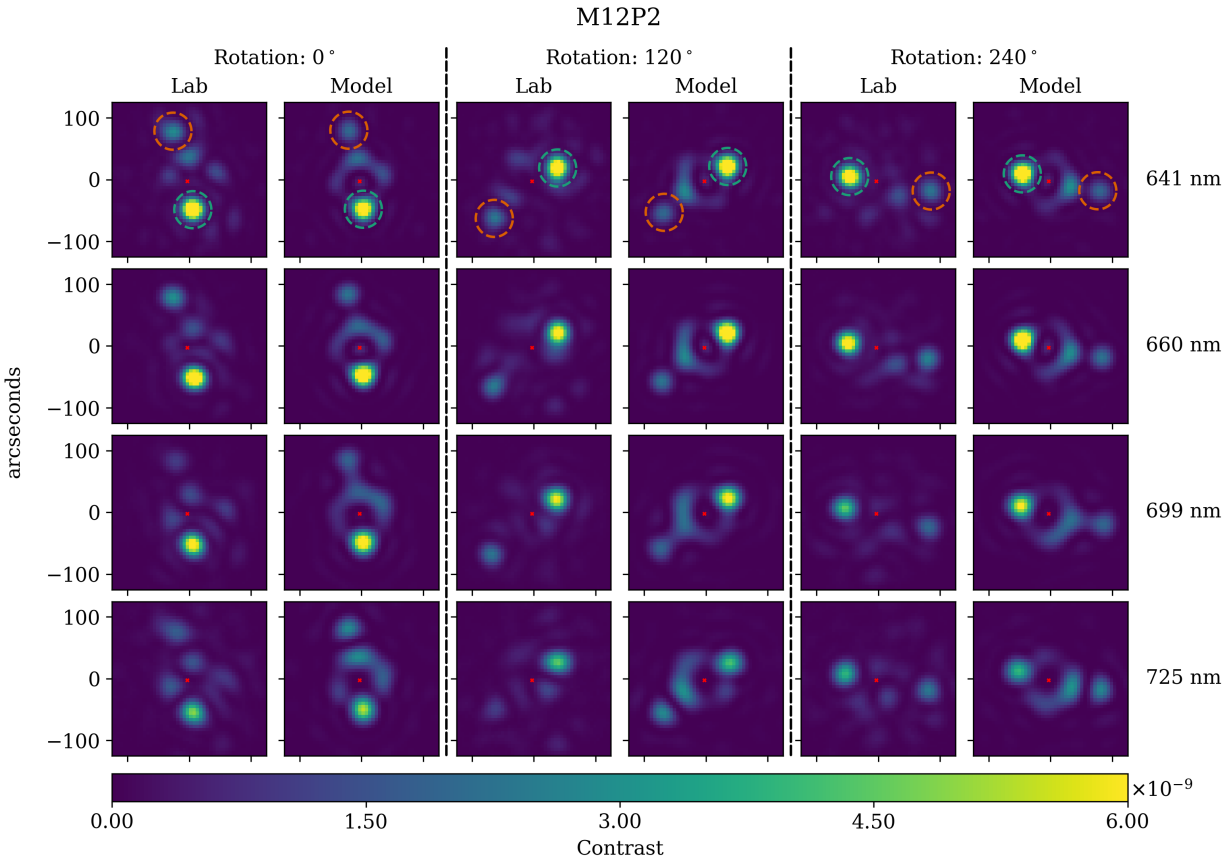

Figure 12: Experimental and vector model images of M12P2. Three groups of two columns show the mask at three rotation angles. Rows correspond to four wavelengths. The color of the circles denote the same perturbation and match the colors in Fig. 13. The red dots indicate the optical axis defined by the point source and the center of the starshade mask.

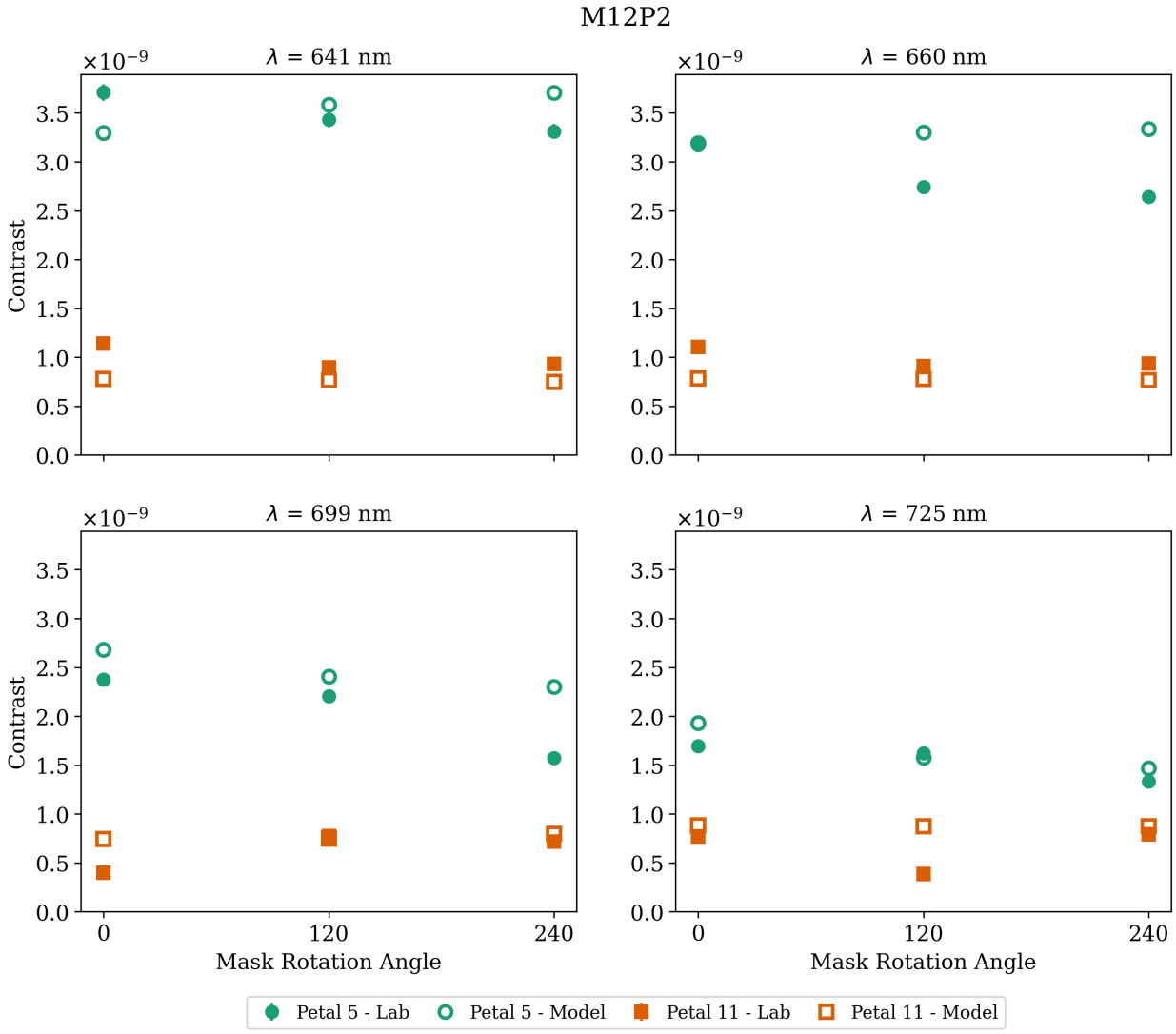

Figure 13: Perturbation contrast for M12P2. Open markers correspond to model contrast. Closed markers correspond to experiment contrast.

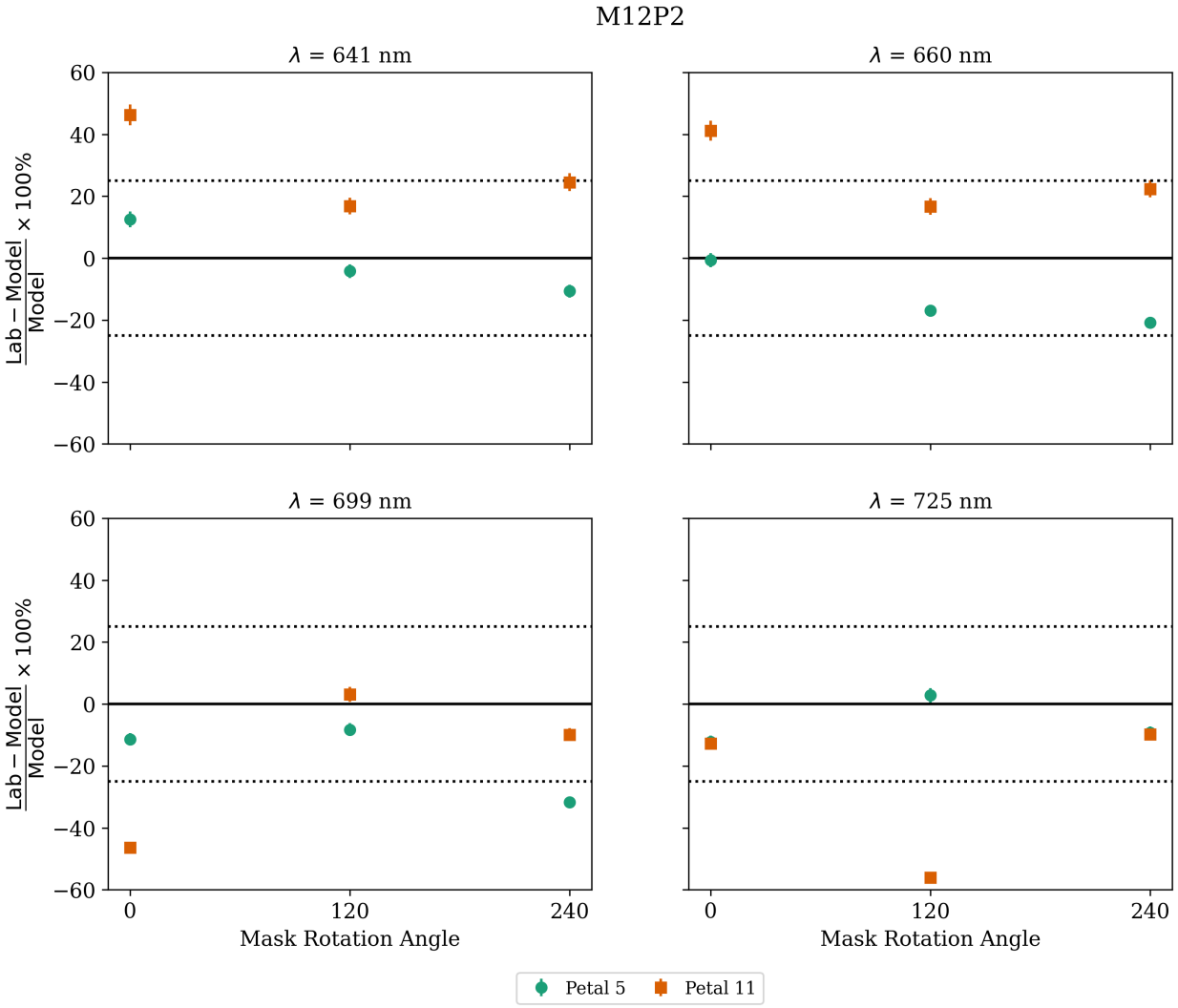

Figure 14: Comparison between experiment and model contrast for M12P2.

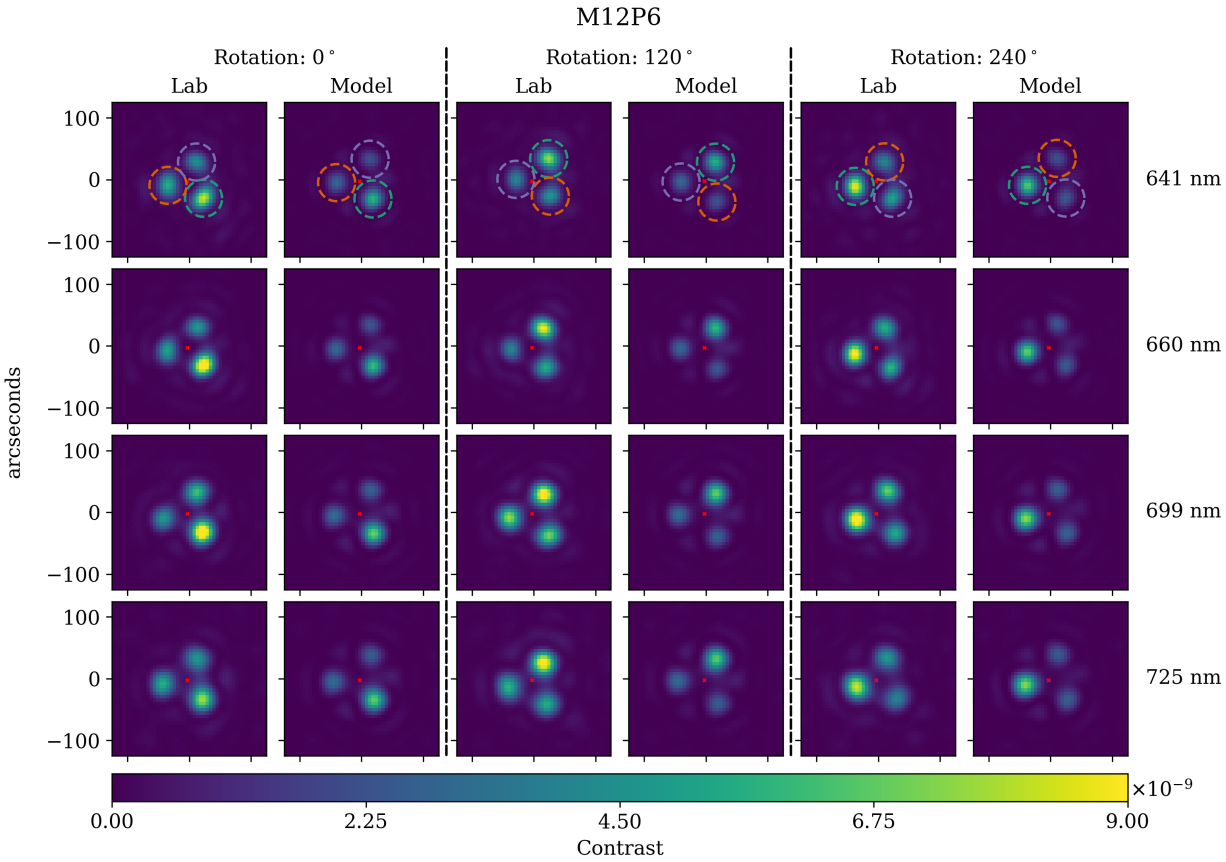

Figure 15: Experimental and vector model images of M12P6. Three groups of two columns show the mask at three rotation angles. Rows correspond to four wavelengths. The color of the circles denote the same perturbation and match the colors in Fig. 16. The red dots indicate the optical axis defined by the point source and the center of the starshade mask.

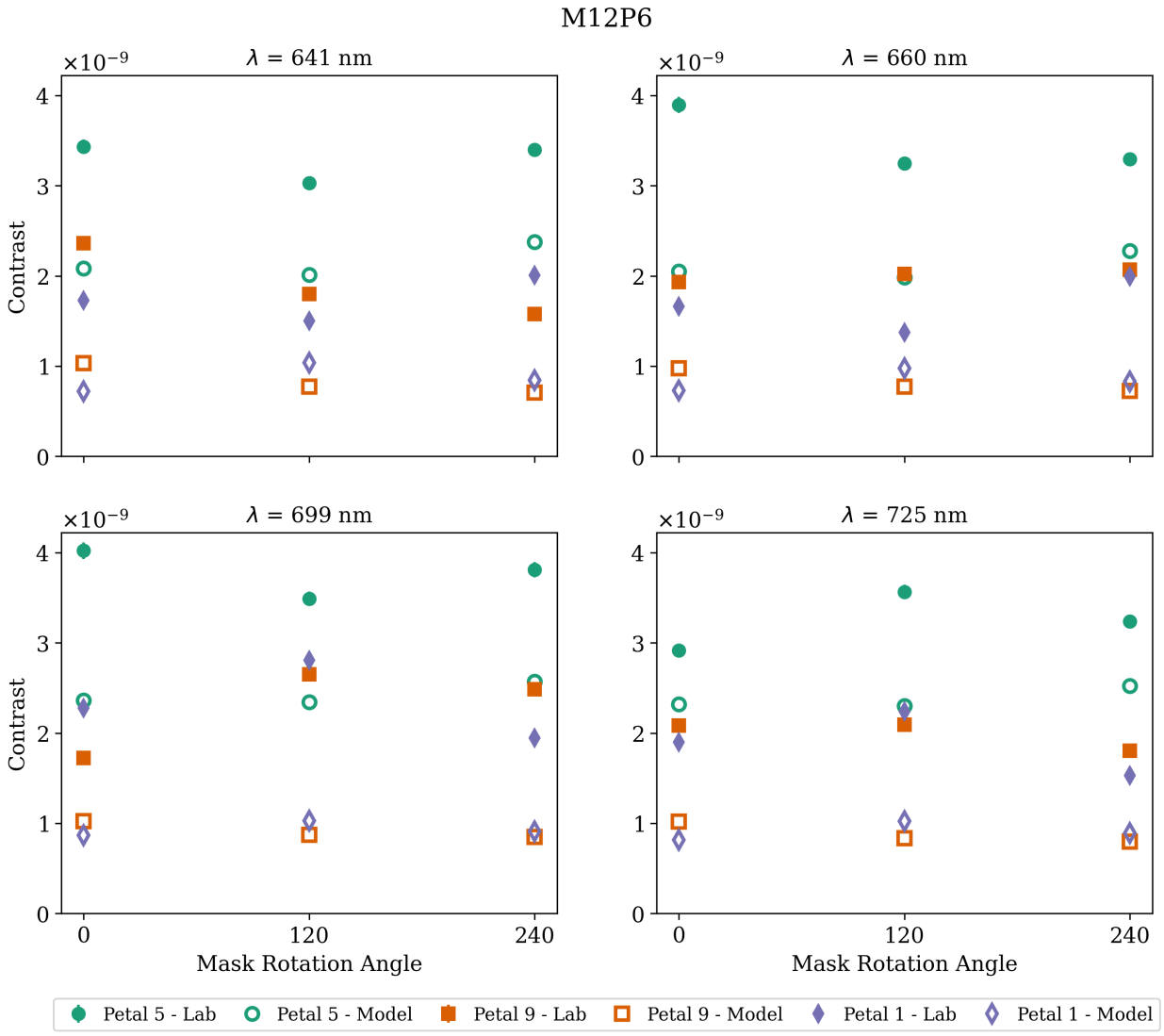

Figure 16: Perturbation contrast for M12P6. Open markers correspond to model contrast. Closed markers correspond to experiment contrast.

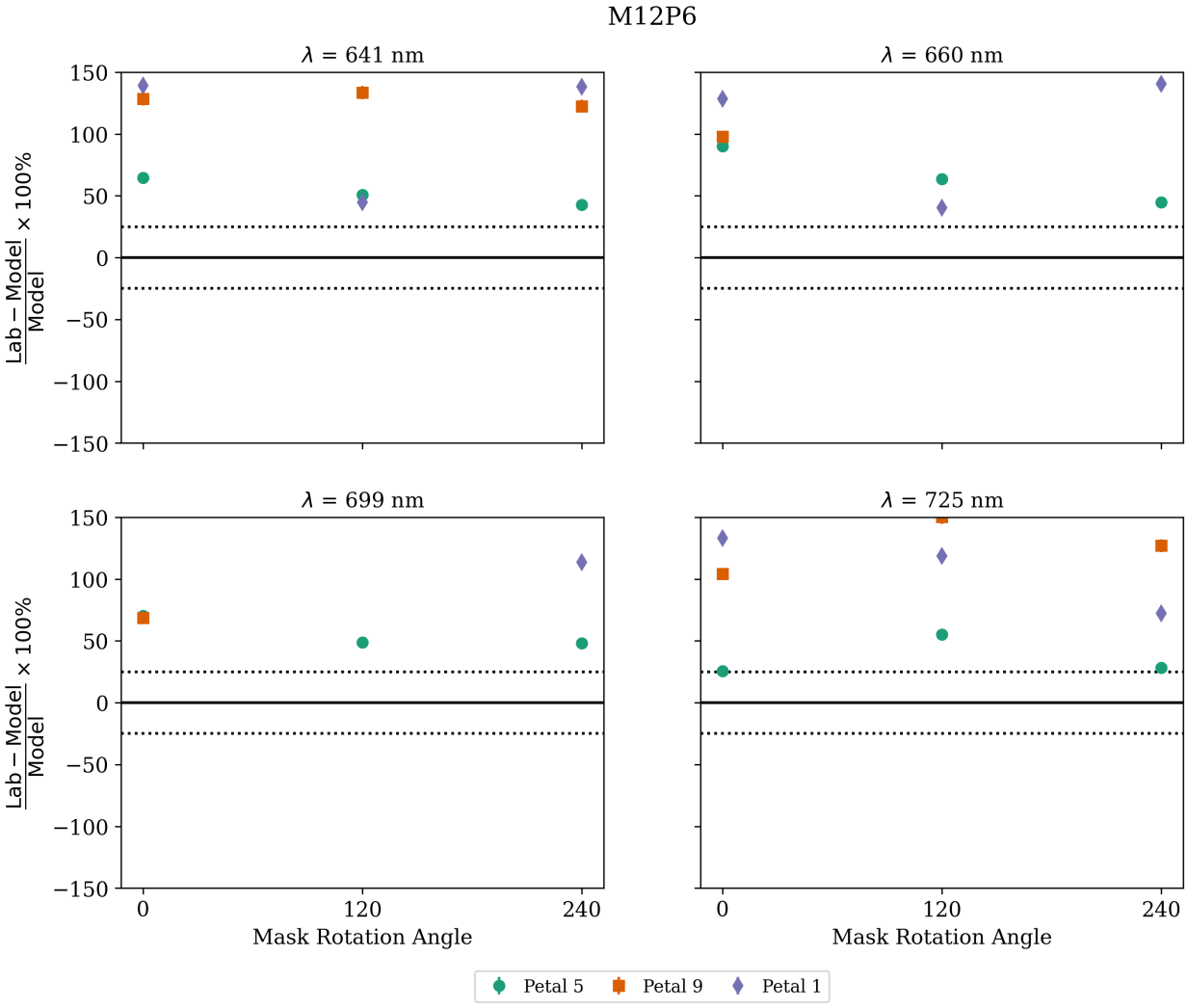

Figure 17: Comparison between experiment and model contrast for M12P6.

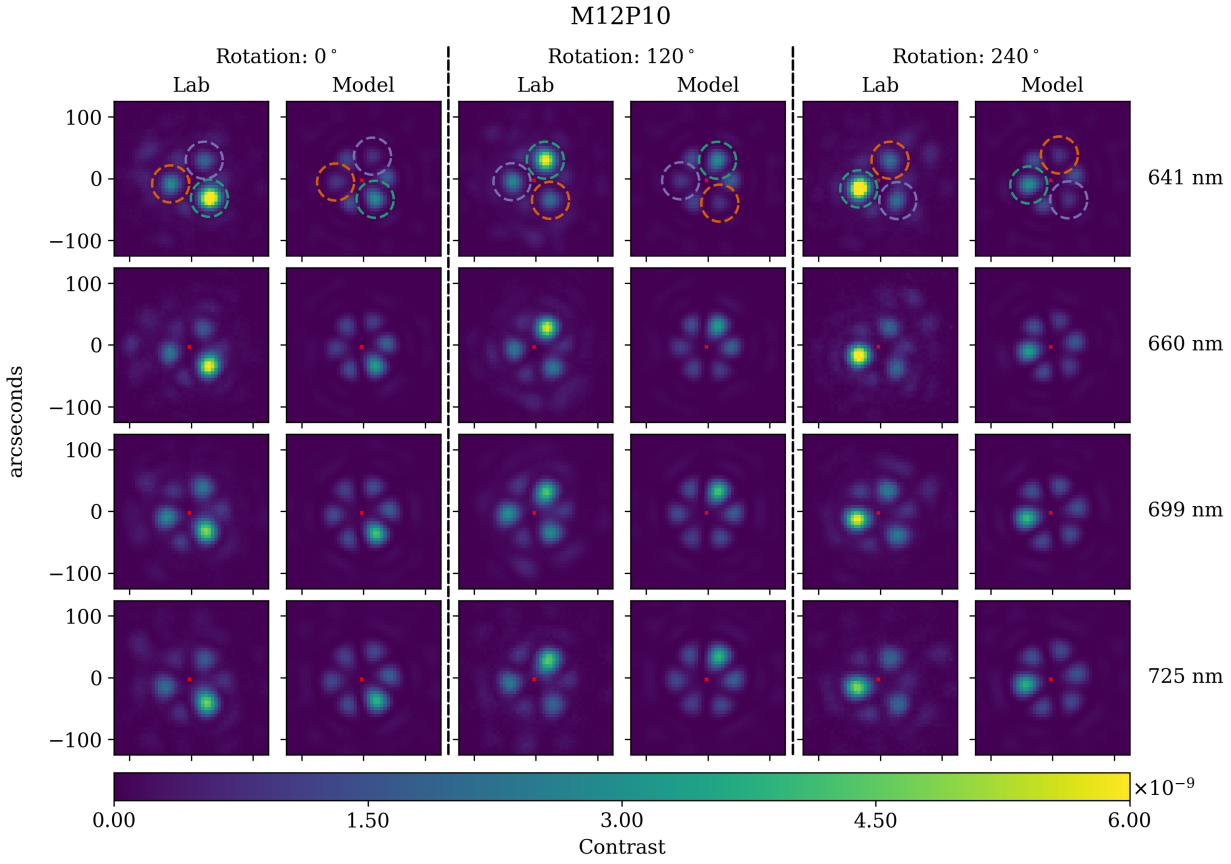

Figure 18: Experimental and vector model images of M12P10. Three groups of two columns show the mask at three rotation angles. Rows correspond to four wavelengths. The color of the circles denote the same perturbation and match the colors in Fig. 19. The differences between the M12P6 and M12P10 images (particularly the extra lobes appearing between the perturbation lobes) are due to the 270nm overetch of M12P10. The red dots indicate the optical axis defined by the point source and the center of the starshade mask.

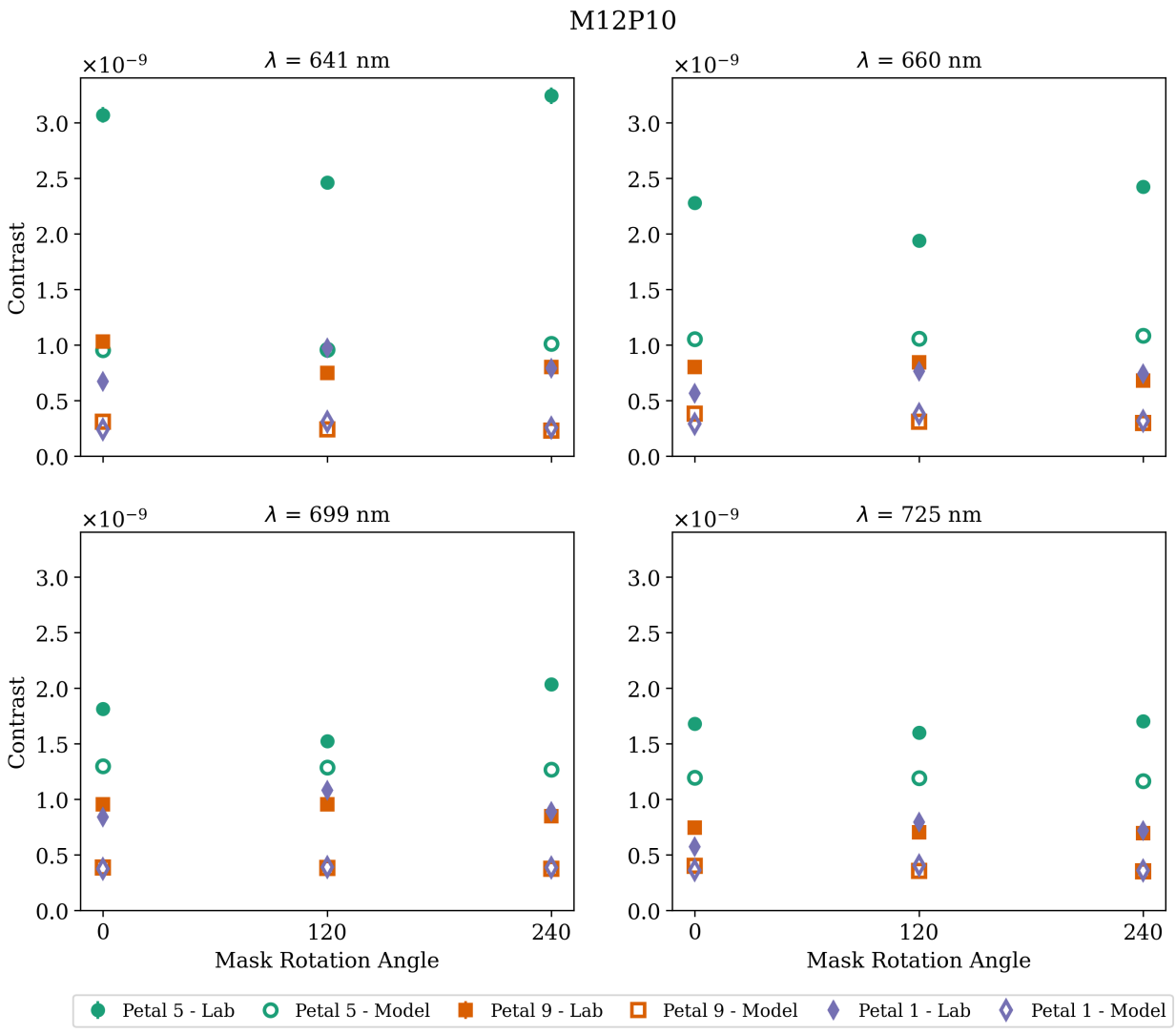

Figure 19: Perturbation contrast for M12P10. Open markers correspond to model contrast. Closed markers correspond to experiment contrast.

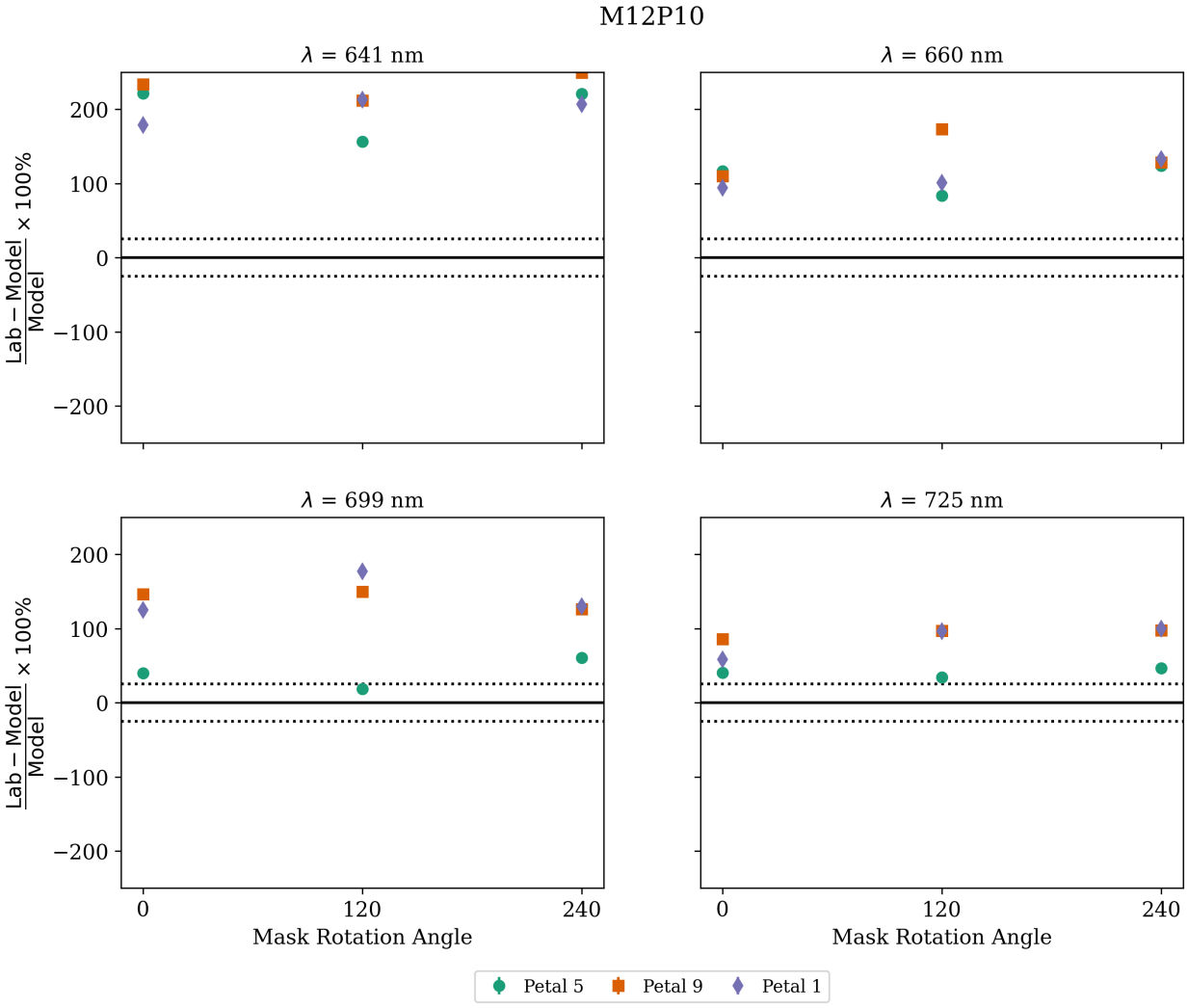

Figure 20: Comparison between experiment and model contrast for M12P10.

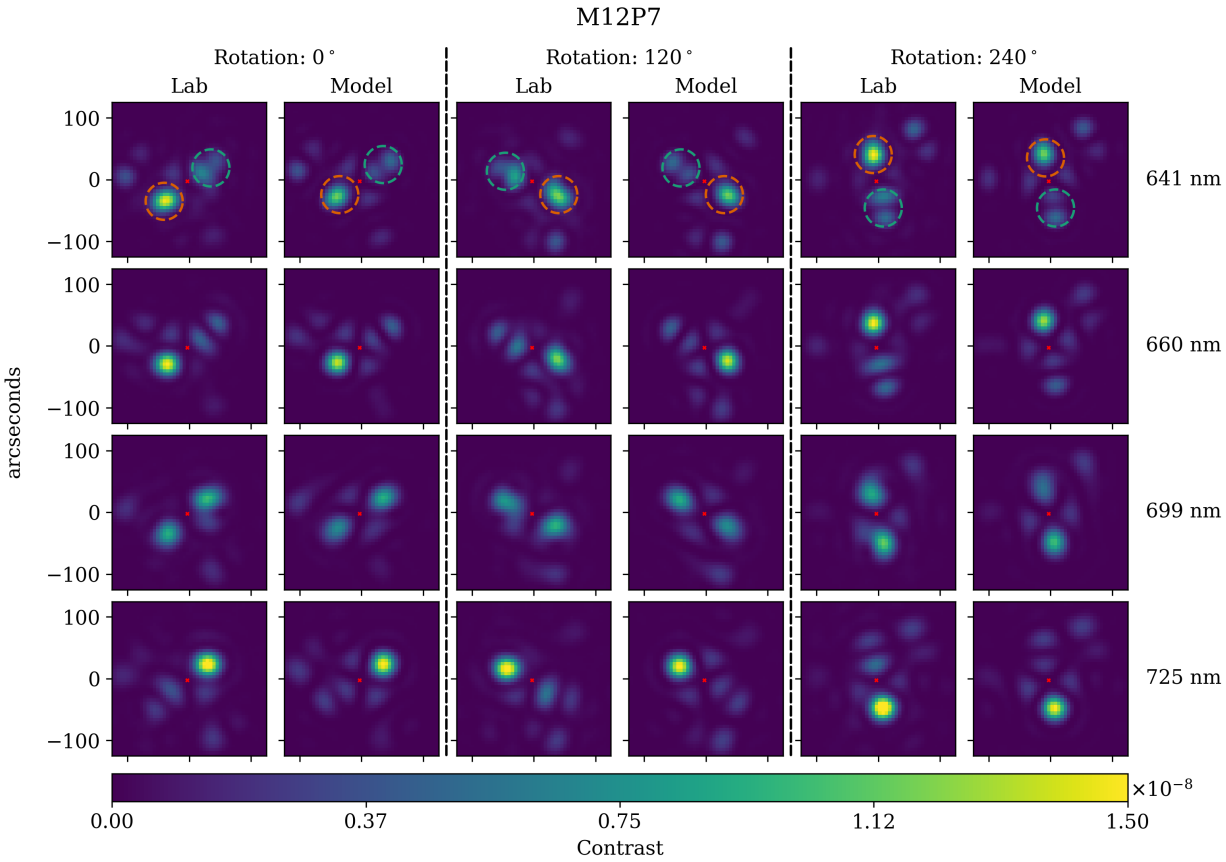

Figure 21: Experimental and vector model images of M12P7. Three groups of two columns show the mask at three rotation angles. Rows correspond to four wavelengths. The color of the circles denote the same perturbation and match the colors in Fig. 22. The red dots indicate the optical axis defined by the point source and the center of the starshade mask.

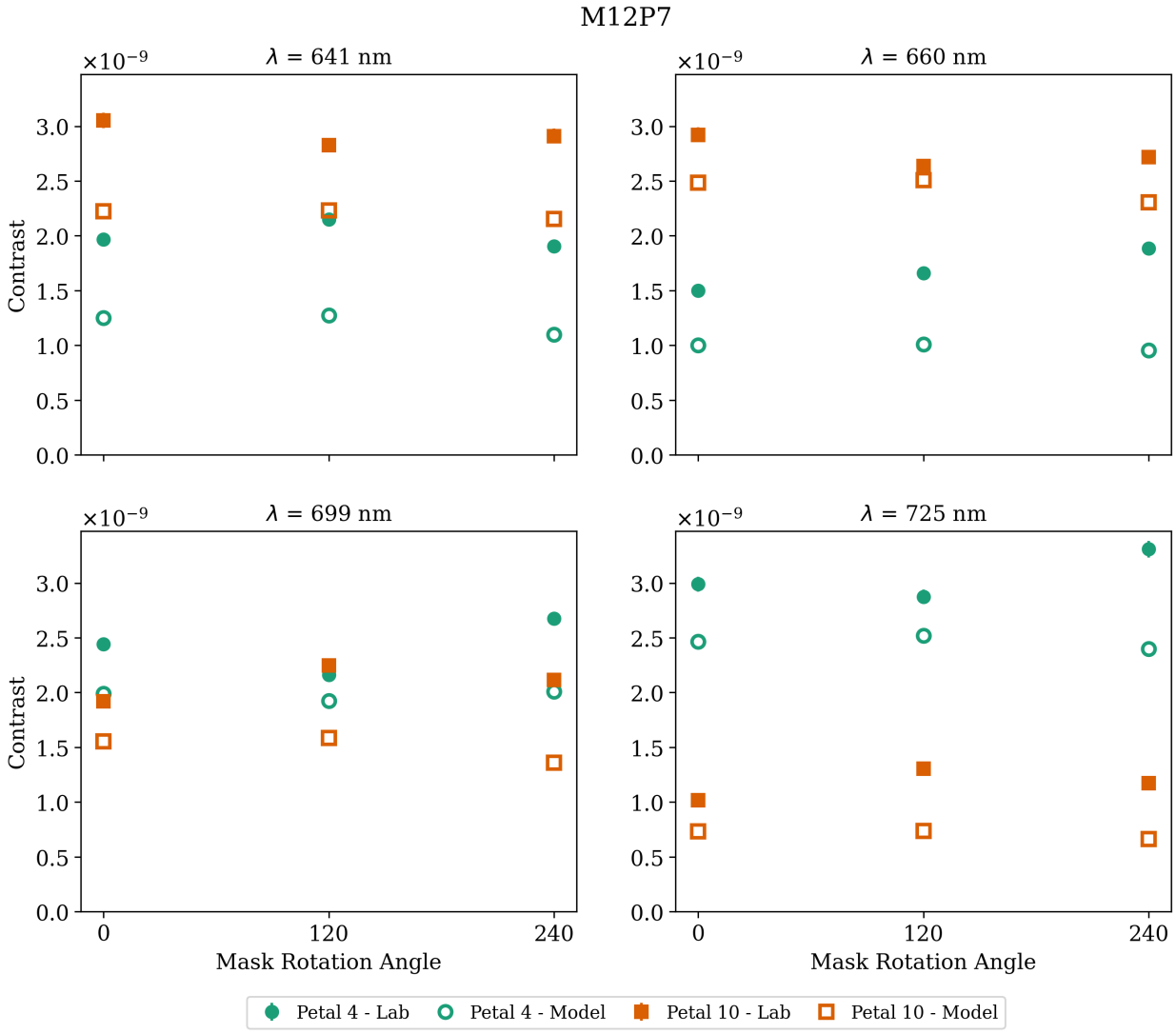

Figure 22: Perturbation contrast for M12P7. Open markers correspond to model contrast. Closed markers correspond to experiment contrast.

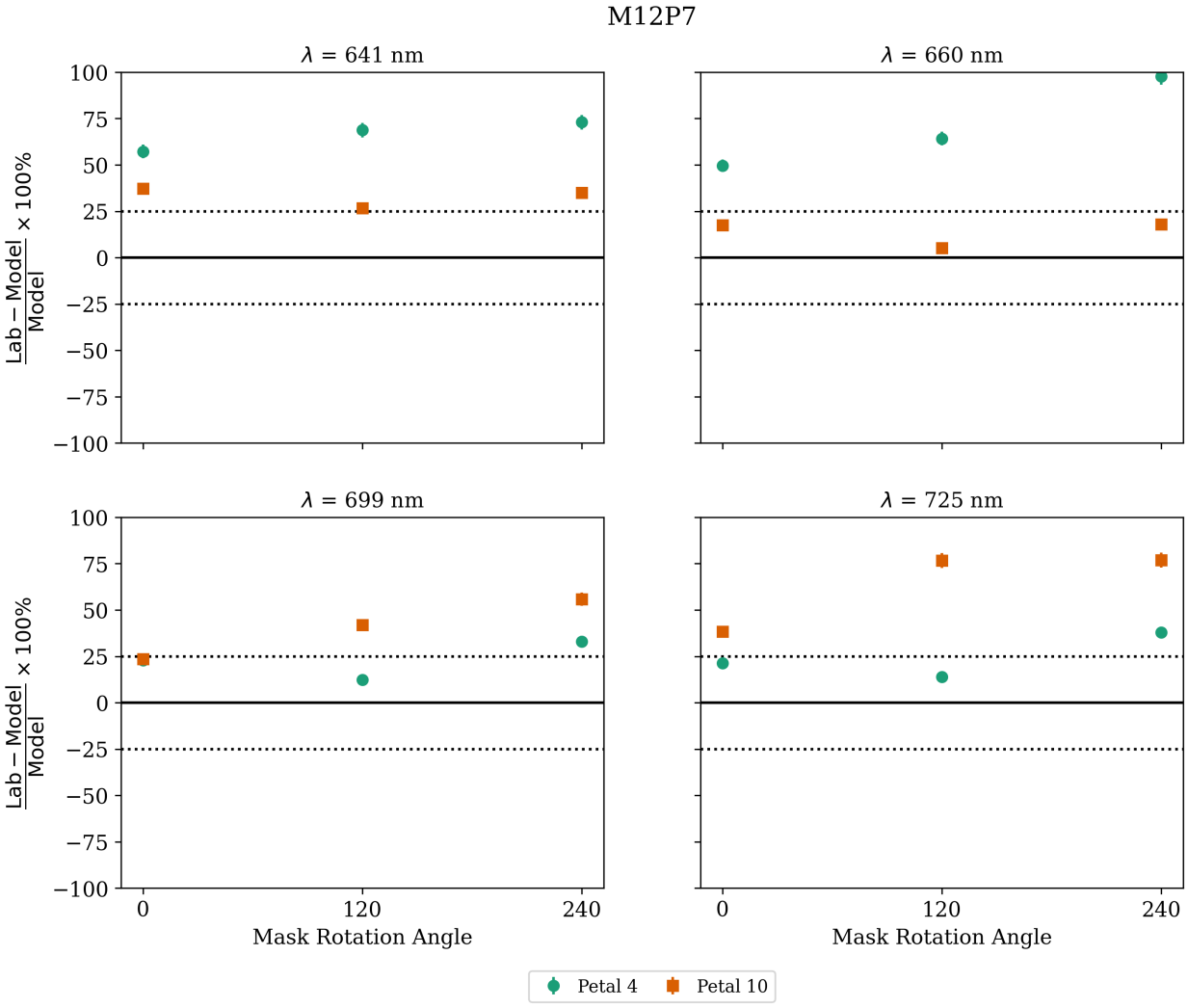

Figure 23: Comparison between experiment and model contrast for M12P7.

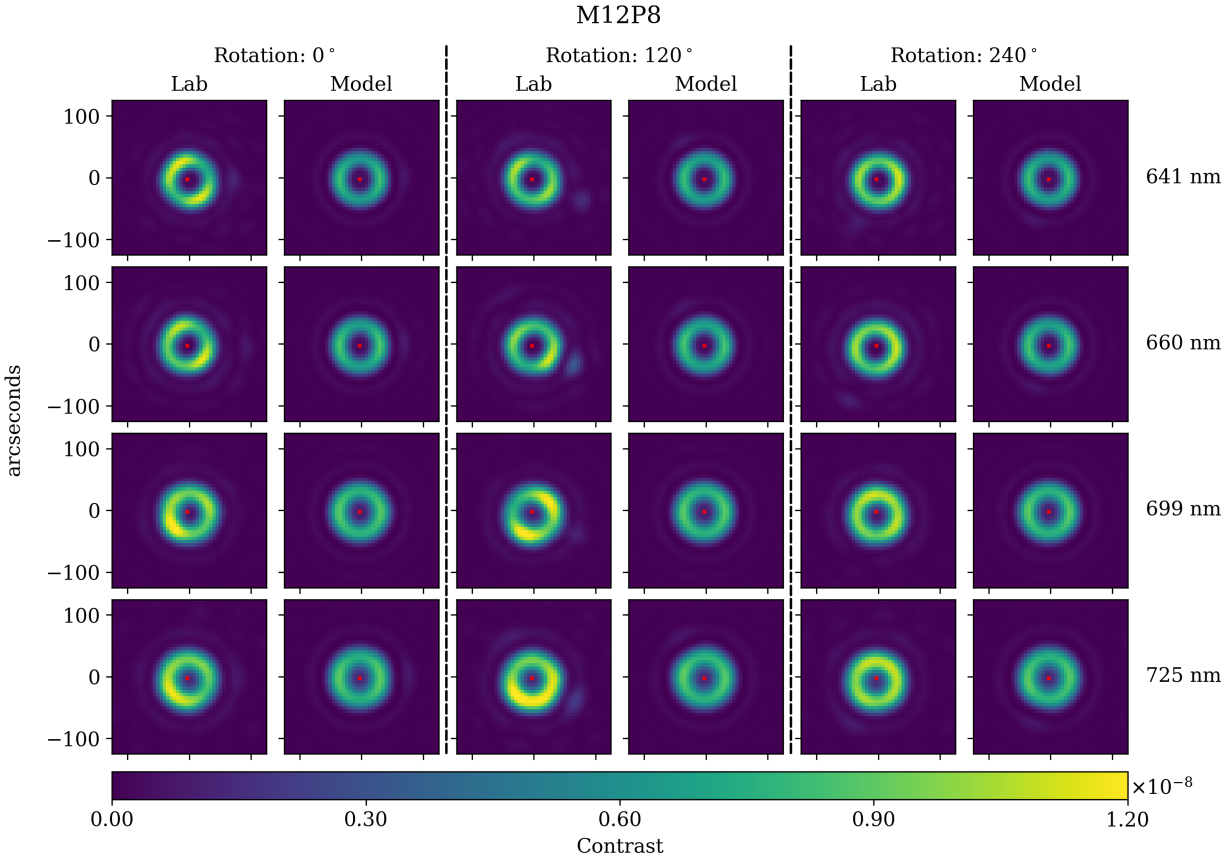

Figure 24: Experimental and vector model images of M12P8. Three groups of two columns show the mask at three rotation angles. Rows correspond to four wavelengths. The red dots indicate the optical axis defined by the point source and the center of the starshade mask.

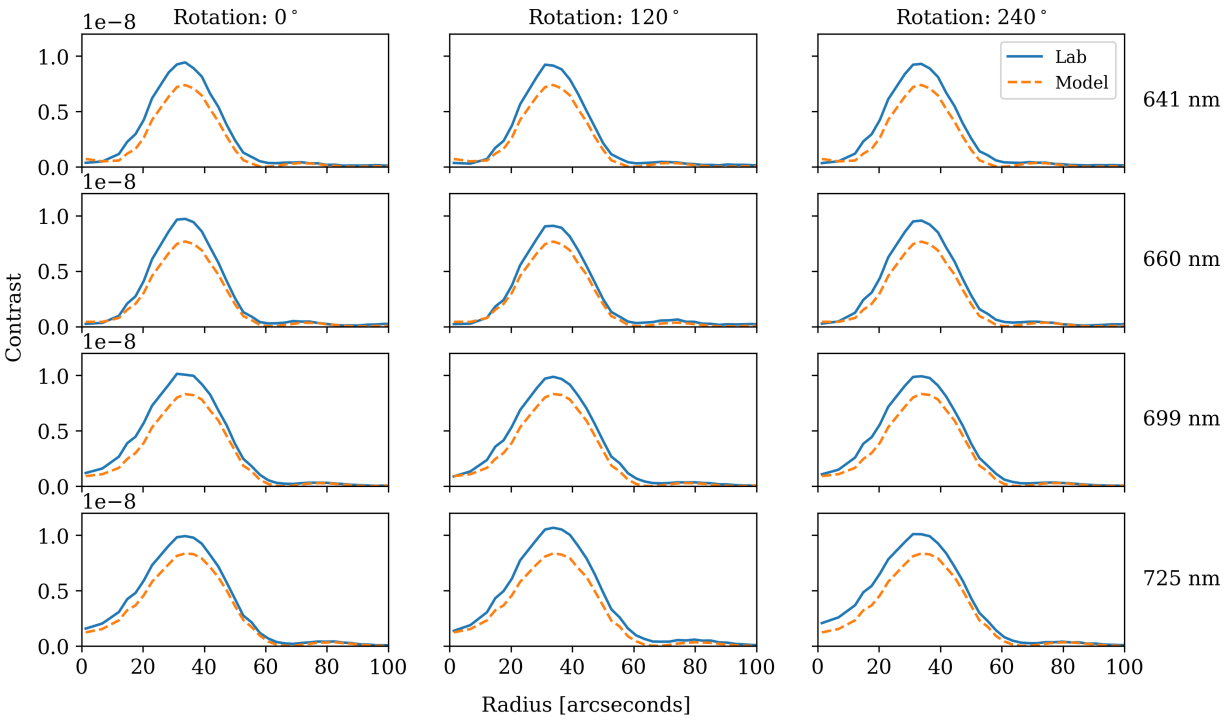

Figure 25: Azimuthally averaged contrast as a function of radius for M12P8. Solid line denotes experimental data; dash line denotes model data. Three columns show the mask at three rotation angles. Rows correspond to four wavelengths.

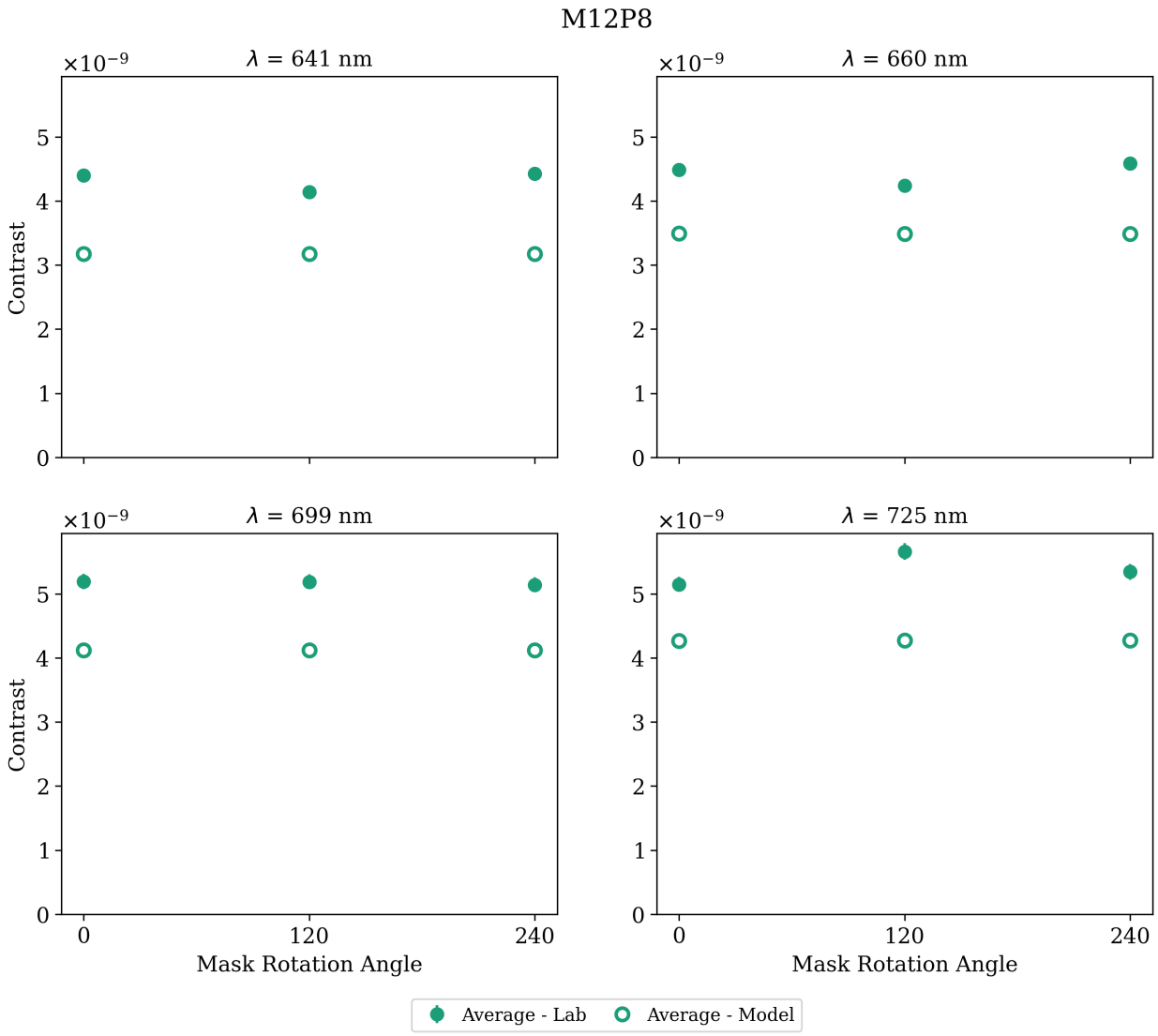

Figure 26: Perturbation contrast for M12P8. Open markers correspond to model contrast. Closed markers correspond to experiment contrast.

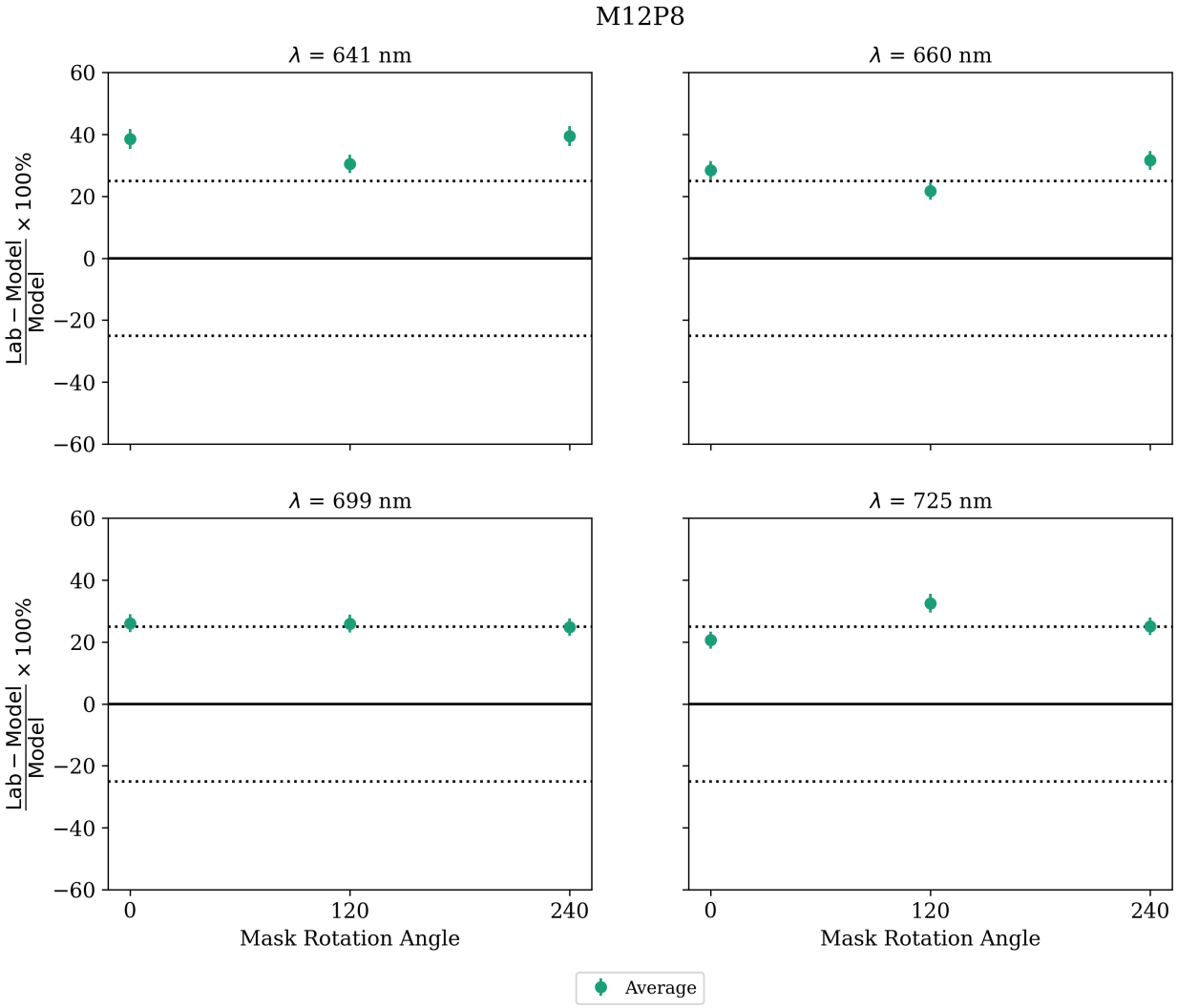

Figure 27: Comparison between experiment and model contrast for M12P8.

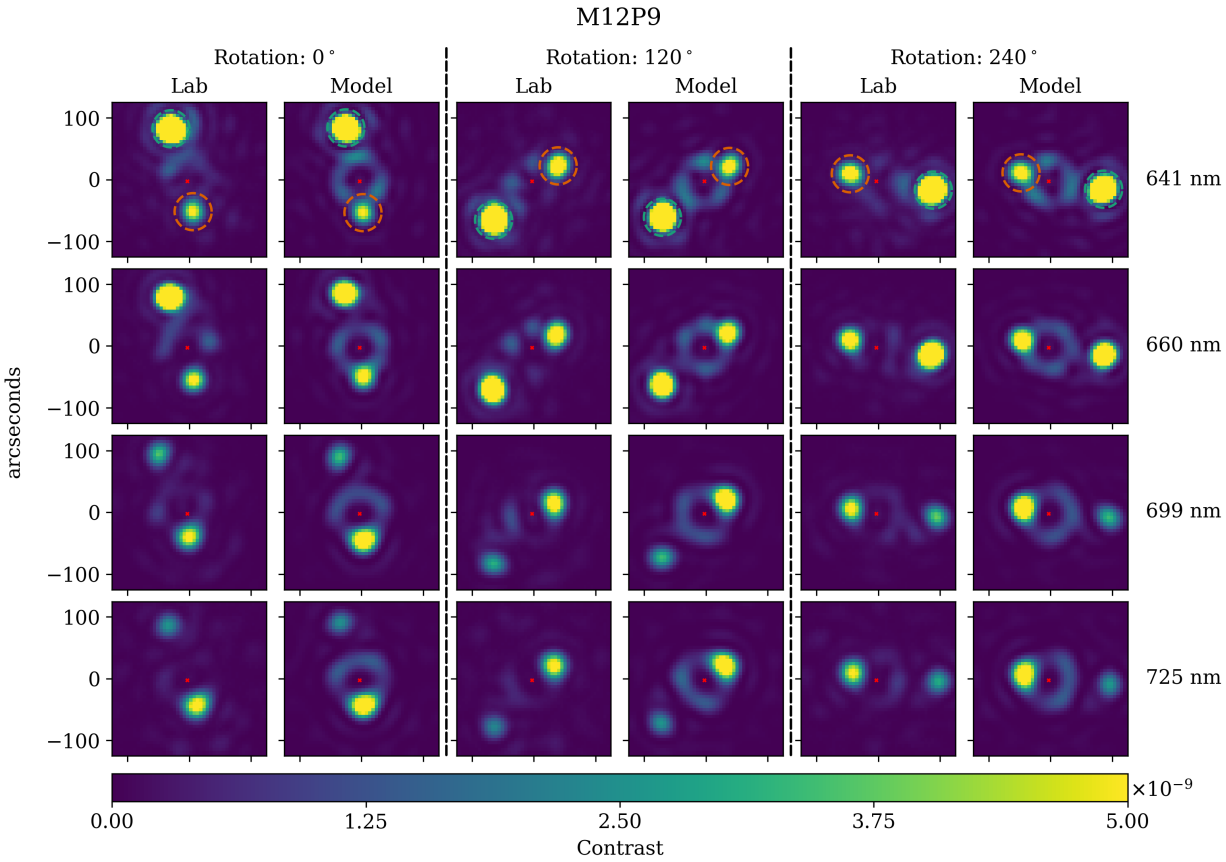

Figure 28: Experimental and vector model images of M12P9. Three groups of two columns show the mask at three rotation angles. Rows correspond to four wavelengths. The color of the circles denote the same perturbation and match the colors in Fig. 29. The red dots indicate the optical axis defined by the point source and the center of the starshade mask.

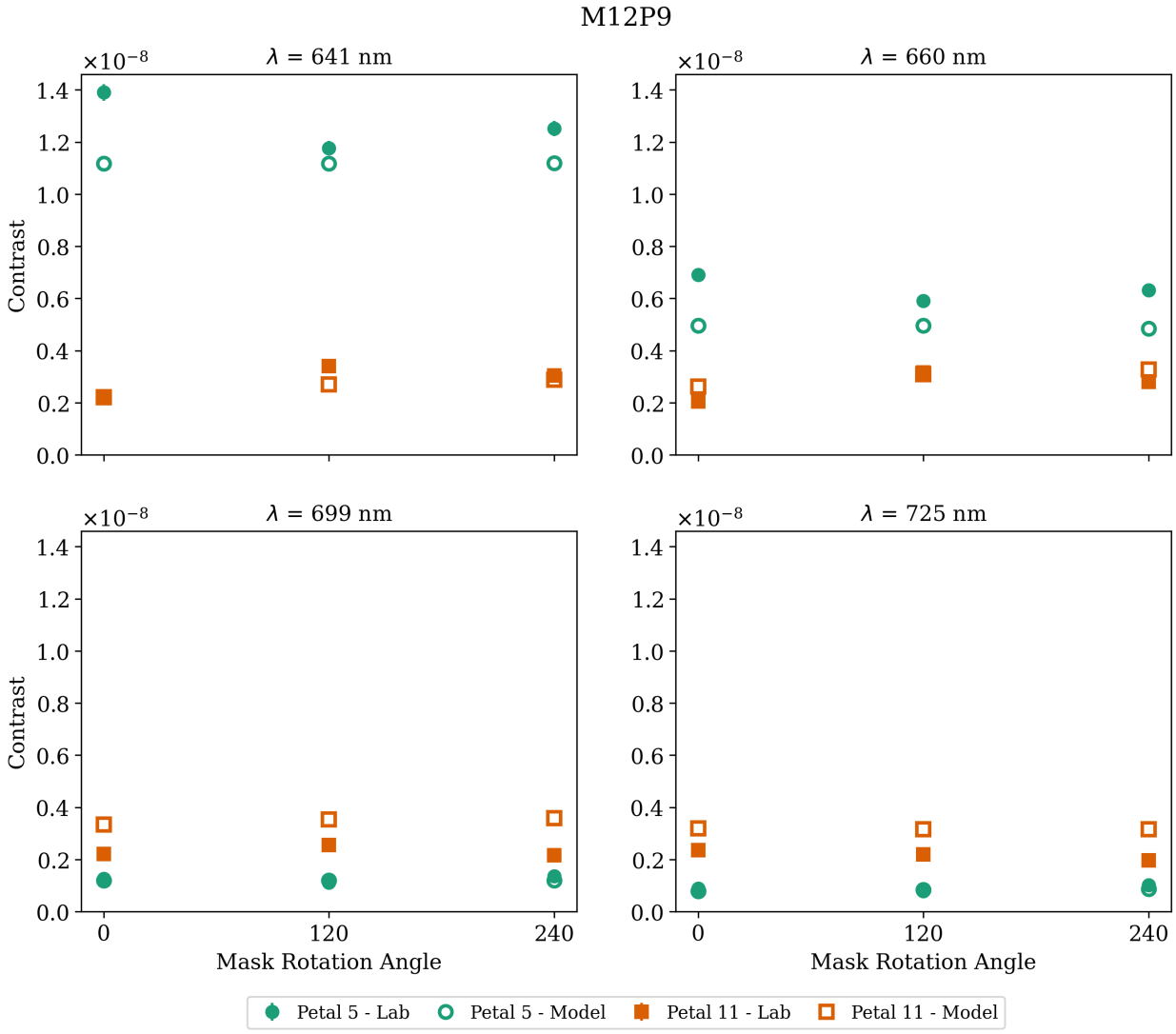

Figure 29: Perturbation contrast for M12P9. Open markers correspond to model contrast. Closed markers correspond to experiment contrast.

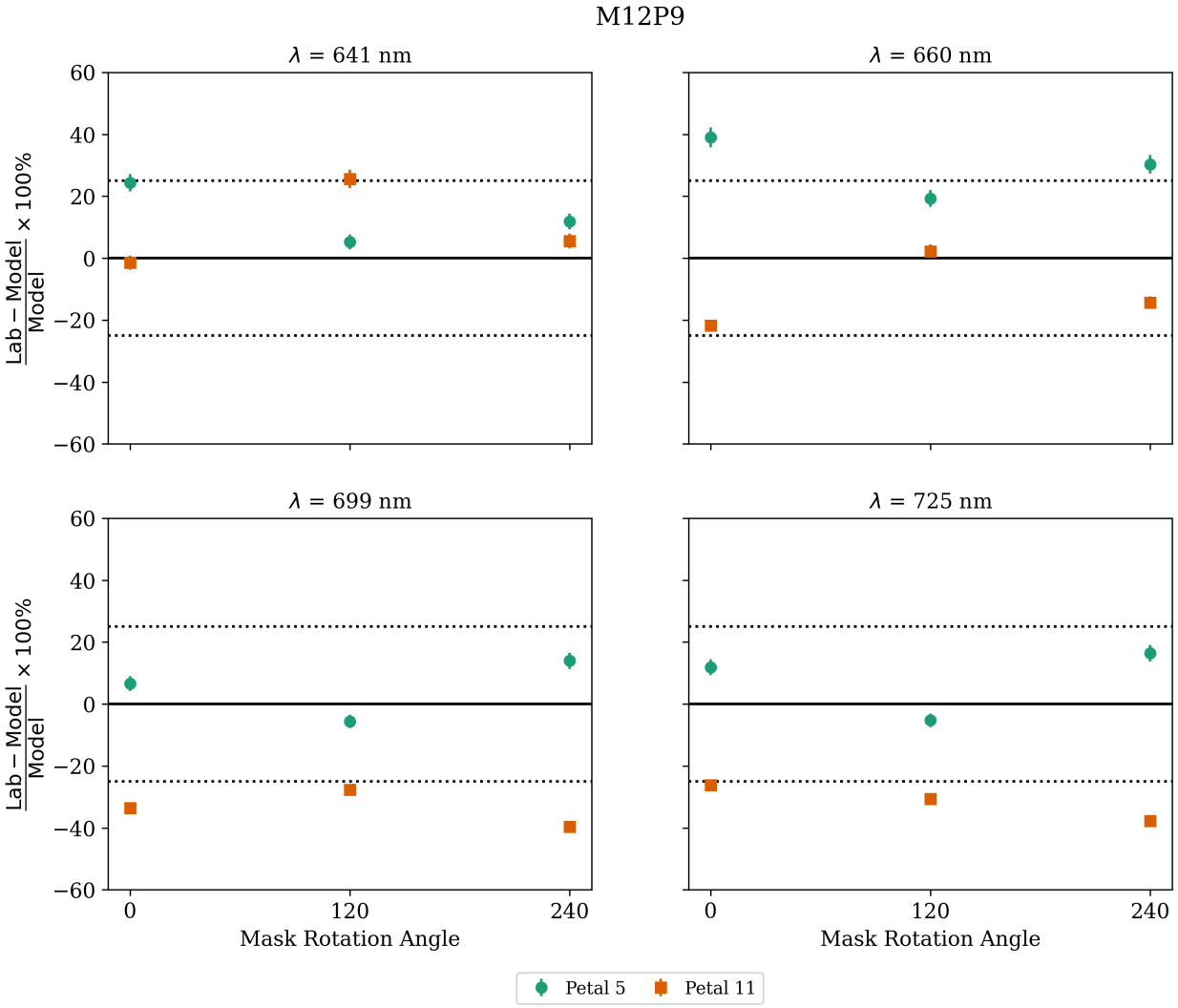

Figure 30: Comparison between experiment and model contrast for M12P9.

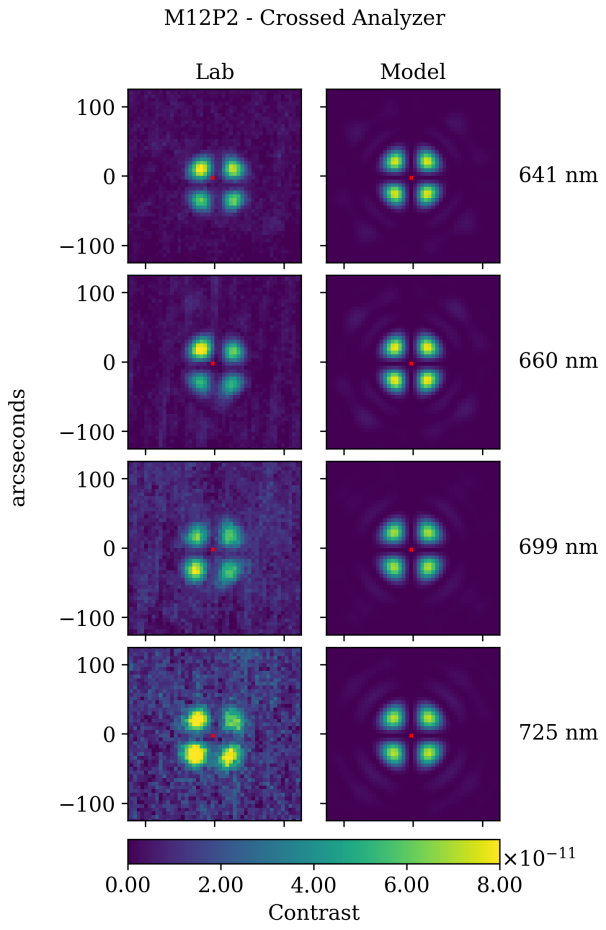

Figure 31: Crossed-analyzer data and model for M12P2.

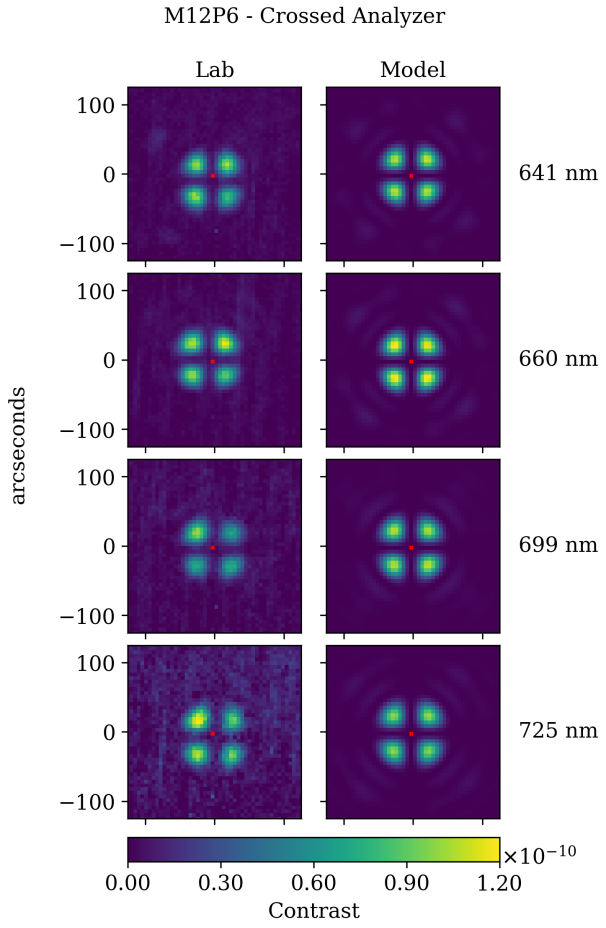

Figure 32: Crossed-analyzer data and model for M12P6.

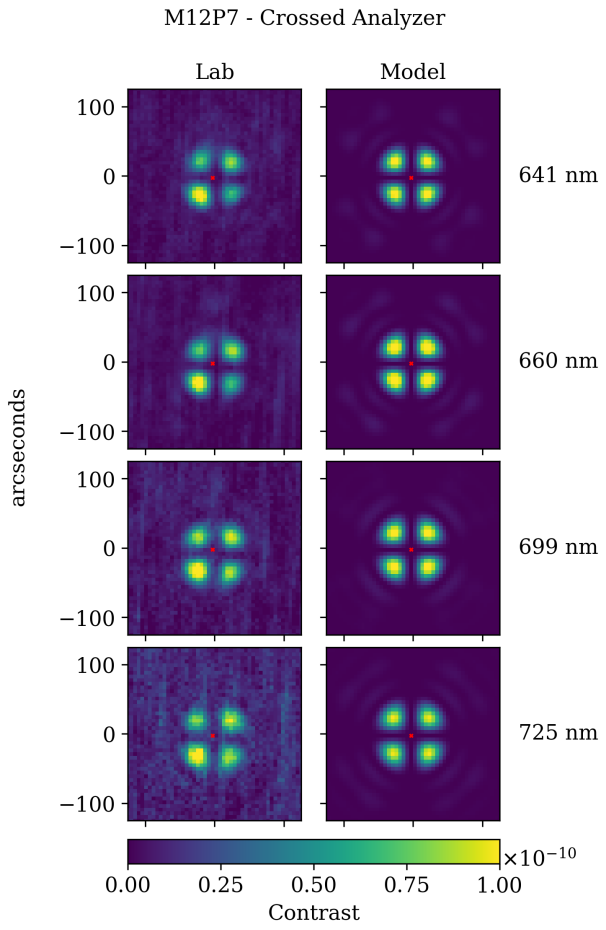

Figure 33: Crossed-analyzer data and model for M12P7.

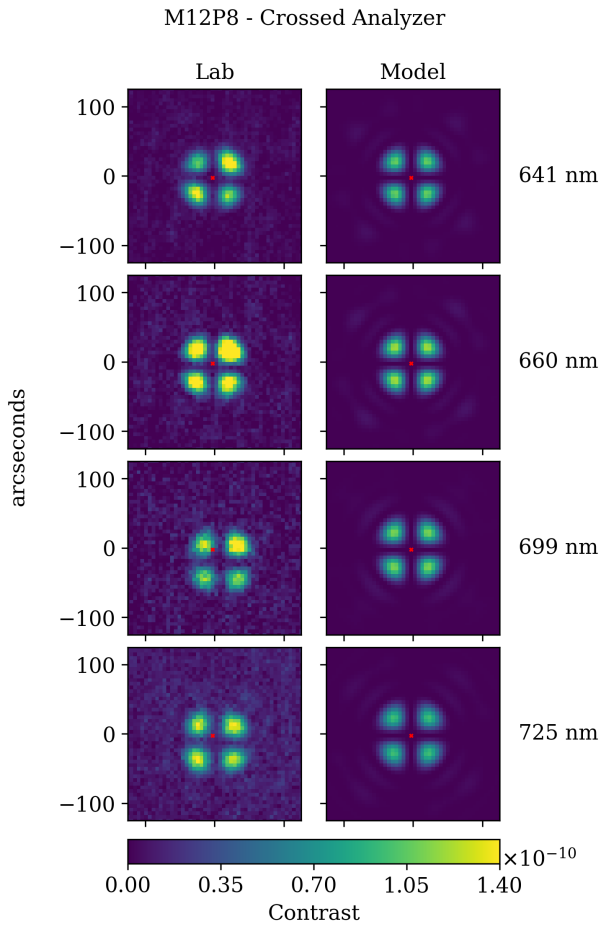

Figure 34: Crossed-analyzer data and model for M12P8.

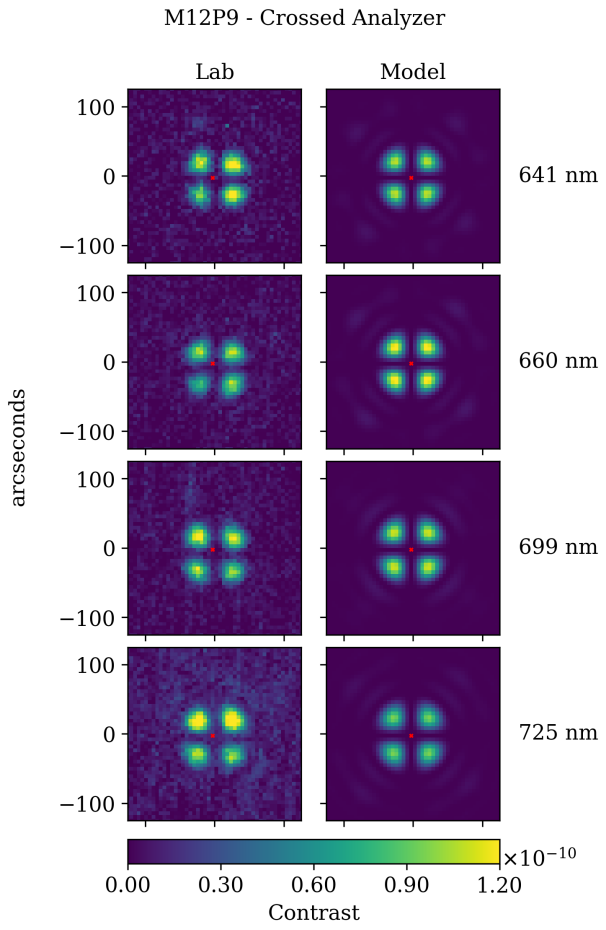

Figure 35: Crossed-analyzer data and model for M12P9.

Appendix B: Mask Edge Images

We show three examples of the etched edges of the 2-um thick Silicon-on-insulator layer that forms the working edge of the mask. The images show the Bosch cycles that form ~ 3 scallops along the edge. No two etching patterns are identical. The individual edge scallop patterns account for differences in the brightness of the vector diffraction lobes, both the 'direct' ones seen with the analyzer parallel to the polarizer, and the cross terms observed with the analyzer at 90°.

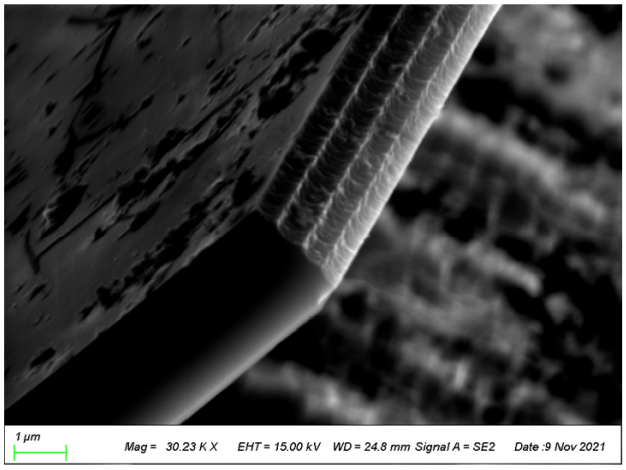

Figure 36: Scanning electron microscope image of the edge of mask M12P5. This mask had several minor flaws and was not used in the final data analysis. The image shows the edge of an uncoated petal that was etched and removed from the mask prior to coating. It had a typical Bosch cycle pattern that has some discernible differences in the location and depth of the scallops compared to other masks.

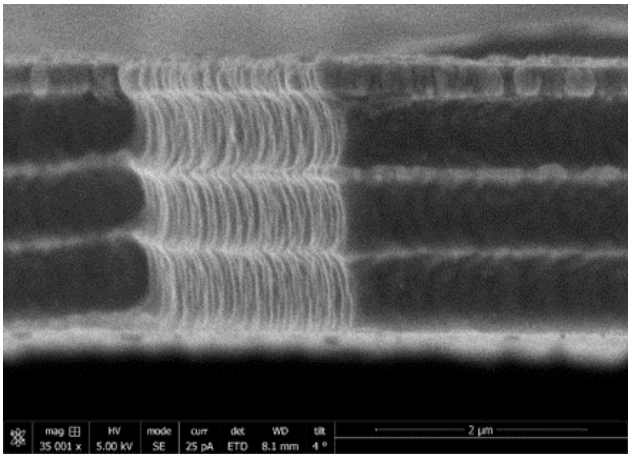

Figure 37: Scanning electron microscope image of the edge of mask M12P6. The taper is clearly visible. The mask had to be destroyed to obtain this image. The top layer is a 250 nm thick Aluminum layer.

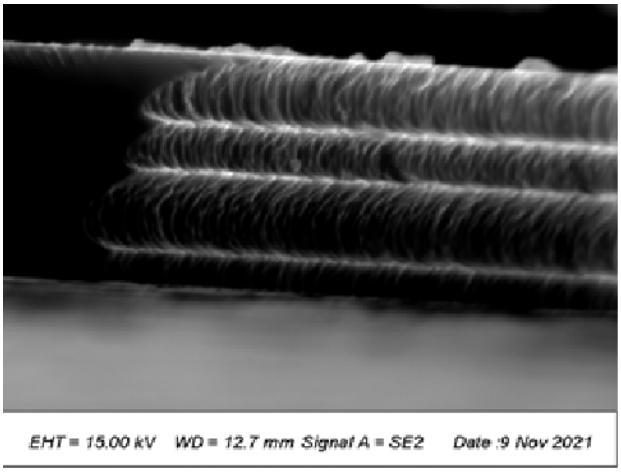

Figure 38: Scanning electron microscope image of the edge of mask M12P7. This image shows the edge of an uncoated petal that was etched and removed from the mask. The top side is the one to be coated.

Completion of model validation experiments at the Princeton starshade testbed

Stuart Shaklan[a], Anthony Harness[b], N. Jeremy Kasdin[b], Michael Galvin[b], K. Balasubramanian[a], Victor White[a], Karl Yee[a], Richard Muller[a], Phillip Willems[a], Philip Dumont[a], Simon Vuong[a], and Doug Lisman[a]

[a]Jet Propulsion Laboratory, California Institute of Technology, Pasadena, CA 91109
[b]Princeton University, Dept. of Mechanical and Aerospace Engineering, Princeton, NJ 08544

ABSTRACT

Following the results of Starshade Milestone 1 in which we demonstrated broadband contrast better than 10^{-10}, we have performed model validation experiments to show that diffraction models accurately predict the contrast due to perturbations representing the building blocks of the instrument error budget. The perturbations include the displacement of petal edge segments, sinusoidal petal edge shape deformations, global petal position errors, and random petal radial placement errors. We also show that the model accurately predicts the combined effects of two errors. The experiments result in a measured Model Uncertainty Factor (MUF) that is then applied to the starshade instrument contrast error budget.

1. INTRODUCTION

The Exoplanet Exploration Program (ExEP) has chartered the Starshade Technology Activity, dubbed S5, to bring the starshade to Technology Readiness Level (TRL) 5 for a future space mission. S5 is focused on optical, mechanical, and formation flying technologies culminating in a series of milestones to be completed between 2019 and 2025.[1] The first three milestones focus on the demonstration of optical performance at flight-required levels.

The Princeton starshade testbed consists of an 80-m long, 1-m diameter tube with a fiber-fed point source at one end, a precision etched silicon wafer mask at a distance of 27.5-m, and a camera placed another 50 m downstream. The experiment operates at nominal atmospheric pressure. After allowing roughly 3 days for the air in the tube to settle, the point spread function shape and position are stable. No wavefront control system is used. The position of the image is passively controlled using translation stages under the camera.

Milestone 1A[2] demonstrated 10^{-10} contrast at the Inner Working Angle (IWA) of a small-scale starshade mask in monochromatic light and verified that we can design a starshade capable of producing scientifically useful contrast levels. Designed with a flight-like Fresnel number, $F = 13$, and with the IWA resolved at 1.7 λ/D by the telescope, these experiments achieved a contrast floor of 2 x 10^{-11}, with contrast better than 10^{-10} over more than 2/3 of the suppression region between the conventional inner starshade and the inverse outer starshade that was used to support the inner one.

Milestone 1B[3] then expanded the results to cover 4 wavelengths, 641 nm, 660 nm, 699 nm, and 725 nm, to form a broadband result covering a 12% bandpass. The noise floor and contrast levels were comparable to those observed in Milestone 1A.

This paper details the experiment and modeling results supporting the completion of Milestone 2. While Milestones 1A and 1B focused on deep contrast, Milestone 2 addresses model validation – the ability to predict the effect of purposely-introduced perturbations on the image. The original wording of Milestone 2 reads: *Small-scale starshade masks in the Princeton Testbed validate contrast vs. shape model to within 25% accuracy for induced contrasts between* 10^{-9} *and* 10^{-8}. Following a set of experiments in which the presence of vector diffraction, solely related to the miniature scale of the starshade mask, limited model accuracy for one class of perturbations, the Milestone was changed with approval of the Exoplanet Exploration Program Technical Advisory Committee (ExoTAC) to read: *Small-scale starshade masks in the Princeton Testbed validate contrast vs. shape model to within 25% accuracy for petal shape and 100% for petal position for induced contrasts between*

10^{-9} *and* 10^{-8}. The required accuracies, 25% and 100%, correspond to model uncertainty factors (MUFs) of 1.25 and 2.0, respectively.

In this paper we show that the relaxed requirement on the petal position MUF has only a minor impact on the instrument contrast error budget. We have demonstrated the ability to accurately position petals and have shown that petal position will induce $< 10^{-12}$ contrast for a range of starshade designs. A factor of 2 MUF will then make only a small contribution toward the required contrast of $< 10^{-10}$.

2. EXPERIMENT DESIGN

The experimental setup and procedures follow similarly from those of Milestones 1A and 1B: a telescope images a light source from within the deep shadow of a starshade and records the efficiency with which the starshade suppresses the on-axis light. Images of the unocculted light source are used to calibrate the image in units of contrast. The telescope is aligned with the starshade by centering on the diffraction pattern incident on the aperture in light outside of the starshade's design bandpass, much as will be done on-orbit.[4,5]

One significant change was made to the testbed since the Milestone 1A/B work. To enable studies of the polarization response, one linear polarizer was added to the light source (fixed in the horizontal position) and another was added on a rotation stage in the optical path of the telescope. Figure 1 shows a cartoon schematic of the laser launching system. As the state of polarization out of the laser's fiber optic varies with external conditions, the power transmitted through the polarizer (and ultimately incident on the starshade) varies with time. To account for this, a beam-splitter after the polarizer sends a fraction of the light to a photometer that records the transmitted power during observations.

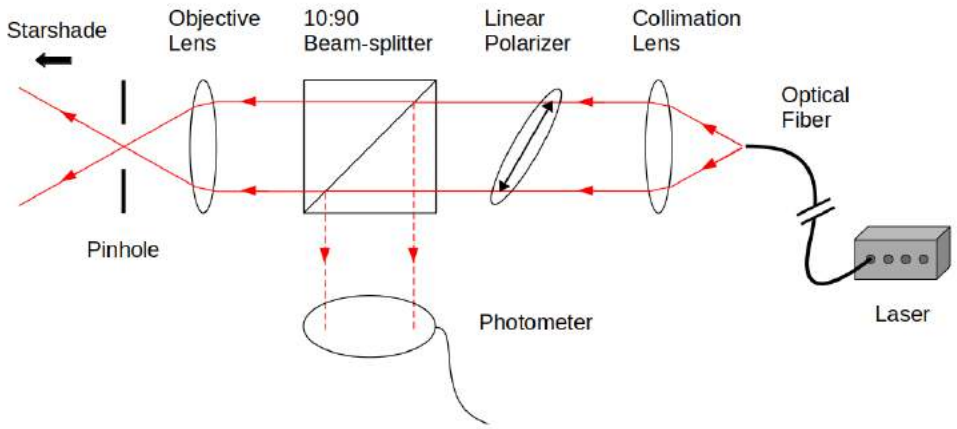

Figure 1: Diagram of laser launching system. The optical fiber enters on the right from the laser outside the testbed. Light is launched from the fiber, collimated, and passes through a linear polarizer before reaching a beam-splitter. 10% of the light is reflected to a photometer to record the throughput. The other 90% continues to an objective lens which sends a diverging beam to the starshade. A pinhole at the focus spatially filters high-order aberrations.

2.1 Perturbed Mask Descriptions

The starshades tested in these experiments start with the same baseline apodization function as the broadband starshades in the Milestone 1B work, except that the number of petals was reduced from 16 to 12. The switch to 12 petals was made to reduce the effects of non-scalar diffraction that were discovered in previous tests to originate from the inner gaps between petals.

An image of a manufactured mask is shown in Figure 2 and parameters common to all the perturbed masks are presented in Table 1. The starshade's Fresnel number is 13.8 at the shortest wavelength, 641 nm, and 12.2 at the longest, 725 nm.

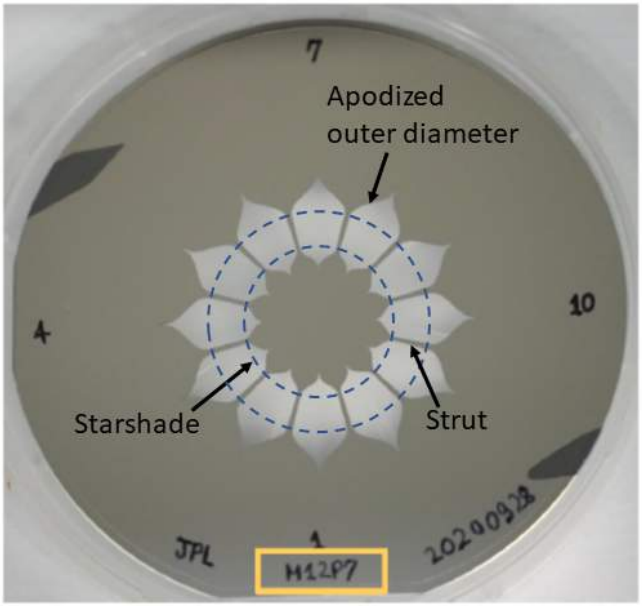

Figure 2: Starshade pattern etched into a silicon-on-insulator (SOI) wafer, manufactured at the Microdevices Lab at JPL. Interior to the inner blue circle is the inner starshade representing a free floating occulter. The inner starshade is supported in the wafer by radial struts. The outer blue circle marks the start of the apodization function of the outer starshade.

Number of Petals	12
Operating Bandpass	640 to 730 nm
Minimum Radius	8.26 mm
Maximum Radius	12.53 mm
Fresnel No. at $\lambda = 641$ nm	13.8
Fresnel No. at $\lambda = 725$ nm	12.2
Petal Gap Width	21.6 µm
Optical Device Layer*	2 µm Silicon
Metal Coating	0.25 µm Aluminum

*Except M12P2, whose device layer is 1 µm Silicon Nitride.

Table 1: Design and manufacturing parameters common to all masks.

Manufacturing No.	Colloquial Name
M12P2	Displaced Edges
M12P6 & M12P10	Shifted Petals
M12P7	Mixed Perturbations
M12P8	Globally Shifted Petals
M12P9	Sine Waves

Table 2: Key relating mask manufacturing number to colloquial name.

The perturbed starshades start from the baseline apodization function and have at least two perturbations added to the two-dimensional shape. The perturbations are sized to have contrasts between 10^{-9} and 10^{-8}, which make them faint enough to be informative to models at flight-like contrast levels, but bright enough to stand out above the contributions from non-scalar diffraction. Table 3 summarizes the different perturbations and the following sections provide additional details on each. Figure 3 show the locations of the perturbations on each mask; in describing the locations of the perturbations, the petal number is given by its clock angle on the mask (modulo a 20° rotation to match the orientation in the lab).

Mask	Perturbation	Description	Location
M12P2	Positive Displaced Edge	2.3×414 μm edge displaced out of petal	Inner Petal 5
	Positive Displaced Edge	1.7×532 μm edge displaced out of petal	Outer Petal 11
M12P6 & M12P10	Shifted Petal	7.5 μm outward shift	Petals 1 & 5
	Shifted Petal	10.5 μm outward shift	Petal 9
M12P7	Shifted Petal	8.5 μm outward shift	Petals 1 & 7
	Negative Displaced Edge	10×80 μm edge displaced into petal	Petal 1
	Positive Displaced Edge	10×80 μm edge displaced out of petal	Petal 7
M12P8	Shifted Petal	5 μm outward shift	All Petals
M12P9	Sine Wave	1.75 μm amp., 4 cycles over 2.9 mm	Inner Petal 5
	Sine Wave	1.75 μm amp., 5 cycles over 2.3 mm	Outer Petal 11

Table 3: Summary of shape perturbations and corresponding manufacturing numbers.

2.1.1 M12P2 - Displaced Edges

The displaced edge perturbation simulates the effect of a petal edge segment being displaced from its nominal position during petal assembly on the ground. Figure 4 shows a 2.3 μm tall displaced edge segment built into the design of the manufactured mask M12P2. We call this type of perturbation a positive displaced edge, as the edge is shifted outwards from the petal and increases the surface area of the petal. In mask M12P7, one of the perturbations is a negative displaced edge, which means it is shifted inwards and decreases the petal's surface area.

2.1.2 M12P6 - Shifted Petals

In the flight system, petals will be kinematically attached to the bays that form the central disk. In mask M12P6, three of its twelve petals are shifted radially outwards by a few microns, the equivalent of a few millimeters on a full-scale starshade; Petals 1 & 5 are shifted by 7.5 μm, while Petal 9 is shifted by 10.5 μm. Only the petals of the inner starshade are shifted - the struts and the outer apodization function do not change.

Figure 5 shows a scanning electron microscope (SEM) image of how this perturbation is built into M12P6. The SEM image is of the gap between two petals, one of which is shifted radially outwards; the effect of shifting the petal outwards creates a step in the radius at which the petal starts, which in turn creates a shelf on one side of the gap. Since the petal has a gap on each side, two steps are made for each shifted petal.

2.1.3 M12P7 - Mixed Perturbations

Mask M12P7 mixes three different types of perturbations: shifted petals, a positively displaced edge segment, and a negatively displaced edge segment. Petals 1 and 7 are shifted radially outward by 8.5 μm and each have a displaced edge segment located on their radial strut. The edge segment on Petal 1 is a negative displacement, while the one on Petal 7 is a positive displacement. The combination of three perturbation types explores the interference between perturbations and results in a strong wavelength dependence.

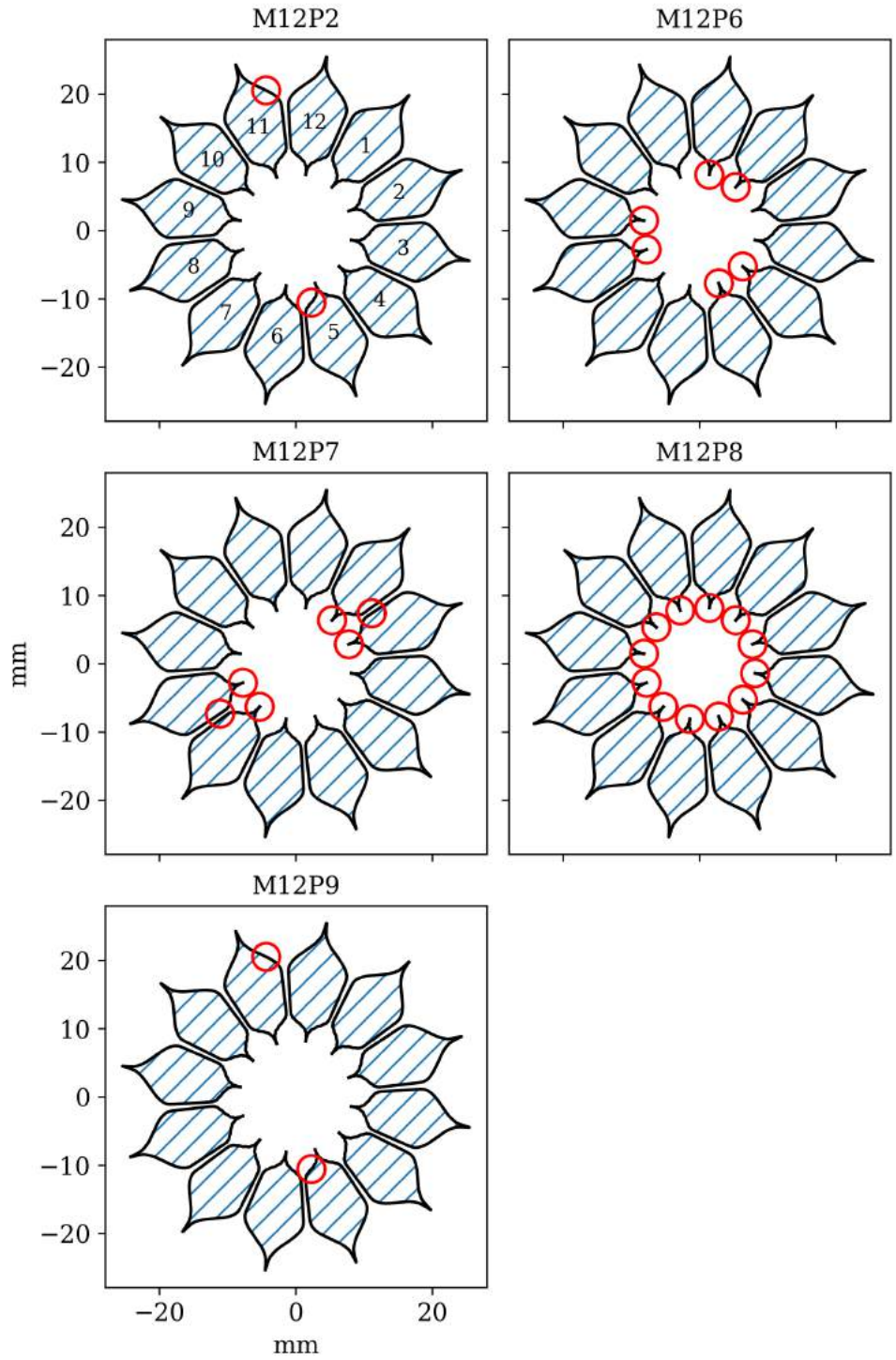

Figure 3: Red circles mark perturbation locations on all masks. The petal number is given by its clock angle on the mask (modulo a 20° rotation to match the orientation in the lab).

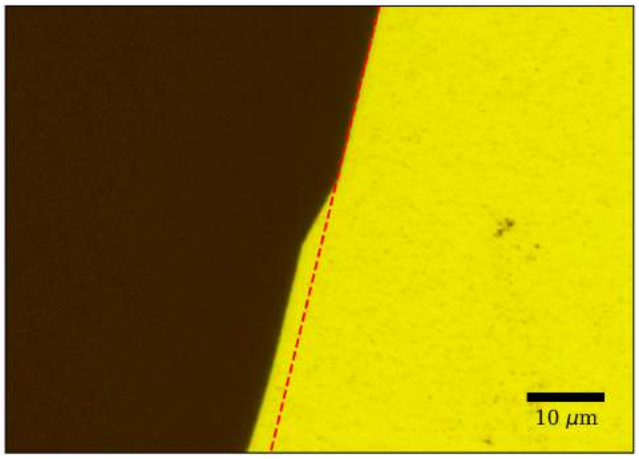

Figure 4: Microscope image of the inner displaced edge perturbation on M12P2. The red line denotes the edge of the nominal starshade shape. The 2.3 μm step in the edge simulates a displaced edge segment.

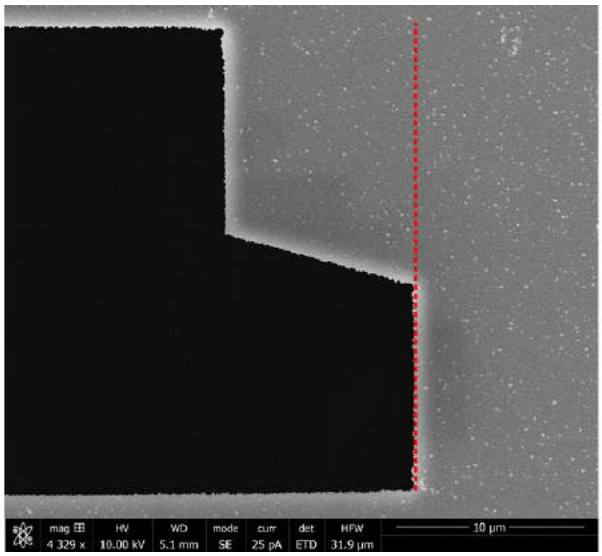

Figure 5: Scanning electron microscope image of the inner gap between a normal petal (bottom) and shifted petal (top) on mask M12P6. The red line marks the petal's original starting position.

2.1.4 M12P8 - Global Petal Shift

Mask M12P8 also has shifted petal perturbations, but applied to every petal; each petal is shifted radially outward by 5 μm. Since petals on both sides of the inner gap are shifted, there is no shelf as is seen in M12P6; in effect, the petals just have a slightly different apodization function from the baseline design.

2.1.5 M12P9 - Sine Waves

Smooth changes to the edge shape can occur if individual edge segments are misshapen, and with thermal variations due to shadowing and material property variations. These smooth changes can be decomposed into a set of sine waves. The diffraction pattern is particularly sensitive to a sinusoidal petal width change if the sine wave is in sync with the Fresnel half-zones and they constructively interfere. This also places a strong wavelength dependence on the contrast they induce. Due to the small amplitude and long wavelength of the sine wave introduced in these experiments, the change to the shape is imperceptible. As such we do not include a microscope image of this perturbation.

2.2 Summary of Experiments

Table 4 summarizes the different configurations that comprise the full suite of experiments conducted. For the milestone data, each mask is imaged in four wavelengths and at three mask rotation angles, resulting in twelve images per mask. Additionally, each mask is imaged in four wavelengths with the polarized analyzer orthogonal to the input polarization direction (horizontal in the lab frame). This "crossed analyzer" configuration is used to constrain physical properties of the optical edge, and has been presented in Ref. 6.

Masks	M12P2, M12P6, M12P7, M12P8, M12P9, M12P10
Wavelengths	641, 660, 699, 725 nm
Mask Rotation Angles	0° , 120° , 240°
Analyzer Angles	0° , 90° ("crossed analyzer")

Table 4: Iteration of configurations that comprise the full suite of experiments.

3. OPTICAL MODEL

The optical performance of the flight-scale starshade should be well described using the Fresnel approximation[7] and Kirchhoff's boundary conditions in solving the scalar diffraction problem. This formulation of the diffraction equation is the model we are validating in this work. However, additional physics must be added to the model to account for the non-scalar diffraction effects, dubbed "thick screen effects", that were first observed in Milestone 1A.

Several methods are available for solving the scalar diffraction problem, all of which have been shown to be in agreement. Two methods, a boundary diffraction wave method[8] and a similar angular integral method[7,9] convert the two-dimensional diffraction equation into a one-dimensional line integral around the occulter's edge and are well suited to capture the large dynamic range of sizes in the starshade shape.

Recently, Barnett[10] developed a highly-efficient method that utilizes non-uniform Fourier transforms to solve the Fresnel diffraction equation. This method assigns Gaussian quadrature weights to the starshade shape and uses non-uniform FFT algorithms[11] to match the accuracy of edge diffraction algorithms while being orders of magnitude faster.[6] In this work, we use Barnett's areal quadrature method to perform the comparison to experimental results. We have modified this approach to handle shape perturbations and to incorporate non-scalar diffraction effects into the scalar diffraction model. The scalar version of this method was cross-checked with the edge algorithms of Refs. 8 and 7.

The areal quadrature method is well-suited to model non-scalar diffraction through the Braunbek method developed in Ref. 12. In the Braunbek method, the standard Kirchhoff boundary conditions (where the incident

field is 0 on the diffracting screen and 1 in the aperture) are replaced with the complex field that arises from local diffraction at the edge of the screen. Since the presence of the screen only affects its immediate surrounding, the boundary conditions are changed only in a narrow seam around the edge of the screen. The exact field in the seam around the edge is solved via a Finite Difference Time Domain (FDTD) simulation[13] of light propagating past the edge of a metal-coated silicon wafer. The model accounts for the cross-sectional profile of the edge including Bosch cycle scalloping and edge taper (Figure 6).

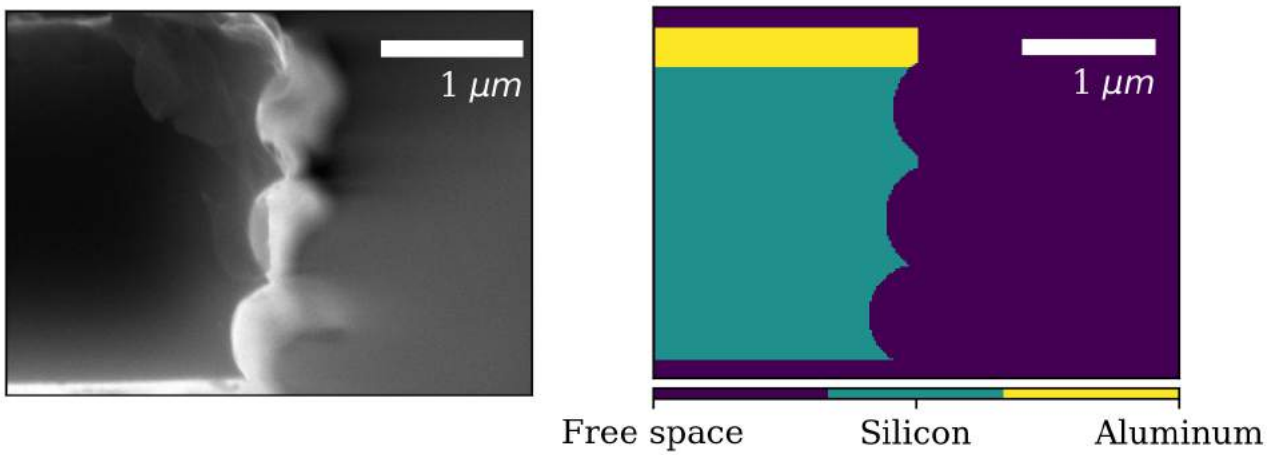

Figure 6: Left: SEM image of the scalloped vertical profile of the wafer edge for a manufactured mask. Right: electric permittivity map of the *Meep*[13] FDTD simulation cell displaying the material geometry.

The masks all have slightly different fabrication properties. The measured physical properties of the optical edge are summarized in Table 5. The etching error, which is the accuracy of the edge position relative to the design, is used by the scalar diffraction model. The etching error could only be measured at the inner and outer tips. If this error changes as a function of radial position and/or gap width, then the model will not accurately represent this sensitive parameter. The other parameters (edge thickness, taper angle, scallop height, and scallop depth) are used by the vector diffraction model. The accuracy of this model is borne out by the cross-polarization measurements described in Refs 6 and 14.

Mask	Etching Error	Edge Thickness	Taper Angle	Scallop Height	Scallop Depth
M12P2	+210nm	1 μm	1°	1.2 μm	0.3 μm
M12P6	+40nm	2 μm	1°	0.6 μm	0.1 μm
M12P7	+50nm	2 μm	1°	0.6 μm	0.1 μm
M12P8	+100nm	2 μm	1°	0.6 μm	0.1 μm
M12P9	+140nm	2 μm	1°	0.6 μm	0.1 μm

Table 5: Model parameters used to model the thick screen effect via the FDTD method. The etching error is not used in the FDTD, but is used in the scalar model; a positive etching error means the mask is under-etched.

4. EXPERIMENT DATA + MODEL COMPARISON

In this section we present the main experimental results and comparisons to the optical model. Experimental and model images are shown for three mask orientations at four wavelengths. In comparisons between experiment

and model, we use the average contrast calculated in a photometric aperture of radius 1 λ/D*, centered on the perturbation. The full derivation of the contrast calculation is presented in Appendix A of Ref. 14. For M12P8, the perturbations appear as a ring at the base of the petals; the contrast for this mask is calculated as the average contrast in a $2 \times \lambda/D$ wide annulus centered on the base of the petals.

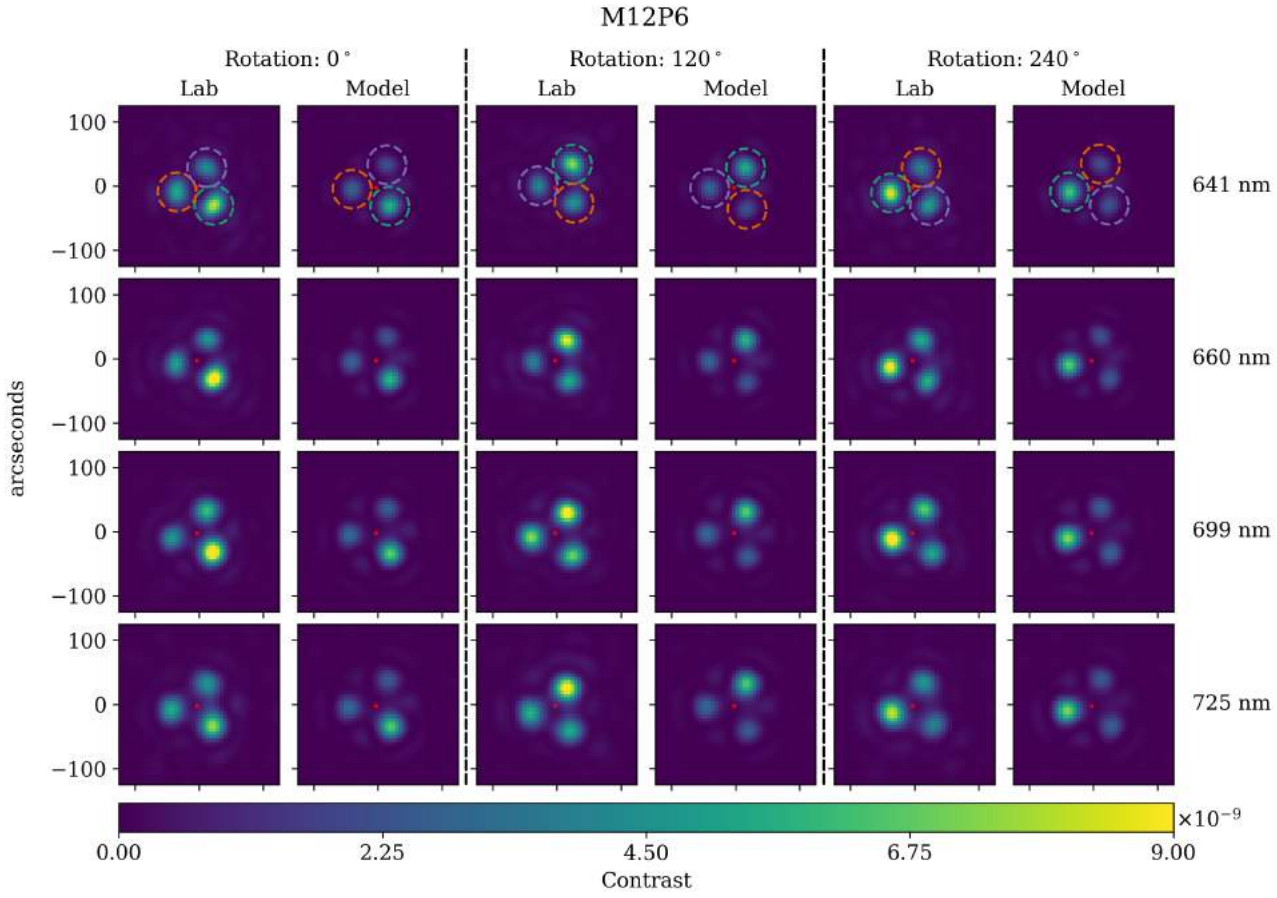

Figure 7: Experimental and vector model images of M12P6. Three groups of two columns show the mask at three rotation angles. Rows correspond to four wavelengths. The circles denote the positions where perturbations are measured in the experimental data and models.

We show image and model comparisons for two cases, the shifted petals mask (M12P6, Figure 7) and the combined perturbation mask (shifted petals plus notches, M12P7, Figure 8). Results for the other three sets of masks look qualitatively similar and have been shown in Refs. 6 and 14. In each figure, we show the measured images and model predictions for three mask orientations and four wavelengths. Clearly the model captures the salient features introduced by the perturbations. In particular, in Figure 8, the model predicts the chromatic change of interference from constructive at 641 nm to destructive at 725 nm for one perturbation (petal shift and negative notch) and from destructive to constructive for the other (petal shift and positive notch).

As with the Milestone 1 data, the contrast floor for these experiments is well below 10^{-10}.

*The perturbations of M12P7 are not point-like, so a photometric aperture of radius $1.5 \times \lambda/D$ is used.

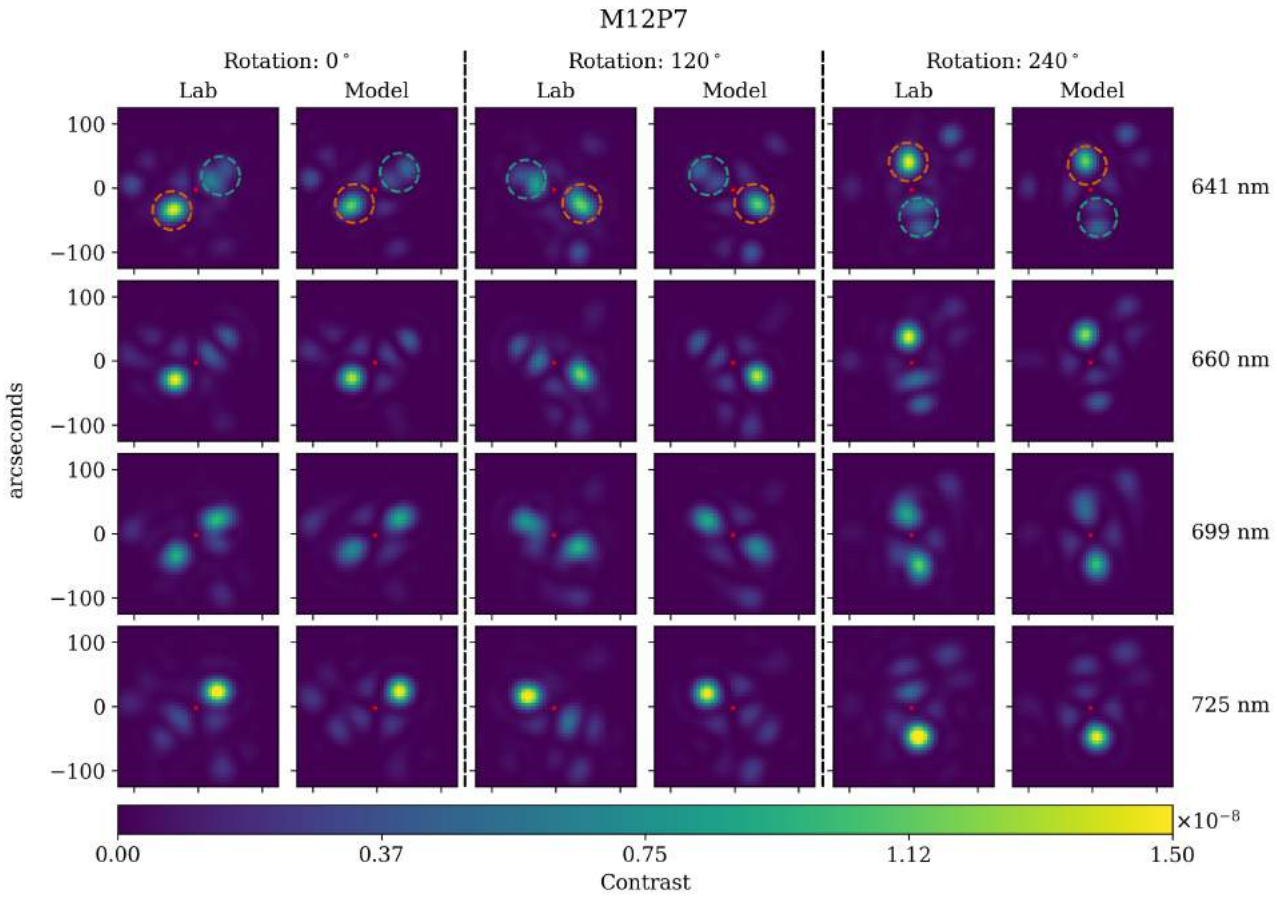

Figure 8: Experimental and vector model images of M12P7. Three groups of two columns show the mask at three rotation angles. Rows correspond to four wavelengths. The circles denote the positions wehre perturbations are measured in the experimental data and models.

5. MILESTONE ANALYSIS

To quantify the agreement between experiment and model, denoted ME, we evaluate the percent difference between the data and the model,

$$\mathrm{ME}_j = \frac{\mathrm{Lab}_j \text{ - } \mathrm{Model}_j}{\mathrm{Model}_j} \times 100\% \,, \tag{1}$$

where the measured value of the scatter from a particular perturbation at one of the four wavelengths is given by Lab_j, and the corresponding model prediction is Model_j. The values of ME_j are plotted in Figures 9 and 10. We summarize the average agreement between the data and model for each type of perturbation in Table 6. Here we have performed an unweighted average of the ME_j data points for each mask (but have combined the two separate petal shift masks since they represent the same type of perturbation), and report the standard error of the mean for each perturbation. These results include updated mask shape and edge parameters that were not available in Ref. 6.

The model is in excellent agreement with the experiment for the edge notches (M12P2), global petal shift (M12P8), and sine waves (M12P9). For these cases, the MUF is below 1.25. But a careful inspection of Figure 7, and the corresponding model fractional error points in Figure 9 shows that the model underestimates the perturbation contrast for M12P6 and M12P10. The underestimate arises from a still unexplained issue in the combination of the scalar and vector models. The issues is most prominent with the petal shift experiment because

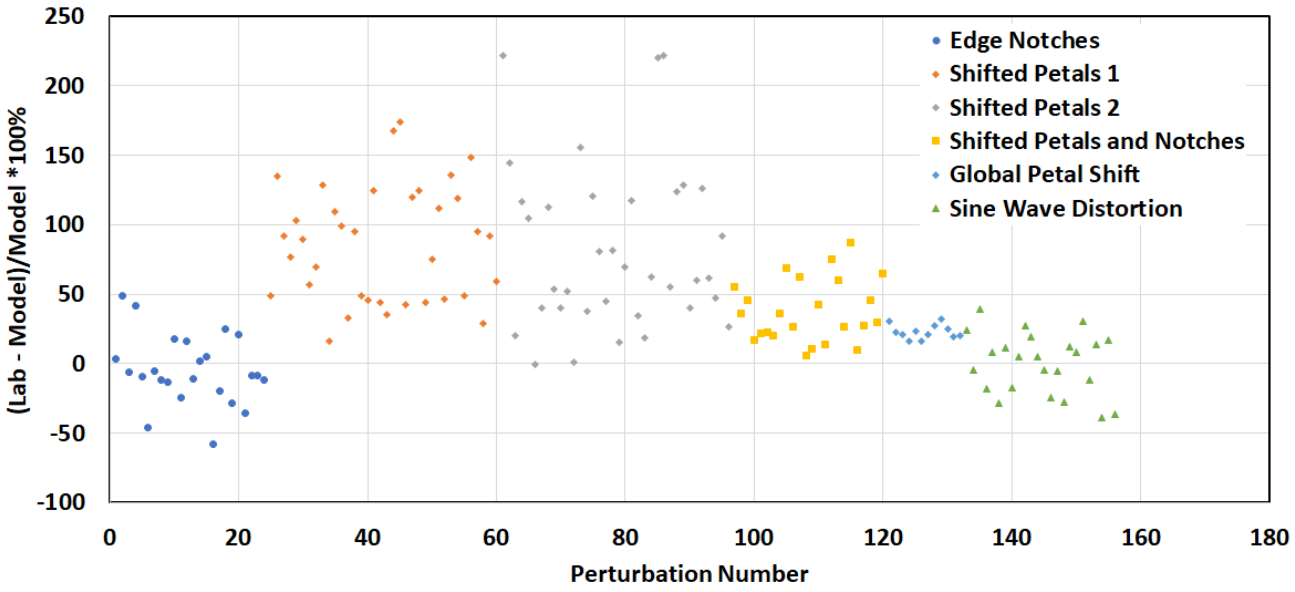

Figure 9: Percent difference between experiment and vector model for all perturbations. For each mask, there are 2 or 3 perturbations, each mask is tested at 4 wavelengths and 3 mask orientations, giving a total of 156 comparison points. The 1-sigma photometric errors relative to the model are less than 6% for all data points.

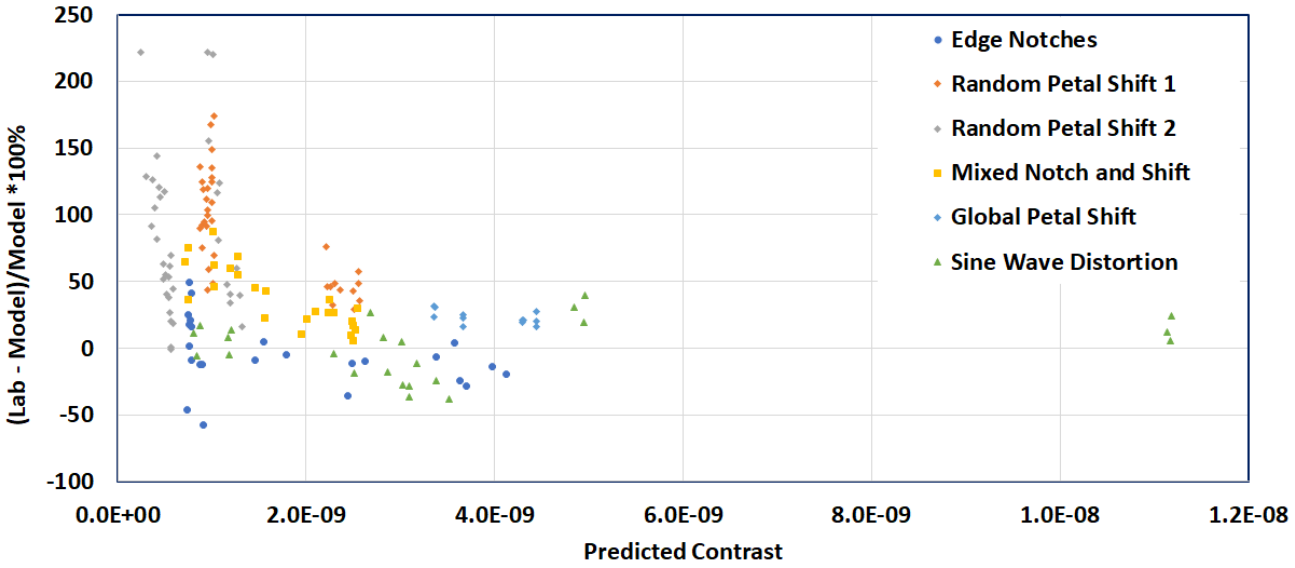

Figure 10: The same data as in Fig. 9 are plotted as a function of the predicted contrast. The largest deviations occur at or below a contrast level of 10^{-9}.

the perturbation contrast appears close to the inner petal tips, near the same radius where the polarization lobes are most prominent. The vector model predicts the amplitude of the polarization lobes with sufficient accuracy to estimate the combined lobe and perturbation contrast to ∼20%, but the model's coherent destructive interference of the lobe field with the perturbation field leads to an underestimate of the observed signal. At the present time, we are unable to explain why the phase of the interference term appears to be incorrect.

The same problem arises, but less prominently, in the multi-perturbation mask M12P7. Here, some of the perturbation light comes from the notches which are near the petal tips and at a radius outside the main polarization lobe. This reduces the coherent overlap of the perturbation and polarization fields.

It is important to keep in mind that the major contributing factor to the 84% estimation error is the contrast of the polarization lobes,∼ 5 x 10^{-10} which is linked to the small scale of the mask. We have shown that the lobe intensity scales as the inverse square of the mask diameter (Appendix B of Ref. 14). It is also a function of the edge thickness and geometry, but regardless of the edge geometry, the polarization effect is confined to be within a few microns of the edge. The starshade size thus drives the polarization lobe contrast. With a flight-scale starshade 1000x larger than the laboratory starshade (e.g. a diameter of 25 m vs. 25 mm), the lobes will be 1,000,000 times fainter on-orbit, with a contrast level of just 5 x 10^{-16}. Polarization of light by the starshade will be negligible at flight scales.

Mask	Perturbation	Model Error	Crossed Analyzer RMS
M12P2	Edge Notches	-5% ± 5%	33%
M12P6 & M12P10	Shifted Petals	84% ± 6%	15%
M12P7	Shifted Petals + Notches	38% ± 11%	18%
M12P8	Global Shifted Petals	23% ± 2%	49%
M12P9	Sine Waves	0% ± 5%	33%

Table 6: Experiment - Vector Model average agreement for each mask and the weighted average for all Model Errors. The model error is the mean agreement between the experiment and model for all orientations, wavelengths, and perturbations for each mask, and the standard error of the mean.

6. FLIGHT STARSHADE ERROR BUDGET WITH UPDATED MUFS

We have developed detailed optical performance error budgets for starshade designs dating back to the Exo-S probe-scale mission concept.[15] We have also studied parametric scaling laws[16] that allow us to estimate the performance of more ambitious missions such as HabEx by considering several factors such as the telescope point-spread function resolution relative to the starshade IWA, the number of petals, and the Fresnel number.

In Figure 11, we show the error budget for the Starshade Rendezvous Mission (SRM),[17] a starshade designed to operate with the Roman Space Telescope. The error budget is evaluated for a wavelength of 800 nm, at the red end of the 615-800 nm band with the 26 m starshade positioned for an IWA of 104 mas. The error budget has been updated to account for completed TRL-5 milestones demonstrating the capability to meet or exceed key performance parameters for petal shape accuracy and stability,[18] petal position accuracy and stability,[19] and most recently, the detailed metrology and assembly process likely to be employed for a flight system (to be published). Each box in the bottom row contains the maximum expected, or 3-sigma, contrast level from assembly errors, deployment repeatability, instabilities including thermal cycles and thermo-elastic shape errors over the maximum expected temperature range. These ranges are ∼ 10-100 microns for petal shape, hundreds of microns for petal position, and a temperature range of -60°C to + 50°C for off-axis solar angles of 83° to 40° respectively.[20]

The error budget includes 100% allowable growth in most key engineering parameters, which in turns leads to a factor of 4 increase in contrast as seen in the second row from the bottom. The SRM budget is shown here in its original form with a MUF of 1.25 applied to both petal shape and petal position contrast. Continuing

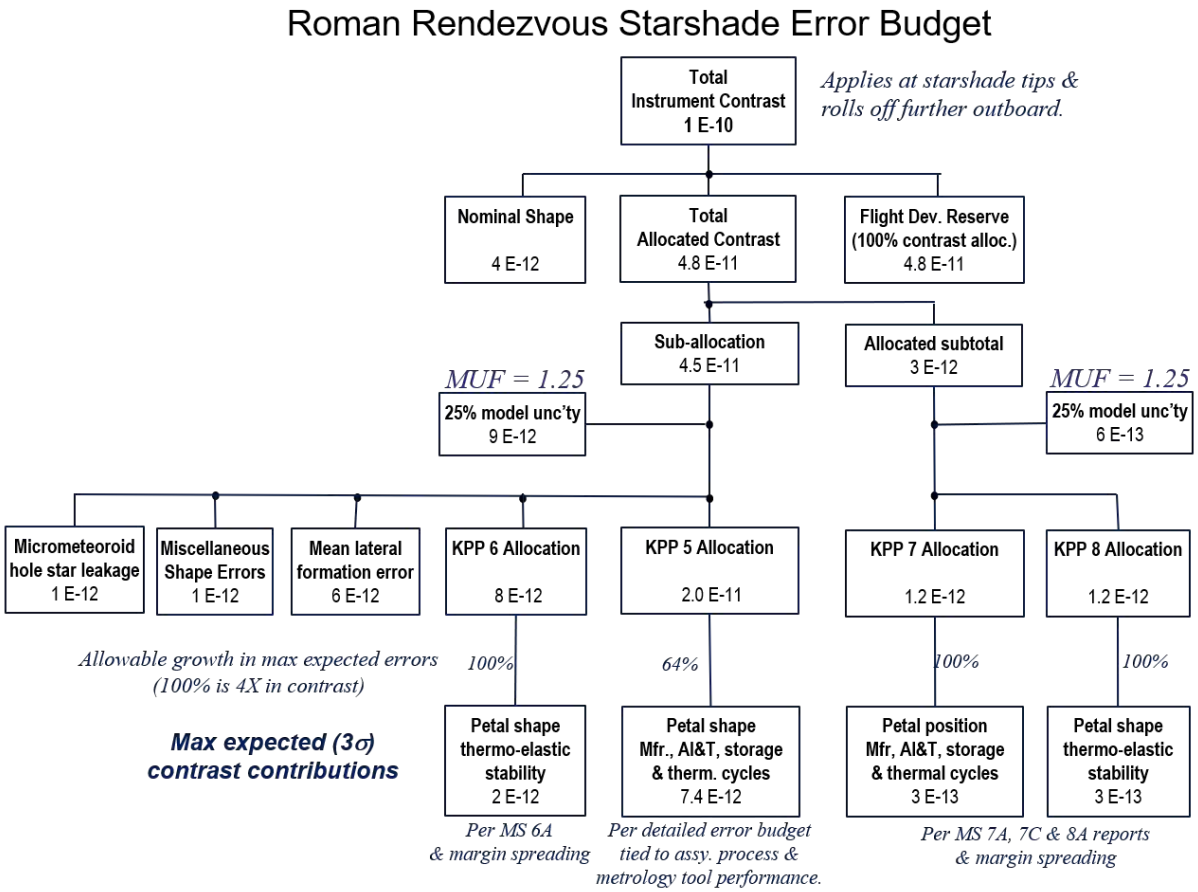

Figure 11: Instrument optical contrast error budget for the 26-m diameter Starshade Rendezvous Mission starshade. The IWA is 104 mas and is at 1.5 λ/D for λ=800 nm.

up the chart, we include a 100% flight development reserve on instrument contrast, leading to a total predicted contrast of 10^{-10}. We note that this contrast is evaluated at the IWA, corresponding to the tips of the starshade. The contrast improves significantly at angles > IWA.

The Astro 2020 report[21] recommends investment in technology development for a 6-m telescope with the ability to image and characterize exoplanets. We have evaluated several starshade designs that would enable an on-axis 6-m telescope to do this with high optical efficiency, broad bandwidth, deep contrast, a relatively simple camera, and perhaps most importantly, without imposing extreme wavefront stability requirements on the optical train. One possible design is a 64-m diameter starshade consisting of a 32 m inner disk supporting 24 16-m long petals. The design, which we call the "Decadal" starshade concept, operates simultaneously over a 250-1000 nm bandpass with IWA = 69 mas. Figure 12 shows the error budget, evaluated at 1000 nm and at the IWA. Here we have assumed that the magnitude of the perturbations scales linearly with starshade size. For example, a 100 micron petal position error on SRM becomes a 64/26 = 246 micron error in the Decadal starshade. This is likely to be a worst case scenario because many assembly errors are limited by metrology noise that is independent of distance, and by workmanship such as mechanical shimming precision that is independent of overall diameter.

There are 2 key differences between the Decadal and SRM error budgets. First, the Decadal telescope resolves the starshade at n = 2 λ/D (1000 nm / 6 m = 34.4 mas) while the 2.4 m Roman telescope resolves the SRM starshade at n = 1.5 λ/D. This matters because most of the scattered light from perturbations in the shape of the starshade originates well within the IWA. The telescope partially resolves and localizes the light so that its

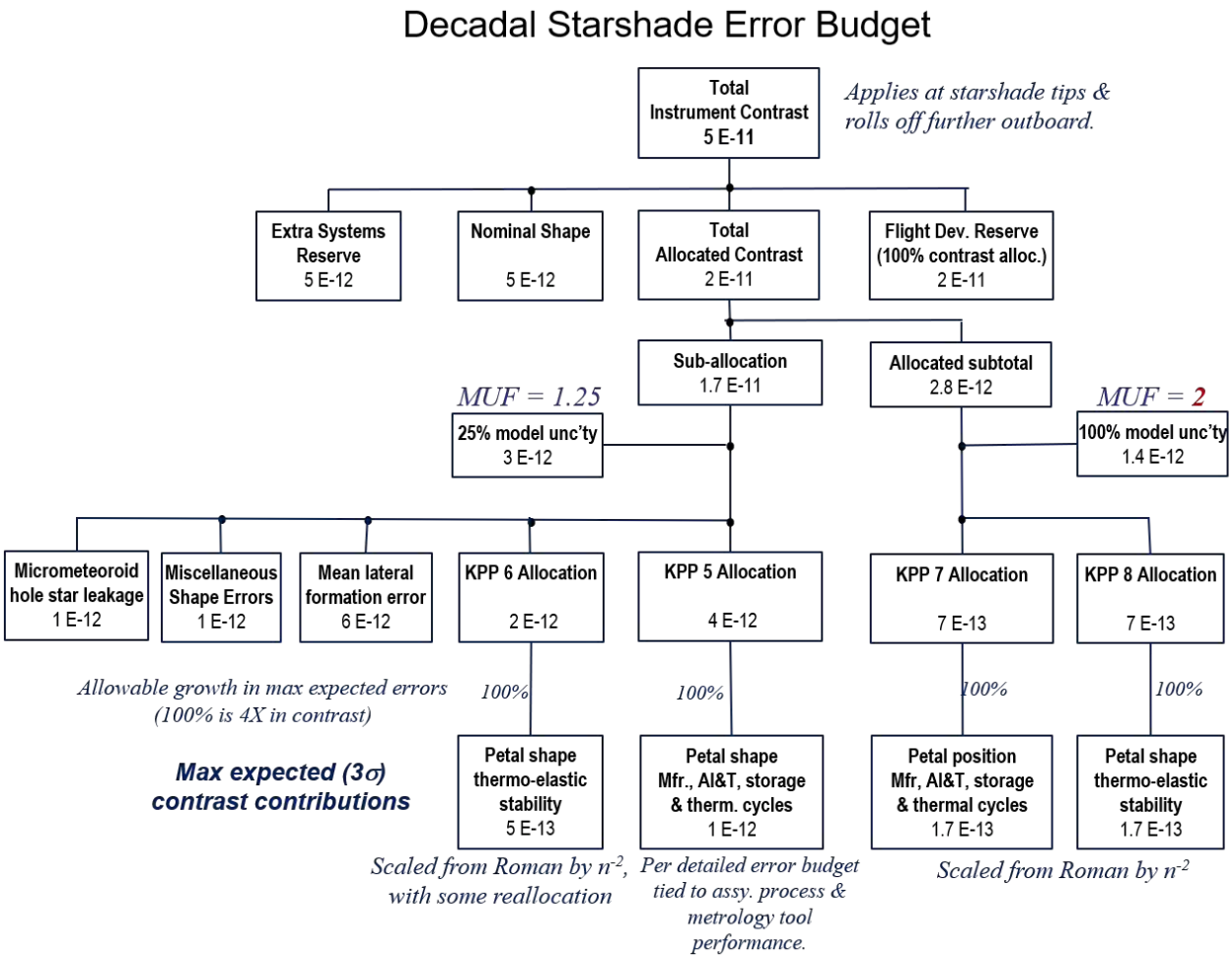

Figure 12: Instrument optical contrast error budget for a 64-m starshade with a 6-m diameter telescope. The wavelength is 1000 nm, and is at 2 λ/D for the λ = 1000 nm.

effect at the IWA is reduced. We have shown[16] that this effect scales approximately as $\sim n^{-3}$, following the radial roll-off of an Airy function. However, for perturbations that are close to the IWA, the roll-off can be less pronounced. We have conservatively assumed that we gain only as n^{-2} in this error budget. Still, that is a decrease in contrast by a factor $(2/1.5)^2 = 1.8$, all else remaining the same.

Second, we have applied a MUF of 2 to the petal position terms. Compared to using MUF=1.25, this adds an additional 10^{-12} to the allocated subtotal for petal position, and another 10^{-12} once the 100% flight development contrast reserve is included. This represents just 4% of the total instrument contrast budget of 5 x 10^{-11}. Thus we conclude that the experimentally measured petal position modeling error is easily absorbed into the starshade error budget.

7. CONCLUSION

Since its "first light" in 2017, the Princeton in-air 80-m starshade testbed has successfully demonstrated deep contrast with a floor of 2 x 10^{-11} over a broad band, at flight-like Fresnel numbers, and has successfully validated optical modelling including accurate predictions of diffraction in purposely distorted starshades.

The model validation experiments addressed the key building blocks of the starshade optical shape error

budget including petal edge manufacturing, petal shape distortion, and petal position. The experiments also validated the contrast predictions when multiple perturbations are present.

Prediction accuracy was limited by the presence of diffraction lobes that are most pronounced at the inner gaps where petals meet. These lobes arise because polarized light interacts with the edges of the starshade. The lobe shape, position, and amplitude are accurately predicted by models that account for the edge shape parameters. However, we found that the interference of the lobes with the perturbations from shifted petals is not in agreement with the models. The laboratory data is in agreement with the model if we include a $\pi/4$ phase shift in the polarized light, and separately if we incoherently combine the polarized and scalar light. But we do not at this time have a viable justification for either of these possibilities. The polarization effect will be negligible in a full-scale starshade because the area of the edge interaction shrinks 1000-fold relative to the area of the starshade when compared to the laboratory scale.

Another possibility is that the polarization model is correct, while our assumption of a uniform over- or under-etch of the petal edge is not. This might be the case because the etch rate, even through our 2 micron thick SOI layer, can be different in the tips and open areas. We can accurately measure the etch with a precision of $\sim$50 nm in the 20 micron wide petal tips. But we have not found a way to make the measurement in the few-mm wide openings that form most of the starshade. This also will not be an issue with a full-scale starshade where we employ 5-micron accurate metrology against petal width requirements of $\sim$ 100 microns.

Nevertheless, the experimental model agreement is better than a factor of two for petal position and better than a factor of 1.25 for petal shape. When the MUFs are applied to assembly and thermal distortion measurements of a 4-m scale petal, and to assembly and repeatability measurements of a 10-m scale inner disk, all appropriately scaled up to full flight scale, the flight starshade error budget yields excellent performance. The error budget predicts that the Decadal starshade will have 2x deeper contrast than SRM. Mainly driven by the telescope resolution relative to the IWA, this dwarfs the effect of the experimentally measured MUF.

With the Milestone 2 optical validation experiments described here, and with the extensive TRL-5 mechanical milestone testing that has so far been completed, the starshade performance predictions are on solid ground. Future optical tests may include a 4x longer testbed that will reduce the polarization lobes by a factor of 4. This would also give us the opportunity to include a simulated exoplanet, a true white-light source, and an active alignment system.

Acknowledgments

This work was performed in part at the Jet Propulsion Laboratory, California Institute of Technology under a contract with the National Aeronautics and Space Administration (80NM0018D0004). Starshade masks were manufactured using the facilities at the Microdevices Lab at JPL. A.H. performed all of the experiments and image contrast analysis reported herein. D. McKeithen contributed modeling to verify FDTD results. This project made use of the resources from the Princeton Institute for Computational Science and Engineering (PICSciE) and the Office of Information Technology's High Performance Computing Center and Visualization Laboratory at Princeton University. The authors acknowledge the use of Princeton's Imaging and Analysis Center, which is partially supported through the Princeton Center for Complex Materials (PCCM), a National Science Foundation (NSF)-MRSEC program (DMR-2011750).

REFERENCES

[1] P. Willems, "Starshade to TRL5 (S5) Technology Development Plan," *Jet Propulsion Laboratory Publications*, 2018. https://exoplanets.nasa.gov/internal_resources/1033.

[2] A. Harness, S. Shaklan, N. J. Kasdin, *et al.*, "Starshade technology development activity Milestone 1A: Demonstration of high contrast in monochromatic light at a flight-like Fresnel number," *Jet Propulsion Laboratory Publications*, 2019. https://exoplanets.nasa.gov/internal_resources/1210.

[3] A. Harness, S. Shaklan, N. J. Kasdin, *et al.*, "Starshade technology development activity Milestone 1B: Demonstration of high contrast in broadband light at a flight-like Fresnel number," *Jet Propulsion Laboratory Publications*, 2019. https://exoplanets.nasa.gov/internal_resources/1211.

[4] S. Martin and T. Flinois, "Simultaneous sensing of telescope pointing and starshade position," *Journal of Astronomical Telescopes, Instruments, and Systems*, vol. 8, no. 1, pp. 014010–1 – 014010–18, 2022.

[5] A. Chen, A. Harness, and P. Melchior, "Lightweight starshade position sensing with convolutional neural networks and simulation-based inference," *arXiv:2204.03853v*, 2022. [doi.org/10.48550/arXiv.2204.03853].
[6] A. Harness, S. Shaklan, P. Willems, N. Kasdin, K. Balasubramanian, *et al.*, "Optical experiments and model validation of perturbed starshade designs," *Proc. SPIE*, vol. 11823, no. 12, pp. 1–9, 2021.
[7] A. Harness, S. Shaklan, W. Cash, and P. Dumont, "Advances in edge diffraction algorithms," *J. Opt. Soc. Am. A*, vol. 35, pp. 275 – 285, Feb. 2018. [doi:10.1364/JOSAA.35.000275].
[8] E. Cady, "Boundary diffraction wave integrals for diffraction modeling of external occulters," *Optics Express*, vol. 20, p. 15196, Jul. 2012. [doi:10.1364/OE.20.015196].
[9] W. Cash, "Analytic modeling of starshades," *The Astrophysical Journal*, vol. 738, p. 76, Aug. 2011. [doi:10.1088/0004-637X/738/1/76].
[10] A. H. Barnett, "Efficient high-order accurate Fresnel diffraction via areal quadrature and the nonuniform fast Fourier transform," *Journal of Astronomical Telescopes, Instruments, and Systems*, vol. 7, no. 2, pp. 1 – 19, 2021.
[11] A. H. Barnett, J. Magland, and L. af Klinteberg, "A parallel nonuniform fast fourier transform library based on an "exponential of semicircle" kernel," *SIAM Journal on Scientific Computing*, vol. 41, no. 5, pp. C479–C504, 2019.
[12] A. Harness, "Implementing non-scalar diffraction in Fourier optics via the Braunbek method," *Optics Express*, vol. 28, 2020.
[13] A. F. Oskooi, D. Roundy, M. Ibanescu, P. Bermel, J. Joannopoulos, and S. G. Johnson, "Meep: A flexible free-software package for electromagnetic simulations by the FDTD method," *Computer Physics Communications*, vol. 181, no. 3, pp. 687 – 702, 2010.
[14] A. Harness, S. Shaklan, P. Willems, N. J. Kasdin, B. K. Balasubramanian, P. Dumont, V. White, K. Yee, R. Muller, and M. Galvin, "Optical verification experiments of sub-scale starshades," *Journal of Astronomical Telescopes, Instruments, and Systems*, vol. 7, no. 2, pp. 021207–1 – 021207–32, 2021.
[15] S. Shaklan, L. Marchen, E. Cady, *et al.*, "Error budgets for exoplanet starshade (exos) probe-class mission study," *Proc. SPIE*, vol. 9605, no. 96050Z, pp. 96050Z–1 – 965050Z–14, 2015.
[16] S. Shaklan, L. Marchen, and E. Cady, "Shape accuracy requirements on starshades for large and small apertures," *Proc. SPIE*, vol. 10400, no. 104001T, pp. 104001T–1 – 104001T–10, 2017.
[17] A. Romero-Wolf, G. Bryden, S. Seager, N. J. Kasdin, *et al.*, "Starshade rendezvous: exoplanet sensitivity and observing strategy," *Journal of Astronomical Telescopes, Instruments, and Systems*, vol. 7, no. 2, pp. 021210–1 – 021210–28, 2021.
[18] D. Webb, M. Arya, S. Bradford, E. Hilgemann, *et al.*, "Advances in starshade technology readiness for an exoplanet characterizing science mission in the 2020's," *Proc. SPIE*, vol. 11117, p. 0P, 2019.
[19] M. Arya, F. Mechentel, D. Webb, *et al.*, "Demonstration of deployment repeatability of key subsystems of a furled starshade architecture," *Journal of Astronomical Telescopes, Instruments, and Systems*, vol. 7, no. 2, pp. 021202–1 – 021202–29, 2021.
[20] D. Webb, J. Steeves, F. Mechentel, M. Arya, *et al.*, "Starshade technology development activity Milestone 6A: Verify petal shape on-orbit stability," *Jet Propulsion Laboratory Publications*, 2021. https://exoplanets.nasa.gov/internal_resources/2008/.
[21] National Academies of Science, Engineering and Medicine, *Pathways to Discovery in Astronomy and Astrophysics*. Washington DC: The National Academies Press, 2021. [doi.org/10.17226/26141].

Optical verification experiments of sub-scale starshades

Anthony Harness[a,*] **Stuart Shaklan**[b] **Phillip Willems**[b] **N. Jeremy Kasdin**[a,c] **Bala K. Balasubramanian**[b] **Philip Dumont**[b] **Victor White**[b] **Karl Yee**[b] **Rich Muller**[b] **and Michael Galvin**[a]

[a]Princeton University, Mechanical and Aerospace Engineering Department, Princeton, New Jersey, United States

[b]Jet Propulsion Laboratory, California Institute of Technology, Pasadena, California, United States

[c]University of San Francisco, College of Arts and Sciences, San Francisco, California, United States

Abstract. Starshades are a leading technology to enable the detection and spectroscopic characterization of Earth-like exoplanets. We report on optical experiments of sub-scale starshades that advance critical starlight suppression technologies in preparation for the next generation of space telescopes. These experiments were conducted at the Princeton starshade testbed, an 80-m long enclosure testing 1/1000'th scale starshades at a flight-like Fresnel number. We demonstrate 10^{-10} contrast at the starshade's geometric inner working angle (IWA) across 10% of the visible spectrum, with an average contrast at the IWA of 2×10^{-10} and contrast floor of 2×10^{-11}. In addition to these high-contrast demonstrations, we validate diffraction models to better than 35% accuracy through tests of intentionally flawed starshades. Overall, this suite of experiments reveals a deviation from scalar diffraction theory due to light propagating through narrow gaps between the starshade petals. We provide a model that accurately captures this effect at contrast levels below 10^{-10}. The results of these experiments demonstrate that there are no optical impediments to building a starshade that provides sufficient contrast to detect Earth-like exoplanets. This work also sets an upper limit on the effect of unknowns in the diffraction model used to predict starshade performance and set tolerances on the starshade manufacture. [DOI: 10.1117/1.JATIS.7.2.021207]

Keywords: starshades; optical model validation; high contrast imaging; exoplanet detection; vector diffraction.

Paper 20111SS received Jul. 31, 2020; accepted for publication Dec. 1, 2020; published online Jan. 8, 2021.

1 Introduction

Starshades have the potential to discover and characterize the atmospheres of Earth-like exoplanets in the habitable zone of nearby stars.[1–3] Their ability to achieve high contrast while maintaining high optical throughput and broad wavelength coverage make them the most promising technology to produce the first spectrum of an exo-Earth atmosphere.[4,5] In recent years, there have been significant technological advances that demonstrate the feasibility of building and deploying a starshade,[6–8] which have led to a significant increase in the community's interest in a future starshade mission. There is interest in a starshade to rendezvous with NASA's next flagship mission, the Nancy Grace Roman Space Telescope,[2] and a starshade is baselined for the proposed flagship mission, the Habitable Exoplanet Observatory (HabEx).[3]

Though significant progress has been made, starshades are still an unproven technology, particularly with respect to their optical performance. The distributed architecture's size (10's of meters diameter over 10,000's of kilometers) and sensitivity (10^{10} relative change in intensity) are unprecedented—when constructed, the starshade will be the largest visible-light

*Address all correspondence to Anthony Harness, aharness@princeton.edu

optic ever made. Consequently, we need a reliable means to experimentally validate the design tools that rely on an accurate prediction of the optical performance. The state-of-the-art optical models[9–12] operate under the assumptions of a scalar theory of diffraction; scale invariance of the Fresnel approximation; and a scalar application of Babinet's principle. The work presented here focuses on demonstrating the validity of the first assumption.

The diffraction equations employed in the starshade context are invariant with Fresnel number, so while it is impossible to test a full-scale starshade on the ground due to its size, we can validate the optical models with sub-scale experiments if conducted at a flight-like Fresnel number. Previous experiments in Refs. 13–19 were conducted at Fresnel numbers much larger than that expected in flight; the experiment in Ref. 20 was done at a flight-like Fresnel number, but its contrast was limited by the atmosphere. With the Princeton starshade testbed presented here, we are for the first time able to achieve 10^{-10} contrast with a starshade at a flight-like Fresnel number.

The Starshade to Technology Readiness Level (TRL) 5 (S5) project was established by the NASA Exoplanet Exploration Program to advance starshade technology to TRL 5 in a time frame compatible with a starshade rendezvous with the Roman mission.[6,8] The work presented here was conducted under S5 to advance the seminal optical technology of starshades—starlight suppression. We group the experiments into two categories, optical verification and model validation, which reflect the two milestones set as the criteria needed to reach TRL 5.[6] Optical verification experiments showed that we can design an apodization function, which specifies the starshade's shape that provides sufficient contrast to achieve our stated science goals. These experiments validate the fundamental operation of the starshade and demonstrate that the aforementioned assumptions are valid. Model validation experiments show that the optical models correctly capture the performance sensitivity to perturbations in the starshade shape and set an upper limit to the model uncertainty used in design tools to derive the starshade shape error budget and tolerances for future missions.

To briefly summarize our main results, we have demonstrated 10^{-10} contrast at the geometric inner working angle (IWA) of a starshade with a flight-like Fresnel number across a 10% bandpass while reaching a contrast floor of 2×10^{-11} beyond the starshade tips. From this, we conclude that we can predict the nominal starshade performance to at least 10^{-10} contrast. The main limitation to the contrast at the laboratory scale comes from a polarization-dependent effect of light propagating through the narrow gap between starshade petals. We provide an explanation of this effect in Sec. 3.1.1. The model validation experiments demonstrate better than 35% (with an average of 20%) model accuracy for a number of different shape perturbations and at multiple wavelengths. This result means we must only carry a contrast margin of 1.35× in the design error budget. The results from these experiments build confidence in our ability to successfully design a starshade that will provide the contrast needed to detect Earth-like exoplanets.

In Sec. 2, we describe the layout and individual components of the starshade testbed and outline the experiments performed. Section 3 presents the results of the optical verification experiments, Sec. 4 presents the results of the model validation experiments, and we discuss the implications of these results in Sec. 5. We summarize and conclude in Sec. 6. Additional details and results from the optical verification experiments can be found in the S5 milestone final reports,[21,22] which have been accepted by the Exoplanet Exploration Program Technical Advisory Committee.[23]

2 Experiment Design

The experiments presented here were conducted at the Princeton starshade testbed, a dedicated facility in the Frick chemistry building on the Princeton campus. The testbed was designed to replicate the flight configuration at 1/1000'th scale as closely as is possible given the differences in size and environment. The scale of the experiment is ultimately limited by the longest separation available in an indoor facility on campus. We use the Starshade Rendezvous Probe Mission[2] (SRM) and HabEx mission[3] as the reference flight configurations; parameters for the flight and laboratory configurations are given in Table 1. The table lists the operational range of the Fresnel number, N, defined as

$$N = \frac{R^2}{\lambda Z_{\text{eff}}}, \tag{1}$$

Table 1 Optical parameters for the laboratory experiments and the SRM and HabEx starshade architectures. The range of Fresnel numbers is set by the wavelength range.

	Laboratory	SRM	HabEx
Telescope diameter (D)	5.0 mm	2.37 m	4.0 m
Starshade diameter ($2R$)	25.06 mm[a]	26 m	52 m
Wavelength (λ) range	641 to 725 nm[a]	616 to 800 nm	300 to 1000 nm
Telescope – starshade sep. (Z_{tel})	50 m	26,000 km	76,600 km
Source – starshade sep. (Z_{src})	27.45 m	>3 parsec	>3 parsec
Fresnel number (N)	**12.2 to 13.8**[a]	**8.1 to 10.5**	**8.8 to 29**

[a]For apodization design C12/C16 in Table 3.

where R is the starshade radius, λ is the wavelength of light, and Z_{eff} is the effective starshade-telescope separation:

$$Z_{\text{eff}} = \frac{Z_{\text{src}} Z_{\text{tel}}}{Z_{\text{src}} + Z_{\text{tel}}}, \tag{2}$$

where Z_{tel} is the distance between telescope and starshade and Z_{src} is the distance between starshade and light source. Z_{eff} accounts for the finite distance to the diverging beam light source in the laboratory configuration and is derived in Eq. (4). For the laboratory experiments, $Z_{\text{eff}} = 17.7$ m; for the flight configuration, the source (target star) is effectively infinitely far away, making $Z_{\text{eff}} \approx Z_{\text{tel}}$.

In this work, we use the geometric IWA ($=R/Z_{\text{tel}}$) as the point of reference, though future design studies should follow Ref. 24 and set requirements relative to the effective IWA, which accounts for the width of the telescope's point spread function (PSF).

For the range of N under study, the Fresnel approximation of diffraction is sufficiently accurate[12] to compute the diffraction pattern to contrast levels better than 10^{-10}, an assertion borne out by the successful demonstration of a dark shadow in these experiments. We use the Fresnel–Kirchhoff (F-K)[25] diffraction equation to describe the diffraction in both the laboratory and flight configurations. We invoke the standard paraxial and Fresnel approximations and assume circular symmetry (with radial coordinate at the starshade r). The electric field incident on the starshade (U_0) is due to a spherical wave of amplitude u_0 emanating at a distance Z_{src}:

$$U_0(r) = \frac{u_0}{Z_{\text{src}}} \exp\left\{\frac{i\pi r^2}{\lambda Z_{\text{src}}}\right\}. \tag{3}$$

We assume the starshade's shape is an approximation of a smooth radial apodization function, $A(r)$, a valid approximation given a sufficient number of petals.[10] The F-K diffraction integral to compute the on-axis electric field U at the telescope pupil plane (dropping the leading phase factor) is given as

$$\begin{aligned} U &= \frac{2\pi}{i\lambda Z_{\text{tel}}} \int_0^R A(r) U_0(r) \exp\left\{\frac{i\pi r^2}{\lambda Z_{\text{tel}}}\right\} r\mathrm{d}r \\ &= \frac{2\pi u_0}{i\lambda Z_{\text{tel}} Z_{\text{src}}} \int_0^R A(r) \exp\left\{\frac{i\pi r^2}{\lambda Z_{\text{src}}}\right\} \exp\left\{\frac{i\pi r^2}{\lambda Z_{\text{tel}}}\right\} r\mathrm{d}r \\ &= \frac{2\pi u_0}{i\lambda Z_{\text{tel}} Z_{\text{src}}} \int_0^R A(r) \exp\left\{\frac{i\pi r^2}{\lambda}\left(\frac{1}{Z_{\text{src}}} + \frac{1}{Z_{\text{tel}}}\right)\right\} r\mathrm{d}r. \end{aligned} \tag{4}$$

The distance terms in the exponential can be combined into an effective separation parameter, Z_{eff}, given by Eq. (2). We set the amplitude of the incident wave to be unity at the starshade, to give $u_0 = Z_{\text{src}}$. Equation (4) can be rewritten as

$$U = \frac{2\pi}{i\lambda Z_{\text{tel}}} \int_0^R A(r) \exp\left\{\frac{i\pi r^2}{\lambda Z_{\text{eff}}}\right\} r\mathrm{d}r \quad = \frac{\pi}{i}\frac{Z_{\text{eff}}}{Z_{\text{tel}}} \int_0^N A(n) \exp\{i\pi n\}\mathrm{d}n, \tag{5}$$

with dimensionless quantity $n = r^2/\lambda Z_{\text{eff}}$ spanning the range of Fresnel numbers up to N.

Written in the dimensionless form of Eq. (5) and neglecting the constant amplitude scale factor ≈1, the integral is independent of R, λ, and Z_{eff}, and depends solely on the Fresnel number. This enables experimental validation via more practical sub-scale experiments: by showing in the laboratory that high contrast is achieved at flight-like values of N, we show that the full-scale, properly shaped starshade will also produce the same level of contrast. This statement is true under the assumption that scalar diffraction theory holds at both scales. The experiments described here show that scalar diffraction theory almost holds at small scales, as long as it is corrected with an additive non-scalar component at the edges. Extending the same modeling approach to flight scale shows that the additive terms makes a negligible contribution (see Appendix B), validating the extension of the scalar diffraction theory result to flight scale.

Due to size constraints of the testbed, the laboratory Fresnel number does not extend as low as those in the full scale configurations (the lowest Fresnel number tested is $N = 11.5$ in Sec. 4.4), but still falls within the range of Fresnel numbers set by the span in wavelength. Additionally, the Fresnel number (N) quoted in Table 1 is in reference to the maximum radius of the starshade, but the diffraction integral starts at the base of the petals with $n \sim 5$ and integrates to N. This means our experiments will demonstrate that we accurately capture the behavior of the apodization function over the range of Fresnel numbers seen in the flight configurations. Testing at $N < 15$ has been determined to be sufficiently adequate for the purposes of model validation.[6]

Altogether, by utilizing an 80-m long facility, we are able to test at a flight-like Fresnel number a starshade that is large enough to be accurately manufactured with existing technology.

2.1 *Summary of Experiments*

The experiments presented here can be sorted into two loose categories that track the two S5 milestones[6] that this work is tasked to complete: optical verification[21,22] (presented in Sec. 3) and model validation (presented in Sec. 4). Table 2 provides a summary of six experiments and the name (production number) of the starshade tested. Improvements to the testbed were made

Table 2 Summary of experiments and production number of starshades tested (see Table 4 for details on specific starshades). Those with OV in the Goal column are optical verification experiments and are presented in Sec. 3. Those with MV in the Goal column are model validation experiments and are presented in Sec. 4.

#	Experiment	Section	Brief description	Goal	Starshade
1	Monochromatic contrast	3.1	Demonstrate best possible contrast at a single wavelength.	OV	DW17
2	Broadband contrast	3.2	Demonstrate $<10^{-10}$ contrast at the IWA across a 10% bandpass.	OV	DW21
3	Exposed petal tips	3.3	Demonstrate high contrast with a starshade with realistic petal tips.	OV	M12P3
4	Shape perturbations	4.2	Validate optical models against starshades with perturbations built into their shape.	MV	M12P2/M12P3
5	Polarization study	4.3	Improve non-scalar diffraction model by studying polarization-dependent effects.	MV	DW9/DW21
6	Varying Fresnel #	4.4	Validate Fresnel number dependence of model by testing at lower Fresnel number.	MV	DW17

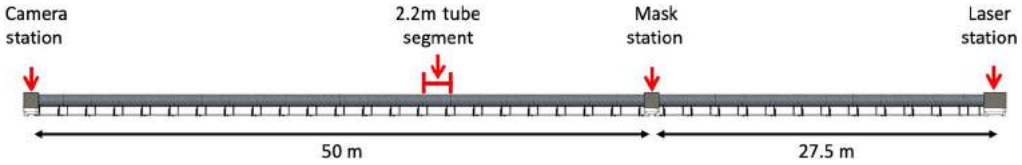

Fig. 1 Layout of testbed showing distances between camera, starshade mask, and laser stations.

between various experiments, the most dramatic of which was the installation of a linear polarizer after the fiber launcher (see Sec. 2.3) and a linear polarizer as analyzer on a rotation stage in front of the camera. This change occurred after completing experiments 1, 2, and 6 of Table 2.

2.2 *Testbed Configuration*

The design of the experiment is simple: image a light source from within the deep shadow created by a starshade and measure the efficiency with which the starshade suppresses the on-axis light. The testbed (shown schematically in Fig. 1) consists of three stations containing a laser, starshade, and camera. The main driver in the testbed design was to maximize the starshade size while maintaining a flight-like Fresnel number, which translates to maximizing the separation. The testbed design is set by the longest, straight-line facility to be found on campus, which gives a total testbed length of 80 m. Since a fraction of the length is needed for propagation of the diverging beam, the effective separation between starshade and telescope is 17.7 m, which sets the starshade size to 25-mm diameter.

The beamline is contained in 1-m diameter steel tubing (not a vacuum) to seal the testbed from stray light and dust and to help stabilize the atmosphere. The tube is wrapped in fiberglass insulation to minimize the effect of external thermal changes. All equipment is built to be remotely operated to minimize how often the testbed is opened, which generates atmospheric turbulence and stirs up dust. Additional details of the testbed design can be found in Refs. 21, 26, and 27.

2.3 *Light Source*

The light source serving as the artificial star is a multi-channel laser diode operating at 405, 638, 641, 660, 699, and 725 nm. The 405-nm light is outside the starshade's operating bandpass and is used for alignment. The laser is located outside the enclosure and fed in via a polarization-maintaining single-mode fiber optic. The polarization out of the fiber depends on external environmental conditions, which vary with time. The fiber terminates with a collimator, and the output Gaussian beam is focused by an objective lens through a pinhole to spatially filter high-order aberrations. Experiments # 1, 2, and 6 of Table 2 were done using the resultant polarization out of the fiber. In the rest of the experiments, a linear polarizer is placed between the collimator and objective lens and is fixed horizontally (in the image and lab frames). As the state of polarization out of the fiber varies with external conditions, the power transmitted through the polarizer (and ultimately incident on the starshade) varies with time. To account for this, a beam-splitter after the polarizer sends a fraction of the light to a photometer, which records the transmitted power during observations and allows for the contrast calibration to be adjusted accordingly. A cartoon diagram of the laser launching system is shown in Fig. 2.

2.4 *Starshade Masks*

The starshades tested are roughly 25 mm in diameter and are etched into a 100-mm silicon wafer. They are positioned in the middle testbed station and are held by a mask changer (shown in Fig. 3) with a motorized planetary gear that allows us to switch between starshade and calibration masks and to image the mask at different rotation angles.

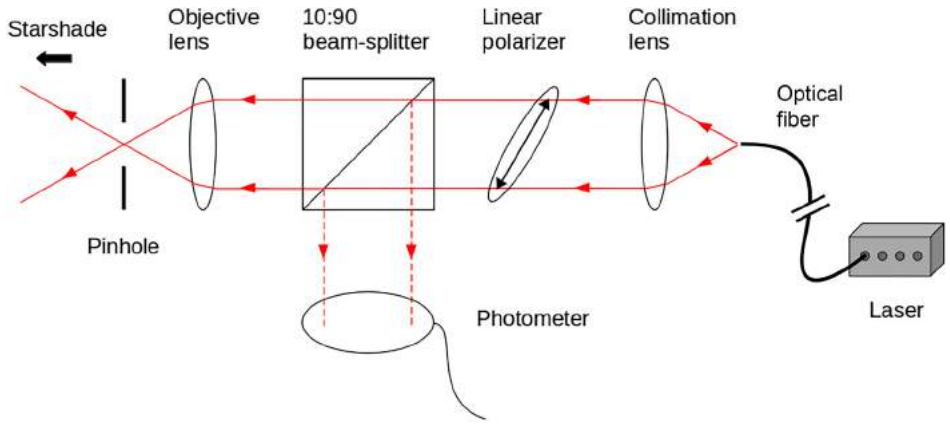

Fig. 2 Cartoon diagram of laser launching system. The optical fiber enters on the right from the laser outside the testbed. Light is launched from the fiber, collimated, and passes through a linear polarizer before reaching a beam-splitter. 10% of the light is reflected to a photometer to record the throughput. The other 90% continues to an objective lens, which sends a diverging beam to the starshade. A pinhole at the focus spatially filters high-order aberrations.

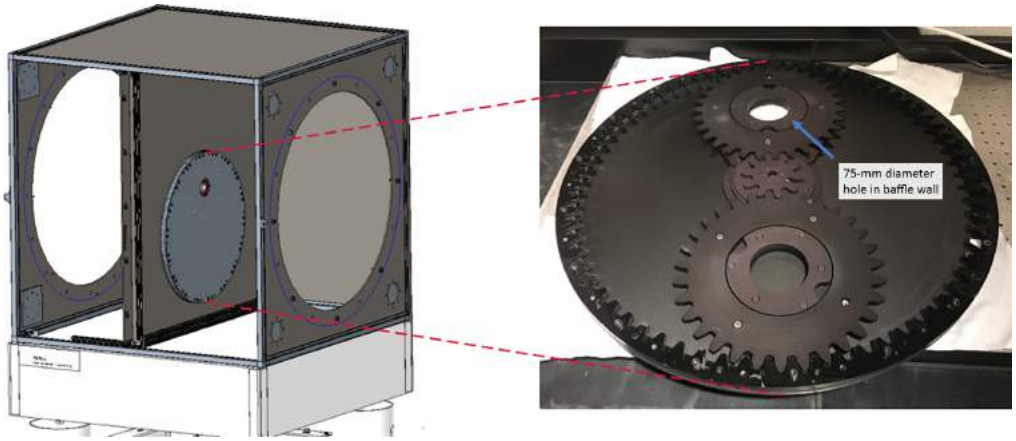

Fig. 3 Left: starshade station located 50 m from the camera. A wall blocks all light expect that passing through the starshade. Right: mask holder with a motorized planetary gear that holds the starshade and calibration masks.

2.4.1 *Design*

The starshade mask (shown in Fig. 4) consists of an inner starshade, representative of a free-floating occulter, that is supported in a silicon wafer via radial struts. The outer diameter of the support wafer is also apodized to minimize the diffraction that would occur from the truncation of the beam by the outer diameter.[15] This design results in the starshade mask consisting of N_p (= number of petals) transmission regions bounded by the petals of the inner starshade, the radial struts, and petals of the outer diameter.

Both apodization profiles (inner and outer) are designed independent of each other using the numerical optimization scheme outlined in Ref. 10. Table 3 details the designs of a number of apodization functions; the minimum radius (R_0) is the radius at which the inner petals start, and the maximum radius (R) is the radius at which the struts start (where the tips of a free floating occulter would be). Design A of Table 3 is an earlier design with smaller gaps and a larger maximum radius. Design B was specifically designed for these experiments. We impose a constraint on the radius of the inner starshade to have Fresnel number <15 and constrain the gaps between the starshade petals to have widths >16 μm to minimize non-scalar diffraction. We found this to be the largest gap width that provides a valid solution to the optimization problem.

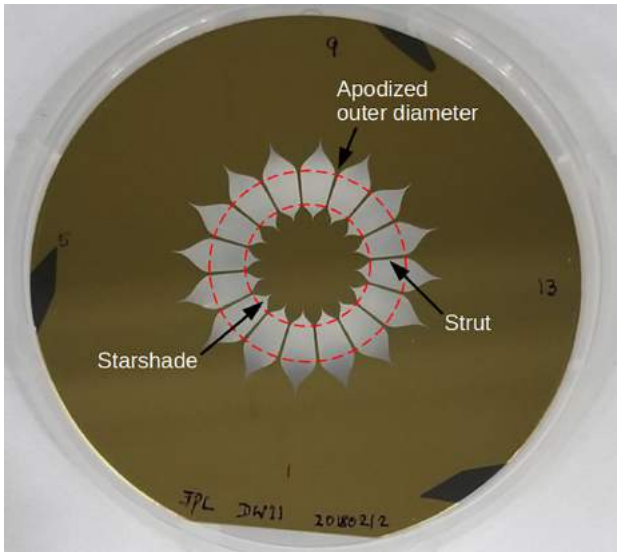

Fig. 4 Starshade pattern etched into a SOI wafer, manufactured at Microdevices Lab at JPL. Interior to the inner red circle is the inner starshade representing a free floating occulter. The inner starshade is supported in the wafer by radial struts. The outer red circle marks the start of the apodization function of the outer diameter.

Table 3 Design of apodization functions including the number of petals, operating bandpass, minimum radius (start of the petals), maximum radius (start of the struts), and gap width between petals.

Design	Number of petals	Operating bandpass (nm)	Minimum radius (R_0) (mm)	Maximum radius (R) (mm)	Gap width (μm)
A	16	600 to 670	8.41	17.35	7.5
B	16	600 to 690	8.02	12.15	16.2
C16	16	640 to 730	8.26	12.53	16.2
C12	12	640 to 730	8.26	12.53	21.6

Design C16 is the same apodization profile as Design B, but is made 3% larger to shift the operating bandpass to cover the laser's available wavelength channels. Design C12 is the same as Design C16, but with 12 petals instead of 16, which was done to minimize the number of inner gaps between petals, which serve as sources of non-scalar diffraction.

After a solution to the optimization problem is found, the apodization profile is multiplied by 0.9 to provide width to the radial struts and is then petalized to become the starshade shape shown in Fig. 4. Since the radial struts consist of a constant multiplication applied to the apodization profile, they do not diffract into the shadow.

2.4.2 *Manufacturing*

The starshade pattern is etched into the device layer of a silicon-on-insulator (SOI) 100-mm wafer via a deep reactive ion etching process. The allowed tolerances on the shape are very small, ~100 nm, which is achievable with a direct write electron beam lithography process. The SOI device layer is made as thin as is practical (1 to 7 μm) to minimize non-scalar diffraction as light propagates past the optical edge. The 350-μm-thick support wafer is etched from the backside to recess it 50 μm from the device layer's optical edge. The final step in the process is to coat the top of the device layer with a thin layer of metal to maintain opacity. Either 0.4 μm of

Table 4 Descriptions of manufactured masks including the apodization design (detailed in Table 3), the thickness of the device layer (optical edge), the thickness and type of metal coating, and the perturbations built into the shape.

Name	Apodization design	Edge thickness (± 0.5 μm)	Metal coating	Shape perturbations
DW9	A	7 μm	Au – 0.4 μm	None
DW17	B	2 μm	Au – 0.4 μm	None
DW21	C16	3 μm	Au – 0.4 μm	None
M12P2	C12	1 μm	Al – 0.25 μm	Displaced edges
M12P3	C12	2 μm	Al – 0.25 μm	Sine waves and exposed tips

gold or 0.25 μm of aluminum is used, both of which have thicknesses more than 50 times greater than their skin depth, so we expect the metal layer to be completely opaque. Details on the manufactured masks are found in Table 4. We refer the reader to Refs. 28 and 29 for more details on the manufacturing process.

2.5 *Optics + Detector*

The optics system in the camera station has pupil plane and focal plane imaging modes that are toggled by remotely flipping a lens in/out of the optical path. Contrast measurements are made in the focal plane imaging mode with the camera focused to the plane of the light source, simulating an exoplanet observation. We use an $f/100$ system with a 5-mm diameter aperture, which provides the same number of resolution elements across the starshade as in the flight design. As will be shown in Sec. 3.2, the contrast improves as light at the geometric IWA rolls off with the telescope's PSF. A telescope that highly resolves the geometric IWA gets an added boost in contrast. As such, to test in a flight-like configuration, we scale the aperture to conserve the number of resolution elements across the geometric IWA: $n_{\mathrm{resolved}} = (R/Z_{\mathrm{tel}})/(\lambda/D)$.

In pupil imaging mode, we observe the out-of-band diffraction pattern incident on the entrance pupil and use the bright spot of Arago to align the camera with the starshade, precisely what is done in the formation flying scheme to maintain starshade alignment.[30,31]

To perform calibration measurements, a neutral density filter (optical density $>10^{-7}$) is toggled into the optical train by a motorized stage. A linear polarizer on a motorized rotation stage serves as a polarization analyzer. The detector is an Andor iXon Ultra 888 EMCCD with 13-μm pixels. For low noise performance, the detector is operated with its conventional amplifier, i.e., not electron-multiplying and is liquid cooled down to -90°C.

2.6 *Calibrations*

A circular aperture mask is used to calibrate the throughput of the system and convert measurements of the occulted light source to a contrast value (see Appendix A for a definition of contrast). The calibration mask is a 50-mm diameter circle etched through a silicon wafer and switches position with the starshade mask via the motorized mask changer. For each set of observations, two sets of images are taken: one with the starshade mask in the beam and one with the calibration mask in the beam. When observing with the calibration mask, a neutral-density filter is placed in the optical path. The measured count rate for both sets of images is used in Eq. (11) of Appendix A to calculate contrast. We refer the reader to Ref. 21 for additional details on the calibration process.

3 Optical Verification Experiments

The first category of experiments is meant to verify the fundamental concept of a starshade by demonstrating that we can design the starshade's shape to provide the optical performance

needed to image exoplanets. These experiments validate most of the assumptions (e.g., binary approximation to a smooth function) made in the equations used to design the apodization function that defines the starshade's shape. Verification is achieved by demonstrating better than 10^{-10} contrast across a wide bandpass with a starshade in a flight-like optical configuration. The results presented in this section represent the completion of Milestones 1A[21] and 1B[22] of the S5 Project, which satisfies the first of two main requirements in the Starlight Suppression technology development plan.[6]

3.1 *Monochromatic Contrast*

In this first experiment, we demonstrate the best contrast achieved with the highest quality mask (DW17) at a single wavelength ($\lambda = 638$ nm). In the contrast image shown in Fig. 5, the brightest features are two lobes that are aligned with the polarization vector of the incident light (the intrinsic polarization of the fiber is slightly elliptical at a 40° angle) and which remain fixed as the mask is imaged at different rotation angles. The bright lobes are due to polarization-dependent changes in the electric field as light propagates through the narrow gaps between petals. We call this the thick screen effect and describe it in detail in Sec. 3.1.1. While these lobes are relatively bright at their peak, they are confined to two lobes at the inner gaps between petals and the contrast significantly improves in regions of the image away from the lobes. This means that despite the lobes, 10^{-10} contrast is achieved over a significant fraction of the image at the geometric IWA. This is a key feature of the starshade: any light leaking around the starshade is confined to the edge of the starshade in the image and rolls off with the telescope's PSF at image locations away from the edge.

The primary impact of the lobes is to slightly reduce the image area over which 10^{-10} contrast is achieved. The contrast is better than 10^{-10} over 44% of a λ/D wide annulus centered at the geometric IWA and quickly rises to 100% at 1.05× the IWA.[21] Figure 8 shows the contrast averaged over a λ/D wide annulus as a function of angular separation and simulates the effect of rotating the starshade during the exposure to smear out the diffracted light. The average contrast at the IWA is 1.15×10^{-10} and quickly falls with angular separation to the contrast floor of 2×10^{-11}. Figure 22 shows that the floor at large angles is set by the non-scalar diffraction lobes and Rayleigh scattering by the atmosphere.[32]

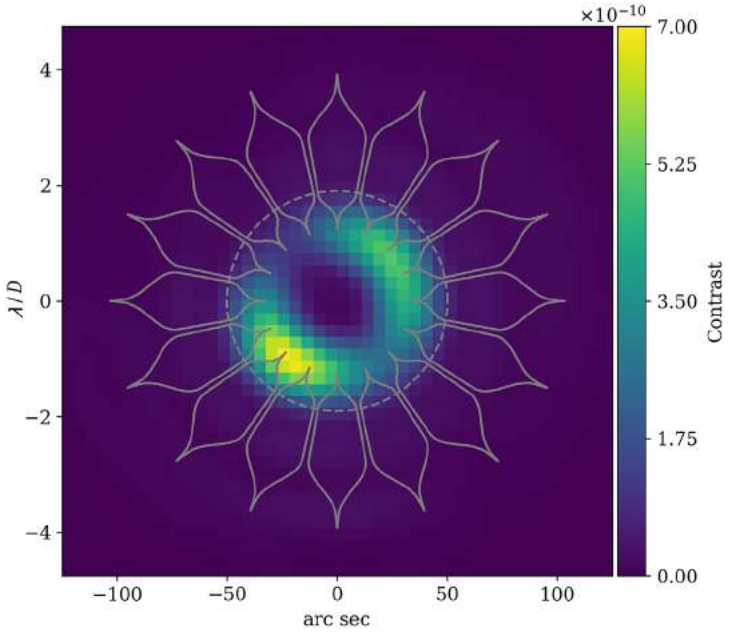

Fig. 5 Contrast map for monochromatic experiment at $\lambda = 638$ nm with mask DW17. The starshade pattern is overlaid and the dashed circle marks the geometric IWA.

3.1.1 *Note on the thick screen effect*

The bright lobes in Fig. 5 are aligned with the input polarization vector, remain stationary as the starshade rotates and have a brightness, i.e., an order of magnitude above that predicted by scalar diffraction theory. This was a new discovery that only appeared once high contrast levels were achieved at a flight-like Fresnel number. We have since developed a theory, deemed the thick screen effect,[33] which readily explains their origin.

The F-K diffraction formula, which is used to derive the apodization function represented by the starshade's shape,[10] makes the assumption that the electromagnetic field can be represented by a single scalar wave function that satisfies the scalar wave equation,[25] a valid assumption for most optical systems with features larger than the wavelength of light. More specifically, F-K diffraction assumes an infinitely thin, perfectly conducting diffraction screen and that the field in the plane of the screen takes Kirchhoff's boundary conditions, where the field is zero on the screen and is unchanged in the aperture.

The starshades in the lab configuration are small enough that these assumptions begin to break down. The gap between two petals is ∼20 wavelengths across and the screen (optical edge) is up to half as thick as the gaps are wide, so the gaps resemble waveguides more than thin screens. As light propagates past the thick edge of the starshade mask (through the waveguide), energy is lost due to the finite conductivity of the walls.[34] The interaction with materials of the edge is polarization-dependent and induces a slight change in the complex field (in both amplitude and phase) and Kirchhoff's boundary conditions are no longer valid—the propagation of light can no longer be described by scalar diffraction theory alone.

The result of the interaction with the edge is an attenuation of the transmission coefficient through the gap. This can be approximated by a ∼ wavelength wide boundary layer[35] around the starshade's edge that blocks light and changes the effective apodization profile of the petal, negating some of the light suppression. In effect, the width of each petal increases by $\sim\lambda$ on each side. The strength of the edge effect is roughly the same moving radially outwards; however, the transmission of the apodization profile rapidly increases radially, so the edge effect is strongest in the narrow gaps between petals where it occupies an appreciable fraction of the transmission area. This explains why the lobes are only seen in the innermost regions. The interaction of light with the edge is also dependent on the polarization of the incident light and thus the morphology of the lobes depends on the input polarization state.

Our theory of the edge effect is supported by a newly developed optical model[36] and its comparison to experimental results is shown in Sec. 4.3. Under this theory, these effects should be negligible at flight scales. The relevant parameter is the width of the thick screen-induced boundary layer relative to the transmission area. The optical edges for a flight starshade will induce roughly the same wavelength wide boundary layer, but the transmission area is 1000× larger, meaning the contribution from non-scalar diffraction is $10^6\times$ lower and can be considered negligible (see Appendix B for a derivation of this argument). Full vector models of flight-scale starshades are beyond the scope of this paper but will be addressed in the future.

3.2 *Broadband Contrast*

Testing over a wider wavelength range increases the applicability of the experiment to a more flight-like configuration and demonstrates that a starshade can maintain its high-contrast performance over a scientifically interesting bandpass. In this experiment, we tested mask DW21 at four discrete wavelengths that span a 10% (85 nm) bandpass. The design of DW21 is identical to, but 3% larger than, DW17 to shift the starshade's operating bandpass to cover the available laser wavelengths. Figure 6 shows again that better than 10^{-10} contrast is achieved at the IWA and that the performance is dominated by the thick screen effect. The contrast is relatively constant across the bandpass, while the peak contrast is higher than in the monochromatic experiment due to DW21 being slightly thicker than DW17, which produces a larger thick screen effect. The morphology of the polarization lobes in the $\lambda = 660$ nm data is most likely due to a misalignment between the camera and starshade—Fig. 7 shows a model image where the camera is shifted off-axis by 1 mm and the lobes are distorted to one side of the starshade. Figure 8 shows the contrast averaged over a λ/D wide annulus, where the contrast is slightly

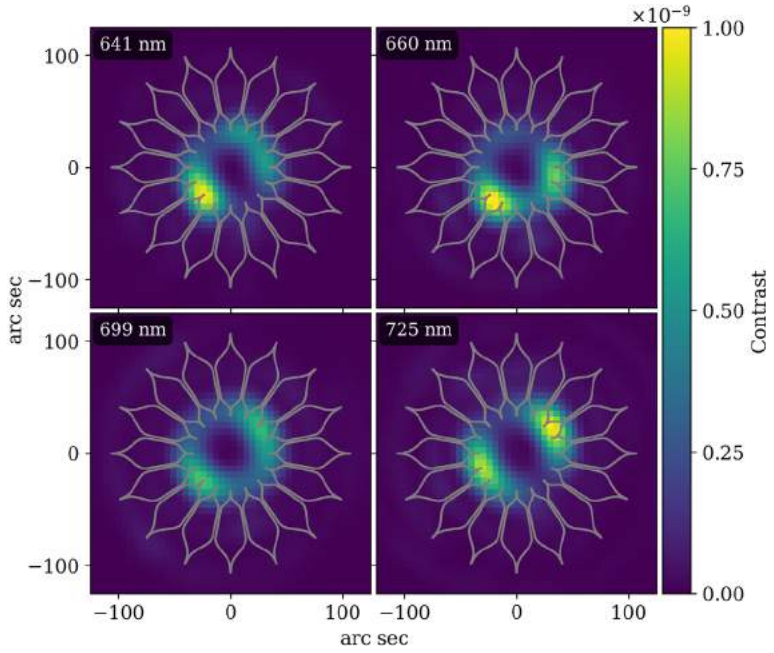

Fig. 6 Contrast images of mask DW21 at four discrete wavelengths spanning a 10% bandpass.

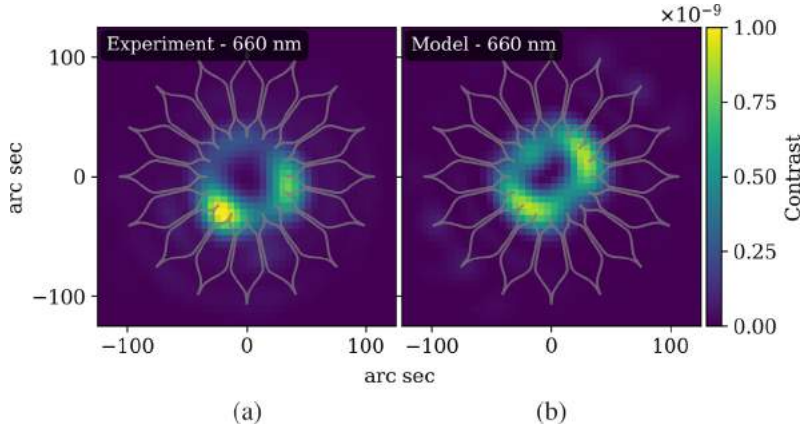

Fig. 7 (a) Experiment and (b) model images of mask DW21 at $\lambda = 660$ nm. In the model the camera is shifted off-axis vertically by 1 mm, which distorts the polarization lobes, suggesting this can account for the morphology of the lobes seen in the data.

worse at longer wavelengths as the PSF broadens and more light from the polarization lobes are leaked into the IWA. The average contrast at the IWA across the wavelengths is 2×10^{-10} This experiment shows the starshade does not suffer any fundamental degradation in performance by operating across a wider bandpass, as is expected by theory.

3.3 *Exposed Tips*

To suspend the fragile silicon starshade in the testbed, the starshade design incorporates radial struts that keep the starshade attached to the outer supporting wafer. This means the end of the petal never terminates at a tip. The diffraction equations show that the critical features of the starshade are the inner valleys between the petals and the outer tips of the petals, i.e., where the petal shape has a large azimuthal component. To verify that critical features such as tips behave in an expected manner, and to make the test article reflect a more flight-like configuration, we tested a mask built with exposed tips. Figure 9 shows the design of mask M12P3 where the inner

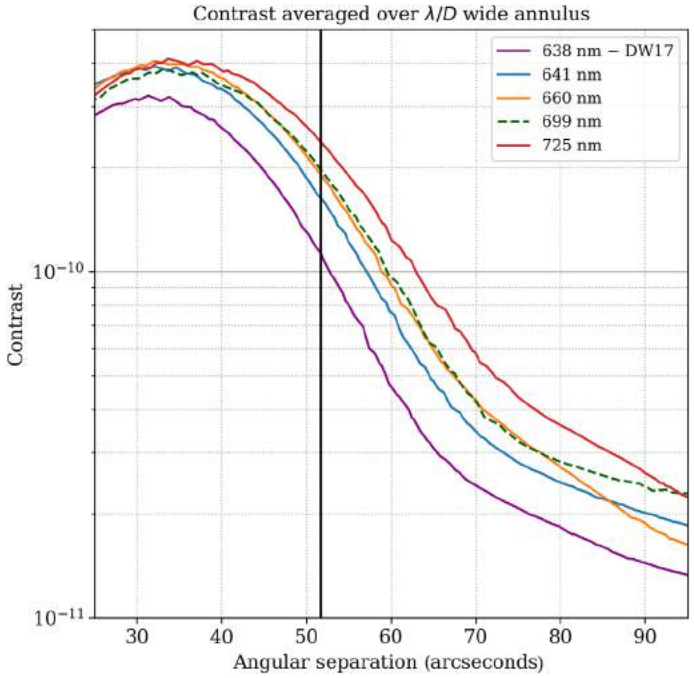

Fig. 8 Contrast averaged over a λ/D wide annulus as a function of angular separation for different wavelength observations of mask DW21. Also included is the monochromatic observation of mask DW17. The solid black line denotes the starshade's geometric IWA.

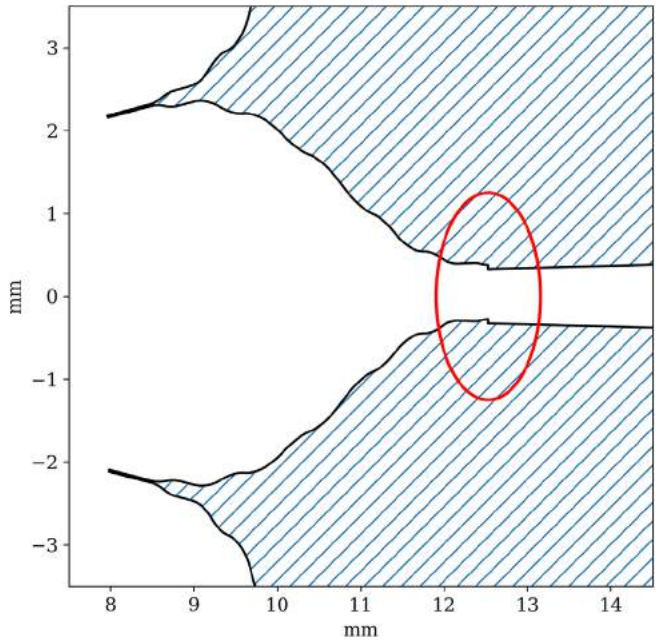

Fig. 9 A closeup of one petal in the design of mask M12P3. The inner starshade is rotated relative to the outer, creating exposed tips at all petals (seen at 12.5 mm). The blue hatched area is transparent; the white area is the silicon wafer.

starshade is slightly rotated relative to the struts and outer apodization function to expose tips at the end of the petals. As the petalized starshade is an approximation to a radial, azimuthally symmetric apodization profile, rotating the inner starshade does not change the approximated radial apodization profile and therefore should achieve the same contrast.

Figure 10 shows the residuals between experiment and model for a stacked image of mask M12P3 at $\lambda = 725$ nm. We imaged the starshade rotated by 0°, 120°, and 240°, de-rotated the

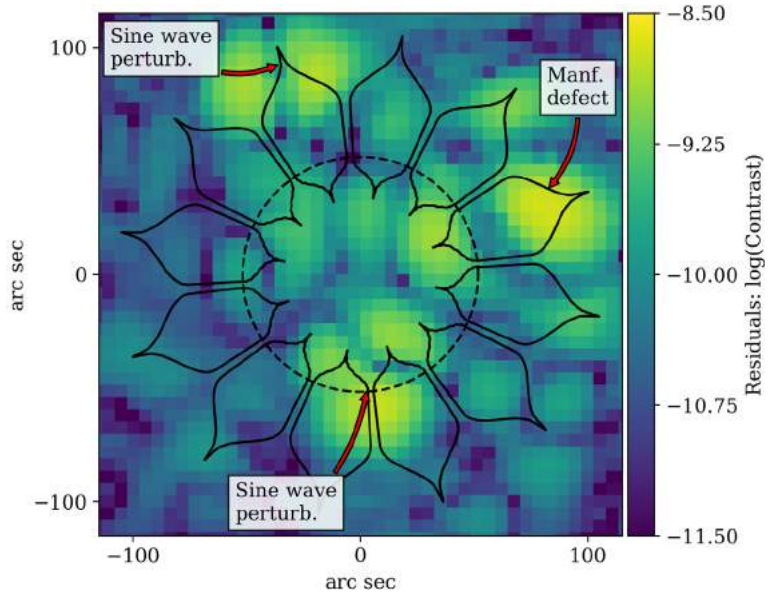

Fig. 10 Residuals between experiment and model of stacked (log-scale contrast) images of mask M12P3 at $\lambda = 725$ nm. Lab and model images were created by median combining images taken at three starshade orientations. The brightest spots are due to intentional sine wave perturbations (see Sec. 4.2.2) and an unintentional manufacturing defect. High contrast is still achieved at the location of the exposed tips (marked by the dashed circle).

images to align on the perturbations, and then median combined. Imaging at different orientations lessens the impact of the central polarization lobes. The residuals (experiment – modell) of the stacked images are shown in Fig. 10. In addition to the exposed tips, M12P3 has sine wave perturbations built into its shape for model validation (see Sec. 4.2.2) and a defect leftover from the manufacturing process, which dominate the contrast in the residual image.

Taking a λ/D wide annulus at the angular separation of the tips, and excluding the portion that lies on the sine wave perturbation (at 6:00 in the image), we find the average residual contrast in the annulus is 7×10^{-11}. Inspection of Fig. 10 shows there is not significant residual light at the location of the tips and that most of the residual are due to leakage of unmodeled non-scalar diffraction from the inner gaps of the starshade and from the perturbations. From this, we conclude that the exposed tips behave as expected (to the 10^{-10} contrast level) and the starshade still provides sufficient contrast outside the IWA.

4 Model Validation Experiments

There will always be slight deformations in the starshade's shape due to manufacturing errors, deployment errors, and thermal and mechanical stresses. A contrast error budget sets tolerances on the allowed deformations by balancing aspects of the mechanical design deemed to be most challenging.[37] One purpose of the model validation experiments is to validate the accuracy at which the models used to derive the error budget capture the sensitivity of contrast performance to shape perturbation; by observing starshades with known perturbations built into the shape, we can validate how the contrast changes in a known way. The validation accuracy set by the experiments determines the model uncertainty factor (MUF) between contrast and shape in the error budget. The MUF is a multiplicative term applied to the intensity (contrast) of each term in the error budget that provides a margin for inaccuracy of the model. Reducing the MUF through experimentation allows us to reduce the contrast margin budgeted to model uncertainty and leads to a more efficient design. The shape changes selected for the validation experiments are related to the mechanical architecture of the SRM design[2] and are representative of the shape errors in the error budget.[37]

The model we are trying to validate uses scalar diffraction only, which is believed to be sufficiently accurate for the flight-scale starshade. However, since the discovery of non-scalar, thick screen effects in the lab configuration, additional work must be done to include these effects in the model to properly demonstrate that the perturbations are accounted for at flight scales.

In this section, we first present results from two experiments testing perturbations that dominate the error budget; experiments on other perturbations are in progress[6] and will be reported at a later date. For the perturbed shape tests, the perturbations are made large enough so that the predicted light leakages are dominated by scalar diffraction, with only slight contributions from the thick screen effect in the inner parts of the starshade. Later in this section, we present results from a polarization study demonstrating the non-scalar model accurately captures the thick screen effect. Estimates of this model applied to flight-scale starshades shows that the effect is negligible as expected (see Appendix B), but a full analysis is saved for a later date. We end this section with an experiment testing the Fresnel number dependence on contrast by testing a starshade at a Fresnel number outside of its designed Fresnel space. We show the model accurately captures this transition, and the transition between the scalar and non-scalar diffraction dominated regimes. The results presented in this section are progress toward Milestone 2 of the S5 Project, which will satisfy the final requirement in the Starlight Suppression technology development plan.[6]

4.1 *Optical Model Summary*

Several methods are available for solving the scalar diffraction problem, all of which have been shown to be in agreement. Two methods, a boundary diffraction wave method[11] and a similar angular integral method,[9,12] convert the two-dimensional diffraction equation into a one-dimensional line integral around the occulter's edge and are well suited to capture the large dynamic range of sizes in the starshade shape. In this work, we use the model of Ref. 36, which uses a two-dimensional Fresnel propagator (shown to be in agreement with the boundary methods[12]) to include non-scalar diffraction. We provide a brief summary of the optical model in Appendix C and we show it in Sec. 4.3 that our implementation of non-scalar diffraction agrees with the data.

4.2 *Perturbed Shape Experiments*

Here, we present results from testing two masks with different classes of perturbations: displaced edges and sine waves. Each mask has two perturbations of different sizes built into its design. The sizes are chosen to produce a signal in the image that is bright enough to overcome contributions from the thick screen effect, but faint enough to be informative to model validation. One perturbation is located on the inner starshade and is made brighter since it is closer to the central polarization lobes; the other defect is located on the outer starshade and is allowed to be fainter. The perturbed masks have 12 petals to minimize the thick screen effect; fewer gaps between petals mean there are fewer sources of non-scalar diffraction and the lobes are $(12/16)^2$ times as bright. Details of the perturbations are given in Table 5, and the locations of inner and outer perturbations are shown in Fig. 11.

In comparing contrasts between experiment and model, we draw a photometric aperture of radius λ/D around the perturbation and calculate the average contrast in that aperture using Eq. (12) of Appendix A, with error given by Eq. (14) of Appendix A. The expected contrast given in Table 5 is the average contrast in the photometric aperture, calculated under the assumption of scalar diffraction only.

4.2.1 *Displaced edge segments*

The displaced edge perturbation simulates the effect of a petal edge segment being displaced from its nominal position during petal assembly on the ground. Figure 12 shows a 2.3-μm tall displaced edge segment built into the design of the manufactured mask M12P2. The locations of the perturbations on the starshade petals are shown in Fig. 11.

Table 5 Description of shape perturbations, including their expected contrast [photometric aperture average, see Eq. (12)] at two wavelengths. Each perturbed mask has an inner and outer perturbation of different size.

			Expected mean contrast	
Perturbation	Location	Description	$\lambda = 641$ nm	$\lambda = 725$ nm
Displaced edge	Inner petal[a]	2.3-μm tall, 414-μm long	2.3×10^{-9}	1.7×10^{-9}
Displaced edge	Outer petal[a]	1.7-μm tall, 532-μm long	6.5×10^{-10}	7.4×10^{-10}
Sine wave	Inner petal[b]	1.75-μm amp., 4 cycles over 2.9 mm	1.9×10^{-9}	1.4×10^{-9}
Sine wave	Outer petal[b]	1.75-μm amp., 5 cycles over 2.3 mm	9.6×10^{-9}	7.3×10^{-10}

[a]M12P2
[b]M12P3

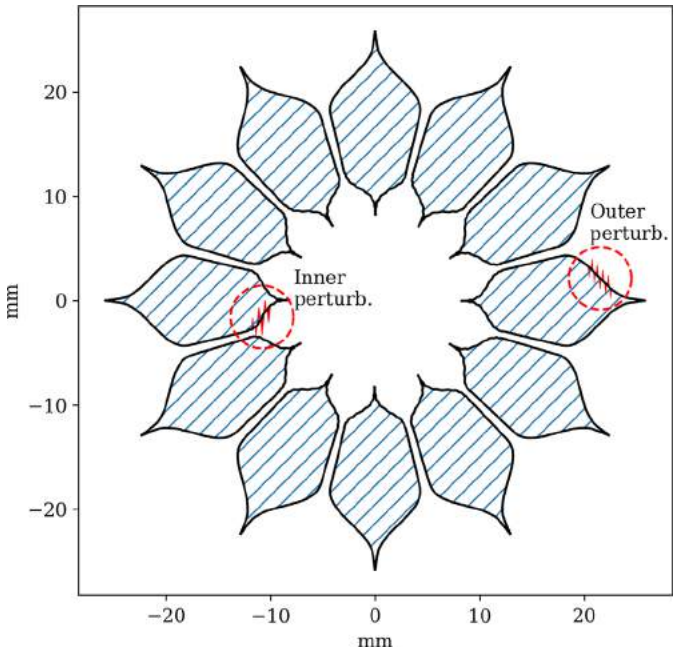

Fig. 11 Location of inner and outer perturbations on the perturbed masks M12P2 and M12P3. The red arrows are a quiver plot of the sine waves on M12P3 with amplitudes greatly exaggerated. The blue hatched area is transparent; the white area is the silicon wafer.

Figure 13 shows the experimental and model contrast images at four wavelengths across the bandpass. The model includes polarization effects and manufacturing defects found on the mask that are larger than 30 square microns. The input polarization vector is horizontal in the image so that the perturbations are away from the inner polarization lobes. Figure 14 plots the average contrast in a λ/D radius photometric aperture centered on each perturbation. By design, the inner perturbation is brightest and drops in contrast with wavelength. The model shows good agreement with the experimental data.

Figure 15 plots the difference in the photometric aperture averaged contrast between the experimental and model data for each of the perturbations. The percent difference is calculated as

$$\text{Percent Difference} = \frac{|\text{Model} - \text{Experiment}|}{\text{Model}} \times 100\%, \tag{6}$$

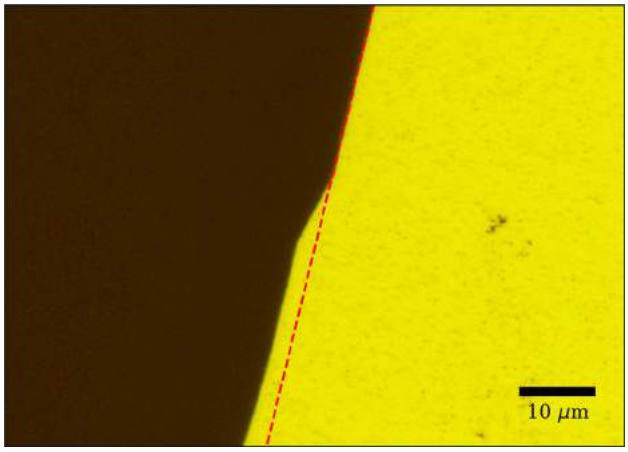

Fig. 12 Microscope image of the inner displaced edge perturbation on M12P2. The red line denotes the edge of the nominal starshade shape. The 2.3-μm step in the edge simulates a displaced edge segment.

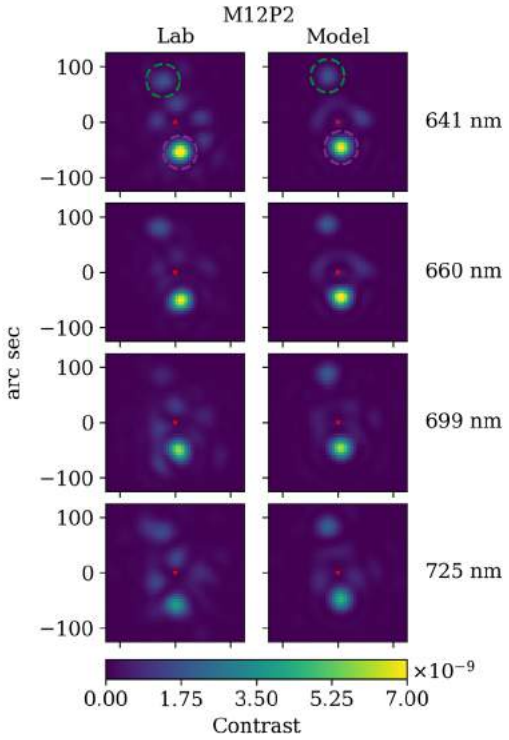

Fig. 13 Contrast images of M12P2—displaced petal edge segment perturbations. Experimental data are in the left column, model data are in the right column. The rows are for the different wavelengths. The perturbation on the inner petal is circled in purple and the perturbation on the outer petal is circled in green. The red "*x*" marks the center of the starshade.

where the values for Model and Experiment are the photometric aperture averaged contrast. The error bars in Fig. 15 are the experimental uncertainty propagated to the percent difference and are calculated as

$$\text{Percent Uncertainty} = \frac{\sigma_{\text{Experiment}}}{\text{Model}} \times 100\%, \tag{7}$$

where $\sigma_{\text{Experiment}}$ is calculated from Eq. (13) of Appendix A.

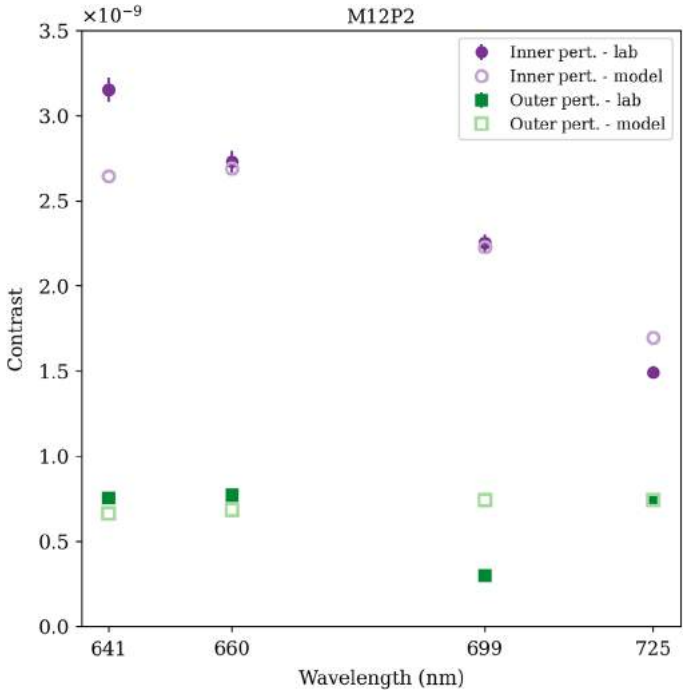

Fig. 14 M12P2—displaced edge perturbations. Contrast for the inner and outer perturbations across the four wavelengths. Solid markers are experimental data; open markers are model data. The contrast is the photometric aperture average given by Eq. (12) and the error bars (on experimental data only) are 1σ, given by Eq. (14). Error bars on experimental data that are not visible are smaller than the symbols.

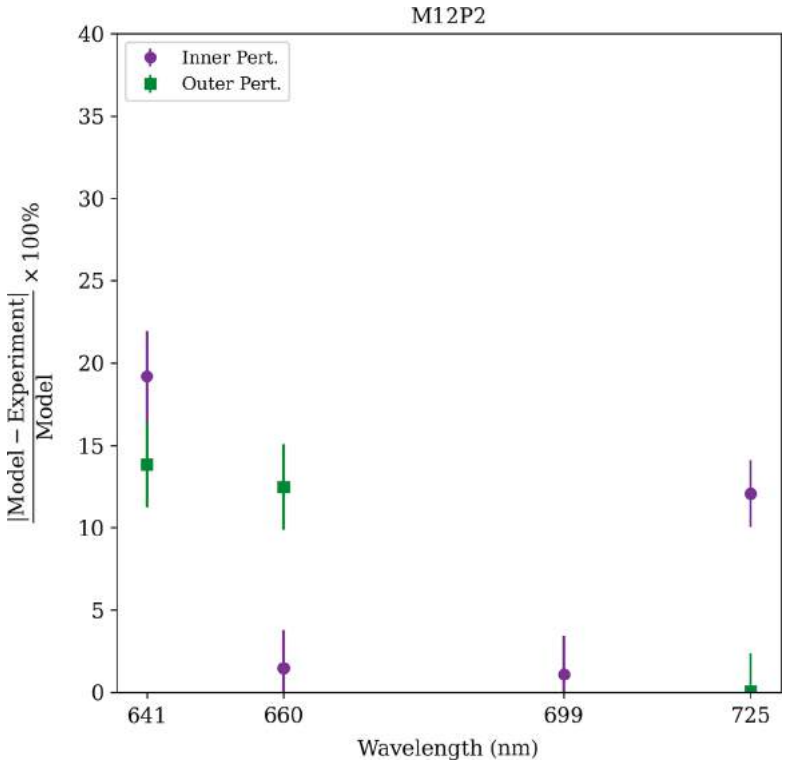

Fig. 15 M12P2—displaced edge perturbations. Percent difference between experimental and model contrast for the Inner and Outer perturbations across the four wavelengths. The contrast is the photometric aperture average given by Eq. (12) and the error bars are the percent uncertainty given by Eq. (7). The value for the Outer perturbation at 699 nm is off the chart (at 60%).

The agreement is better than 20% for all perturbations except for the outer perturbation at $\lambda = 699$ nm. The difference for the outer perturbation at 699 nm is ~60%; Fig. 13 shows that it is much dimmer than expected and does not follow the trend of the different wavelengths. This effect is seen in three orientations of the mask (rotated by $\pm 120°$) and has been repeated several times. We currently do not have a good explanation as to why this happens, but we are continuing to refine the characterization and model of the optical edges in hopes of explaining this observation.

4.2.2 *Sine waves*

Sinusoidal changes to the edge shape can occur if individual edge segments are misplaced in such a way that their envelope creates a sine wave with respect to the nominal edge position. This is a particularly harmful perturbation if the sine wave is in sync with the Fresnel half-zones and they constructively interfere. This also places a strong wavelength dependence on the contrast they induce. The locations of the sine wave defects are shown in Fig. 11.

Figure 16 shows the images taken of this perturbed mask. For M12P3, in addition to the intentional perturbations, a large defect is left over from the manufacturing process and is the brightest source in the image. SEM images show this is a large defect that extends vertically below the wafer's device layer and has a complicated, protruding structure. We estimate the area to be ~750 to 1500 square microns, but projection effects make it difficult to know how much is seen by the camera. In the model, we adjust the area of the defect to 1375 square microns to match the data and contribute the appropriate amount of leakage to the other perturbations.

Figure 17 shows the average contrast in a photometric aperture centered on each perturbation. The sine wave perturbation has a strong response with wavelength, and the inner and outer perturbations occasionally switch which is brightest, behavior that agrees with model predictions.

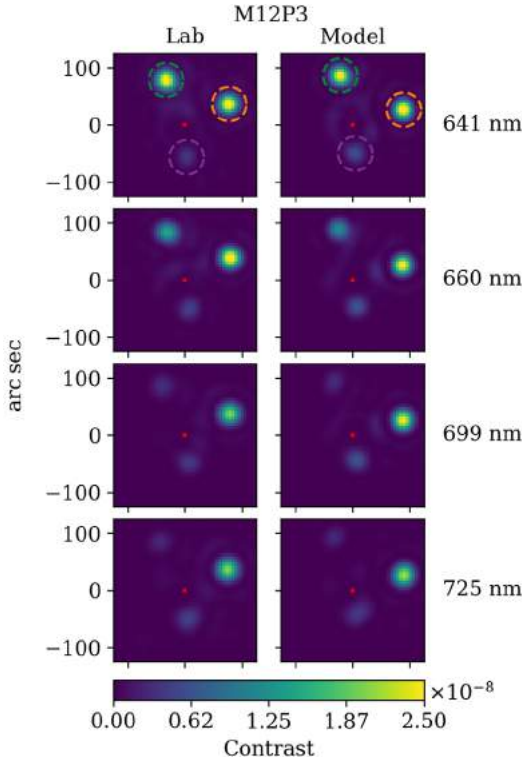

Fig. 16 Contrast images of M12P3—sine wave perturbations. Experimental data are in the left column, model data are in the right column. The rows are for the different wavelengths. The perturbation on the inner petal is circled in purple, the perturbation on the outer petal is circled in green, and the unintentional manufacturing defect is circled in orange. The red *x* marks the center of the starshade.

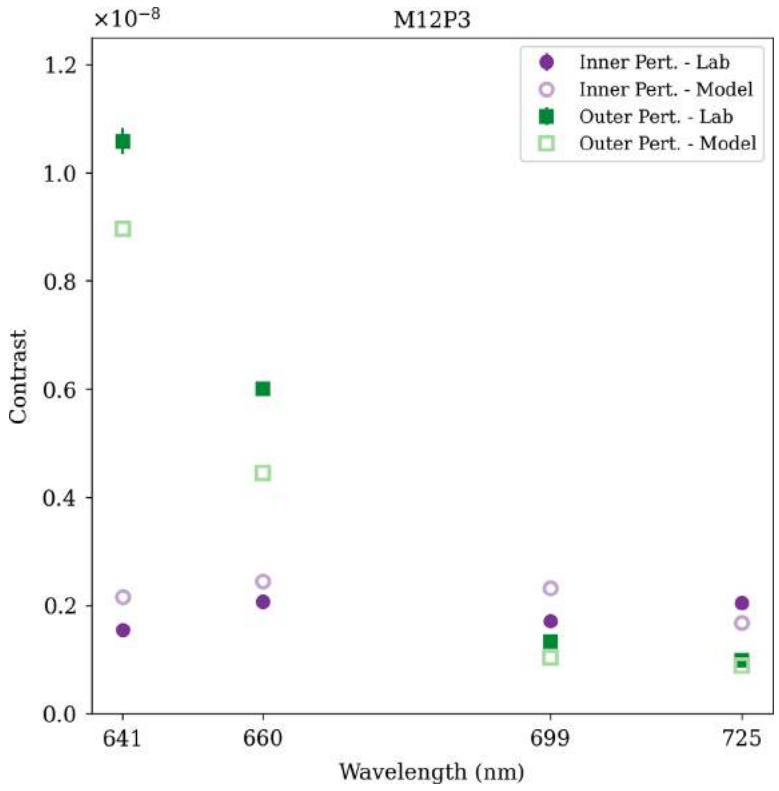

Fig. 17 M12P3—sine wave perturbations. Contrast for the Inner and Outer perturbations across the four wavelengths. Solid markers are experimental data; open markers are model data. The contrast is the photometric aperture average given by Eq. (12) and the error bars (on experimental data only) are 1σ, given by Eq. (14). Error bars on experimental data that are not visible are smaller than the symbols.

Figure 18 shows the comparison between the experimental and model contrasts, with the percent difference calculated from Eq. (6) and the uncertainty on that difference calculated from Eq. (7). For this mask, since the inner and outer perturbations are of equal brightness, the inner one generally performs worse as it is closer to and suffers more contamination from the central polarization lobes. Both the inner and outer perturbations agree with the model to better than 35% at all wavelengths. This agreement is not as good as that of the displaced edges mask, which we attribute to the presence of the large manufacturing defect. Due to the complicated, three-dimensional structure of the manufacturing defect, it is difficult to model the interaction between the defect and the sine wave perturbations. We believe this unmodeled interaction is the source of the larger discrepancy.

4.3 *Polarization Study*

Our proposition that the bright central lobes are due to the thick screen effect can be validated by examining the polarization induced as light propagates past the mask. In the explanation provided in Sec. 3.1.1, the change in the electric field is dependent on the polarization direction relative to the sidewall of the mask. The effect is dominant in the inner gaps between petals, which can be approximated by parallel plates aligned with the clocking angle of the petal. Assuming horizontal linearly polarized light, petals at the 3:00 and 9:00 positions have all *s*-polarization (electric field parallel to wall), petals at 12:00 and 6:00 have all *p*-polarization (electric field perpendicular to wall), and petals in between have a mix of both. The *s*-polarization is subject to a greater change in the electric field (the field goes to zero at the walls of a perfect conductor[34]), so the polarization lobes are aligned with the input polarization direction. Figure 19 confirms this as we view horizontally polarized input light with an analyzing polarizer in front of the camera rotated to different angles. When the analyzer is exactly orthogonal to the

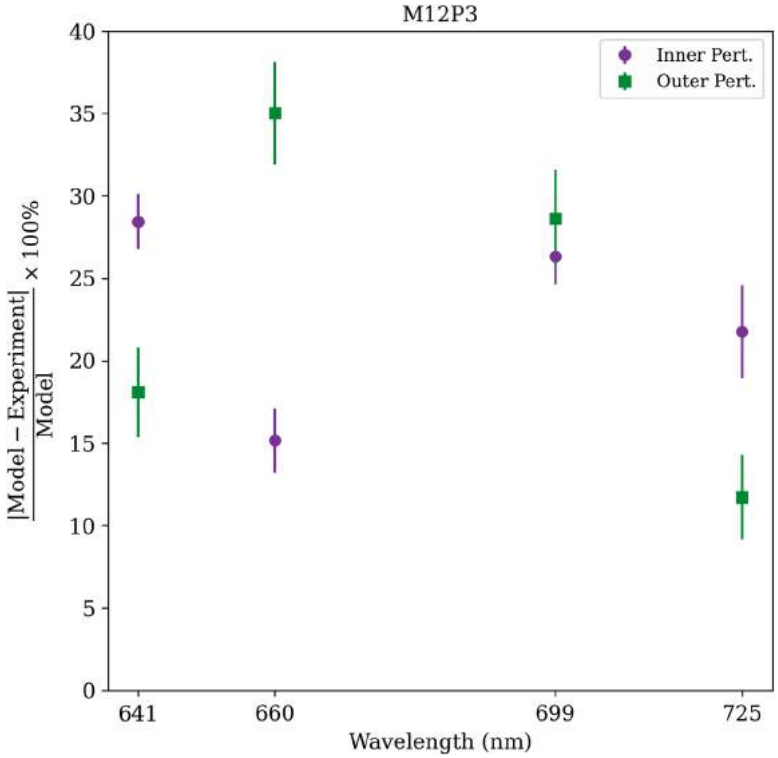

Fig. 18 M12P3—sine wave perturbations. Percent difference between experimental and model contrast for the Inner and Outer perturbations and the unintentional manufacturing defect across the four wavelengths. The contrast is the photometric aperture average given by Eq. (12) and the error bars are the percent uncertainty given by Eq. (7).

input polarizer, scalar diffraction theory predicts no light should be visible. However, we see four lobes that are the result of unbalanced vertical polarization induced by the petals at 45°, 135°, 225°, and 315°.

Figure 20 shows experimental and model data at $\lambda = 641$ nm for the 7-μm-thick mask DW9 with the analyzer aligned and crossed with the input polarization. The model agrees well with the experiment and is able to replicate the major polarization features, even at contrast levels below 10^{-10}. Figure 21 shows experimental and model data at $\lambda = 641$ nm for the 3-μm-thick mask DW21 (these data are taken with linear polarizer installed and thus differ from the DW21 data taken in Sec. 3.2). Again, the model agrees well and the peak contrast (with the analyzer aligned) is ∼2.3× fainter than those of DW9, which is consistent with the thick screen effect scaling

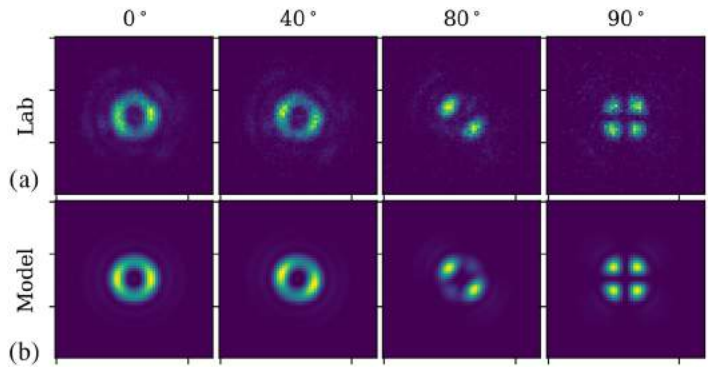

Fig. 19 (a) Experimental and (b) model images of mask DW9 imaged with the camera analyzer rotating relative to the input polarizer direction (horizontal in the image). The angle given is that between the analyzer and polarizer, where 0° means they are aligned, 90° means they are crossed. Data are taken with $\lambda = 641$ nm.

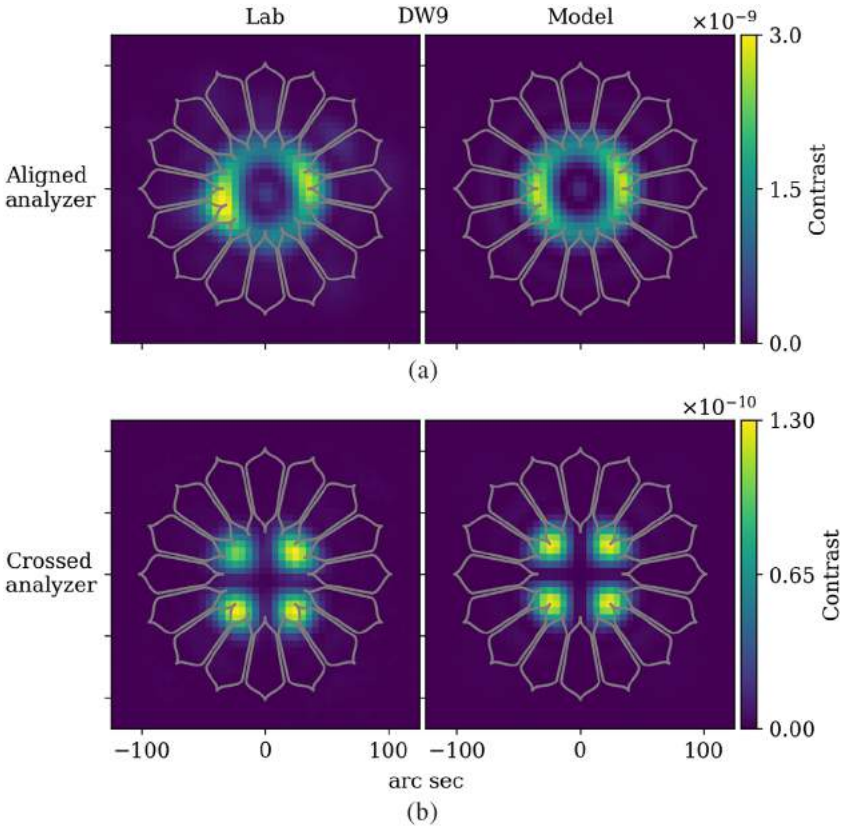

Fig. 20 (a) Experimental and (b) model images of mask DW9 at $\lambda = 641$ nm. In the top row, the camera analyzer is aligned with the input polarizer (with a slight 15° misalignment). In the bottom row, the camera analyzer is crossed with the input polarizer. It is worthy to note the difference in colorbar scales.

linearly with edge thickness, as should be expected. This demonstration shows that we understand the source of the non-scalar diffraction, are able to replicate its dependency on edge thickness, and that it is due solely to the small scale of the experiment and will not be an issue for flight. Appendix B provides an estimate of the strength of this effect at flight scales.

4.4 *Contrast Dependence on Fresnel Number*

The sub-scale experiments presented here are informative for a starshade mission because of the scale invariance of the diffraction equations under the Fresnel approximation. Therefore it is critical to validate this assumption via an exploration of the Fresnel parameter space, starting in regions of high contrast and watching the contrast degrade as the experiment moves beyond the design space. Future testing should deconstruct the Fresnel number into its three constituent parts (R, λ, Z) and explore the contrast dependence of each around the flight-like Fresnel number,[38] however, the size of this testbed puts a practical constraint on how much of the Fresnel parameter space can be explored. Section 3.2 explored the wavelength dependence within the designed Fresnel space; in this section, we explore the size dependence and push beyond the designed Fresnel space to where the contrast begins to degrade. This experiment is a first step in an exploration of Fresnel space and should be followed by more extensive tests in the future.

Figure 22 shows the results of testing a starshade outside of its designed Fresnel space, where the change in Fresnel number is achieved by changing the size of the starshade. Masks DW17 and DW21 have identical apodization functions, but DW21 is 3% larger, which means $\lambda = 725$ nm light is in the designed Fresnel space of DW21 $(N = 12.2)$, but outside that of DW17 $(N = 11.5)$. Figure 22 shows the results of both masks at 725 nm; the contrast rises steeply with Fresnel number and the model captures this transition well, with even better

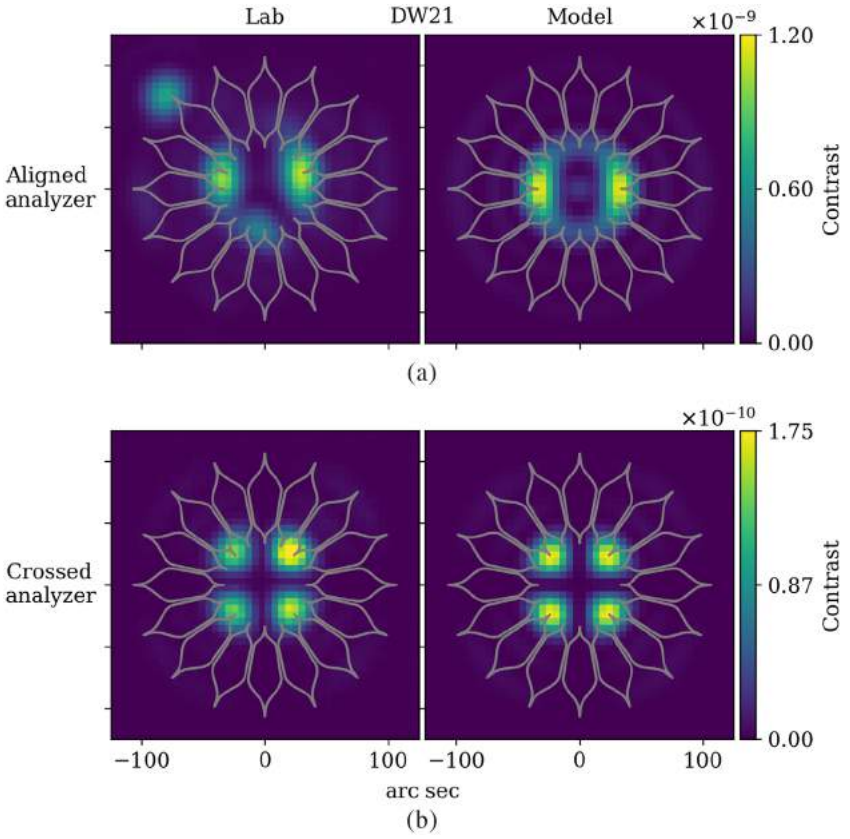

Fig. 21 (a) Experimental and (b) model images of mask DW21 at $\lambda = 641$ nm with polarized light. In the top row, the camera analyzer is aligned with the input polarizer. The bright spot at 10:00 is dust on the mask. In the bottom row, the camera analyzer is crossed with the input polarizer. It is worthy to note the difference in colorbar scales.

model-experiment agreement at the brighter contrast. At these brighter contrast levels, the diffraction is completely dominated by scalar diffraction and both the scalar and non-scalar models converge. As the model agreement improves as the experiment moves beyond the regime where non-scalar diffraction is present and into a scalar-only regime, we build confidence that the scalar model will accurately predict performance in configurations where non-scalar diffraction is less prominent.

5 Discussion

The starshade enables the detection of exoplanets because it provides high contrast at a small IWA, which means it operates at a moderately low Fresnel number where the diffraction is governed by complicated, near field equations. The apodization function that provides sufficiently high contrast is found by solving an optimization problem that minimizes the electric field in the F-K diffraction equation. This radial apodization function is then approximated by a petalized binary occulter that is the starshade's edge. Until now, it had not been shown that we have the tools capable of designing an apodization function that sufficiently suppresses diffraction at low Fresnel numbers and that the petalized approximation is valid. As the Fresnel number is decreased, diffraction becomes harder to control as the apodization function spans fewer Fresnel zones over which to average out imperfections. As such, it was necessary to demonstrate that high contrast was achievable at low Fresnel numbers. The experiments presented here showed for the first time that the design tools used to solve for the apodization function are capable of achieving 10^{-10} contrast at a flight-like Fresnel number. The experiment contrast floor was $\sim 10^{-10}$ at the IWA and $\sim 10^{-11}$ near the outer starshade, allowing us to conclude that approximations in the model are no worse than 10^{-10} for the nominal starshade design.

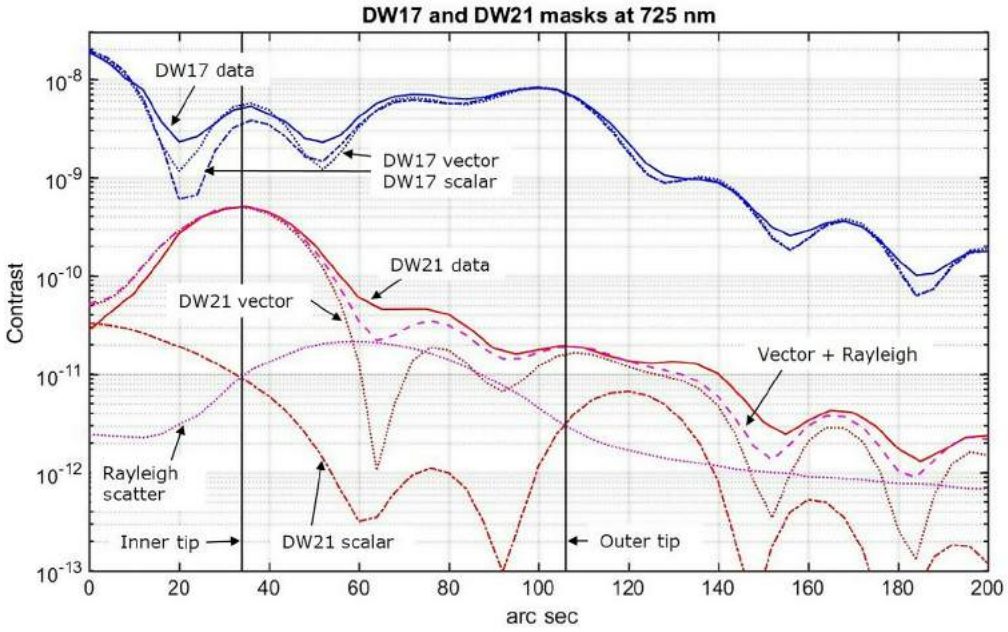

Fig. 22 Azimuthally averaged contrast for masks DW17 and DW21 at $\lambda = 725$ nm, and the corresponding vector and scalar propagation models. The vertical lines mark the tip of the inner and outer apodization profiles. Also shown are estimates of Rayleigh scattering generated from the models of Ref. 32.

The observed thick screen effect represents a worst case scenario in which our assumption of a purely scalar theory of diffraction is no longer valid and the optimized apodization is no longer applied to the appropriate problem. However, even at the small scales of the laboratory configuration, the contribution from non-scalar diffraction is below the target contrast level. Additionally, we expect deviations from scalar diffraction theory to go away at larger scales as the sizes of features get much larger than the wavelength; scaling to a larger starshade for flight should work in our favor. If our theory of the thick screen is correct, the edges of the full-sized starshade will induce the same wavelength wide boundary layer near the edge, but the size of the starshade will be 1000× larger, meaning the impact of the non-scalar diffraction will be $10^6\times$ smaller in intensity and will be reduced to a negligible amount (see Appendix B). Additional work may be needed to complete the validation of the non-scalar diffraction model, but the experiments completed thus far have built confidence that we can achieve the same, if not better, contrast at larger scales. Given historic understanding of how light behaves around features with sizes comparable to the wavelength, it was known non-scalar diffraction could be present, but we previously did not have adequate tools to quantify the effect. The experiments in this work have helped to develop those tools and will allow us to apply them to future configurations.

The model validation experiments aim to determine the accuracy to which the model can predict the contrast sensitivity to known effects. Some of the experimental noise is due to unknown manufacturing errors, misalignment, turbulence, and stray reflections and is not attributable to the model. Without detailed measurements of these error sources, we can only set an upper limit to the model inaccuracy. The results presented in Sec. 4.2 show the model remains accurate to at least the 35% level, with an average difference of 20%. The model agreement is even better (<20%) for the displaced edge perturbation data on mask M12P2, as that mask did not have a large manufacturing defect as mask M12P3 did. This leads us to believe that the dominant source of model disagreement is due to uncharacterized perturbations in the manufactured mask, where due to the thick screen effect, the three-dimensional structure of the mask becomes relevant. The large manufacturing defect in M12P3 has a complex vertical structure that is difficult to adequately characterize and thus difficult to include in the model. Global defects, such as a variable overetching, are also difficult to characterize and can contribute to the model disagreement.

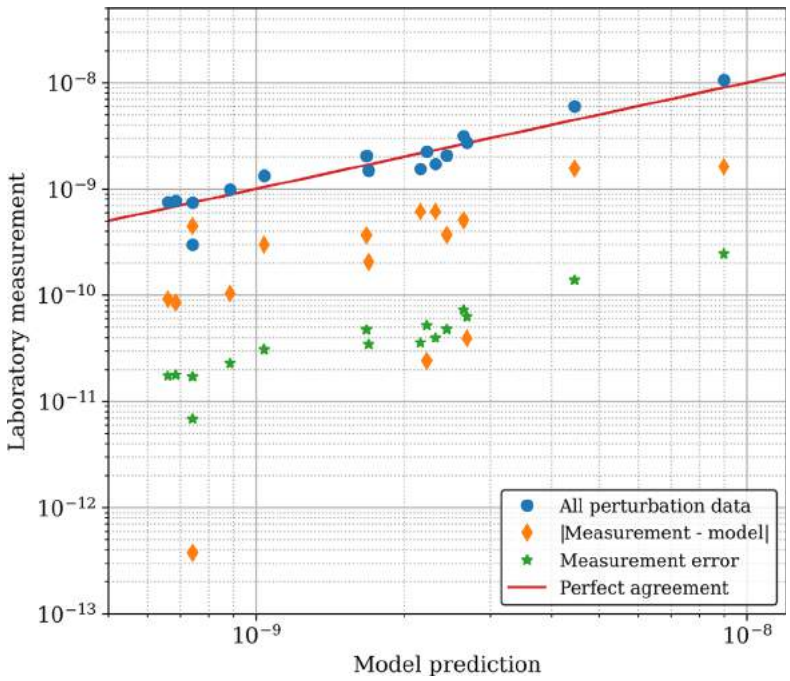

Fig. 23 Model versus measured data for all perturbations on the displaced edge and sine wave perturbations and four wavelengths. The absolute difference between model and measured data and the measurement error are also shown.

Figure 23 shows the measured contrast against the model prediction for all perturbation data, along with the absolute difference between the two and the measurement error. The measurements track well with the model, even down to the lowest contrast levels. The combined photometric and calibration measurement error is well below the model-experiment difference, suggesting the difference is due to modeling error. This modeling error could be due to physics not captured in the diffraction model (i.e., additional non-scalar diffraction contribution from the three dimensional structure) or error in the knowledge of the perturbations (i.e., inaccurate measurement of the size and position all known and unknown shape perturbations). The measurement-model difference and the measurement error follow the same trend as the measurements, meaning the fractional error is not increasing. These results show that the model inaccuracy scales with the size of the perturbation and thus justifies the use of a multiplicative MUF. To provide sufficient margin in the error budget due to model uncertainty, the contrast from each perturbation must be increased by a factor of 1.35×. While this conclusion certainly holds for perturbations down to 10^{-9} contrast, due to the non-scalar diffraction present in the laboratory configuration, comment on the behavior of perturbations at lower contrast levels requires a cautious extrapolation of the trend seen in Fig. 23.

The experiments presented here are only the first of a suite of model validation experiments, so these conclusions on model accuracy are not complete. Future experiments[6] will include global and mixed perturbations and will help us further investigate coherent effects.

6 Conclusion

We have presented results from a number of experiments demonstrating the best contrast achieved with a starshade at a flight-like Fresnel number. We achieved better than 10^{-10} contrast, the level needed to detect Earth-like exoplanets, at the geometric IWA and across a scientifically interesting bandpass. The starshades tested were not perfectly manufactured, their small size introduced non-scalar diffraction, and the experiments were conducted in air. That we were able to achieve such high contrast even in the presence of these factors shows the efficiency and robustness in which starshades operate and should garner confidence in the community for a successful starshade mission in the future.

In future work, we will continue model validation experiments on test masks with more perturbations representative of those in flight. These include: displacing a single petal radially; displacing all petals radially; and combining an edge segment displacement with a petal displacement. We will also continue to refine the thick screen model through tests of masks with different thicknesses and formally apply that model to the flight design to show these effects are negligible at flight scales. Completion of these experiments will advance the starlight suppression technology for starshades to TRL 5 and starshades will be ready for selection for the next exoplanet mission.

7 Appendix A: Contrast Definition

Contrast is defined as the amount of light within a resolution element of a telescope (at the image plane), divided by the peak brightness of the main light source as measured by that telescope when there is no starshade in place. The following equations define the contrast in terms of quantities measured in the lab; Table 6 gives descriptions of the variables used in the definition.

Free space propagation is not possible in the confinements of the lab, thus we use a circular calibration mask to measure the unocculted brightness and convert to a free space brightness through modeling. In the following definitions, the subscript of a symbol will denote the observation mode, with m denoting measurements made when the starshade mask is in place and u denoting unocculted measurements when the calibration mask is in place.

We define the contrast at pixel i as

$$C^i = \frac{\Gamma^i_m}{\Gamma^0_{\text{free space}}} = \frac{\Gamma^i_m}{\gamma A^2 \Gamma^0_u}, \tag{8}$$

which is a theoretical construct specifying the reduction in brightness the starshade mask provides, relative to the on-axis unocculted source.

Table 6 List of variables used in contrast definition.

Symbol	Description
C^i	Contrast at pixel i
Γ^i	Transfer function mapping to pixel i
γ	Ratio of PSF peak after propagation through free space to that of the calibration mask
A	Peak value of apodization function $(= 0.9)$
s^i	Counts collected in pixel i during exposure of length t (ct)
P	Laser power (W)
ν	Neutral density filter transmission
ε	Transmission through atmosphere
τ	Throughput of camera optics
Q	Quantum efficiency of detector (e^-/ph)
E	Photon energy (J/ph)
G	Camera inverse-gain (e^-/ct)
t	Exposure time (s)
m	Denotes mask measurement
u	Denotes unocculted/calibration measurement

The peak value of the apodization function (A^2) in the denominator accounts for the fraction of light that is blocked by the radial struts supporting the inner starshade. The value γ is the ratio of the peak of the PSF after propagation through free space to that after propagation through the circular calibration mask, and relates the contrast measured in the lab to that expected from a free-floating starshade. More details on this conversion can be found in Ref. 21. The transfer function is tied to a measurement through the equation

$$s_x^i = \left(\frac{P\nu\varepsilon Q\tau t\Gamma^i}{EG}\right)_x, \tag{9}$$

where $x \in \{m, u\}$. We drop the superscript on s_u and assume it is on-axis. We assume there is no ND filter during starshade measurements ($\nu_m = 1$, $\nu_u \equiv \nu$) and that the photon energy, camera gain, and camera throughput do not change between observation modes. Substituting Eq. (9) into Eq. (8), we rewrite the contrast as

$$C^i = \left(\frac{\nu s_m^i t_u P_u}{\gamma A^2 s_u t_m P_m}\right)\left(\frac{\varepsilon_u Q_u}{\varepsilon_m Q_m}\right). \tag{10}$$

We assume that values in the right parentheses have the same mean between observation modes, but whose true value during a given observation is distributed normally around the mean with variance σ^2. In other words, $Q_u = Q_m \equiv Q$, $\sigma_{Q_u}^2 = \sigma_{Q_m}^2 \equiv \sigma_Q^2$, and similarly for ε. This simplifies the contrast definition to

$$C^i = \frac{\nu s_m^i t_u P_u}{\gamma A^2 s_u t_m P_m}. \tag{11}$$

For model validation, we calculate the average contrast over n pixels that lie in a photometric aperture of radius λ/D centered at that pixel as

$$C = \frac{1}{n}\sum_i^n C_i \quad = \frac{1}{n}\frac{\nu t_u P_u}{\gamma A^2 s_u t_m P_m}\sum_i^n s_m^i \quad \equiv \alpha \sum_i^n s_m^i, \tag{12}$$

where we have wrapped values independent of pixel into the constant variable α. The uncertainty in α is given by

$$\frac{\sigma_\alpha^2}{\alpha^2} = \frac{\sigma_{s_u}^2}{s_u^2} + \frac{\sigma_\gamma^2}{\gamma^2} + \frac{\sigma_\nu^2}{\nu^2} + \frac{\sigma_{P_u}^2}{P_u^2} + \frac{\sigma_{P_m}^2}{P_m^2} + 2\frac{\sigma_\varepsilon^2}{\varepsilon^2} + 2\frac{\sigma_Q^2}{Q^2}. \tag{13}$$

The variance in the counts of the unocculted image, $\sigma_{s_u}^2$, is given by Eq. (15). We estimate the values of the rest of the uncertainties of α in Ref. 21 to find $\sigma_\alpha \sim 2.5\%$. Assuming independent measurement errors, the uncertainty in the average contrast is propagated to

$$\frac{\sigma_C^2}{C^2} = \frac{\sigma_\alpha^2}{\alpha^2} + \frac{\sum_i^n \sigma_{s_m^i}^2}{\left(\sum_i^n s_m^i\right)^2}, \tag{14}$$

where $\sigma_{s_m^i}^2$ is the variance of pixel i in the mask image.

The dominant contributions to the uncertainty in counts collected during each exposure (s_u, s_m) are: photon noise from the source, background light, and detector dark noise and read noise. We can ignore noise from clock induced charge in the detector electronics, as this is estimated to be $<3 \times 10^{-3}$ events/pixel. Read noise is estimated from the variance of 2 bias frames of 10 μs exposure time to be $\sigma_R = 3.20$ e$^-$/pixel/frame. We combine the number of counts from background light and detector dark noise into the variable d, which is estimated from dark exposures taken with an equal exposure time. The uncertainty in the measurement of s counts in a single image j is given as

$$\sigma_{s_j}^2 = \frac{s_j}{G} + 2\sigma_d^2 + \sigma_R^2. \tag{15}$$

For each observation mode, a number (n_{frames}) of frames are taken and median-combined into a master image. The variance in s counts obtained from n_{frames} frames is given as

$$\sigma_s^2 = \frac{\sigma_{s_j}^2}{n_{\text{frames}}}. \tag{16}$$

Additional details on noise sources and calibrations can be found in Ref. 21.

8 Appendix B: The Thick Screen Effect at Flight Scales

In this appendix, we estimate how the thick screen effect scales with starshade size and argue the effect is negligible at flight scales. To start, we derive an expression for the change in intensity at the telescope due to the thick screen effect (assuming it induces a local change in amplitude only) and show that the expression is consistent with experimental results. We then apply the expression to the flight-scale starshade and show the effect is negligible.

8.1 *Derivation of Intensity Estimation*

We begin with the F-K diffraction equation and assume an incident plane wave with $z = Z_{\text{eff}}$. The on-axis electric field U is given as

$$U = \frac{2\pi}{i\lambda z}\int_0^R A(r)\exp\left\{\frac{i\pi r^2}{\lambda z}\right\} r\mathrm{d}r, \tag{17}$$

where $A(r)$ is the circularly symmetric apodization function. We characterize the thick screen effect as a change in the apodization function (α) relative to the nominal shape (A_0) such that $A(r) = A_0(r) + \alpha(r)$. Equation (17) then becomes

$$\begin{aligned} U &= \frac{2\pi}{i\lambda z}\int_0^R [A_0(r) + \alpha(r)]\exp\left\{\frac{i\pi r^2}{\lambda z}\right\} r\mathrm{d}r \\ &= \frac{2\pi}{i\lambda z}\int_0^R A_0(r)\exp\left\{\frac{i\pi r^2}{\lambda z}\right\} r\mathrm{d}r + \frac{2\pi}{i\lambda z}\int_0^R \alpha(r)\exp\left\{\frac{i\pi r^2}{\lambda z}\right\} r\mathrm{d}r \\ &= U_{\text{nominal}} + \Delta U. \end{aligned} \tag{18}$$

U_{nominal} is the nominal electric field in the scalar diffraction limit and ΔU is the change in electric field as a result of the thick screen effect. In Sec. 3.1.1 we posited, and the models confirm,[36] that the presence of the thick screen induces a change in the electric field in a narrow ($\sim\lambda$) boundary layer around the edge. For now, we restrict ourselves to the case where the presence of the screen induces a change in amplitude only, resulting in a $\sim\lambda$ wide boundary layer around the starshade edge with zero transmission. Since the width of the boundary layer, which we define as δ, is roughly constant for each edge (we neglect differences between polarization states), the change in the apodization function is related to the boundary layer width as

$$\alpha(r) = \begin{cases} 0, & r < R_0 \\ \frac{\delta N_p}{2\pi r}, & R_0 \le r \le R \end{cases}, \tag{19}$$

where N_p is the number of starshade petals, R_0 is the minimum radius at which the petals start, and we've acknowledged that there is no change in the apodization before the petals starts. The thick screen effect can now be written as

$$\Delta U = \frac{2\pi}{i\lambda z}\int_{R_0}^R \left(\frac{\delta N_p}{2\pi r}\right)\exp\left\{\frac{i\pi r^2}{\lambda z}\right\} r\mathrm{d}r \quad = \frac{\delta N_p}{i\lambda z}\int_{R_0}^R \exp\left\{\frac{i\pi r^2}{\lambda z}\right\}\mathrm{d}r. \tag{20}$$

The integral in Eq. (20) can readily be evaluated in terms of Fresnel integrals. We define the complex Fresnel integral as

$$\mathcal{F}(u) \equiv C(u) + iS(u) \equiv \int_0^u e^{i\pi t^2/2}\mathrm{d}t, \tag{21}$$

and make the appropriate substitutions to write the thick screen effect as

$$\Delta U = \left(\frac{\delta N_p}{i\lambda z}\right)\sqrt{\frac{\lambda z}{2}}\left[\mathcal{F}\left(\sqrt{2N}\right) - \mathcal{F}\left(\sqrt{2N_0}\right)\right], \tag{22}$$

where N is the Fresnel number at the starshade radius and N_0 is the Fresnel number at the start of the petals. The change in (on-axis) intensity due to the thick screen effect is then

$$|\Delta U|^2 = \frac{\delta^2}{\lambda z}\frac{N_p^2}{2}\left|\mathcal{F}\left(\sqrt{2N}\right) - \mathcal{F}\left(\sqrt{2N_0}\right)\right|^2. \tag{23}$$

We note that the leading factor looks like a Fresnel number across the width of the boundary layer.

8.2 *Comparison to Experimental Results*

We will now use Eq. (23) to estimate the change in intensity for the laboratory configuration and compare to experimental results of mask DW9. Equation (23) is the change in on-axis intensity at the telescope plane, so we will compare our estimates to the suppression values calculated from pupil plane images. Suppression is the total intensity incident on the telescope's aperture when the starshade is occulting the star, relative to the total intensity of the unblocked star.

At a wavelength of $\lambda = 638$ nm, finite-difference time-domain (FDTD) simulations of the mask DW9 geometry yield an average change in amplitude consistent with a boundary layer width of $\delta = 0.45$ μm (averaging over polarization states). We input the parameters from Table 3 into Eq. (23) to estimate the change in intensity to be $|\Delta U|^2 = 1.6 \times 10^{-8}$. Figure 24 shows the suppression plot (image of the pupil plane) for DW9 at $\lambda = 638$ nm. These data were taken without any polarizing elements, so represent a rough average over polarization states. The peak suppression is 1.5×10^{-7} and the average over the aperture is 6.3×10^{-8}, which is greater than, but within an order of magnitude of, that predicted by Eq. (23). These results show our estimate of the thick screen effect is within reason and we note that Eq. (23) was a lower limit as it assumed an amplitude-only change in field due to the thick screen.

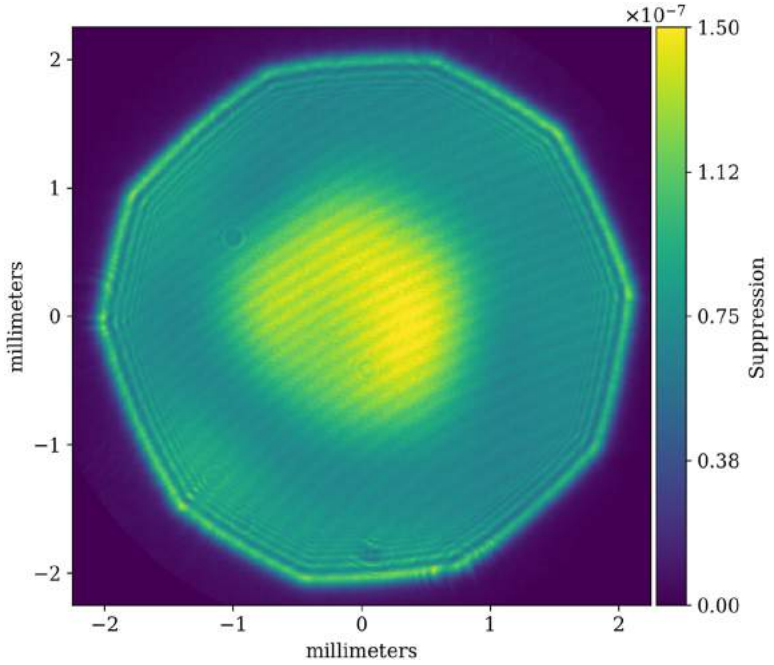

Fig. 24 Suppression (pupil plane) image of DW9 at $\lambda = 638$ nm, without any polarizing elements.

8.3 *Scaling Up to Flight*

By examining Eq. (23), we can see why the non-scalar diffraction should be negligible at flight scales. Scaling from the lab configuration to that of flight, the Fresnel numbers are the same and δ will be roughly the same (the optical edges of the flight design are of similar thickness to those in the lab), so the thick screen effect intensity goes as $|\Delta U|^2 \sim z^{-1}$. The effective starshade-telescope separation for flight is $10^6\times$ that in the lab (the starshades are 1000^{th} scale and the separation scales quadratically with size for a given Fresnel number), so we can expect the non-scalar diffraction to be $10^6\times$ lower in intensity.

Replacing λz in the denominator of Eq. (23) with R^2N gives $|\Delta U|^2 \sim \delta^2/R^2$, which is the same argument given in Sec. 3.1.1 that the thick screen effect goes as the area of the boundary layer relative to the transmission area. A final observation: the leading factor in Eq. (23) is similar to a Fresnel number across the boundary layer, which becomes increasingly small at large separations (because the width remains constant), meaning there is little phase variance across the width.

9 Appendix C: Optical Model Description

The optical model summarized here is presented in full in Ref. 36. The scalar diffraction problem we are solving uses the standard Fresnel and Kirchhoff assumptions that allow us to express the diffraction propagation as a Fourier transform. Because the inner starshade is connected to the outer supporting wafer via the radial struts, the starshade pattern can be treated as individual apertures and standard Fourier techniques sufficiently resolve the starshade.[12] If the coordinates of the screen and observation planes are given as (ξ, η) and (x, y), respectively, we can write the F-K diffraction equation as

$$U(x,y) \propto \mathcal{F}\left[U_0(\xi,\eta)\cdot A(\xi,\eta)\cdot e^{\frac{ik}{2z}(\xi^2+\eta^2)}\right]_{(x,y)}, \tag{24}$$

where U_0 is the initial field incident on the screen, A represents the aperture function of the screen, and $\mathcal{F}[\cdot]_{(x,y)}$ is the Fourier transform. Using the Kirchhoff boundary values, A is a binary function that is 0 on the screen and 1 in the aperture. Our method implements non-scalar diffraction into this model by replacing the boundary values of A with a complex field that arises from local diffraction at the edge of the screen. The presence of the screen only affects its immediate surrounding, so we only change the values of A in a narrow ($\sim 10\lambda$ wide) seam around the edge of the screen, similar to the method proposed by Braunbek.[35]

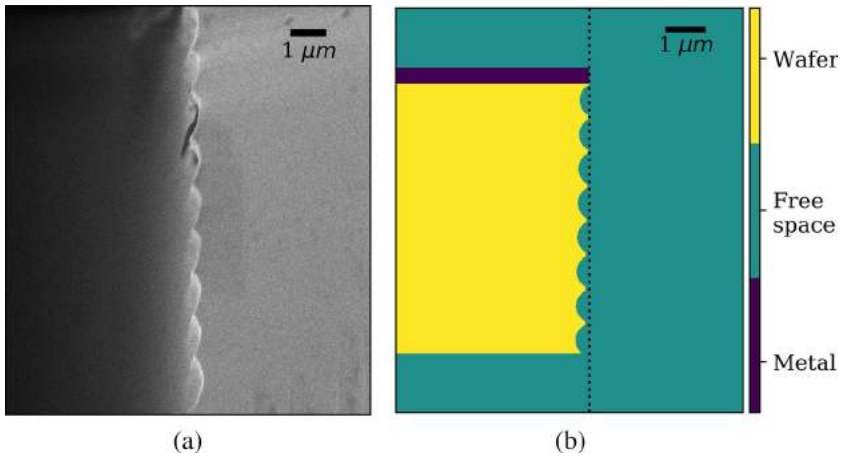

Fig. 25 (a) SEM image of the scalloped vertical profile of the wafer edge for a manufactured mask. (b) Electric permittivity map of the Meep[39] FDTD simulation cell displaying the material geometry.

The field in the seam around the edge is solved via an FDTD simulation[39] of light propagating past the edge of a metal-coated silicon wafer. This simulation solves Maxwell's equations near the edge and allows us to simulate the geometry and material properties of the manufactured starshade masks. To get the model to match the results of Sec. 4.3, we had to account for scalloping and tapering of the mask sidewalls left by the etching process. The edge properties that produced the best fit to the data (1° taper angle and scallops 0.8-μm tall and 0.2-μm deep) were confirmed to be those of the real mask from scanning electron microscope images of the edge of a manufactured mask. Figure 25 shows the simulated geometry of the edge along with SEM images of a manufactured mask, confirming we are properly simulating the complex edge structures.

Acknowledgments

The authors thank Jonathan Arenberg for his helpful and constructive comments. This work was performed in part at the Jet Propulsion Laboratory, California Institute of Technology, under a contract with the National Aeronautics and Space Administration. Starshade masks were manufactured using the facilities at the Microdevices Lab at JPL. This project made use of the resources from the Princeton Institute for Computational Science and Engineering (PICSciE) and the Office of Information Technology's High Performance Computing Center and Visualization Laboratory at Princeton University. Some of the work presented here is included in the S5 Milestone Reports of Refs. 21, 22, and 40. Anthony Harness is a guest editor for this special section.

References

1. W. Cash, "Detection of Earth-like planets around nearby stars using a petal-shaped occulter," *Nature* **442**, 51–53 (2006).
2. S. Seager, N. J. Kasdin, and S. R. P. Team, "Starshade rendezvous mission probe concept," American Astronomical Society Meeting Abstracts #231, 2018, https://smd-prod.s3.amazonaws.com/science-red/s3fs-public/atoms/files/Starshade2.pdf.
3. S. Gaudi et al., "The Habitable exoplanet observatory (HabEx) mission concept study final report," Jet Propulsion Laboratory Publications, https://www.jpl.nasa.gov/habex/pdf/HabEx-Final-Report-Public-Release-LINKED-0924.pdf (2020).
4. D. Spergel and THEIA Collaboration, "THEIA: telescope for habitable exoplanets and interstellar/intergalactic astronomy," in *Am. Astron. Soc. Meeting Abstracts 215* (2010).
5. M. Turnbull et al., "The search for habitable worlds. 1. The viability of a starshade mission," *Publ. Astron. Soc. Pac.* **124**, 418 (2012).
6. P. Willems, "Starshade to TRL5 (S5) technology development plan," Jet Propulsion Laboratory Publications, 2018, https://exoplanets.nasa.gov/internal_resources/1033.
7. B. Crill and N. Siegler, "Exoplanet Exploration Program: 2019 technology plan appendix," Jet Propulsion Laboratory Publications D-102506, 2018, https://exoplanets.nasa.gov/internal_resources/1123/.
8. P. Willems, "NASA's starshade technology development activity," *J. Astron. Telesc. Instrum. Syst.* **7**(2), 021203 (2021).
9. W. Cash, "Analytic modeling of starshades," *Astrophys. J.* **738**, 76 (2011).
10. R. J. Vanderbei, E. Cady, and N. J. Kasdin, "Optimal occulter design for finding extrasolar planets," *Astrophys. J.* **665**, 794–798 (2007).
11. E. Cady, "Boundary diffraction wave integrals for diffraction modeling of external occulters," *Opt. Express* **20**, 15196 (2012).
12. A. Harness et al., "Advances in edge diffraction algorithms," *J. Opt. Soc. Am. A* **35**, 275–285 (2018).
13. D. Leviton et al., "White-light demonstration of one hundred parts per billion irradiance suppression in air by new starshade occulters," *Proc. SPIE* **6687**, 465–476 (2007).
14. R. Samuele et al., "Starlight suppression from the starshade testbed at NGAS," *Proc. SPIE* **7440**, 21–29 (2009).
15. E. Cady et al., "Progress on the occulter experiment at Princeton," *Proc. SPIE* **7440**, 38–47 (2009).

16. R. Samuele et al., "Progress at the starshade testbed at Northrop Grumman Aerospace Systems: comparisons with computer simulations," *Proc. SPIE* **7731**, 1733–1744 (2010).
17. D. Sirbu et al., "Optical verification of occulter-based high contrast imaging," *Proc. SPIE* **8151**, 416–427 (2011).
18. T. Glassman et al., "Measurements of high-contrast starshade performance," *Proc. SPIE* **9143**, 805–817 (2014).
19. T. Glassman et al., "2012 TDEM: demonstration of starshade starlight-suppression performance in the field. Final report," Jet Propulsion Laboratory Publications, 2012, https://exoplanets.nasa.gov/exep/files/exep/GlassmanTDEM2012_FinalReport.pdf.
20. A. Harness, W. Cash, and S. Warwick, "High contrast observations of bright stars with a starshade," *Exp. Astron.* **44**, 209–237 (2017).
21. A. Harness et al., "Starshade technology development activity Milestone 1A: demonstration of high contrast in monochromatic light at a flight-like Fresnel number," Jet Propulsion Laboratory Publications, 2019, https://exoplanets.nasa.gov/internal_resources/1210.
22. A. Harness et al., "Starshade technology development activity Milestone 1B: demonstration of high contrast in broadband light at a flight-like Fresnel number," Jet Propulsion Laboratory Publications, 2019, https://exoplanets.nasa.gov/internal_resources/1211.
23. A. Boss et al., "ExoTAC report on starshade S5 milestones #1A and #1B review," Jet Propulsion Laboratory Publications, 2019, https://exoplanets.nasa.gov/internal_resources/1214/.
24. J. W. Arenberg et al., "Optical performance of the New Worlds Occulter," *C.R. Phys.* **8**, 438–447 (2007).
25. M. Born and E. Wolf, *Principles of Optics*, 7th ed., Cambridge University, New York (1999).
26. M. Galvin et al., "Design and construction of a 76 m long-travel laser enclosure for a space occulter testbed," *Proc. SPIE* **9912**, 2031–2048 (2016).
27. Y. Kim et al., "Experimental study of starshade at flight Fresnel numbers in the laboratory," *Proc. SPIE* **9904**, 1143–1153 (2016).
28. K. Balasubramanian et al., "High contrast internal and external coronagraph masks produced by various techniques," *Proc. SPIE* **8864**, 644–652 (2013).
29. K. Balasubramanian et al., "Fabrication of coronagraph masks and laboratory scale starshade masks: characteristics, defects, and performance," *Proc. SPIE* **10400**, 74–89 (2017).
30. M. Bottom et al., "Starshade formation flying I: optical sensing," *J. Astron. Telesc. Instrum. Syst.* **6**(1), 015003 (2020).
31. L. Palacios, A. Harness, and N. J. Kasdin, "Hardware-in-the-loop testing of formation flying control and sensing algorithms for starshade missions," *Acta Astronaut.* **171**, 97–105 (2020).
32. P. Willems and A. Harness, "Rayleigh scattering in the Princeton starshade testbed," *Proc. SPIE* **11117**, 193–201 (2019).
33. J. Tirapu-Azpiroz, P. Burchard, and E. Yablonovitch, "Boundary layer model to account for thick mask effects in photolithography," *Proc. SPIE* **5040**, 1611–1619 (2003).
34. J. D. Jackson, *Classical Electrodynamics*, 3rd ed., John Wiley & Sons, New York (1998).
35. W. Braunbek, "Neue Näherungsmethode für die Beugung am ebenen Schirm," *Z. Phys.* **127**, 381–390 (1950).
36. A. Harness, "Implementing non-scalar diffraction in Fourier optics via the Braunbek method," *Opt. Express* **28**, 34290–34308 (2020).
37. S. Shaklan et al., "Error budgets for the Exoplanet Starshade (Exo-S) probe-class mission study," *Proc. SPIE* **9605**, 314–327 (2015).
38. G. Blackwood et al., "Starshade Readiness Working Group recommendation to astrophysics division director," Jet Propulsion Laboratory Publications CL#16-5333, 2016, https://exoplanets.nasa.gov/system/internal_resources/details/original/339_SSWG_APD_briefing_final.pdf.
39. A. F. Oskooi et al., "Meep: a flexible free-software package for electromagnetic simulations by the FDTD method," *Comput. Phys. Commun.* **181**(3), 687–702 (2010).
40. A. Harness et al., "Demonstration of 1e-10 contrast at the inner working angle of a starshade in broadband light and at a flight-like Fresnel number," *Proc. SPIE* **11117**, 185–192 (2019).

Anthony Harness is an associate research scholar in the Mechanical and Aerospace Engineering Department at Princeton University. He received his PhD in astrophysics in 2016 from the University of Colorado Boulder. He currently leads the experiments at Princeton validating starshade optical technologies.

Stuart Shaklan is the supervisor of the High Contrast Imaging Group in the Optics Section of the Jet Propulsion Laboratory. He received his PhD in optics at the University of Arizona in 1989 and has been with JPL since 1991.

Philip Willems is an optical engineer at the Jet Propulsion Laboratory, where he is the manager of the S5 Starshade Technology Development Activity. He received his BS degree in physics from the University of Wisconsin–Madison in 1988, and his PhD in physics from the California Institute of Technology in 1997.

N. Jeremy Kasdin is the assistant dean for engineering at the University of San Francisco and the Eugene Higgins professor of Mechanical and Aerospace Engineering, emeritus, at Princeton University. He received his PhD in 1991 from Stanford University. After being the chief systems engineer for NASA's Gravity Probe B spacecraft, he joined the Princeton faculty in 1999 where he researched high-contrast imaging technology for exoplanet imaging. From 2014 to 2016, he was vice dean of the School of Engineering and Applied Science at Princeton. He is currently the adjutant scientist for the coronagraph instrument on NASA's Wide Field Infrared Survey Telescope.

Biographies of the other authors are not available.

Optical experiments and model validation of perturbed starshade designs

Harness, Anthony, Shaklan, Stuart, Willems, Phil, Kasdin, N. Jeremy, Balasubramanian, K., et al.

Anthony Harness, Stuart Shaklan, Phil Willems, N. Jeremy Kasdin, K. Balasubramanian, Victor White, Karl Yee, Philip Dumont, Rich Muller, Simon Vuong, Michael Galvin, "Optical experiments and model validation of perturbed starshade designs," Proc. SPIE 11823, Techniques and Instrumentation for Detection of Exoplanets X, 1182312 (1 September 2021); doi: 10.1117/12.2595409

SPIE.

Event: SPIE Optical Engineering + Applications, 2021, San Diego, California, United States

Optical experiments and model validation of perturbed starshade designs

Anthony Harness[a], Stuart Shaklan[b], N. Jeremy Kasdin[a,c], Phillip Willems[b], K. Balasubramanian[b], Philip Dumont[b], Victor White[b], Karl Yee[b], Rich Muller[b], Simon Vuong[b], and Michael Galvin[a]

[a]Princeton University, Mechanical & Aerospace Engineering Dept., Princeton, New Jersey
[b]Jet Propulsion Laboratory, California Institute of Technology, Pasadena, California
[c]University of San Francisco, College of Arts and Sciences, San Francisco, California

ABSTRACT

Starshades are a leading technology to enable the direct detection and spectroscopic characterization of Earth-like exoplanets. Critical starshade technologies are currently being advanced through the S5 Project and at the Princeton starshade testbed. We report on the status of Milestone 2 of the S5 Project, optical model validation. We present results from optical experiments of starshades with intentional perturbations built into their design. These perturbations are representative of the type of perturbations possible in a flight design and serve as points of validation for diffraction models and error budgets. We show experimental results for two perturbed shapes, a mask with all petals shifted radially outward by 5 μm and a mask with shallow sine waves built into two petals. We compare these data to outputs of the optical model and demonstrate better than 25% agreement. We also present images taken in crossed polarized light and use those data to constrain physical parameters of the optical edge. Bringing in previously obtained results for other perturbed shapes, we show an agreement between experiment and model of better than 25% and argue that this satisfies the Milestone 2 criteria.

Keywords: Starshades, High Contrast Imaging, Model Validation, Exoplanet Detection

1. INTRODUCTION

Starshades are a leading technology to detect and characterize Earth-like exoplanets and are being considered in a number of mission concept designs.[1,2] As part of the Starshade to TRL 5 (S5) activity, the starlight suppression gap is being advanced to TRL 5 through optical verification experiments of sub-scale starshades.[3] Previous optical verification experiments[4] satisfied Milestones 1A[5] and 1B[6] of the S5 development plan[3] by demonstrating better than 10^{-10} contrast at the inner working angle of a starshade at a flight-like Fresnel number across a 10% wavelength bandpass. The Milestones 1A and 1B work validated the fundamental operation of a starshade and showed no optical impediments to achieving 10^{-10} contrast.

The work presented here focuses on optical model validation and continues the testing of starshades with intentional perturbations built into their shape that was started in Refs. 4,7. This work represents additional progress towards satisfying Milestone 2 of the S5 development plan.[3]

Milestone 2: Small-scale starshade mask in the Princeton Testbed validates contrast vs. shape model to within 25% accuracy for induced contrast between 10^{-9} and 10^{-8}.

We present results from testing two perturbed starshade designs: mask M12P8 has all of its petals shifted radially outward by 5 μm; mask M12P9 has shallow sinusoidal perturbations built into the shape of two of its petals. Imaging these masks in crossed polarized light helps to further constrain the physical parameters of the optical edge and thus helps constrain the resultant vector diffraction effects.

In Section 2 we provide an update on the optical model, where we are now solving the Fresnel diffraction equation via an areal quadrature method.[8] Section 3 presents the experiment and model results for the two perturbed masks. In Section 4, we present images taken with a polarized analyzer orthogonal to the input polarization direction. In Section 5, we bring in previously obtained results for a discussion on Milestone 2 and argue that we have satisfied the criteria. Finally, we conclude in the last section.

Email: aharness@princeton.edu

Techniques and Instrumentation for Detection of Exoplanets X, edited by Stuart B. Shaklan, Garreth J. Ruane,
Proc. of SPIE Vol. 11823, 1182312 · © 2021 SPIE · CCC code: 0277-786X/21/$21 · doi: 10.1117/12.2595409

2. MODEL UPDATE

The optical model was recently updated to adopt the highly-efficient areal quadrature method developed in Ref. 8 to solve the Fresnel diffraction equation. This method assigns Gaussian quadrature weights to the starshade shape and uses non-uniform FFT algorithms[9] to match the accuracy of edge diffraction algorithms while being orders of magnitude faster. We have modified this approach to model the shape perturbations we are testing and to incorporate non-scalar diffraction effects into the scalar diffraction model. The areal quadrature method is well-suited to model non-scalar diffraction through the Braunbek method developed in Ref. 10. The narrow seam around the starshade's edge is easily resolved by the Gaussian quadrature and the vector diffraction field calculated via FDTD[11] methods can be included directly in the quadrature weights. A section of the narrow seam around the starshade edge is shown in Figure 1 (greatly exaggerated for clarity), where we plot the distance from the edge calculated at the quadrature points. This distance is used to interpolate the vector diffraction field calculated in the FDTD simulation and apply a complex field value to the quadrature weights. The seam width used in the calculations extends 25 μm on the illuminated side, beyond which the vector diffraction field has completely decayed.

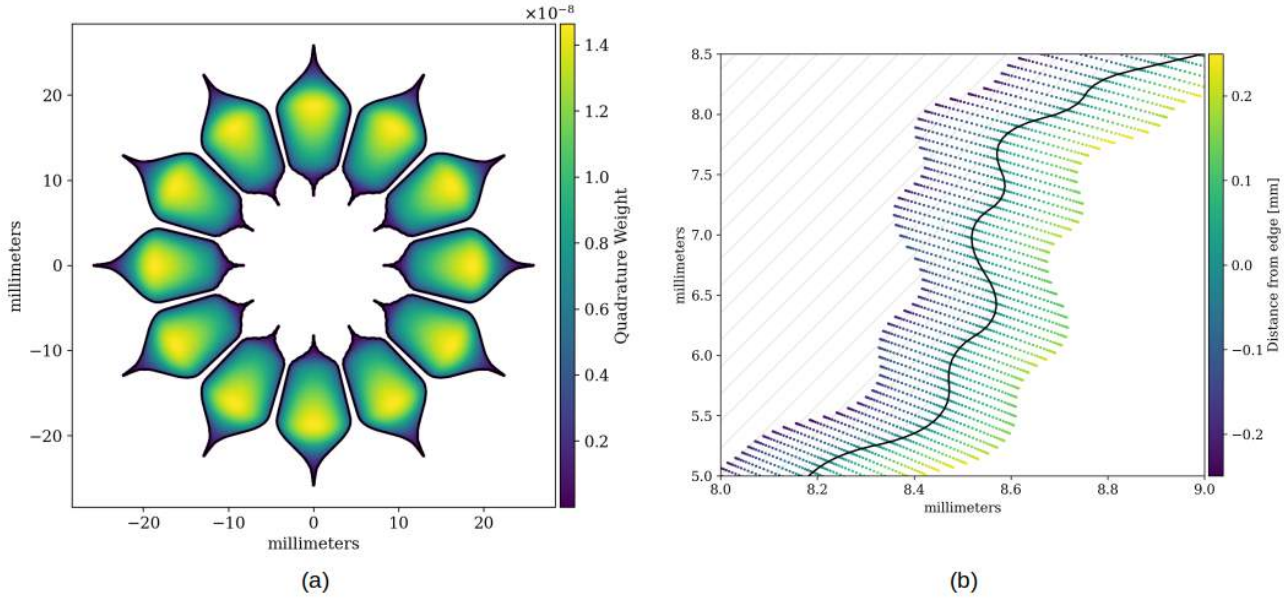

Figure 1. (a) Quadrature weights in the transmission regions of the lab starshade. (b) A section of the starshade's edge with the opaque starshade denoted by the hatch marks. Overplot in color is the distance from the edge calculated at the quadrature points. The size of the seam is greatly exaggerated for clarity.

3. PERTURBED SHAPE TESTS

Model validation experiments are done by testing starshade masks with intentional shape perturbations built into their design; these perturbations are representative of the shape errors included in the error budget of mission designs. The accuracy to which the model captures the sensitivity of contrast performance to shape perturbation determines the Model Uncertainty Factor (MUF), which adds contrast margin to the error budget. We have previously reported on experiments testing various shape perturbations: a displaced petal edge segment;[4] sine waves along the petal;[4] three radially shifted petals;[7] and a mask with both shifted petals and displaced edges. In this report, we present results from testing a new perturbation type - globally shifted petals - along with results from a new sine wave mask, as the previously tested sine wave mask had a large manufacturing defect.

The two starshade masks and their perturbations are summarized in Table 1. Mask M12P8 is built with all twelve of its petals shifted radially outward by 5 µm. Mask M12P9 is built with a sinusoidal perturbation to the shape of two of its petals. The perturbations are sized to be large enough to generate a clear signal above any non-scalar diffraction contribution, but small enough to be informative to the error budget. Both of the starshades have the apodization design C12 of Table 4 in Ref. 4, and have a 2 µm edge thickness with a 0.25 µm aluminum coating. The following sections present the results from testing these two masks. In each experiment, the input (linear) polarization vector is horizontal in the image and the camera analyzer is parallel to this vector. We compare the experimental results to those produced by our diffraction model that includes effects from non-scalar diffraction.

Mask	Perturbation	Description	Location
M12P8	Shifted Petal	5 µm outward shift	All Petals
M12P9	Sine Wave	1.75 µm amp., 4 cycles over 2.9 mm	Inner Petal 5
	Sine Wave	1.75 µm amp., 5 cycles over 2.3 mm	Outer Petal 11

Table 1. Description of masks with shape perturbations. The petal number corresponds with its clock angle.

3.1 Global Shifted Petals

The mask M12P8 is built with all twelve petals of the inner starshade shifted radially outward by 5 µm (along the direction of the radial spokes). Figure 2 (a) shows experimental and model contrast images of M12P8 across four wavelengths. Shifting the petals outward changes the apodization profile (the amount of light transmitted as a function of radius) from its optimized design and the starshade no longer achieves its optimal starlight suppression. Diffracted light emerges from the base of each petal, which is blended together by the point spread function of the telescope and appears as a ring at the base of the petals. Figure 2 (b) shows the azimuthally averaged contrast values for the experimental and model images and shows better than 10% agreement between experiment and model.

3.2 Sine Waves

The mask M12P9 is a remake of the sine wave perturbation mask M12P3 presented in Ref. 4, which suffered from a large manufacturing defect. There are shallow sine waves built into the design of the petals at the 5 o'clock and 11 o'clock positions, which show up as bright spots in the image. Figure 3 shows experimental and model contrast images across four wavelengths. Figure 4 (a) plots the average contrasts calculated in a λ/D radius photometric aperture centered on each perturbation. Figure 4 (b) plots the percent difference between the experimental and model contrasts. All perturbations agree to better than 25%, with the root mean square (RMS) difference ∼15%.

4. CROSSED ANALYZER DATA

In addition to observing the contrast response of the perturbations, we observe each mask with the polarized analyzer at the camera aligned orthogonal to the input polarization direction. Figure 5 shows these experimental and model data for M12P8 and M12P9. The faint light in these images are completely due to vertical polarization induced by the mask while propagating past the thick optical edge. These data help to constrain the physical parameters (thickness, taper angle, scallop size from Ref. 10) of the optical edge profile, with the crossed analyzer data being strongly dependent on the scallop size.

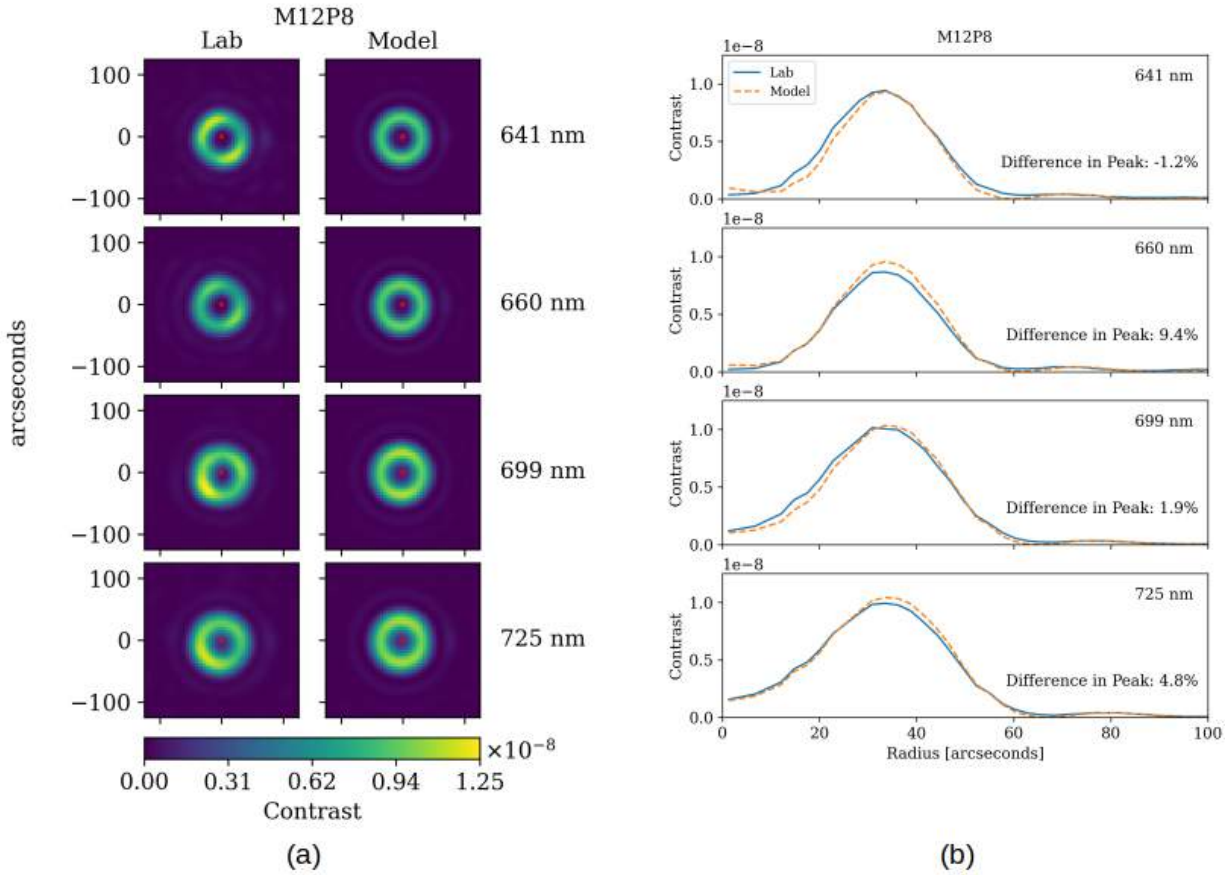

Figure 2. M12P8 – global shifted petal perturbations. (a) Experimental data are in the left column, model data are in the right column. The rows are for the different wavelengths. (b) Azimuthally averaged data for experimental data (blue solid line) and model data (orange dashed line).

5. DISCUSSION OF MILESTONE 2

The experiments presented here represent the final two perturbed masks to be tested for model validation in Milestone 2, which is defined in Section 1. To assess the progress towards meeting the Milestone 2 criteria, we collect the contrast results from all perturbed mask experiments and compare to the outputs generated from the latest model with non-scalar diffraction effects included. A summary of the perturbed masks is presented in Table 2.

Mask	Perturbation	No. Perts.	Reference
M12P2	Displaced Edges	2	Ref. 10
M12P6	3 Shifted Petals	3	Ref. 7
M12P7	Shifted Petals + Displaced Edges	2	Ref. 7
M12P8	Global Petal Shift	1	This Work
M12P9	Sine Waves	2	This Work

Table 2. Mask name, perturbation type, number of perturbations, and reference for all perturbed masks to be used in Milestone 2 analysis.

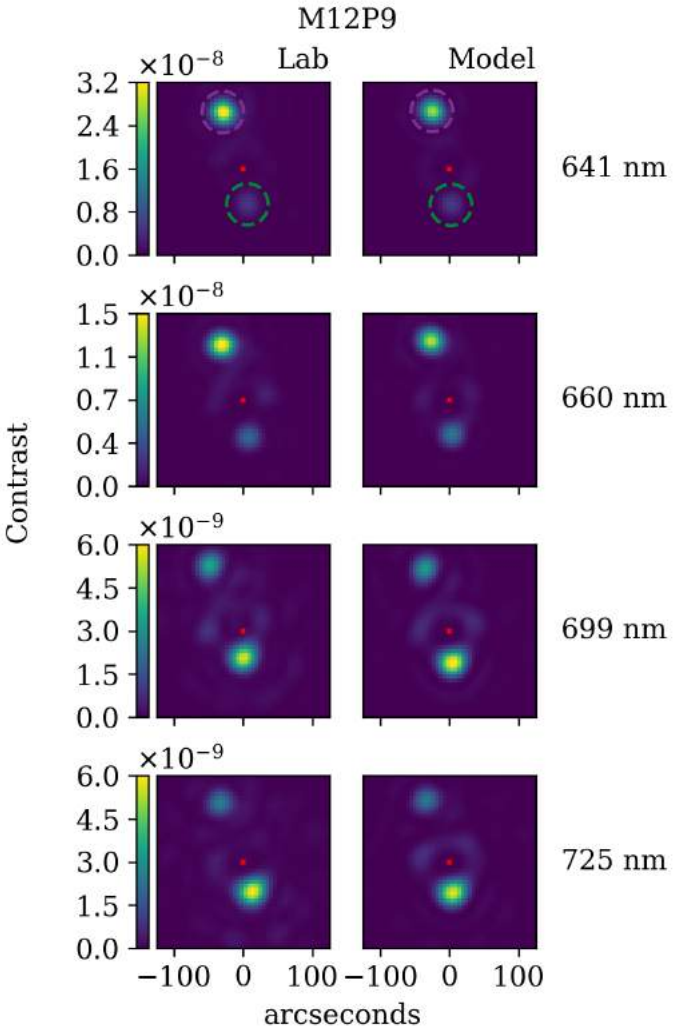

Figure 3. Contrast images of M12P9 − sine wave perturbations. Experimental data are in the left column, model data are in the right column. The rows are for the different wavelengths. The red 'x' marks the center of the starshade. The color of the circles distinguish the perturbations in later plots.

Each mask is observed at 4 wavelengths, at 3 orientations (clocking angle) per wavelength, and each mask has 2 or 3 perturbations, which gives 24 - 36 perturbation combinations per mask. M12P8 only has 1 perturbation, as we use the peak contrast of the azimuthally averaged image. In Figure 6 we plot the percent difference for each perturbation combination for both the scalar and vector models. The inclusion of vector diffraction effects in the model significantly improves the agreement for M12P2 and M12P9, and slightly improves that of M12P8. The agreement gets worse for M12P6, which already has a large number of points with poor agreement. Work is in progress to adjust the physical parameters of the optical edge in order to bring the vector diffraction model of M12P6 into agreement.

To quantify the agreement between experiment and model, we use the root mean square (RMS) difference in contrast between experiment and model. The contrast is the average in a λ/D radius photometric aperture

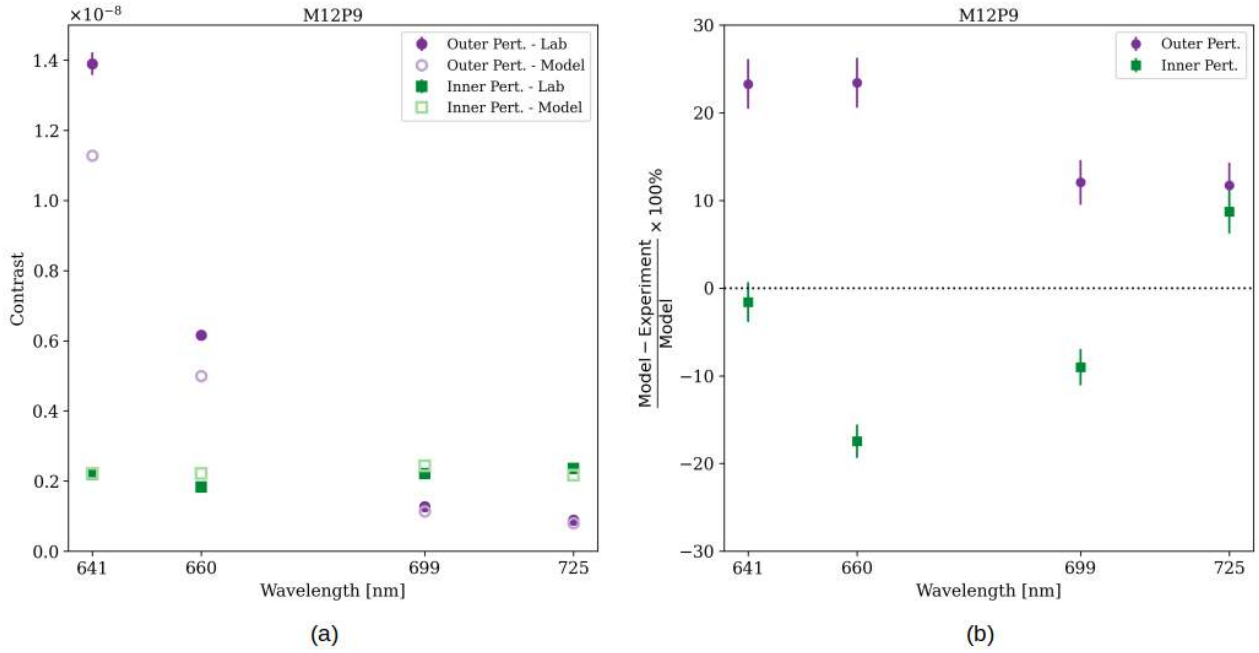

Figure 4. M12P9 − sine wave perturbations. (a) Contrast for the two perturbations across the four wavelengths. Solid markers are experimental data; open markers are model data. (b) Percent difference between experimental and model contrast across the four wavelengths.

centered on the perturbation. The RMS difference is defined as

$$\mathrm{RMS} = \sqrt{\frac{1}{N}\sum_{j}^{N}\left(\frac{\mathrm{Lab}_j - \mathrm{Model}_j}{\mathrm{Model}_j}\right)^2} \times 100\%\,, \tag{1}$$

where N is the number of combinations of perturbations, either for a given mask or over all masks. In Table 3, we report the RMS difference in the perturbation contrast for each mask and for all the data combined. We also report the RMS difference of the crossed analyzer data (the average contrast in the four lobes). While there is no formal requirement on the agreement of the crossed analyzer data, it helps to constrain the physical parameters of the optical edge.

Table 3 shows that if all data are taken into account, the RMS difference is 23%, which we argue satisfies the Milestone 2 criteria. The crossed analyzer data agrees to 34%, which gives confidence in our treatment of the vector diffraction effects. Figure 7 plots the model agreement as a function of model contrast. We find that 95% of perturbations with contrasts $> 2 \times 10^{-9}$ agree to better than 25%. While only 70% of perturbations with contrasts $< 2 \times 10^{-9}$ do so. At lower contrast levels, there is a stronger influence of non-scalar diffraction as well as contributions from manufacturing errors, both of which are more difficult to model correctly than the perturbations themselves. Indeed M12P2 has the largest amount of manufacturing errors and this should help explain the four outliers seen in the data.

As previously mentioned, the largest disagreement comes from M12P6, which performs worse with vector diffraction included. This could be due to that mask having a different optical edge profile than the other masks, and thus requiring a different vector diffraction solution. The manufacturing process should be similar between masks, but the different masks were made over a span of multiple years, where changes in the etching tool performance are probable. There is also uncertainty in the thickness (± 0.5 μm) of the device layer of each silicon

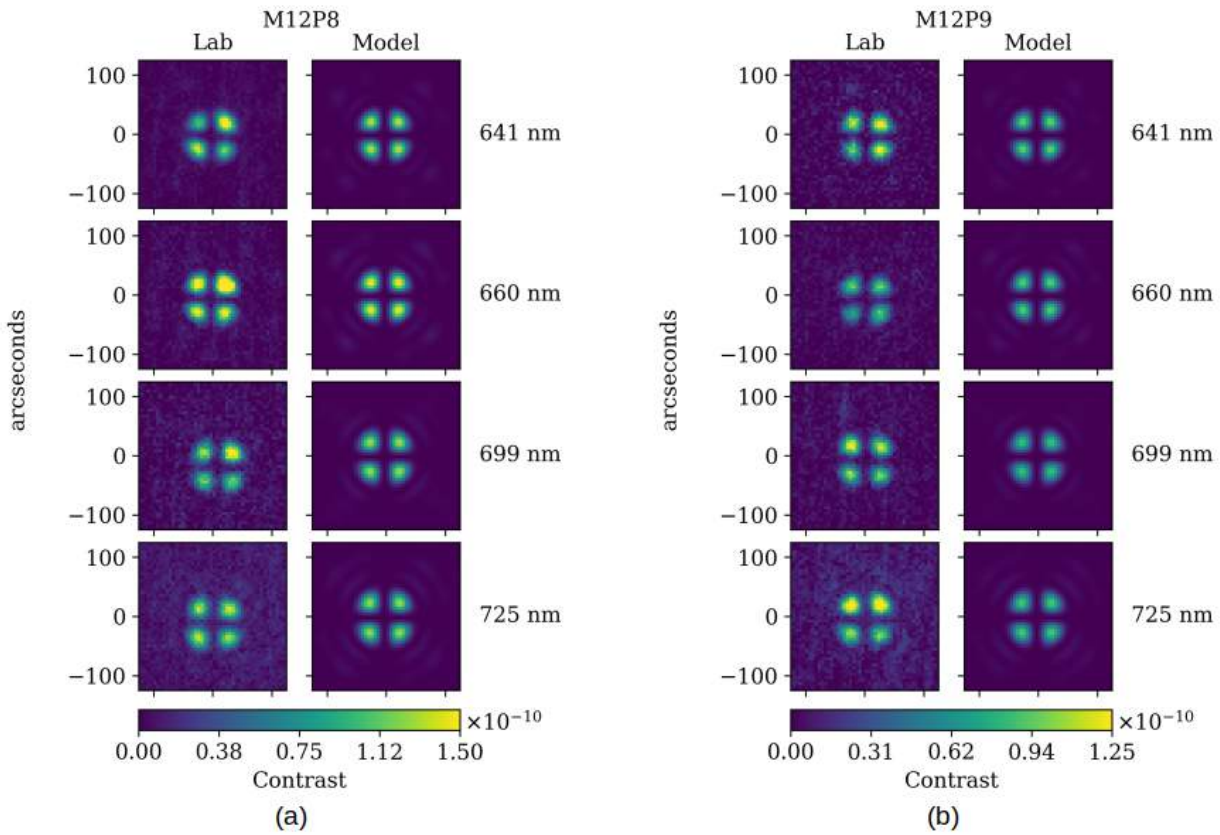

Figure 5. Observations with polarized analyzer orthogonal to the input polarization direction. (a) M12P8 − global shifted petal perturbations. (b) M12P9 − sine wave perturbations. Experimental data are in the left column, model data are in the right column. The rows are for the different wavelengths.

Mask	Perturbation RMS	Crossed Analyzer RMS
M12P2	24%	37%
M12P6	30%	29%
M12P7	19%	31%
M12P8	7%	32%
M12P9	15%	42%
Combined	**23%**	**34%**

Table 3. Experiment - Vector Model agreement for each mask and for all data combined. The middle column shows the RMS difference for the perturbation contrast. The right column shows the RMS difference for the crossed analyzer data.

wafer when received from the manufacturer. As it is not feasible to image the edge profile without destroying the mask, we will continue to model different edge profiles to find one that best fits the M12P6 data.

The experimental results we have presented here, along with previous results, show a 23% RMS agreement between experiment and model and lead us to argue that we have satisfied the Milestone 2 criteria. We have shown that our optical model accurately captures the sensitivity of the contrast to various perturbation types and sizes. Places where the model does not agree with experimental data can be explained by non-scalar diffraction effects that will be negligible at flight scales.

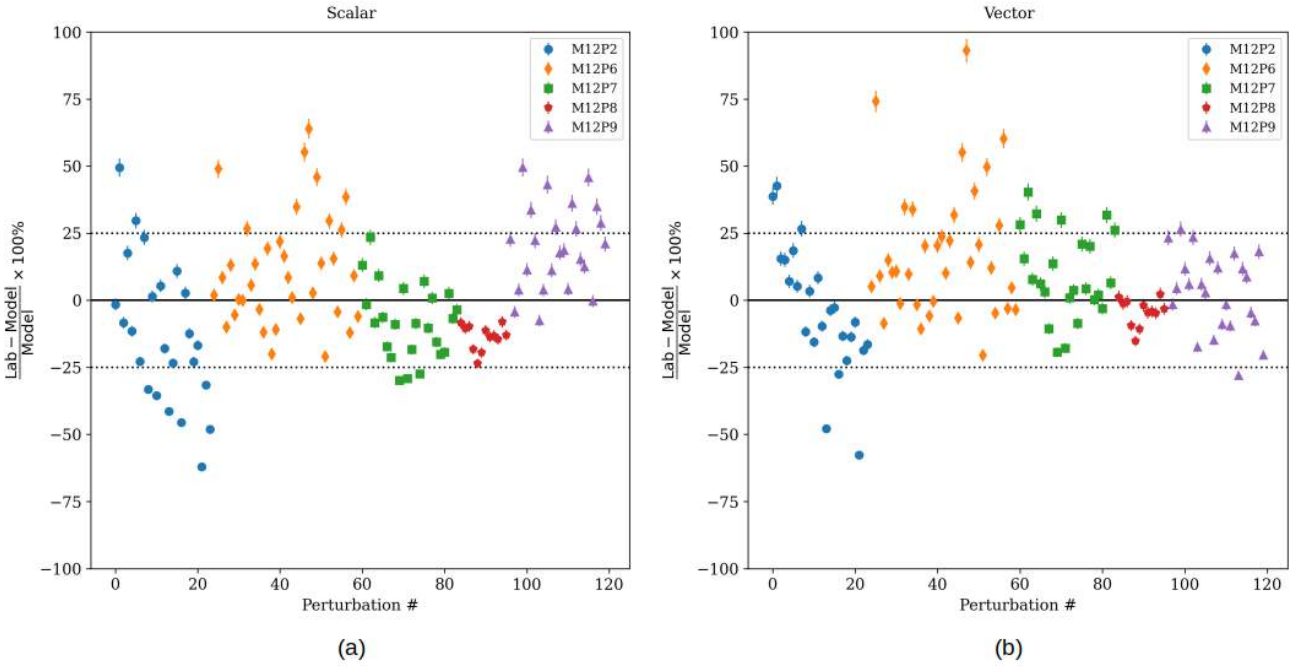

Figure 6. Percent difference between experiment and model for all perturbations, including data previously reported. The model in (a) is scalar-only; the model in (b) includes non-scalar diffraction effects. For each mask, there are 2 or 3 perturbations, each mask is tested at 4 wavelengths and 3 mask orientations, giving a total of 120 comparison points.

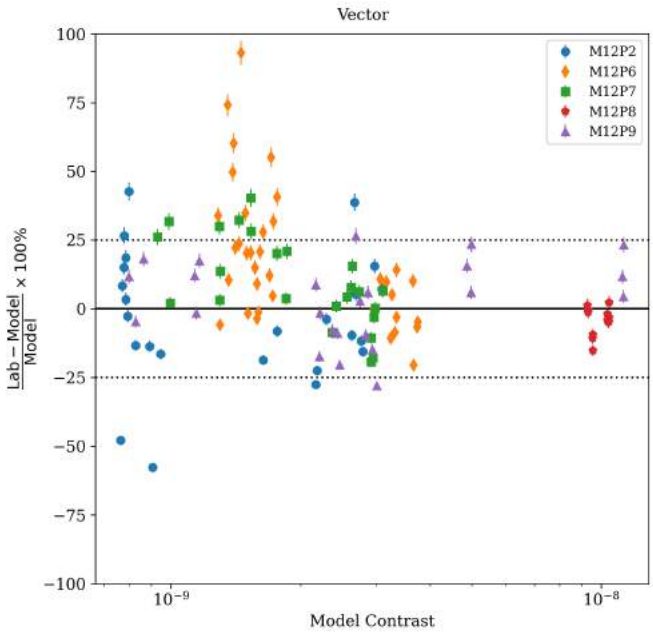

Figure 7. Percent difference between experiment and model for all perturbations, as a function of model contrast.

6. CONCLUSION

We have presented experimental results from the final two perturbed starshade designs tested for Milestone 2 of the S5 Project. A new areal quadrature method[8] for solving the diffraction equation allowed for efficient implementation of non-scalar diffraction effects, which helped bring the optical model into agreement with experimental results. Images taken in with a polarized analyzer orthogonal to the input polarization direction validates our treatment of the non-scalar diffraction effects. Combining the results from this work with previously obtained results, we demonstrate a 23% RMS agreement between model and experiment and lead us to argue that we have met the Milestone 2 criteria. Additional work is in progress to find the physical parameters of the optical edge for mask M12P6 that helps to mitigate the disagreement of some of the perturbations. Once the NASA Exoplanet Technical Advisory Committee (ExoTAC) has deemed Milestone 2 to be met, the starlight suppression technology of starshades will be at TRL 5.

ACKNOWLEDGMENTS

This work was performed in part at the Jet Propulsion Laboratory, California Institute of Technology under a contract with the National Aeronautics and Space Administration. Starshade masks were manufactured using the facilities at the Microdevices Lab at JPL. This project made use of the resources from the Princeton Institute for Computational Science and Engineering (PICSciE) and the Office of Information Technology's High Performance Computing Center and Visualization Laboratory at Princeton University.

REFERENCES

[1] Seager, S., Kasdin, N. J., and Team, S. R. P., "Starshade Rendezvous Mission probe concept," in [*American Astronomical Society Meeting Abstracts #231*], **231** (Jan. 2018). https://smd-prod.s3.amazonaws.com/science-red/s3fs-public/atoms/files/Starshade2.pdf.

[2] Gaudi, S., Seager, S., Mennesson, B., et al., "The Habitable Exoplanet Observatory HabEx mission concept study final report," *arXiv e-prints* (Jan. 2020). https://arxiv.org/abs/2001.06683.

[3] Willems, P., "Starshade to TRL5 (S5) technology development plan," *Jet Propulsion Laboratory Publications* (2018). https://exoplanets.nasa.gov/internal_resources/1033.

[4] Harness, A., Shaklan, S., Willems, P., Kasdin, N. J., Balasubramanian, B. K., Dumont, P., White, V., Yee, K., Muller, R., and Galvin, M., "Optical verification experiments of sub-scale starshades," *Journal of Astronomical Telescopes, Instruments, and Systems* **7**(2), 1 – 32 (2021).

[5] Harness, A., Shaklan, S., Kasdin, N. J., et al., "Starshade technology development activity Milestone 1A: Demonstration of high contrast in monochromatic light at a flight-like Fresnel number," *Jet Propulsion Laboratory Publications* (2019). https://exoplanets.nasa.gov/internal_resources/1210.

[6] Harness, A., Shaklan, S., Kasdin, N. J., et al., "Starshade technology development activity Milestone 1B: Demonstration of high contrast in broadband light at a flight-like Fresnel number," *Jet Propulsion Laboratory Publications* (2019). https://exoplanets.nasa.gov/internal_resources/1211.

[7] Harness, A., Shaklan, S., Kasdin, N. J., Willems, P., Balasubramanian, K., Dumont, P., White, V., Yee, K., Muller, R., Vuong, S., and Galvin, M., "Validation of diffraction models with experimental results from the Princeton starshade testbed," in [*Space Telescopes and Instrumentation 2020: Optical, Infrared, and Millimeter Wave*], Lystrup, M., Perrin, M. D., Batalha, N., Siegler, N., and Tong, E. C., eds., **11443**, 286 – 299, International Society for Optics and Photonics, SPIE (2020).

[8] Barnett, A. H., "Efficient high-order accurate Fresnel diffraction via areal quadrature and the nonuniform fast Fourier transform," *Journal of Astronomical Telescopes, Instruments, and Systems* **7**(2), 1 – 19 (2021).

[9] Barnett, A. H., Magland, J., and af Klinteberg, L., "A parallel nonuniform fast fourier transform library based on an "exponential of semicircle" kernel," *SIAM Journal on Scientific Computing* **41**(5), C479–C504 (2019).

[10] Harness, A., "Implementing non-scalar diffraction in Fourier optics via the Braunbek method," *Optics Express* **28** (2020).

[11] Oskooi, A. F., Roundy, D., Ibanescu, M., Bermel, P., Joannopoulos, J., and Johnson, S. G., "Meep: A flexible free-software package for electromagnetic simulations by the FDTD method," *Computer Physics Communications* **181**(3), 687 – 702 (2010).

Research Article | Vol. 28, No. 23 / 9 November 2020 / Optics Express 34290
Optics EXPRESS

Implementing non-scalar diffraction in Fourier optics via the Braunbek method

ANTHONY HARNESS*

Mechanical & Aerospace Engineering Department, Princeton University, Princeton, NJ 08544, USA
*aharness@princeton.edu

Abstract: Fourier optics is a powerful and efficient tool for solving many diffraction problems, but relies on the assumption of scalar diffraction theory and ignores the three-dimensional structure and material properties of the diffracting element. Recent experiments of sub-scale starshade external occulters revealed that the inclusion of these physical properties is necessary to explain the observed diffraction at 10^{-10} of the incident light intensity. Here, we present a methodology for implementing non-scalar diffraction while maintaining the efficiency and ease of standard Fourier optics techniques. Our methodology is based on that of Braunbek, in which the Kirchhoff boundary values are replaced with the exact field in a narrow seam surrounding the edge of the diffracting element. In this paper, we derive the diffraction equations used to implement non-scalar diffraction and outline the computational implementation used to solve those equations. We also provide experimental results that demonstrate our model can replicate the observational signatures of non-scalar diffraction in sub-scale starshades, in effect validating our model to better than 10^{-10} in relative intensity. We believe this method to be an efficient tool for including additional physics to the models of coronagraphs and other optical systems in which a full electromagnetic solution is intractable.

1. Introduction

For many optical systems, appropriate assumptions can be made to enable the use of Fourier optics as a powerful and efficient tool for understanding diffraction and the propagation of light. The most consequential assumption necessary is that all components of the electromagnetic field obey an identical scalar wave equation. This assumption, and the resultant scalar diffraction theory, is valid if propagating in a dielectric medium that is linear, isotropic, homogeneous, and nondispersive [1]. It is also necessary for diffracting elements to be much larger than the wavelength of light to ensure no coupling between field components at the boundaries [1]. For most optical systems, particularly visible wavelength astronomical telescopes, these assumptions are sufficiently valid. The optical models for exoplanet detection instruments such as high contrast coronagraphs [2] and starshade external occulters [3–5] rely on Fourier optics and the scalar diffraction assumption to predict the performance to $<10^{-10}$ of the incident light. Up to this point, standard physical optics propagation techniques based on Fourier optics have been sufficient for many applications, including starshades. However, recent laboratory experiments with sub-scale starshades have revealed the presence of non-scalar diffraction, a phenomenon which we deem the *thick screen effect*, as light propagates past the thick optical edges that form the narrow gaps between starshade petals [6].

In order to properly validate starshade optical models with sub-scale experiments, the models need to account for the material properties and geometry of a thick diffraction screen, along with polarization effects, which are available through Maxwell's equations. However, resorting to solutions of Maxwell's equations nullifies the efficiency with which Fourier optics operates. It is intractable to directly solve Maxwell's equations over the entirety of the starshade because its overall dimensions are much larger than the wavelength of light (the diameter of a sub-scale starshade is $\sim 50,000\lambda$).

#405485 https://doi.org/10.1364/OE.405485
Journal © 2020 Received 14 Aug 2020; revised 2 Oct 2020; accepted 14 Oct 2020; published 28 Oct 2020

Optics EXPRESS

Our approach, based on an insight provided by Braunbek [7], is to use the solution to Maxwell's equations in a narrow seam around the edge of the diffraction screen and apply those results to the scalar model through standard Fourier optics techniques. Ref. [8] uses the Braunbek method and Sommerfeld's solution to derive a Maggi-Rubinowicz vector potential for a perfectly conducting screen, but the vector potential cannot be generalized for more complex edge geometries and materials. Our methodology provides that generalization. This technique is necessary to replicate experimental data on sub-scale starshades, but we also believe it to be useful for coronagraphs and other optical systems that possess a large dynamic range in size.

Section 2 of this paper introduces the thick screen effect observed in sub-scale starshade experiments that prompted the need for a new modeling technique. Section 3 gives the formal derivation of the model. Section 4 summarizes the computational implementation that integrates non-scalar diffraction into the Fourier optics model. Section 5 outlines the finite-difference time-domain (FDTD) code used to solve Maxwell's equations for realistic optical edges. Section 6 provides experimental data that show our method agrees with experimental results at relative intensity levels of $<10^{-10}$. Section 7 restates the conclusions drawn from this work.

2. Thick screen effect in sub-scale starshade experiments

Optical experiments of $1/1000^{\text{th}}$-scale starshades are being conducted to verify optical performance and validate optical models at flight-like Fresnel numbers [6]. Recent results have shown contrast (relative intensity) levels that are orders of magnitude above that predicted by scalar diffraction theory and with a morphology dependent on the input polarization state. This was deemed the thick screen effect [9] and was first reported in Ref. [6]. We briefly summarize the thick screen effect below.

The petalized shape of a starshade is a binary approximation to a radial apodization function that has been numerically optimized to suppress starlight by >10 orders of magnitude. The optimization routine [10] that solves for the apodization function assumes an infinitely thin optical edge and that all features of the starshade are much larger than the wavelength of light and thus the scalar diffraction assumption holds. This assumption is likely to be valid for large starshades in a space mission where the minimum feature size is on the order of millimeters, however, the starshades tested in the laboratory are 1000× smaller and have minimum feature sizes on the order of microns. Once starshade experiments reached 10^{-10} contrast levels at a low Fresnel number, the presence of bright polarization-dependent lobes revealed a break down in scalar diffraction theory [6].

The starshades tested in these experiments are 25 mm in diameter and etched out of silicon-on-insulator (SOI) wafers. The gap width between starshade petals is as small as 7.5 μm and the device layer of the SOI wafer that serves as the optical edge is as thick as 7 μm, meaning the edge can no longer be considered a thin screen as required in the Fresnel-Kirchhoff diffraction equation. As light propagates, through the narrow gaps between petals, and past the thick screen, it interacts in a polarization-dependent manner with the material properties of the edge that induce a slight change in the electric field (in both amplitude and phase). The change in the field translates to a change in the effective apodization profile of the petal and negates some of the optimized light suppression. The resultant contrast appears as bright lobes that are aligned with the input polarization vector, as can be seen in Fig. 1 and will be discussed further in Sec. 6.

As Braunbek [7] and Keller [11] have pointed out, and as the FDTD simulations in Sec. 5 show, diffraction is a local phenomenon affecting only the immediate surrounding of the edge (akin to a boundary layer). Interaction with the edge is present in all optical systems, but for those that have apertures much larger than the wavelength, the contribution from a few λ-wide boundary layer is negligible. For the $\sim 10\lambda$ wide gaps in the sub-scale starshades, the boundary layer occupies an appreciable fraction of the aperture and thus it has a significant effect, especially when the shape of that aperture is precisely designed to suppress the light intensity by 10 orders

Optics EXPRESS

of magnitude. This explanation is supported by the degradation in contrast only appearing at the narrow inner gaps between petals, where the fraction of the aperture occupied by the λ-wide boundary layer is greatest. The degradation in contrast is not seen in the gaps at the outer regions of the mask because at larger radii the Fresnel number is larger and thus the sensitivity to changes in the apodization profile is lower. This physical description of the thick screen effect helps inform the derivation of the model in the following section.

3. Model derivation

In the derivation of the Fresnel-Kirchhoff diffraction equation, it is assumed that the field in the aperture of a diffraction screen is not affected by the presence of the screen. Thus in the plane of the screen, one can assign Kirchhoff's boundary values, where the field is zero on the screen and equal to the incident field (U_0) in the aperture [12]. The main insight introduced by Braunbek was to replace the boundary values of Kirchhoff with the exact value of the field in a narrow seam (a few λ's wide) around the screen's edge [7]. Braunbek obtained the exact value in the seam from Sommerfeld's solution to the perfectly conducting half-plane. The approach of this work is to adapt Braunbek's insight to replace the boundary values in the seam around the edge, with the exact field that results from the presence of the thick screen. The exact field in the presence of an arbitrary screen can be calculated via numerical solution of Maxwell's equations, as will be demonstrated in Sec. 5.

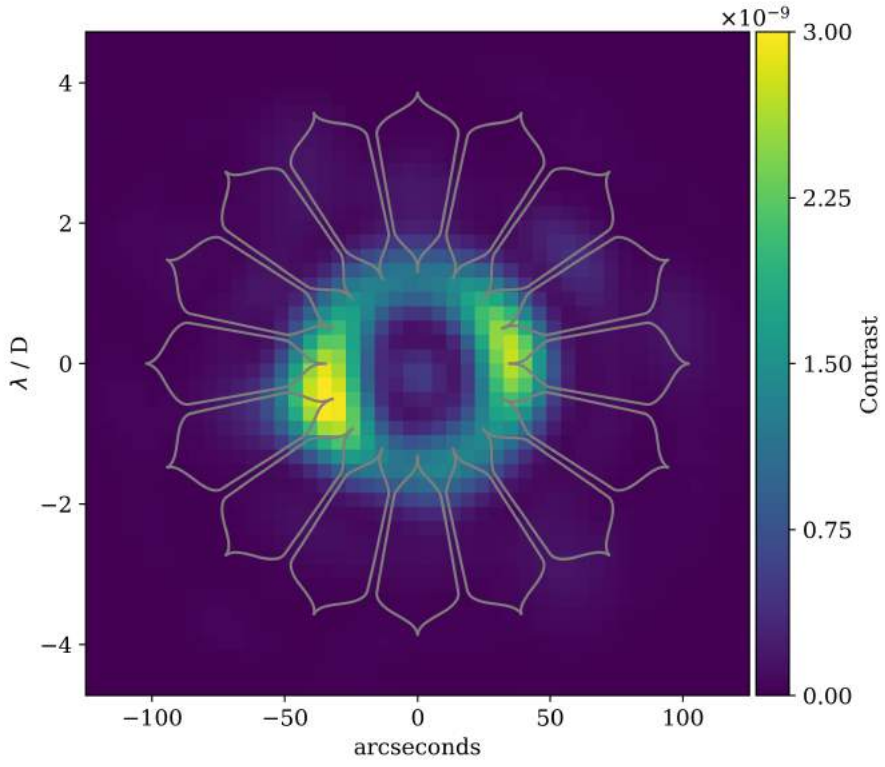

Fig. 1. Experimental contrast image of mask DW9 at λ = 641 nm. The starshade pattern is overlaid.

We assume that the electromagnetic field can be described by a scalar potential U; later when polarization is taken into account, we will assume that this holds for each component of the field.

Optics EXPRESS

Starting with the integral theorem of Helmholtz and Kirchhoff [12], the disturbance at a point P is given by

$$U(P) = \frac{1}{4\pi} \iint_{\Omega} \left(U \frac{\partial G}{\partial n} - \frac{\partial U}{\partial n} G \right) dA, \tag{1}$$

where $\partial/\partial n$ is differentiation normal to the screen and both U and the Green's function G satisfy the Helmholtz equation. The integral is taken over the entire surface Ω (see Fig. 2). We assume the screen is flat in the $z = 0$ plane such that $\partial/\partial n = \partial/\partial z$.

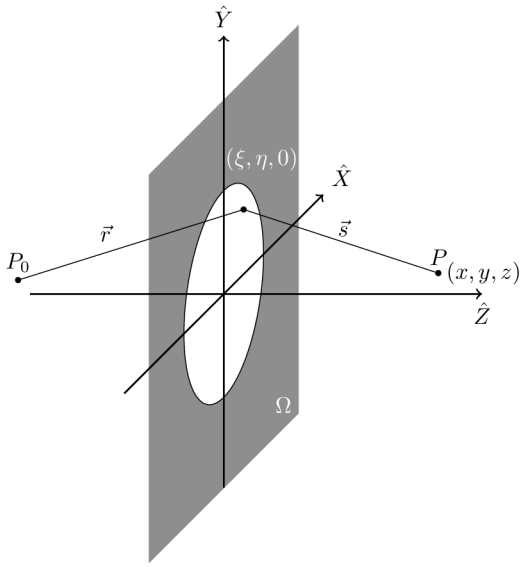

Fig. 2. Definition of the lab coordinate system used for the derivation of the model. The source is located at P_0, the diffraction screen is located flat in the $z = 0$, plane the integral is taken over the entire $z = 0$ surface Ω, and the observation point is at P.

Building on Braunbek's methodology, we split the entire surface into four distinct regions: $\Omega = S \cup S' \cup O' \cup O$, where S is the screen (excluding the seam), O is the aperture (excluding the seam), S' is the screen side of the seam, and O' is the aperture side of the seam (see Fig. 3). We assume the field in the seam is a superposition of the incident field and an additional field δ, which is induced by the presence of the screen. In other words, the boundary values on a surface A are given by

$$U = \begin{cases} 0, & A \subseteq S \\ \delta, & A \subseteq S' \\ U_0 + \delta, & A \subseteq O' \\ U_0, & A \subseteq O\,. \end{cases} \tag{2}$$

The additive field (δ) can be considered a better approximation to the true boundary values near the edge of the screen. Its existence can be physically understood as due to a boundary diffraction wave emanating from the edge of the screen [13], but δ is not formally equivalent to the boundary diffraction wave. Although, Kirchhoff's solution can be written as the sum of the incident wave and the boundary diffraction wave [13], that analysis still assumes Kirchhoff's boundary values in which $\delta = 0$.

Optics EXPRESS

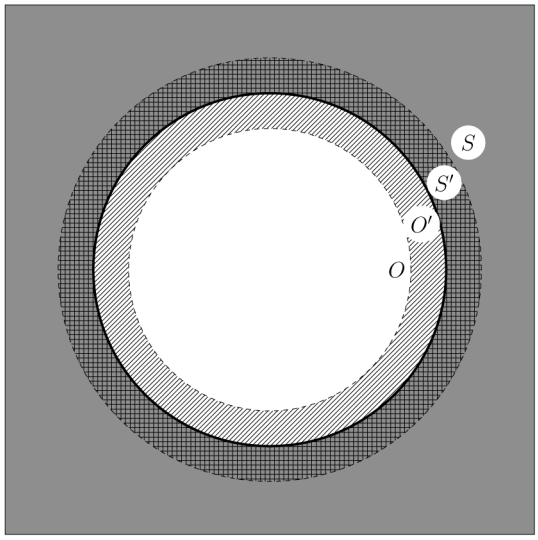

Fig. 3. The surface Ω is divided into four regions: the screen S, the screen side of the seam S', the aperture side of the seam O', and the aperture O. The screen edge is the solid black line between the S' and O' surfaces. The size of the seam is exaggerated for clarity.

Substituting Eq. (2) into Eq. (1), the Helmholtz-Kirchhoff integral can be split into two integrals,

$$U(P) = U_K(P) + U_B(P), \tag{3}$$

with one term representing the standard Kirchhoff diffraction integral:

$$U_K(P) = \frac{1}{4\pi} \iint_{O'+O} \left(U_0 \frac{\partial G}{\partial z} - \frac{\partial U_0}{\partial z} G \right) dA, \tag{4}$$

and an additional term, deemed the Braunbek integral, due to the additional field in the seam:

$$U_B(P) = \frac{1}{4\pi} \iint_{S'+O'} \left(\delta \frac{\partial G}{\partial z} - \frac{\partial \delta}{\partial z} G \right) dA\,. \tag{5}$$

Note that the two integrals are of identical form, but use different boundary values and are taken over different domains (see Eq. (2)). The Kirchhoff solution is calculated over the entire aperture (including the seam), but not over the screen as the incident field on the screen is zero. The Braunbek solution is calculated over the entire seam. The surface O' is integrated over by both solutions, as O' sees both the incident field and the additive Braunbek field.

From here, we can follow standard practice to simplify the integrals to a more usable form. We make the paraxial approximation and assume the distances from the source and the observation point to the screen are much larger than the wavelength. We assume a spherical incident wave, which we write as

$$U_0 = \frac{e^{ikr}}{r}, \frac{\partial U_0}{\partial z} \approx ik \frac{e^{ikr}}{r} = ikU_0, \tag{6}$$

and write the Green's function on the observation side as

$$G = \frac{e^{iks}}{s}, \frac{\partial G}{\partial z} \approx -ik \frac{e^{iks}}{s}\,. \tag{7}$$

If the Fresnel approximation is made on distances r, s, keeping the first order term in amplitude and second order term in phase, we can write the Kirchhoff integral as the Fresnel diffraction

Optics EXPRESS

equation:

$$U_K(x,y,z) = \frac{e^{ikz}}{i\lambda z}\iint_{O'+O} U_0 e^{\frac{ik}{2z}\left[(\xi-x)^2+(\eta-y)^2\right]}\,d\xi\,d\eta\,. \tag{8}$$

We can follow a similar derivation for the Braunbek integral, but first need to transition from a purely scalar description of the electromagnetic field to one that takes polarization into account. We define an edge coordinate frame in Fig. 4 and assume that the screen is in the plane orthogonal to $\hat{z}$ so that $\hat{z}_{\text{edge}} = \hat{z}$; $\hat{n}$ is normal to the edge in the plane of the screen (this is different from n in Eq. (1)); and $\hat{t}$ is tangent to the edge in the clockwise direction. For each point on the edge, the edge is treated as an infinite half-plane (the radii of curvature of the edges are $>>\lambda$) making the field independent of $\hat{t}$. Our problem is now two-dimensional and the field can be described in terms of a single dependent variable, which behaves in a scalar fashion [12]. We break the field into two independent polarization states: s-polarization, where the electric field is parallel to the edge and the complete field is described by E_t; and p-polarization, where the magnetic field is parallel to the edge and the field is described by H_t. We can now apply the same derivation of the Kirchhoff integral to E_t and H_t.

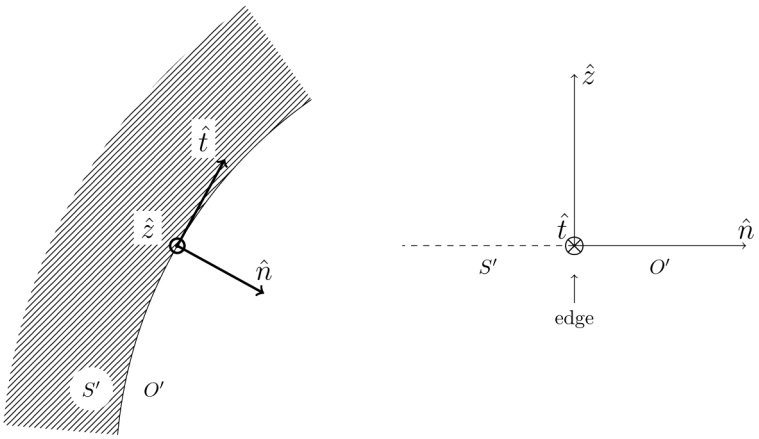

Fig. 4. Definition of the edge coordinate system centered at each edge point. $\hat{n}$ is normal to the edge, $\hat{t}$ is tangent to the edge and points clockwise, and $\hat{z}$ points towards the observer. Left: front facing view from the observation point. Right: view in the plane of the screen looking clockwise along the edge.

In Table 1, we relate $\partial\delta/\partial z$ to field components using Maxwell's equations in free space. Inserting these values and those of Eq. (7) into Eq. (5), and making the Fresnel approximation, we write the Braunbek integral for s- and p-polarization as

$$U_{B,\,\substack{s\\p}}(x,y,z) = \frac{e^{ikz}}{i\lambda z}\iint_{S'+O'}\left(E_{\substack{t\\n}} \mp H_{\substack{n\\t}}\right) e^{\frac{ik}{2z}\left[(\xi-x)^2+(\eta-y)^2\right]}\,d\xi\,d\eta\,. \tag{9}$$

Table 1. Electric and magnetic field values taken by the additive field for a given polarization.

Polarization	δ	$\partial\delta/\partial z$
s	E_t	$\partial E_t/\partial z = -ikH_n$
p	H_t	$\partial H_t/\partial z = ikE_n$

Again, the diffraction equations for the Kirchhoff and Braunbek solutions are the same, but with different initial field values on the surfaces. We will calculate both integrals in the same

Optics EXPRESS

manner, so we write both integrals in the general form,

$$U_\gamma(x,y,z) = \frac{e^{ikz}}{i\lambda z}\iint_{A_\gamma} P_\gamma e^{\frac{ik}{2z}\left[(\xi-x)^2+(\eta-y)^2\right]}\,d\xi\,d\eta\,. \tag{10}$$

where $\gamma = \{K, s, p\}$ indicates the solution (Kirchhoff; s, p polarizations of Braunbek) and P_γ is the corresponding initial field over the surface A_γ, which also takes into account the aperture function. P_γ is described in Sec. 4.1. Equation (10) can be simplified as the Fourier transform (represented as $\mathcal{F}\{\}$) of the initial field times a Fresnel kernel:

$$U_\gamma(x,y,z) = \frac{e^{ikz}}{i\lambda z}e^{\frac{ik}{2z}(x^2+y^2)}\mathcal{F}\left\{P_\gamma e^{\frac{ik}{2z}(\xi^2+\eta^2)}\right\}_{(x,y)}\,. \tag{11}$$

This shows that both the Kirchhoff and Braunbek solutions can be efficiently calculated with standard Fourier techniques.

4. Computational implementation

In Eq. (11), we formulated the diffraction equation as the Fourier transform of a Fresnel kernel times a map of the initial field values(P_γ) on the surface (A_γ), whose value depends on the solution being calculated (γ) and whether or not the surface is inside the seam $\left(A_\gamma \subseteq S' \cup O'\right)$. Braunbek posited the seam to be a few λ's wide [7], after which the field approaches the value of the incident field. We select the width to be that in which the contrast solution is numerically converged, typically $\sim$ 10 μm total seam width for the experiment described in Sec. 6. This section will describe the construction of P_γ, the implementation of polarization effects, and the numerical computation of the diffraction equation.

4.1. Greypixel map of initial field

To enable the use of efficient Fourier transform algorithms, we represent P_γ and the coordinates ξ, η as square two-dimensional matrices spanning the integral surface. At the edge of the screen, there is a sharp discontinuity in the binary aperture function where the discretization of the matrix reduces the accuracy of the calculation. Standard practice for minimizing the effect of discretization is to soften the discontinuity by giving cells that lie on the edge a value between 0 and 1, depending on what fraction of the cell lies inside the aperture. We call a matrix with this sub-pixel resolution a "greypixel map" and the technique is employed below.

For cells outside the Braunbek seam, only the Kirchhoff solution is used; those in the aperture are given value 1, those on the screen are given value 0. A winding number algorithm [14] can determine if the cell is inside or outside the aperture.

For each cell in the seam, we find the nearest edge point (see Fig. 5) and calculate the implicit line equation for the edge (assuming it has no curvature), along with the angle normal to the edge. We divide the cell into a $N \times N$ sub-pixel grid (sub-pixel size $\Delta\xi \times \Delta\eta$) and for each sub-pixel, we calculate the distance $d_{i,j}$ projected to the edge segment via the implicit line equation. From the edge distance, we calculate the field value for each sub-pixel and integrate (via the trapezoidal rule) over the cell to give the total field in the cell. Thus the initial field at each cell is given by

$$P_\gamma(\xi,\eta) = \Delta\xi\Delta\eta\sum_{i=0}^{N}\sum_{j=0}^{N} f_\gamma\left(d_{i,j}\right)\,. \tag{12}$$

Here, f_γ is the initial field due to the edge effect as a function of distance, for solution γ. For $\gamma = K$, i.e., the scalar Kirchhoff solution, the edge function is represented by the incident field

Optics EXPRESS

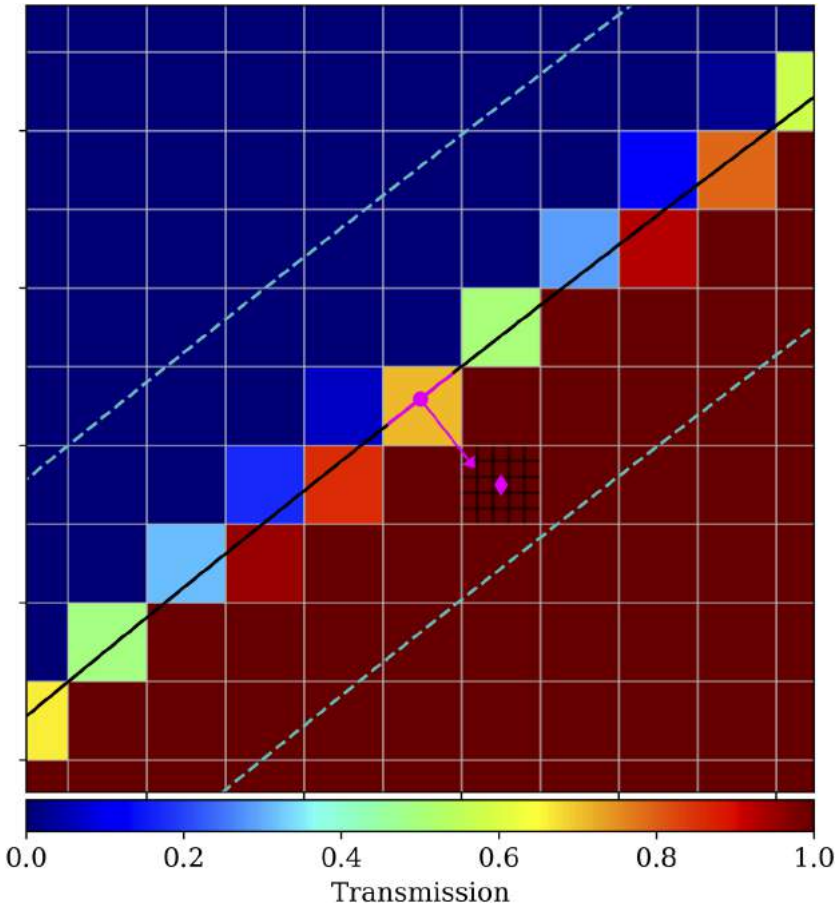

Fig. 5. Example greypixel map showing scalar aperture transmission ((f_K/U_0)). The black line is the aperture edge and the cyan dashed lines mark the 10 μm wide seam. For each cell under consideration (magenta diamond) the nearest edge point (magenta circle) is found and the distance along the normal (magenta arrow) is calculated. The cell is subdivided into subpixels to integrate the field function as in Eq. (12).

Optics EXPRESS

times the Heaviside step function:

$$f_K(d) = U_0 \begin{cases} 0, & d<0 \\ 1, & d \geq 0\,. \end{cases} \tag{13}$$

The distance d is signed, with negative values on the side of the screen. Inspection of Eq. (13) shows it yields the Kirchhoff boundary values of Eq. (2): when d is negative (the screen side of the edge), the field is zero; when d is positive (the aperture side of the edge), the field is equal to the incident field. For those cells in which the edge passes through, the aperture function is between 0 and 1, providing the greypixel effect to enhance resolution. Figure 5 shows an example greypixel map for the Kirchhoff solution.

For the Braunbek solutions, f_γ is complex-valued as it accounts for both amplitude and phase. If we assume the screen is thin and perfectly conducting, f_γ is given analytically by Sommerfeld's solution to diffraction by a half-plane [12,15]. For more complex edge geometries and materials, f_γ is a function interpolating the output of an FDTD solution to Maxwell's equations (see Sec. 5.).

4.2. Polarization

The initial field in the greypixel map depends on the incident polarization state relative to the local edge, therefore we must rotate into the edge frame for each cell to determine the relative contribution of s- and p-polarized light. We assume the polarization of the incident light (in the lab frame) is

$$\vec{U}_0 = A\hat{\xi} + B\hat{\eta}, \tag{14}$$

where $A = ae^{i\phi_a}, B = be^{i\phi_b}$ represent the complex values of two orthogonal waves whose linear combination create the incident wave (normalized to $|U_0| = 1$). For linearly polarized light, $\phi_a = \phi_b$; for circularly polarized light, $a = b = 1/\sqrt{2}$ and $\phi_a = \phi_b = \pm\pi/2$; for elliptically polarized light, $a \neq b$ and $\phi_a \neq \phi_b$.

If the normal angle of the edge (relative to vertical in the lab frame) is given by α, and we assume horizontally polarized incident light, the polarized field diffracted by the edge (in the lab frame) is given by

$$\vec{U} = R_\alpha^T \left(P_s\hat{\xi} + P_p\hat{\eta}\right) R_\alpha \vec{U}_0, \tag{15}$$

where R_α is the two-dimensional rotation matrix of angle α, which rotates from the lab frame to the edge frame. Completing the matrix multiplication, the initial field components in the lab frame are

$$\begin{aligned} U_\xi &= AM_H + BM_X\,, \\ U_\eta &= AM_X + BM_V\,, \end{aligned} \tag{16}$$

where

$$\begin{aligned} M_H &= P_s\cos^2\alpha + P_p\sin^2\alpha\,, \\ M_V &= P_s\sin^2\alpha + P_p\cos^2\alpha\,, \\ M_X &= \sin\alpha\cos\alpha\left(P_p - P_s\right)\,. \end{aligned} \tag{17}$$

The matrices $M_{H,V,X}$ are the initial field maps to be applied in the Fourier transform and allows any polarization state to be applied after computing four Fourier transforms (the three in Eq. (17) and one for the scalar Kirchhoff field). By construction, the input polarization is horizontal, so M_H represents the primary contribution from s-polarization, M_V is the primary contribution from p-polarization, and M_X is the cross-term due to induced polarization from the difference between the responses to s- and p-polarization. The scalar Kirchhoff field is given by

$$M_K = P_K\,. \tag{18}$$

For a calculation with only scalar diffraction, $M_H = M_V = M_X = 0$.

Optics EXPRESS

4.3. Propagation of total field

The electric field propagated to the observation point (in the observation frame), is given by

$$\begin{aligned} U_X &= C\left[A\left(F_K + F_H\right) + BF_X\right] , \\ U_Y &= C\left[B\left(F_K + F_V\right) + AF_X\right] , \end{aligned} \tag{19}$$

where the function F is the Fourier transform of the initial field maps $\sigma = \{K, H, V, X\}$ times the Fresnel kernel:

$$F_\sigma = \mathcal{F}\left\{M_\sigma e^{\frac{ik}{2z}\left(\xi^2+\eta^2\right)}\right\}_{(x,y)} , \tag{20}$$

and the leading constant is given by

$$C = \frac{e^{ikz}}{i\lambda z} e^{\frac{ik}{2z}\left(x^2+y^2\right)} . \tag{21}$$

The Fourier transform in Eq. (20) is calculated with the matrix Fourier transform algorithm [16], which provides efficient computation when the input and output planes have largely different sampling requirements. If observed without a polarizing element at the observation point, the intensity is

$$I = |U_X|^2 + |U_Y|^2 . \tag{22}$$

If observed with a polarized analyzer with angle β in the lab frame, the intensity is given by

$$I = |U_X \cos\beta + U_Y \sin\beta|^2 . \tag{23}$$

4.4. Summary of diffraction calculation

(1) For each cell in the seam, calculate the edge normal angle α and $P_{K,s,p}$ using Eq. (12).

(2) Generate four initial field maps $M_{K,H,V,X}$ using Eq. (17) and Eq. (18).

(3) Propagate maps to the observation plane with Fourier transforms via Eq. (20).

(4) Use the incident polarization state components A, B to generate the total field with Eq. (19).

(5) Apply polarized analyzer to calculate the intensity via Eq. (22) or Eq. (23).

4.5. Numerical considerations

The Fourier optics approach using the greypixel approximation for the Kirchhoff solution has been shown to be in agreement with accurate edge diffraction algorithms [5]. For the starshades modeled in Sec. 6, the scalar solution agrees with the edge diffraction algorithms with a grid size of $2^{13} \times 2^{13}$. The non-scalar solutions are numerically converged with a $2^{13} \times 2^{13}$ grid size, $N = 100$ in Eq. (12), and a total seam width of 10 μm.

5. Calculation of boundary values in Braunbek seam

The Braunbek method requires us to know the exact field in the seam near the edge of the screen (f_γ in Eq. (12)). For a scalar-only solution, the field is given by the Heaviside step function as in Eq. (13). For a perfectly conducting thin screen, the field is given by Sommerfeld's solution [12,15]. For more complicated materials and geometries, we solve for the field past the screen using an FDTD solution to Maxwell's equations with the open-source software *Meep* [17], and f_γ is the interpolation of the results as a function of distance from the edge.

The edges of the sub-scale starshades tested in Ref. [6] are comprised of a silicon wafer coated with a thin layer of metal. Figure 6 shows a cartoon diagram of the computational cell for an

Optics EXPRESS

FDTD simulation of light propagating past an edge. We assume the curvature of the edge in the plane of the screen is much larger than the wavelength, so that the edge can be treated as an infinite half-plane extending in the $\hat{t}$-direction, reducing the problem to two dimensions. In the simulation, we build an edge with a silicon wafer and metal coating and propagate a plane wave past the edge; perfectly matched layer (PML) boundary conditions surround the cell to eliminate numerical reflections at the boundaries. We run the simulation until the field stabilizes to a converged value and record the field at the bottom of the edge. A similar simulation is run without any edge materials to generate the incident field. Subtracting the results of the two simulations yields the additive field (δ) that is the boundary value in the Braunbek seam. These simulations are run for each polarization (s, p) and both the electric and magnetic fields are saved to provide the boundary values of Table 1.

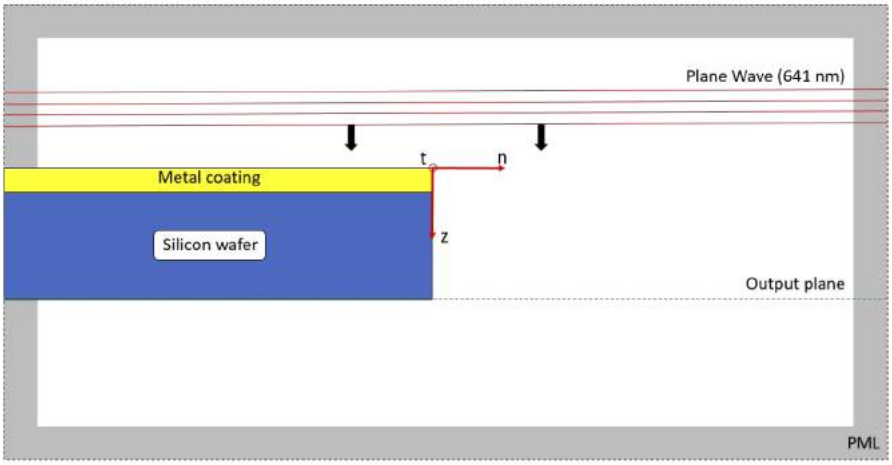

Fig. 6. Cartoon diagram of the computational cell geometry for the *Meep* [17] FDTD simulation. The cell is padded by perfectly matched layer (PML) boundary conditions. The resultant field is extracted at the output plane (green dashed line) at the bottom of the wafer. The horizontal extent of the cell is truncated for clarity.

Figure 7 shows the resultant electric fields for an s-polarized simulation of a 7 μm silicon wafer with a 0.4 μm gold coating, and for a thin, perfectly conducting edge (the Sommerfeld solution). Also shown is the additive field (δ) calculated by subtracting the incident field. We can see that the thicker screen has a stronger impact on the electric field and that the additive field is larger in the seam of the aperture, which leads to a larger thick screen effect. In generating the greypixel map, the complex field as a distance from the edge (f_γ in Eq. (12)) is provided by numerically interpolating the additive field in Fig. 7 as a function of distance from the edge.

The simulation geometry shown in Fig. 6 assumes a half-plane extending infinitely behind the edge and free space in front of the edge. For the inner gaps between the petals of the starshades tested in the laboratory [6], the gaps are only 7 μm - 16 μm across and must be simulated as a slit rather than a half-plane. For 600 nm light, the results of a slit and half-plane converge for slit widths >30 μm. For sharp corners in the screen, we could run an FDTD simulation of the corner and use those results for the surrounding pixels, but the total area affected by the corners is small enough to ignore this effect.

The etching process of the starshade masks results in an optical edge that is neither flat nor vertical, both of which affect how light interacts with the edge and needs to be accounted for in the FDTD model. We are unable to generate model results that match experimental data if we assume a flat vertical edge, but a scalloped and tapered edge produces models that agree well with the data (see Sec. 6). In the scanning electron microscope (SEM) image of Fig. 8, we

Optics EXPRESS

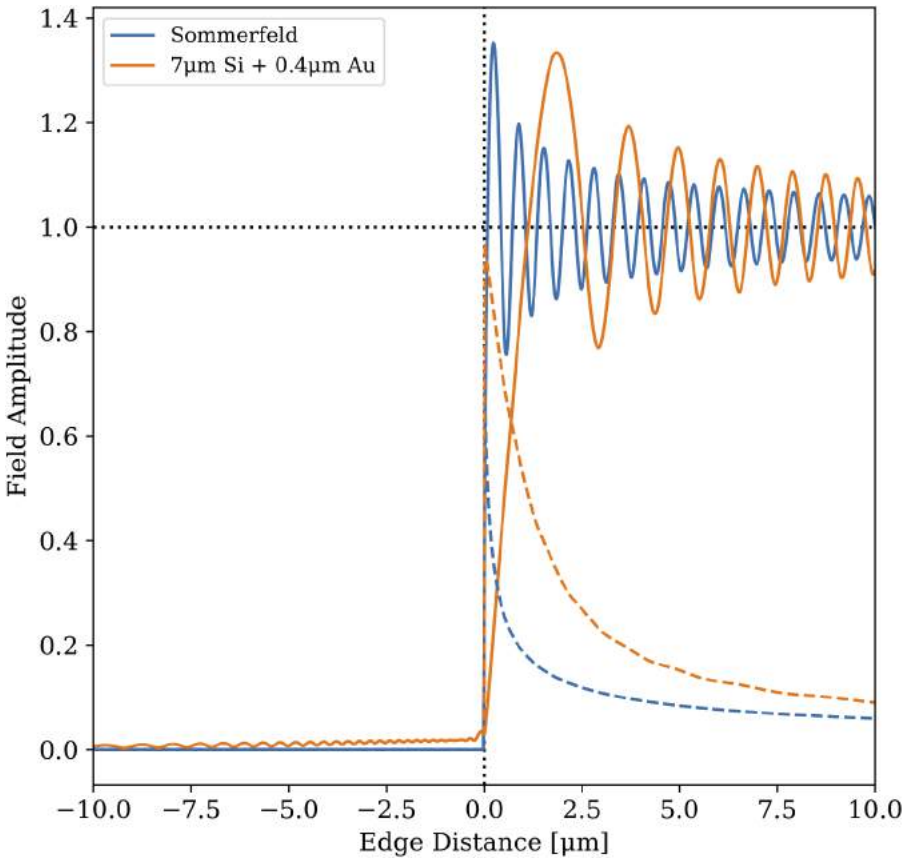

Fig. 7. FDTD simulation results for *s*-polarized light. The solid lines are the electric fields at the bottom of the screen for simulations of a 7 μm silicon wafer with a 0.4 μm gold coating and of a thin, perfectly conducting edge (the Sommerfeld solution). The dashed lines are the additive fields (δ) calculated by subtracting the incident field. On the screen side (edge distance <0), the solid and dashed lines overlap as there is no incident field on the screen.

can see the Bosch etching process "scallops" the vertical wall of the wafer and leaves divots $\sim$ 0.2 μm deep and $\sim$ 0.8 μm tall. The etching process can also result in a non-vertical wall, though it is more difficult to extract the wall's tapering angle from SEM images. In Sec. 6, we detail the analysis used to find the taper angle that best matches the experimental data. Figure 8 shows the simulated vertical edge profile using scallop parameters inferred from the SEM image and a 1° taper angle that best fits the data.

Optics EXPRESS

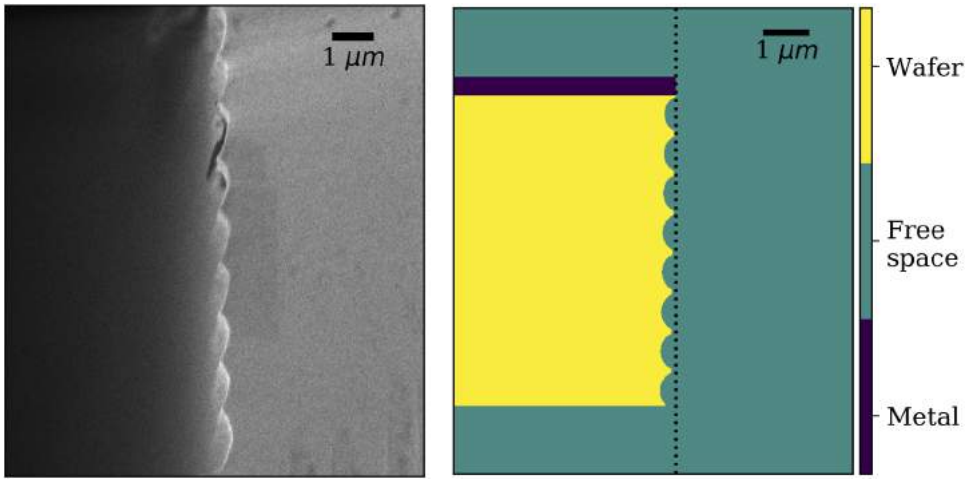

Fig. 8. Left: SEM image of the vertical profile of the wafer edge for a manufactured mask. The edge scalloping is a result of the Bosch etching process (figure provided courtesy of K. Yee, Jet Propulsion Laboratory, California Institute of Technology). Right: electric permittivity map of the *Meep* FDTD simulation cell displaying the material geometry. In the simulation, we can replicate the scalloping of the edge and taper the vertical wall.

6. Experimental validation

The sub-scale starshade experiments presented in Ref. [6] provide an excellent opportunity to validate our model because of the large dynamic range provided by the starshade (10^{-10} in intensity) and the sensitivity of the performance to the starshade's shape. Fractional changes in the field propagating past an edge leads to order of magnitude changes in the resulting contrast. In this section, we briefly summarize results presented in Ref. [6] to provide experimental validation of our approach.

The experiment design is simple: a 641 nm laser source with a diverging beam, a 25 mm diameter starshade, and a lens imaging onto a detector sit aligned in an 80 m long enclosed testbed [6]. From within the deep shadow produced by the starshade, we measure the efficiency with which the starshade suppresses the on-axis light. The laser light is linearly polarized and an analyzing polarizer on a rotation stage in front of the detector allows us to measure the polarized response of the starshade. We present results from experiments testing two different starshade masks, both etched out of a silicon wafer coated with 0.4 μm of gold. Mask DW9 has a 7 μm thick silicon edge with 7.5 μm wide gaps between petals. Mask DW21 has a 3 μm thick silicon edge with 16.2 μm wide gaps between petals. The apodization profile for the two designs are different. Note that the starshade design (seen in Fig. 9) consists of an inner starshade that is held to the silicon wafer by radial struts, and that the outer supporting wafer is also apodized. This results in 16 individual apertures formed by the inner starshade petals, radial struts, and outer apodization. More details can be found in Ref. [6].

Figure 9 shows an experimental image testing DW9 λ= 641 nm with the analyzer nearly aligned with the horizontal input polarization vector (there is a slight 15° misalignment of the analyzer). The bright lobes along the polarization axis stand out at 3×10^{-9} contrast. Also shown in Fig. 9 are three models that use different field functions (f_γ in Eq. (12)) to generate the greypixel map. In these models, we assume the seam around the edge is 10 μm wide. The top right model uses the field function from an FDTD simulation of a 7 μm thick silicon wafer coated with a 0.4 μm gold layer, and with an edge taper angle and scalloping profile as described in Sec. 5. The bottom left model uses the Sommerfeld solution and the bottom right model uses the scalar only

Optics EXPRESS

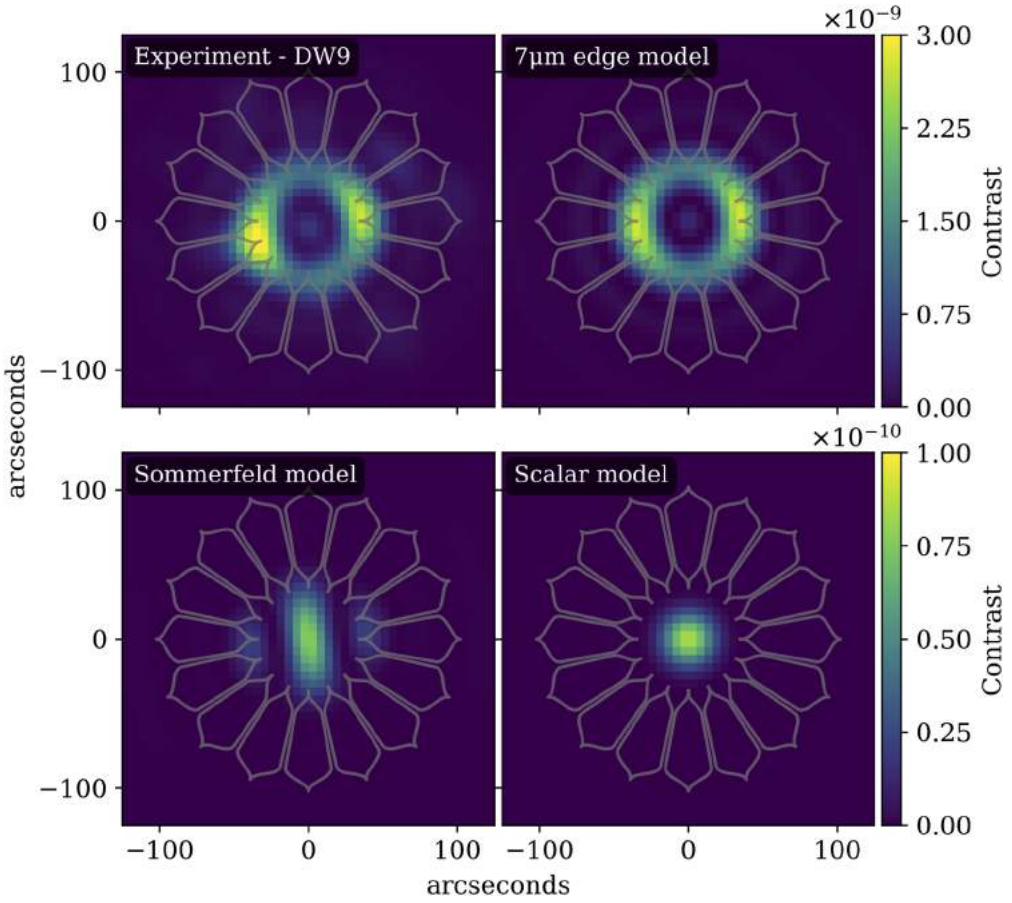

Fig. 9. Experimental (top left) and model images of mask DW9 with starshade pattern overlaid. Top right model uses the results from an FDTD simulation of a 7 µm manufactured edge. Bottom left model uses Sommerfeld's solution for the edge. Bottom right model is scalar diffraction only. In each model the analyzer is rotated 15° (from horizontal) to be consistent with the experiment. The input polarization is horizontal in the image. **Note** the order of magnitude difference in colorbar range between the top and bottom rows.

Optics EXPRESS

Kirchhoff solution. There is an order of magnitude difference between the experimental data and the Sommerfeld and Kirchhoff solutions, while the 7 μm edge model matches well. Figure 10 shows an image of DW9 with the camera analyzer orthogonal to the input polarizer, along with the 7 μm edge model. Light in this polarization is due solely to polarization induced by the thick screen effect. We see that our model matches the experimental data in two orthogonal polarization angles. Even with the complex geometries of the manufactured edge, the agreement is better than 10^{-10} contrast, which we believe highlights the power of our approach.

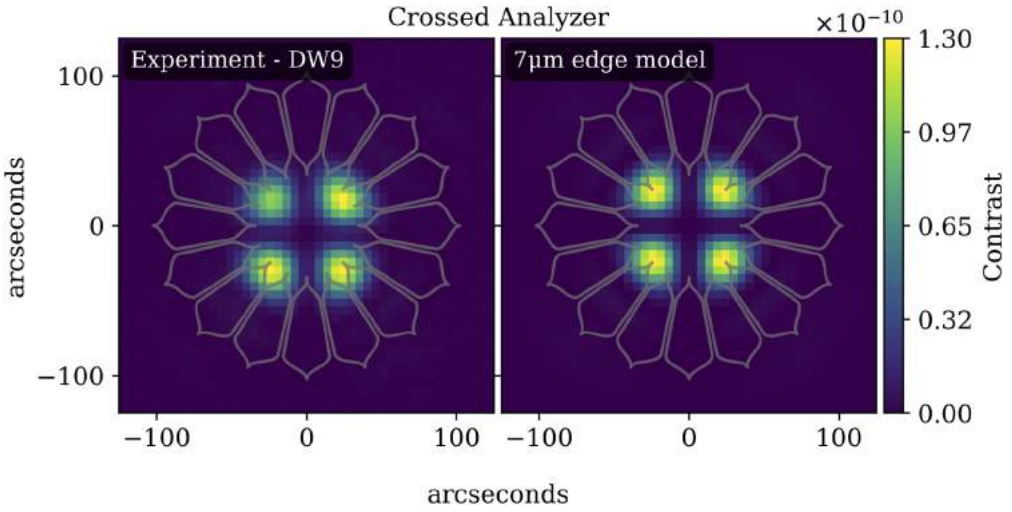

Fig. 10. Experimental (left) and model (right) images of mask DW9. The camera analyzer is crossed (aligned vertical in the image) with the input polarizer (horizontal in the image); light of this polarization is solely due to the thick screen effect.

The observed morphology of the polarization lobes agree with our understanding of their source. The boundary layer caused by the interaction with the edge occupies a significant fraction of the aperture only in the inner gaps between petals and thus the degradation of contrast is dominant there. The strength of the edge interaction is dependent on the polarization relative to the sidewall of the edge; *s*-polarization, where the electric field is parallel to the wall, has a greater effect as the electric field goes to zero on a perfect conductor. The inner gaps can be thought of as parallel plates aligned with the petal. If we assume horizontally polarized light, petals at the 3:00 and 9:00 positions have all *s*-polarization and petals at the 6:00 and 12:00 positions have all *p*-polarization. Since *s*-polarization has a stronger interaction, the bright lobes are aligned with the petals that have their walls parallel to the input polarization. For petals in between those positions, with walls at an angle to the polarization vector, they see both *s*- and *p*-polarization and if there is an imbalance in the interaction strength of the two, they induce a component orthogonal to the input polarization. This is seen in the four lobes of Fig. 10, where the analyzer (vertical in the image) is orthogonal to the polarization vector (horizontal in the image). The morphology of the lobes at various angles can be seen in Fig. 11, where we show images of DW9 with the analyzer rotated to different angles relative to the input polarization direction. As the contrast difference between the aligned analyzer and crossed analyzer is only a factor of 30, there are not tight constraints on the extinction of the analyzer nor on the linearity of the incident polarization; the >>100:1 extinction of our polarizing element is sufficient.

In Sec. 5, we mentioned that the model results do not match the experimental data unless we simulate an edge with a vertical profile that matches that of the manufactured mask. The size of the edge scallops can be inferred from an SEM image of the edge (see Fig. 8), but the taper angle

Optics EXPRESS

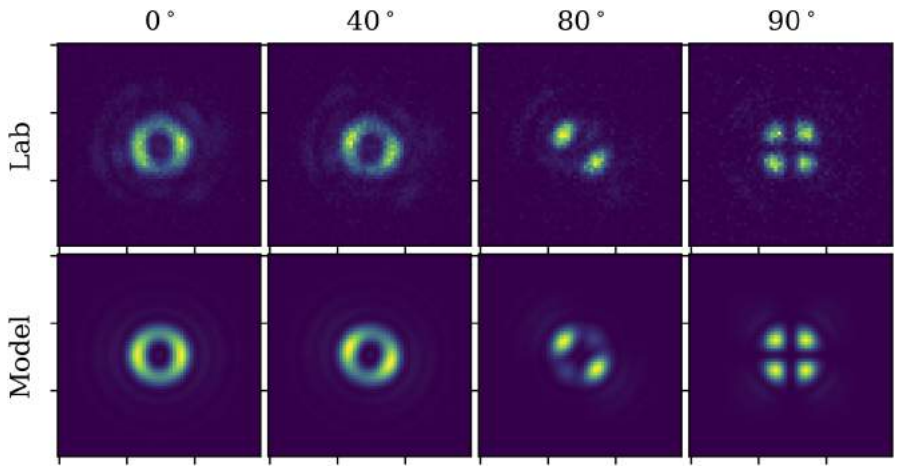

Fig. 11. Experimental (top) and model (bottom) images of mask DW9 imaged with the camera analyzer rotating relative to the input polarizer direction (horizontal in the image). The angle given is that between the analyzer and polarizer, where 0° means they are aligned, 90° means they are crossed. Exposure times are increased for larger angles.

cannot. To match the taper angle, we ran a suite of simulations varying the angle to find which produced the best fit. The data we use to match the model with experiment are the contrasts of the primary polarization lobe (at 3:00 and 9:00 in Fig. 8), the secondary polarization lobe (at 6:00 and 12:00 in Fig. 9), and the lobes in the crossed analyzer data (four equal brightness lobes in Fig. 10). Figure 12 shows the contrast trends as a function of scallop depth and taper angle. The three experimental measurements of mask DW9 (contrast at the primary, secondary, and crossed analyzer lobes) are shown as dotted horizontal lines. The simulated data points closest to the horizontal lines yield the best estimations of the scallop depth and taper angle. The crossed analyzer contrast is a steep function of scallop depth, but does not depend on taper angle. The primary lobe contrast is moderately dependent on both, and the secondary lobe contrast is weakly coupled to scallop depth, but is dependent on taper angle. The crossed analyzer data is inconsistent with any scallop depth other than 0.2 μm, which is consistent the value estimated from the SEM image. Given that, the best fit taper angle is 1°, which matches well with all three data points. We sample the scallop depth and taper angle coarsely as a demonstration of the concept; more exact values could be extracted, but is beyond the scope presented here.

For additional confirmation of the technique, in Fig. 13 we show the comparison between experimental and model images for the 3 μm thick mask DW21. The 3 μm thick edge model again matches the experimental data well. The best fit model has a scallop depth of 0.25 μm and taper angle of 5°. As the gaps of this mask are wider and the edge thicker, it is reasonable to expect a different edge profile as a result of the manufacturing process. The peak contrast in the primary lobes are ~ 2.3× fainter than those of DW9, which is consistent with the thick screen effect scaling linearly with edge thickness, as should be expected. We believe the lack of secondary lobe at the 12:00 position is due to interference from the manufacturing defect seen on the outer edge at the 10:00 position; the thinner mask results in a smaller degradation in contrast, which is more susceptible to interference from manufacturing defects. The dominant parameter driving the thick screen effect is the edge thickness and the resulting change in the field. Since the apodization profile is different for masks DW9 and DW21, it is not practical to compare the effect of the different gap widths between masks, however modeling results show the change in gap widths have a small effect on the degradation in contrast for masks of the same size.

Optics EXPRESS

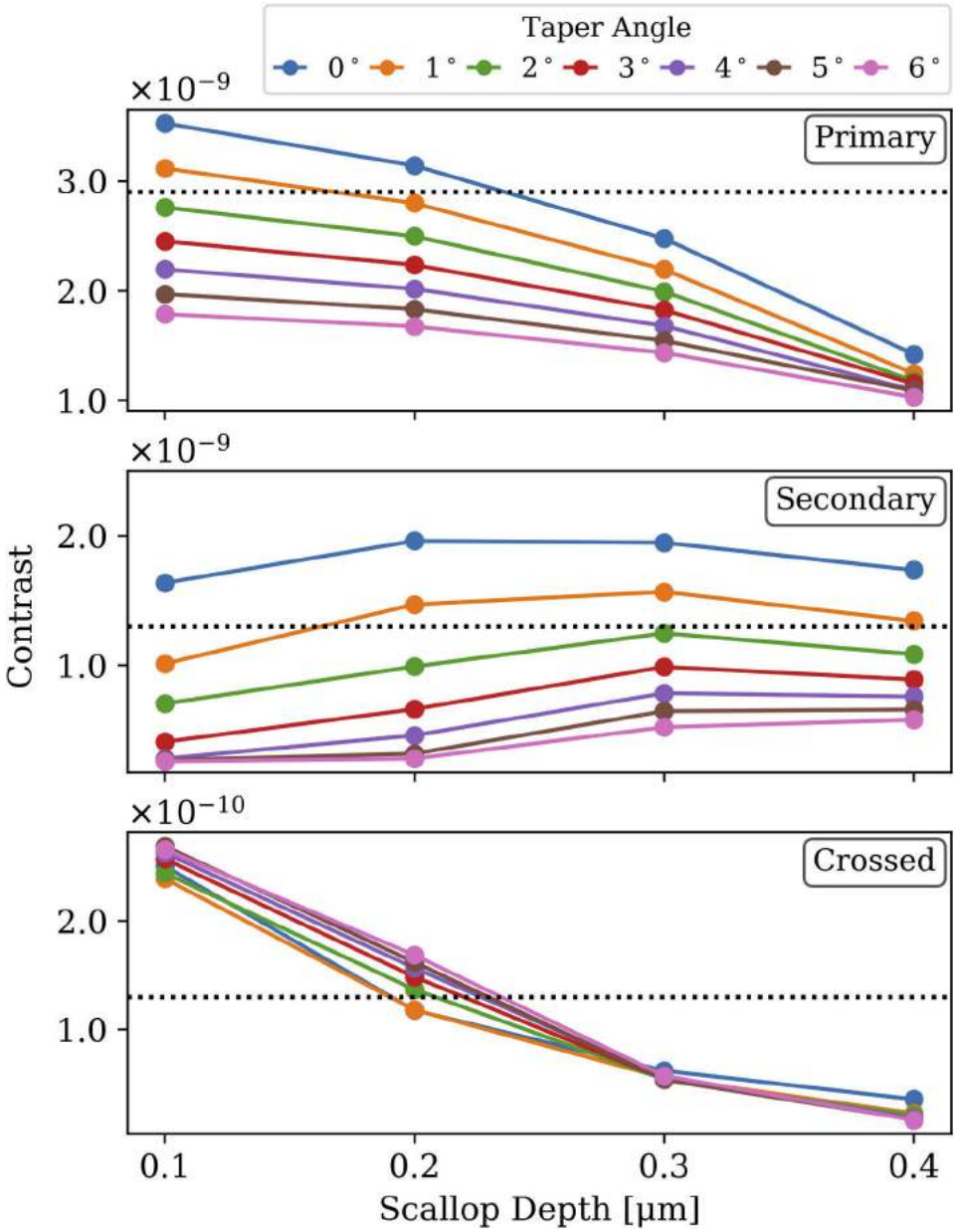

Fig. 12. Simulated contrast as a function of scallop depth and taper angle. The dotted horizontal lines are the experimental values for mask DW9, where the scallop depth and taper angle are unknown. The top plot corresponds to the primary polarization lobes, the middle plot the secondary polarization lobes, and the bottom plot the lobes in the crossed analyzer data.

Optics EXPRESS

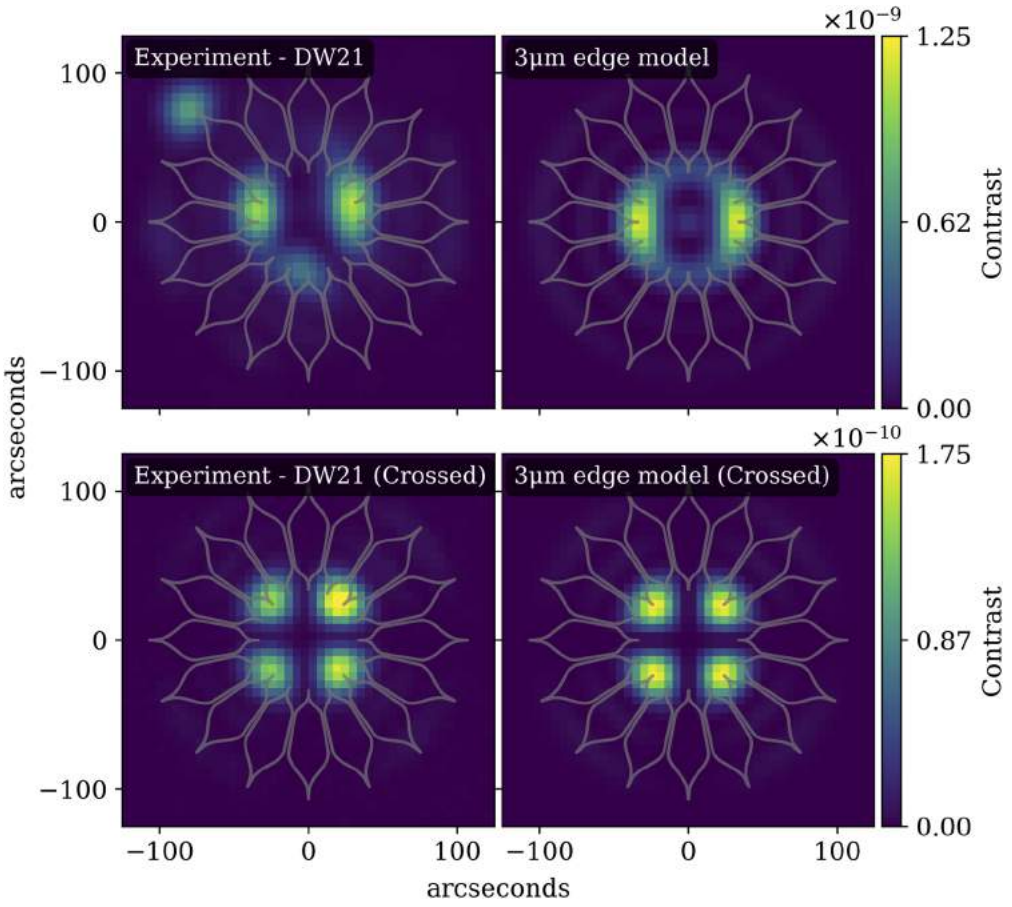

Fig. 13. Experimental (left column) images of mask DW21 and model (right column) images of a 3μm thick edge. In the top row, the analyzer and input polarizer are aligned, in the bottom row they are crossed. The bright spot at the 10:00 position is a manufacturing defect on the mask.

7. Conclusions

The method outlined in this paper provides a means to implementing non-scalar diffraction while maintaining the efficiency of Fourier optics. We derived the equations for the model that takes the complex field downstream of the edge of any diffracting element and calculates the far field diffraction for any input polarization state. We also outlined how to computationally solve for the diffraction using a greypixel map to represent the geometry of the diffracting element and its resulting edge effect. Finally, we validated the model using experimental results of sub-scale starshades and demonstrated the model replicates the observed diffraction pattern at the 10^{-10} contrast level and captures the sensitivity of the thick screen effect to the edge thickness.

By restricting the area in which we deviate from scalar diffraction to a narrow seam around the edge, we only need a full electromagnetic solution over a few microns, which is readily calculated via the FDTD method. This makes the problem tractable for large optical systems that are many times the size of the wavelength of light, such as the sub-scale starshades that have features as small as 7 μm and a total extent of 50 mm. We believe this method can be used to simulate the edge effect for full-scale starshades that are 10's of meters across and to show the non-scalar effect is negligible for the large starshades. This method could also be used to include the effects

Optics EXPRESS

of a thick mask and polarization in shaped pupil and Lyot coronagraphs [18], which are also represented as binary masks and propagated via Fourier optics.

Funding

Jet Propulsion Laboratory, California Institute of Technology.

Acknowledgments

The author would like to thank the starshade testbed team for contributions to the experiment and modeling: Stuart Shaklan, Jeremy Kasdin, Phil Willems, K. Balasubramanian, Philip Dumont, Victor White, Karl Yee, Michael Galvin, Rich Muller, Simon Vuong, and Dylan McKeithen. The author would also like to thank the anonymous referees for helpful suggestions. This project made use of the resources from the Princeton Institute for Computational Science and Engineering (PICSciE) and the Office of Information Technology's High Performance Computing Center and Visualization Laboratory at Princeton University.

Disclosures

Experimental results are also presented in Ref. [6].

References

1. J. W. Goodman, *Introduction to Fourier optics* (Roberts and Company Publishers, 2005), 3rd ed.
2. J. E. Krist, "PROPER: an optical propagation library for IDL," Proc. SPIE **6675**, 66750P (2007).
3. W. Cash, "Analytic modeling of starshades," Astrophys. J. **738**(1), 76 (2011).
4. E. Cady, "Boundary diffraction wave integrals for diffraction modeling of external occulters," Opt. Express **20**(14), 15196 (2012).
5. A. Harness, S. Shaklan, W. Cash, and P. Dumont, "Advances in edge diffraction algorithms," J. Opt. Soc. Am. A **35**(2), 275–285 (2018).
6. A. Harness, S. Shaklan, P. Willems, N. J. Kasdin, K. Balasubramanian, P. Dumont, V. White, K. Yee, R. Muller, and M. Galvin, "Optical verification experiments of sub-scale starshades," J. Astron. Telesc. Instruments, Syst. **7** (2020). Submitted.
7. W. Braunbek, "Neue Näherungsmethode für die Beugung am ebenen Schirm," Eur. Phys. J. A **127**(4), 381–390 (1950).
8. R. Meneghini, "Application of the Braunbek method to the Maggi—Rubinowicz field representation," J. Opt. Soc. Am. **73**(3), 321–327 (1983).
9. J. Tirapu-Azpiroz, P. Burchard, and E. Yablonovitch, "Boundary layer model to account for thick mask effects in photolithography," Proc. SPIE **5040**, 1611–1619 (2003).
10. R. J. Vanderbei, E. Cady, and N. J. Kasdin, "Optimal occulter design for finding extrasolar planets," Astrophys. J. **665**(1), 794–798 (2007).
11. J. B. Keller, "Geometrical theory of diffraction," J. Opt. Soc. Am. **52**(2), 116–130 (1962).
12. M. Born and E. Wolf, *Principles of Optics* (Cambridge University, 1999), 7th ed.
13. A. Rubinowicz, "Thomas Young and the theory of diffraction," Nature **180**(4578), 160–162 (1957).
14. W. H. Press, S. A. Teukolsky, W. T. Vetterling, and B. P. Flannery, *Numerical recipes in C. The art of scientific computing* (Cambridge University, 1992), 2nd ed.
15. A. Sommerfeld, "Mathematische Theorie der Diffraction," Math. Ann. **47**(2-3), 317–374 (1896).
16. R. Soummer, L. Pueyo, A. Sivaramakrishnan, and R. J. Vanderbei, "Fast computation of Lyot-style coronagraph propagation," Opt. Express **15**(24), 15935–15951 (2007).
17. A. F. Oskooi, D. Roundy, M. Ibanescu, P. Bermel, J. Joannopoulos, and S. G. Johnson, "Meep: A flexible free-software package for electromagnetic simulations by the FDTD method," Comput. Phys. Commun. **181**(3), 687–702 (2010).
18. D. P. Ceperley, A. R. Neureuther, M. D. Lieber, N. J. Kasdin, and T.-M. Shih, "Vector scattering analysis of TPF coronagraph pupil masks," Proc. SPIE **5526**, 228–239 (2004).

PROCEEDINGS OF SPIE

SPIEDigitalLibrary.org/conference-proceedings-of-spie

Modeling non-scalar diffraction in the Princeton starshade testbed

Harness, Anthony, Kasdin, Jeremy , Shaklan, Stuart, Dumont, Philip, Balasubramanian, K.

Anthony Harness, Jeremy Kasdin, Stuart Shaklan, Philip Dumont, K. Balasubramanian, "Modeling non-scalar diffraction in the Princeton starshade testbed," Proc. SPIE 10698, Space Telescopes and Instrumentation 2018: Optical, Infrared, and Millimeter Wave, 1069865 (24 July 2018); doi: 10.1117/12.2310187

SPIE.

Event: SPIE Astronomical Telescopes + Instrumentation, 2018, Austin, Texas, United States

Modeling non-scalar diffraction in the Princeton starshade testbed

Anthony Harness[a], N. Jeremy Kasdin[a], Stuart Shaklan[b], Philip Dumont[b], and K. Balasubramanian[b]

[a]Princeton University, Princeton, NJ 08544
[b]Jet Propulsion Laboratory, California Institute of Technology, Pasadena, CA 91109

ABSTRACT

Starshades provide a leading technology to enable the direct detection and spectroscopic characterization of Earth-like exoplanets. Two key aspects to advancing starshade technology are the demonstration of starlight suppression at science-enabling levels and validation of optical models at this high level of suppression. These technologies are addressed in current efforts underway at the Princeton Starshade Testbed. Recent experimental data suggest we are observing the effects of vector (non-scalar) diffraction, which are limiting the starshade's performance and preventing the scalar optical models from agreeing with experimental results at the deepest levels of suppression. This report outlines a model developed to simulate vector diffraction in the testbed using a full solution to Maxwell's equations propagating through narrow features of the starshade. We find that experimental results can be explained by vector diffraction as light traverses the thickness of the starshade mask and that our model is in rough agreement with observations. We provide simulation results of a number of starshade geometries as a first attempt to understand the relation of these effects to properties of the starshade masks. Finally, we outline a number of possible solutions aimed to minimize vector effects and to allow us to reach our milestone of 10^{-9} suppression.

Keywords: Starshade, High Contrast Imaging, Optical Modeling, Vector Diffraction

1. INTRODUCTION

Starshades provide a leading technology to enable the direct detection and spectroscopic characterization of Earth-like exoplanets.[1] Their high throughput and inherent broadband coverage bring the technically challenging goal of spectroscopy of extremely faint exoplanets into the realm of possibility. However, before a starshade mission can be committed to, a major technical tall pole in need of further development is the validation of optical models used to predict starshade performance at high suppression levels.[2] The main question in validity of the models is the assumption that the relevant optical physics can be represented by scalar diffraction theory only, i.e., that the electric field can be completely described by a scalar value and that vector propagation effects such as polarization are negligible.

The Princeton Starshade Testbed was designed to perform the sub-scale tests of starshades needed to experimentally validate the optical models at a flight-like Fresnel number. The testbed houses a 50 mm diameter starshade, located 50 m from a camera, with the goal of demonstrating 10^{-9} suppression at a flight-like Fresnel number (~ 15). A detailed description of the testbed can be found in Refs. 3–5 and a description of the scalar optical model can be found in Refs. 6, 7. The starshade mask is lithographically etched in a Silicon wafer and coated with a thin metallic layer. Details on the manufacturing process can be found in Refs. 8–10.

Recent tests of starshades with improved manufacturing precision have produced results that suggest the suppression of the starshade is being limited by a non-scalar component of diffraction. This also means that our optical models are failing to match experimental results at these high suppression levels and that scalar model validation cannot succeed until these problems are rectified. This report investigates this claim by simulating the effects of vector diffraction using a full solution to Maxwell's equations. We find that experimental results can be explained by non-scalar diffraction occurring as light traverses the thickness of the starshade mask.

E-mail: anthony.harness@princeton.edu

Space Telescopes and Instrumentation 2018: Optical, Infrared, and Millimeter Wave, edited by Makenzie Lystrup, Howard A. MacEwen, Giovanni G. Fazio, Proc. of SPIE Vol. 10698, 1069865
 · doi: 10.1117/12.2310187

We provide updates to the testbed in Section 2 and recent experimental results in Section 3. Section 4 details the vector diffraction model recently developed and Section 5 presents results of that model. Section 6 provides starshade performance predictions generated by the vector model integrated into the scalar starshade model and compares those results to the experimental observations. We provide possible solutions to eliminating non-scalar effects in Section 6.3.

2. RECENT UPGRADES TO STARSHADE TESTBED

We begin with upgrades made to the testbed intended to increase the efficiency of testing masks and to improve the agreement between experiment and model results.

Figure 1: Princeton Starshade Testbed with newly installed 2" thick fiberglass insulation covering the 78 m long tube.

2.1 Thermal insulation

Previous results[6] showed a degradation in suppression in the presence of strong atmospheric turbulence, which existed immediately following the closure of the testbed stations. After the testbed was closed to the ambient atmosphere, it took 3-5 days for the atmosphere to settle to a state of stable suppression. After the suppression had stabilized, there was still a long period motion observed in the diffraction pattern; on the order of 100s of microns motion over hour-timescales. We believed the largest contributor to the atmospheric instability was due to temperature gradients in the tube caused by uneven exposure to the building's HVAC system. To minimize the disturbance of the external HVAC system, we covered the entirety of the tube and each station with 2 inch thick fiberglass insulation (see Figure 1). We have found that the insulation helped reduce the settling time of the atmosphere after the testbed is closed and thus the overhead time of installing and testing a new mask is reduced. However, the long period motion of the diffraction pattern was still present and we now believe this motion is not due to the atmosphere, but rather it is due to flexing of the building itself as it reacts to outdoor temperature changes.

2.2 Incorporating SEM images into optical model

In an attempt to add higher fidelity to our optical model and more accurately represent the design of the as-built mask, we have developed software to convert images taken by a scanning electron microscope (SEM) into shape coordinates to be fed directly into the edge diffraction integral.[7] This functionality is most useful for accurately representing the width of the valleys between petals and edge defects left by the manufacturing process. The software uses simple computer vision algorithms that take advantage of the contrast of the SEM images to find the edge of the mask and assign it a coordinate. Figure 2a shows an SEM image of the 7.5 μm-wide inner valley between two petals and Figure 2b shows the edge points automatically detected by the software. The "chip" in

the bottom left of the valley is easily detected and can now be incorporated into the optical model. From these images, we can also estimate the etching accuracy of each petal and we apply an over-etch to the entire petal. In future tests, defects found from optical microscopy will be imaged by the SEM to allow the more accurate representation of the defect to be included in the model.

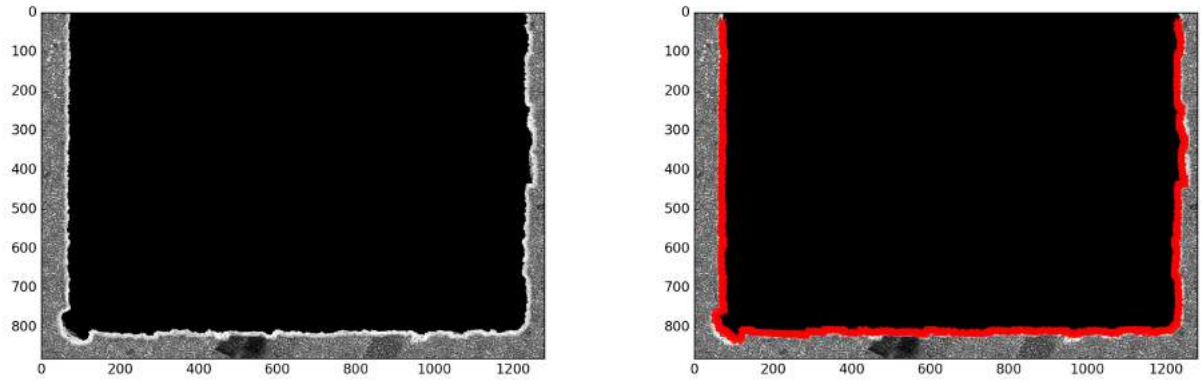

(a) (b)

Figure 2: SEM image of 7.5 μm-wide inner valley between petals. The red points in **(b)** are the automatically detected locations of the edge that are incorporated into the optical model.

3. LATEST EXPERIMENTAL RESULTS

The previously tested masks[5,6] were limited to a total suppression of $S_{12} \sim 4 \times 10^{-8}$ by a global over-etching of the mask in its manufacturing process. With good agreement between experimental and simulated results, the over-etch was estimated to be $\sim$0.4 μm. To help combat the etching woes, masks built since then have not included the additional 1 μm thick SiN layer that served as the optical edge. Skipping the addition of the SiN layer yielded a mask with a much better over-etch ($\sim$0.15 μm), but the optical edge is now the 7 μm device layer of a SOI wafer instead of 1 μm of SiN. Figure 3 shows schematic cross sections of the mask with the two different optical edges. Figure 4 shows the most recent mask with a 7 μm Si device layer coated with 400 nm of gold coating as the optical edge. The sizes and distances for the testbed are provided in Table 1.

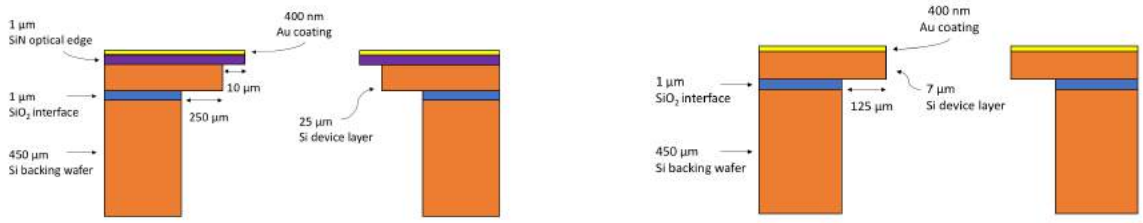

(a) (b)

Figure 3: Cross-section of starshade mask with different optical edge definitions. **(a)** is the previously used mask with the optical edge defined by a 1 μm SiN layer. **(b)** is the most recent mask with the optical edge defined by a 7 μm Si device layer.

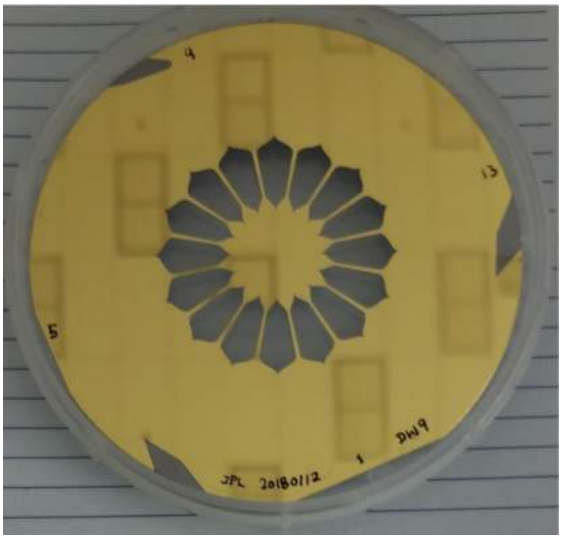

Figure 4: Latest starshade mask manufactured at Micro Devices Lab at JPL.

Starshade diameter (to peak apodization)	34.7 mm
Mask diameter	50 mm
Camera - starshade separation	50 m
Starshade - laser separation	27 m
Fresnel number ($\lambda = 633$ nm)	27
Aperture diameter	4.0 mm

Table 1: Parameters for Princeton Starshade Testbed. The starshade diameter and Fresnel number are calculated to the radius at which the apodization function reaches it's peak value of 0.9.

The experimental results for this mask are shown in Figure 5 and Figure 6. Despite the smaller over-etch, this mask produced a higher suppression value of $S_{12} = 6.0 \times 10^{-8}$. Additionally, the scalar models are in stark disagreement with the experimental results. A comparison of contrast and suppression values for the experimental results and scalar model are shown in Table 2. Defined further in Ref. 6, suppression is calculated in the pupil plane, while contrast is calculated in the focal plane. The mean contrast is calculated in the annular region between the inner and outer apodization profiles, which is denoted by the overlaid black circles.

This model includes defects in the valleys and over-etch measured by SEM images and large defects (>4 μm) found by optical microscopy. This mask was built with little over-etch and few defects and the expected suppression was $S_{12} = 3.0 \times 10^{-10}$, orders of magnitude better than that measured in the lab and better than our 10^{-9} goal. As we will explore in the following section, this disagreement suggests that we are seeing non-scalar diffraction, which is not accounted for in our optical model.

4. VECTOR DIFFRACTION MODEL

Recent experimental results testing a thicker mask show evidence of non-scalar diffraction, which is not accounted for in our scalar optical model. The primary goal of these starshade experiments is to prove that scalar diffraction theory is sufficient for predicting the performance of a starshade, requiring non-scalar (vector) diffraction to be negligible in our experiments*. While it is thought that the full-scale starshade lies well within the limits of the scalar diffraction approximation (to be validated in part by these experiments), the size scales involved in the

*If we find that we cannot neglect non-scalar effects, it is a matter of debate whether or not we can accomplish our primary goal of model validation using a combination of scalar and vector diffraction models.

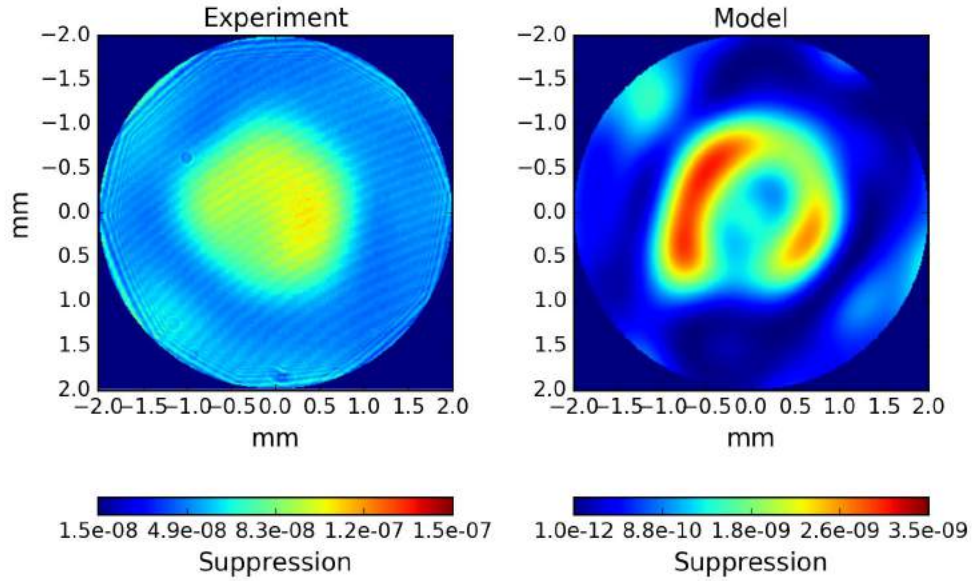

Figure 5: Comparison of **pupil** plane image for experimental data **(left)** and **scalar** diffraction model **(right)**.

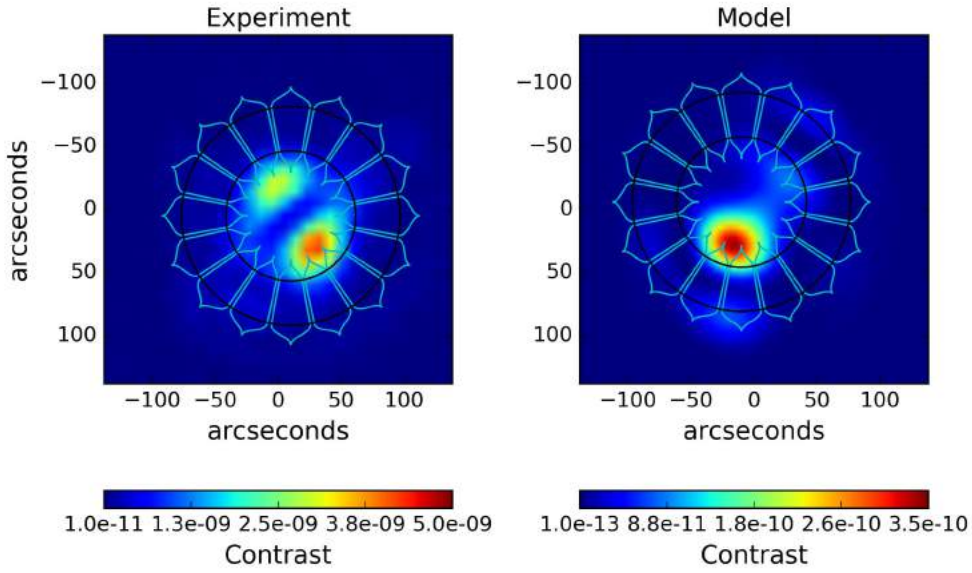

Figure 6: Comparison of **focal** plane image for experimental data **(left)** and **scalar** diffraction model **(right)**.

	Total Suppression	Mean Contrast
Experiment	6.0×10^{-8}	2.5×10^{-10}
Scalar Model (Figs. 5, 6)	8.2×10^{-10}	1.5×10^{-11}
Vector Model (Figs. 19, 20)	3.3×10^{-8}	2.6×10^{-10}
Vector Model w/ 10 nm Au on sidewall (Figs. 16, 17)	6.1×10^{-8}	5.2×10^{-10}

Table 2: Total suppression values and average contrast in annular region between inner and outer apodization function (overlaid black circles) as calculated in experimental images, scalar model, vector model, and vector model with 10 nm Au coating on sidewalls. Model results also include manufacturing defects and over-etching.

sub-scale experiment are pushing up against the regime where this approximation may break down. In particular, the valleys between the starshade petals are only ∼10 wavelengths wide and are of a similar thickness. This may be in the scalar regime for most applications, but the high suppression levels we are trying to achieve results in a high sensitivity to phase and amplitude changes.

From here on, we will use "vector" and "non-scalar" synonymously, which will also encapsulate any effects that depend on the material properties of the diffracting element. This section describes a first attempt at modeling vector diffraction in the testbed to determine if our experimental results can be explained by those effects.

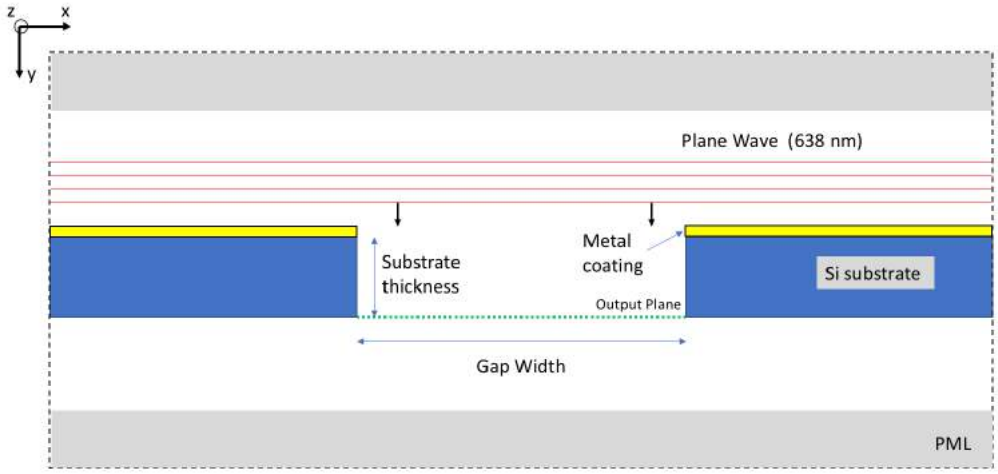

Figure 7: Schematic of computational cell for 2D FDTD simulation. A plane wave is incident on a metal coated Si substrate. The cell is lined with Perfectly Matched Layers (PML) to absorb numerical reflections.

4.1 FDTD electromagnetic simulation

Accounting for vector effects in the propagation of light requires a full solution of Maxwell's equations, which is computationally expensive, especially over the large size scales involved in the starshade architecture. Our strategy for incorporating vector diffraction effects into our optical model is to solve Maxwell's equations only in the thickness of the starshade mask, at the valleys between the petals, and to use the change in electric field across that thickness as inputs into our scalar starshade model.

We use the free and open-source software *Meep*[11,†], which uses a Finite Difference Time Domain (FDTD) integration scheme, to solve Maxwell's equations within the thickness of the mask. The simulation geometry

[†] https://meep.readthedocs.io

is shown in Figure 7, where we restrict ourselves to a two-dimensional problem and simulate a plane wave propagating through a cross-section of the mask. The materials of the substrate (silicon) and metal coating (aluminum, gold) are specified with a complex permitivitty and are given thicknesses to represent a given manufacturing recipe. The gap of free space represents the distance between petal edges on the mask (i.e., the distances expressed in Figure 8). The top and bottom of the computational cell are padded with "perfectly matched layers" (PML) to absorb numerical reflections at the boundary. Periodic boundary conditions are used on the other dimensions. A continuous wave serves as the electric field source with polarization in the 'X' (TM polarization) or 'Z' (TE polarization) directions. The simulation is stepped in the time domain until a steady state is reached, at which point the complex field at the output plane, located at the bottom of the substrate, is recorded to be implemented into the scalar model. A similar effort was conducted in the context of shaped pupils in Ref. 12.

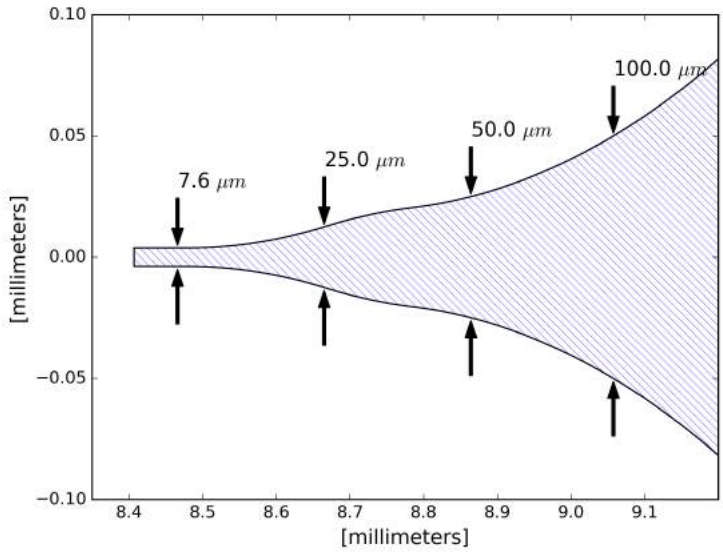

Figure 8: The inner valley between petals. The white region denotes the **opaque** mask, the blue hatched region denotes the **transparent** absence of the mask. The numbers tell the distances between the two arrows and refer to the "gap width" used in the FDTD simulations (and shown in Figure 7).

4.2 Implementation in scalar model

A sample output of the FDTD simulation, the complex field for one polarization component at the bottom of the substrate, is shown in Figure 9. To implement this result in the scalar model, each component field is propagated to the aperture in the far field with a scalar Fresnel propagation. This acts to filter out spatial modes that do not reach the aperture. Also shown in Figure 9 is the result of using an angular spectrum method to propagate a scalar field through the thickness of the mask. Fresnel ringing from the truncation of the field can be seen, but this is only due to scalar diffraction. This field is also propagated to the far field and the difference between scalar and vector fields at the camera is used as the input into the scalar model.

If the far-field scalar and vector complex electric fields are E_s, E_v, respectively, then the amplitude of the far field vector field in units of the amplitude of the scalar field (ε) and the phase difference between vector and scalar fields (ϕ) are given by,

$$\begin{aligned} \varepsilon &\equiv \left| \frac{E_v}{E_s} \right| \\ \phi &\equiv arg \left[\frac{E_v}{E_s} \right] \end{aligned} \tag{1}$$

The vector effects are then implemented into the scalar model similar to a wavefront error incident onto the mask. We calculate the far field diffraction at a distance y of a given mask ($M(x,z)$) as,

$$E = FFT\left[M(x,z)\, e^{\frac{ik}{2y}\left(x^2+z^2\right)} \varepsilon(r)\, e^{i\phi(r)}\right] \tag{2}$$

Although Figure 9 shows a non-uniform electric field exiting the gap, modes are filtered out as the field propagates to the camera in the far field, and we can replace the field exiting the gap with a uniform field equal to the filtered value. Since the 2D FDTD simulation corresponds to a given gap width, which is a function of radius (see Figure 11a), ε and ϕ are functions of radius only.

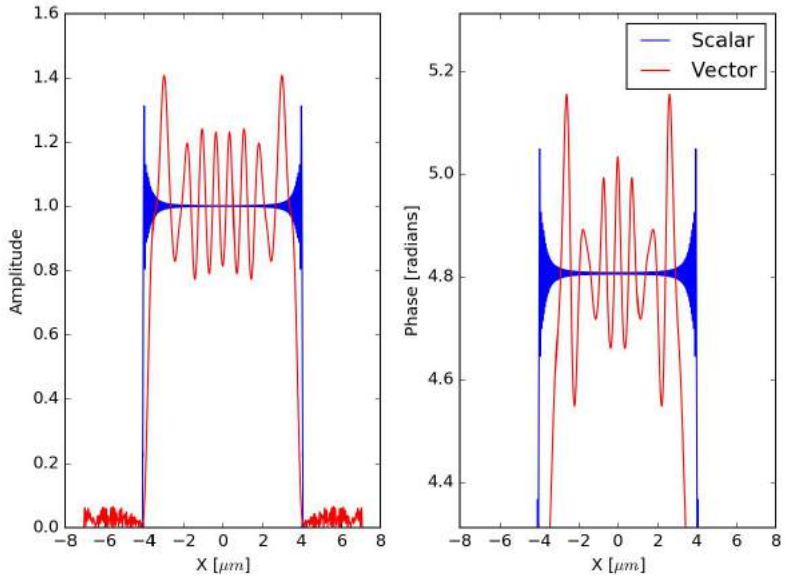

Figure 9: The **red** line shows the amplitude (**left**) and phase (**right**) at the output plane of an FDTD simulation. The simulation is of a 2 μm thick Si substrate coated with 200 nm of Al, with an 8.1 μm wide gap and illuminated with z-polarized light. The **blue** line corresponds to a scalar angular spectrum propagation of a plane wave through an identically-sized gap.

For a given mask thickness, we run the FDTD simulation for a number of gap widths ranging from the smallest width in the mask (7.5 μm) to a width at which vector effects are considered negligible (100 μm). The resulting amplitude and phase differences as a function of gap width for a 2 μm thick mask are shown in Figure 10. These values are interpolated as a function of width (Figure 11b) and applied over the first 800 μm of the mask until the gap width exceeds 100 μm.

4.2.1 Polarization

The FDTD simulations are run for two polarizations, one parallel (ξ, or z in Figure 7) to the length of the slot and one perpendicular (η, or x in Figure 7). The contribution of each polarization to the starshade model depends on the type of polarization we choose to simulate and the angle each petal makes with the dominant orientation direction of the polarization. We assume linearly polarized light, polarized at angle ψ, incident on a valley at angle θ; both angles relative to the global X axis. The strength of the incident fields parallel and perpendicular to the valley direction are given by,

$$\begin{aligned} E_{0,\xi} &= \cos(\psi - \theta) \\ E_{0,\eta} &= \sin(\psi - \theta) \end{aligned} \tag{3}$$

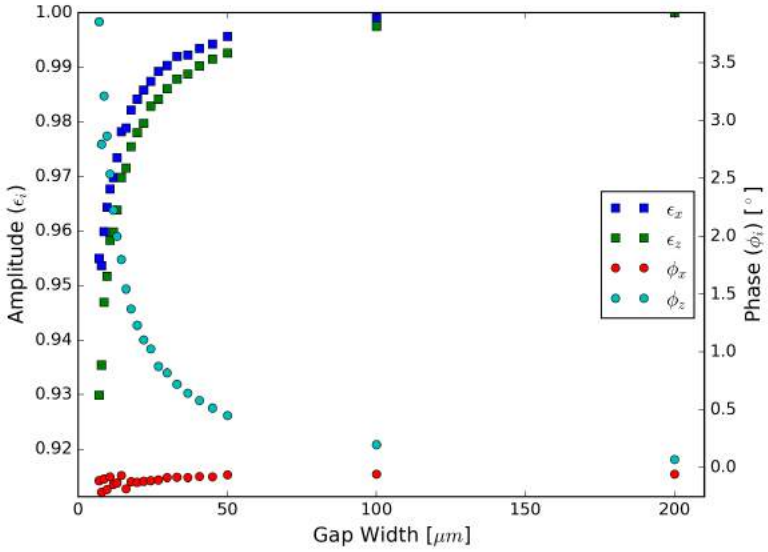

Figure 10: The amplitude and phase difference between scalar and vector fields (see Equation 1) as a function of gap width for a **2** μm **thick** Si mask coated with 200 nm of Al. The subscript refers to the polarization.

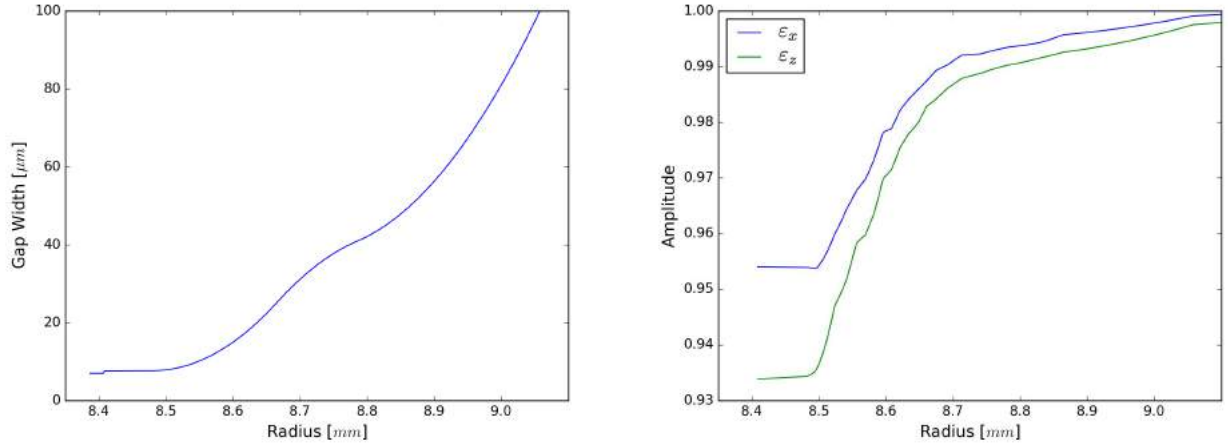

(a) (b)

Figure 11: **(a)** shows the width between starshade petals as a function of radius for the inner valley of the current starshade design. **(b)** shows the amplitude of the vector field change for both polarizations as a function of radius, which were generated by interpolating the amplitude as a function of width from Figure 10 onto the width as a function of radius in (a).

Denoting the vector field change after propagating through the gap for the parallel and perpendicular ($j = \{\xi, \eta\}$) polarizations as,

$$\delta_j = \varepsilon_j e^{i\phi_j} \tag{4}$$

we can express the contribution of polarized light in the global lab coordinate system (X, Z) as

$$\begin{aligned} E_X &= \delta_\xi \cos(\psi - \theta)\cos\theta - \delta_\eta \sin(\psi - \theta)\sin\theta \\ E_Z &= \delta_\xi \cos(\psi - \theta)\sin\theta + \delta_\eta \sin(\psi - \theta)\cos\theta \end{aligned} \tag{5}$$

In reality, our light source is elliptically polarized, which we simulate with a linear combination of linearly polarized states. If the resultant fields after propagation of horizontally and vertically polarized light are,

$$\begin{aligned} \vec{H} &= E_X\left(\psi=0\right)\hat{X} + E_Z\left(\psi=0\right)\hat{Z} \\ \vec{V} &= E_X\left(\psi=\frac{\pi}{2}\right)\hat{X} + E_Z\left(\psi=\frac{\pi}{2}\right)\hat{Z} \end{aligned} \tag{6}$$

the field for an elliptically polarized source is given by,

$$\vec{E} = a\vec{H} + b\vec{V}e^{-i\delta} \tag{7}$$

where a, b, δ are determined from the observable Stokes' parameters.

$$\begin{aligned} I &= a^2 + b^2 \\ Q &= a^2 - b^2 \\ U &= 2ab\cos\delta \\ V &= 2ab\sin\delta \end{aligned} \tag{8}$$

Measurements in the lab show the output from the laser fiber is partially elliptically polarized with normalized Stokes' parameters, I=1, $Q = 0.69$, $U = -0.33$, $V = -0.38$, and polarization fraction $p = 0.86$. We represent this by the polarization ellipse (with eccentricity $e = 0.93$) in Figure 12. For simplicity, we neglect the vector effects of the unpolarized contribution and simulate the light source as 100% polarized.

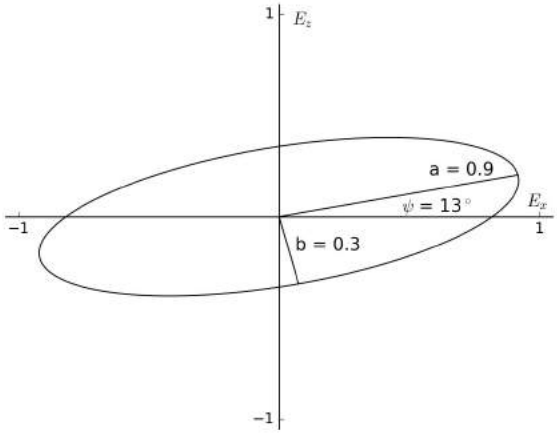

Figure 12: Polarization ellipse, with major axis (a), minor axis (b), and orientation angle (ψ) as calculated from Stokes' parameters measured in the lab.

5. EM SIMULATION RESULTS

The results of simulations using Maxwell's equations to propagate electric fields through the narrow gaps between starshade petals are shown in Figure 10 and Figure 13, where we plot the phase and amplitude changes as a function of gap width for different thicknesses of mask. These results show there is up to a 15% decrease in field amplitude and phase change of 10° for propagation through a 7 μm mask. As expected, the field change is more significant for thicker masks, as there is more opportunity for non-scalar interactions with the sidewalls. The effect is close to linear with thickness. The different polarizations have similar amplitude profiles, but the phase change is more drastic for the z polarization.

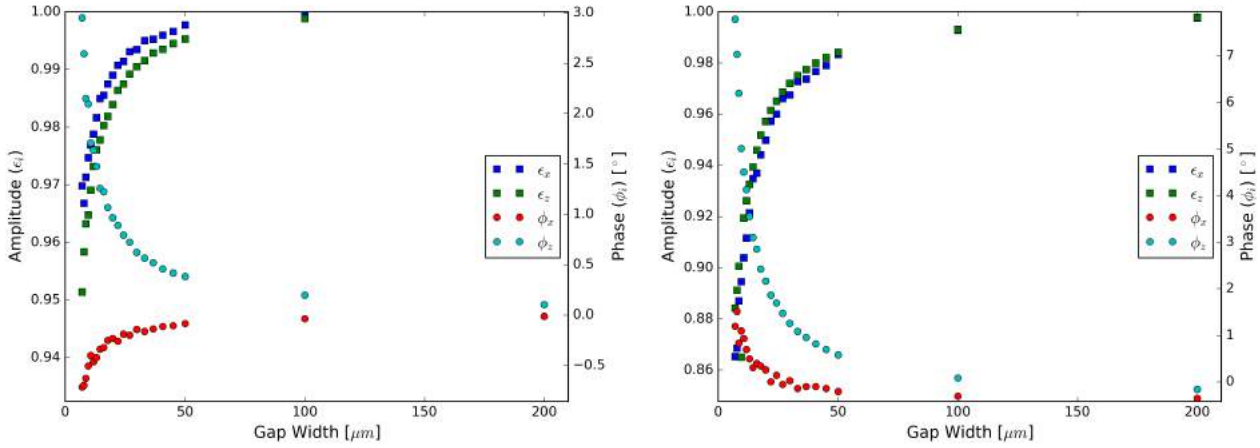

(a) 1 μm thick

(b) 7 μm thick

Figure 13: The amplitude and phase difference between scalar and vector fields (see Equation 1) as a function of gap width for **(a)** 1 μm thick and **(b)** 7 μm thick Si masks coated with 200 nm of Al. The subscript refers to the polarization. Note the factor of ∼2 difference in vertical axis range between (a) and (b).

The steady state electric field for a 7 μm mask (with a 400 nm top layer of gold and a 7 μm wide gap) is shown in Figure 14a. The most obvious feature seen is the 50% reduction in amplitude along the sidewalls, which grows in width as it propagates through the thickness of the mask. Some of this energy is reflected back into the air gap, where it interferes with reflections from the opposite wall and creates the visible interference pattern. Some of this energy is also leaked into the semi-transparent Silicon substrate, where the energy is lost from the system.

5.1 Metal-coated sidewalls

We also ran simulations with a 100 nm layer of gold coated to the vertical sidewalls; the phase and amplitude changes as a function of gap width are shown in Figure 15. Figure 14b shows the steady state electric field for this simulation. In this case, the field does not penetrate into the Silicon substrate and no energy is lost, but a surface plasmon wave is developed down the sidewalls, which leads to a larger phase and amplitude change.

It is assumed that no gold was applied to the sidewalls in the manufacturing process, but Figure 16 and Figure 17 show that the model with a 10 nm layer of gold on the sidewalls is a closer match to the observed data and suggests that this assumption is not correct for the as-built starshade. This also illustrates the increase in difficulty in modeling an exact representation of the as-built mask, as we must now include a three dimensional structure and material properties.

6. STARSHADE MODEL PREDICTIONS

6.1 Starshade (scalar + vector) model results

The specific apodization function of the starshade is chosen to control the contributions of electric field of a given phase to result in a near-perfect cancellation of field in the shadow region. Amplitude or phase changes on any section of the starshade effectively changes the apodization function and changes the contribution of field from that phase. While the changes may be small, the electric fields at this level of light suppression are highly sensitive to changes in the apodization function.

Applying the vector model outputs to our starshade model, we predict the performance of masks with varying thicknesses. Figure 18 shows the suppression and contrast for masks of 1 μm, 2 μm, and 7 μm thickness. Again, the suppression and contrast are worse for thicker masks, and follow close to a linear relationship.

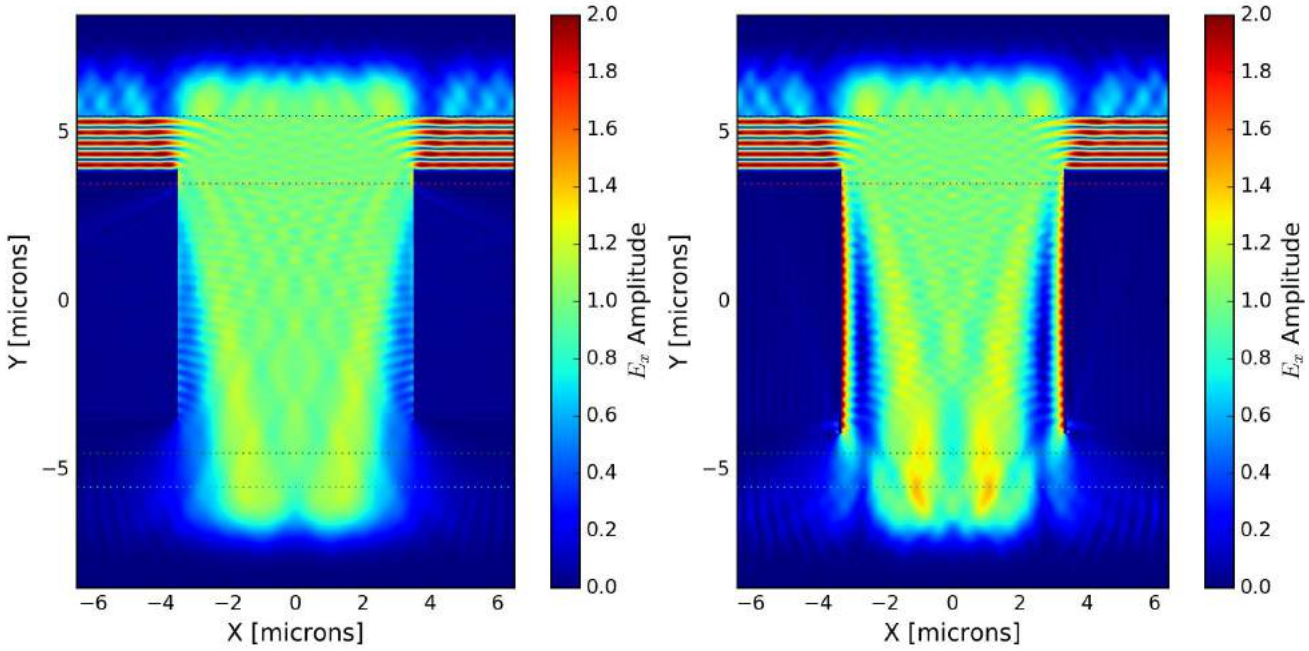

(a) (b)

Figure 14: Steady state electric field (amplitude of x-component) for simulation of 7 μm thick Si substrate with 400 nm Au coating and 7 μm wide gap. **(a)** is without and **(b)** is with 100 nm of Au coating the vertical sidewalls. Light propagates from top to bottom. The **black** line marks the location of the line source of electrical field (and start of the top PML), the **red** line marks the bottom of the Au coating and top of the Si substrate, the **green** line marks the observation point, and the **cyan** line marks the start of the bottom PML.

6.2 Comparison to experimental data

We simulate a mask representative to the one tested in the lab, which includes a 7 μm Si device layer, with a 400 nm gold coating on the top side. We use an elliptically polarized light source that represents the polarization measured in the lab (see Section 4.2.1). The comparison of lab data and model are shown in Figures 19, 20 and Figures 16, 17 (with metal-coated sidewalls) and while the match is not perfect, it is much closer than that of the scalar model and we are confident that this new model can explain our observations. Future work will attempt to provide more accurate, three-dimensional measurements of the mask to have our model better represent reality.

6.3 Design of future masks

The apodization function that describes the profile of the starshade petal is numerically determined using the scalar diffraction approximation. When non-scalar phase changes are introduced into the system, the apodization fails and the starshade is no longer able to obtain high suppression. Here, we consider a number of design considerations to pursue in attempt to minimize non-scalar diffraction effects.

6.3.1 Increase valley widths

As the results of the FDTD simulations show, changes in phase and amplitude quickly decrease with increasing gap width. The quickest way to mitigate the problem is to design the mask without any small features (where "small" is considered ~ 100 μm). Constraints into the optimization routine used to design the starshade[13] can limit the minimum feature size, but it is not guaranteed that it will converge to a solution. Widening the valleys creates a sharp discontinuity at the start of the petal that diffracts a large amount of light into the pupil, which

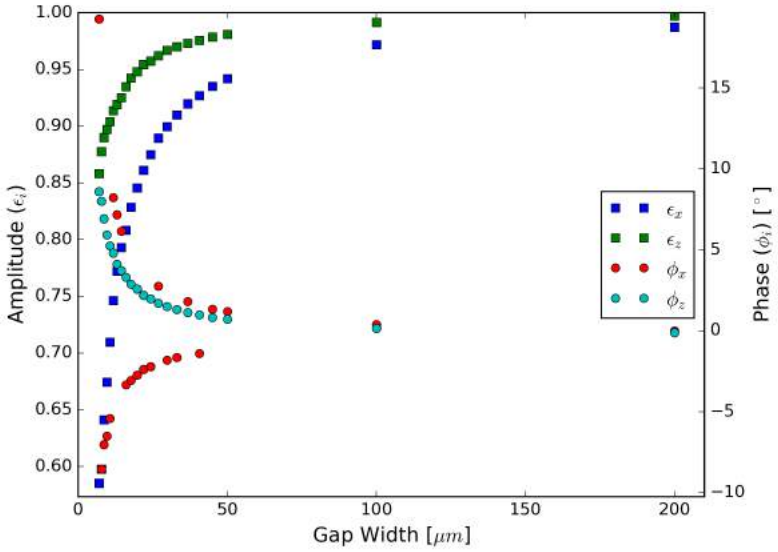

Figure 15: The amplitude and phase difference between scalar and vector fields (see Equation 1) as a function of gap width for a 7 μm thick Si mask top-coated with 400 nm of Au and with 100 nm of Au coating the vertical sidewalls. The subscript refers to the polarization.

then must be canceled by adding ripples along the edge of the petal. For a finite bandpass and resolution on edge profile, there exists a maximum valley width that can achieve high suppression. A new design effort must be done to see how wide we can design the valleys and if that is large enough to eliminate non-scalar effects.

6.3.2 Coat mask with dielectric

If the changes in electric field are due to interactions with the metal/semiconductor material on the sidewalls of the mask, one possible solution is to coat the sidewalls with a dielectric that insulates the field from the Si wafer and does not interact with the field. Additional modeling efforts are needed to know whether or not this is an adequate solution.

6.3.3 Optimize with vector effects included

Finally, if we find we cannot effectively remove the non-scalar interactions with the mask, a possible solution could be to trust our model of the electric field propagation and include the expected phase and amplitude changes in the optimization that determines the apodization profile. This will result in a non-linear optimization problem that will be more difficult to solve for a sufficient apodization profile, but a solution may still be possible. Whether or not this provides adequate suppression will depend on how accurately our vector model represents the as-built mask.

7. CONCLUSIONS

Recent experiments in the Princeton Starshade Testbed have shown evidence of non-scalar diffraction that can be explained by changes in the phase and amplitude as light propagates through the narrow valleys between starshade petals. These effects limit the effectiveness of the starshade's apodization profile and limit our suppression at 6×10^{-8}, worse than our milestone suppression.

The vector model outlined in this paper is a first attempt to include non-scalar diffraction in the starshade models that this testbed is meant to validate. We have shown rough agreement between this model and experimental results, but have also shown that the complexity of this new model requires a more accurate representation of the three dimensional structure and material properties of the manufactured mask. Work in the immediate

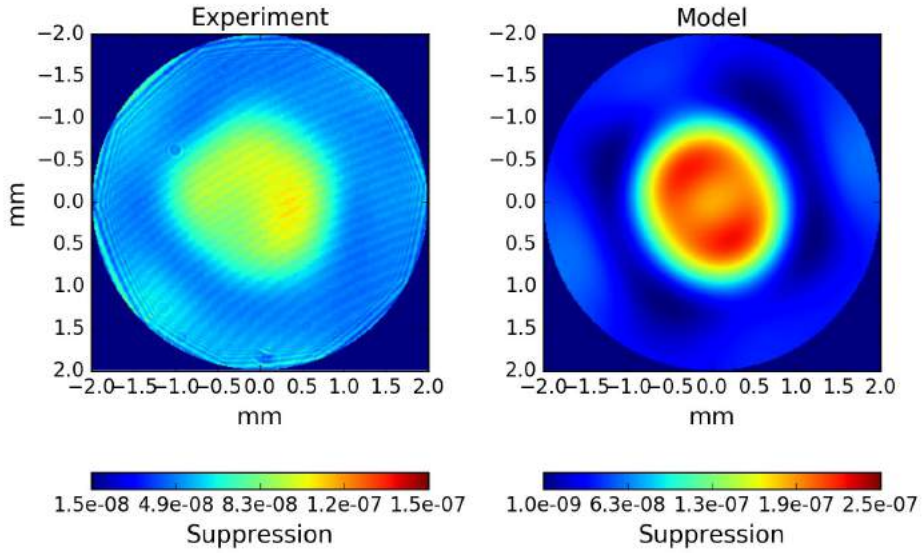

Figure 16: Comparison of **pupil** plane image for experimental data **(left)** and **vector** diffraction model with 10 nm of Au coated to the sidewalls **(right)**.

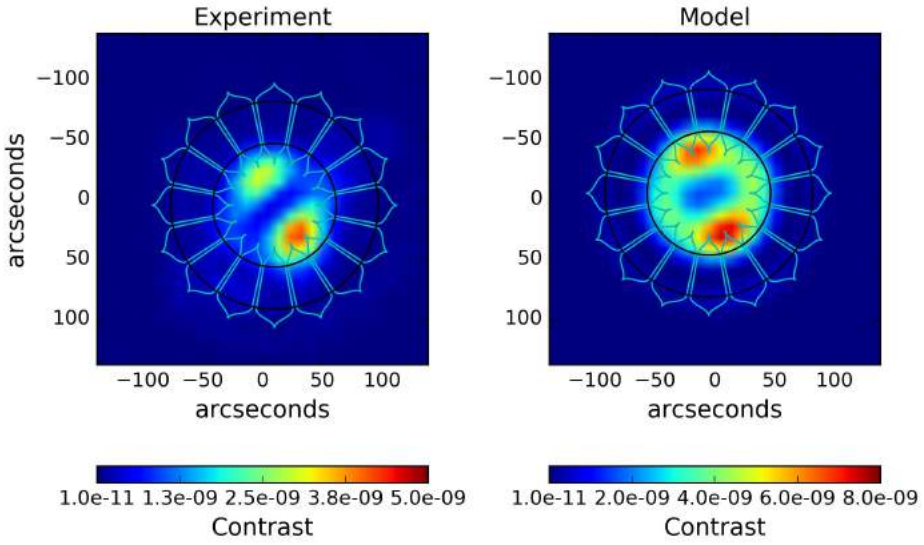

Figure 17: Comparison of **focal** plane image for experimental data **(left)** and **vector** diffraction model with 10 nm of Au coated to the sidewalls **(right)**.

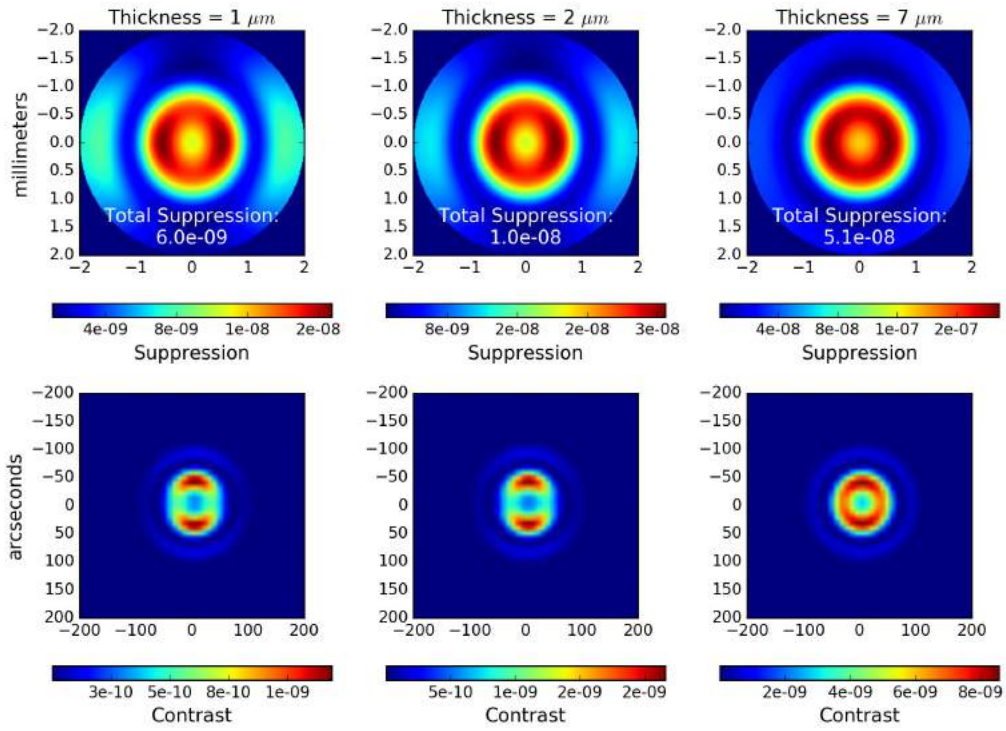

Figure 18: Pupil plane **(top)** and focal plane **(bottom)** images of perfect starshade masks with 200 nm coating of Al and with varying thicknesses. The input light source is horizontally polarized.

future will refine the vector propagation model and will also attempt to design a new starshade mask that has negligible vector effects and will allow us to reach our milestone suppression of 10^{-9}.

Until now, starshade design work has operated under the assumption that the effects of non-scalar diffraction can be ignored, for both the sub-scale tests and the flight design. The sensitivity of the starshade's performance to the non-scalar effects seen in the lab puts doubt on that assumption and further work is needed to verify that these effects will not be an issue for the full-scale starshade. The new starshade model presented here, with both vector and scalar diffraction, needs to be developed further and applied to the full-scale starshade.

ACKNOWLEDGMENTS

The authors would like to thank Victor White and Karl Yee of JPL Micro Devices Lab for fabricating the starshade masks and continually supporting the efforts of the testbed. We also thank Michael Galvin and Katherine Mumm for support with the testbed. SEM images were taken at the Princeton Micro/Nano Fabrication Laboratory. This work was performed under NASA Grant #NNX14AQ63G.

REFERENCES

[1] W. Cash, "Detection of Earth-like planets around nearby stars using a petal-shaped occulter," *Nature* **442**, pp. 51–53, July 2006.

[2] B. Crill and N. Siegler, "Exoplanet Exploration Program Technology Plan Appendix: 2018," *Jet Propulsion Laboratory Publications* **JPL Document No. D-101271**, 2018.

[3] Y. Kim, D. Sirbu, M. Galvin, N. J. Kasdin, and R. J. Vanderbei, "Experimental study of starshade at flight Fresnel numbers in the laboratory," *Proc. SPIE* **9904**, p. 99043G, July 2016.

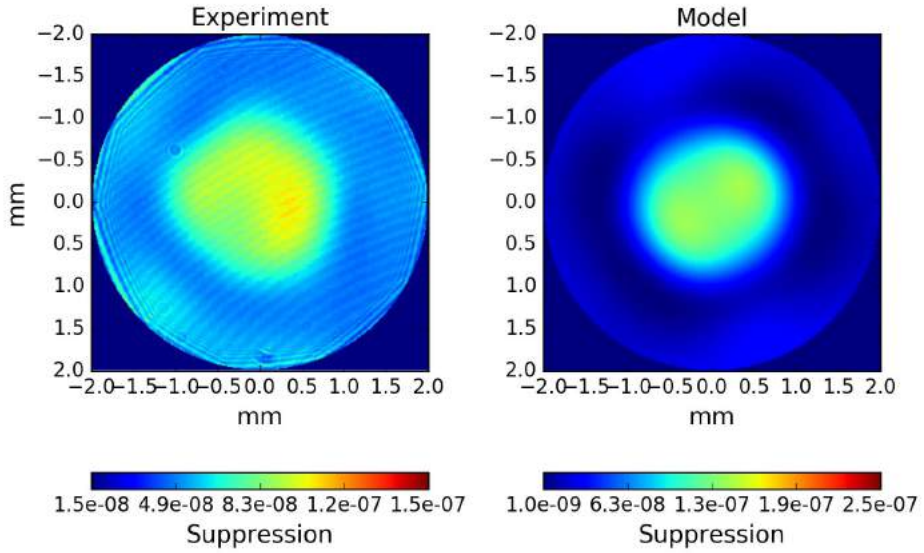

Figure 19: Comparison of **pupil** plane image for experimental data **(left)** and **vector** diffraction model **(right)** (with no sidewall coating).

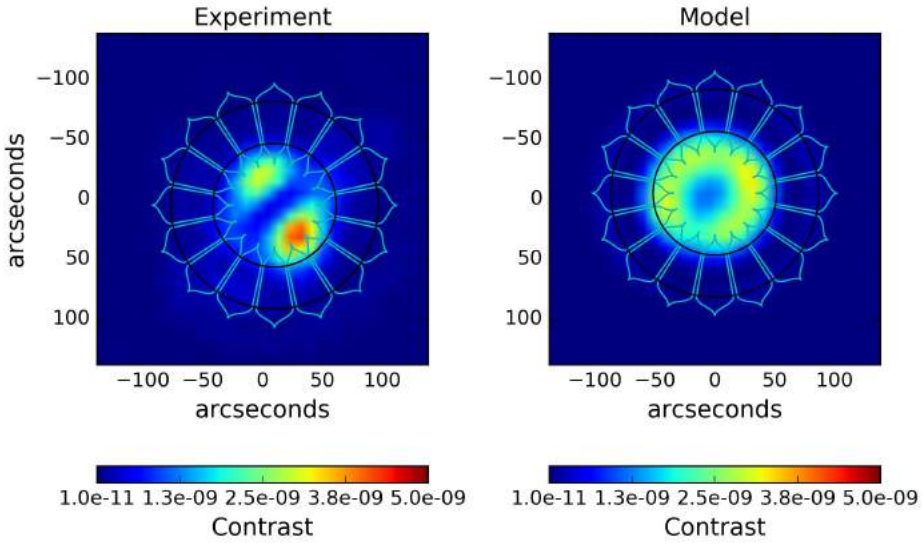

Figure 20: Comparison of **focal** plane image for experimental data **(left)** and **vector** diffraction model **(right)** (with no sidewall coating).

[4] M. Galvin, Y. Kim, N. J. Kasdin, D. Sirbu, R. Vanderbei, D. Echeverri, G. Sagolla, A. Rousing, K. Balasubramanian, D. Ryan, S. Shaklan, and D. Lisman, "Design and construction of a 76m long-travel laser enclosure for a space occulter testbed," *Proc. SPIE* **9912**, pp. 99126N–99126N–18, 2016.

[5] Y. Kim, A. Harness, D. Sirbu, M. Hu, M. Galvin, N. J. Kasdin, R. J. Vanderbei, and S. Shaklan, "Optical demonstration of a starshde at flight Fresnel numbers in the laboratory," *Proc. SPIE* **10400**, pp. 10400–43, Aug. 2017.

[6] A. Harness, S. Shaklan, P. Dumont, Y. Kim, and N. J. Kasdin, "Modeling and performance predictions for the princeton starshade testbed," *Proc.SPIE* **10400**, pp. 10400 – 10400 – 20, 2017.

[7] A. Harness, S. Shaklan, W. Cash, and P. Dumont, "Advances in edge diffraction algorithms," *J. Opt. Soc. Am. A* **35**, pp. 275–285, Feb 2018.

[8] K. Balasubramanian, V. White, K. Yee, P. Echternach, R. Muller, M. Dickie, E. Cady, C. M. Prada, D. Ryan, I. Poberezhskiy, B. Kern, H. Zhou, J. Krist, B. Nemati, A. J. Eldorado Riggs, N. T. Zimmerman, and N. J. Kasdin, "WFIRST-AFTA coronagraph shaped pupil masks: design, fabrication, and characterization," *Journal of Astronomical Telescopes, Instruments, and Systems* **2**, p. 011005, Jan. 2016.

[9] K. Balasubramanian, A. Eldorado Riggs, E. Cady, V. White, K. Yee, D. Wilson, P. Echternach, R. Muller, C. Mejia Prada, B.-J. Seo, F. Shi, D. Ryan, S. Fregoso, J. Metzman, and R. C. Wilson, "Fabrication of coronagraph masks and laboratory scale star-shade masks: characteristics, defects and performance," *Proc. SPIE* **10400**, pp. 10400–12, 2017.

[10] K. Balasubramanian, S. Shaklan, V. White, K. Yee, R. Muller, S. Velling, S. Vuong, A. Harness, and N. J. Kasdin, "Recent progress in the fabrication of starshade masks for laboratory demonstration of concepts," *Proc. SPIE* **10698**, pp. Poster 10698–224, 2018.

[11] A. F. Oskooi, D. Roundy, M. Ibanescu, P. Bermel, J. Joannopoulos, and S. G. Johnson, "Meep: A flexible free-software package for electromagnetic simulations by the fdtd method," *Computer Physics Communications* **181**(3), pp. 687 – 702, 2010.

[12] D. Ceperley, A. Neureuther, M. Miller, M. Lieber, and J. Kasdin, "Stray-light sources from pupil mask edges and mitigation techniques for the tpf coronagraph," *Proc.SPIE* **6271**, pp. 6271 – 6271 – 12, 2006.

[13] R. J. Vanderbei, E. Cady, and N. J. Kasdin, "Optimal Occulter Design for Finding Extrasolar Planets," *ApJ* **665**, pp. 794–798, Aug. 2007.

Demonstration of 1e-10 contrast at the inner working angle of a starshade in broadband light and at a flight-like Fresnel number

Harness, Anthony, Shaklan, Stuart, Kasdin, N. Jeremy, Galvin, Michael, Willems, Phillip, et al.

Anthony Harness, Stuart Shaklan, N. Jeremy Kasdin, Michael Galvin, Phillip Willems, Kunjithapatham Balasubramanian, Victor White, Karl Yee, Richard Muller, Philip Dumont, Simon Vuong, "Demonstration of 1e-10 contrast at the inner working angle of a starshade in broadband light and at a flight-like Fresnel number," Proc. SPIE 11117, Techniques and Instrumentation for Detection of Exoplanets IX, 111170L (9 September 2019); doi: 10.1117/12.2528445

SPIE.

Event: SPIE Optical Engineering + Applications, 2019, San Diego, California, United States

Demonstration of 1e-10 contrast at the inner working angle of a starshade in broadband light and at a flight-like Fresnel number

Anthony Harness[a], Stuart Shaklan[b], N. Jeremy Kasdin[a], Michael Galvin[a], Phil Willems[b], Kunjithapatham Balasubramanian[b], Victor White[b], Karl Yee[b], Richard Muller[b], Philip Dumont[b], and Simon Vuong[b]

[a]Princeton University, Princeton, NJ
[b]Jet Propulsion Laboratory, California Institute of Technology, Pasadena, CA

ABSTRACT

Starshades are a leading technology to enable the direct detection and spectroscopic characterization of Earth-like exoplanets. Starshade starlight suppression technology is being advanced through sub-scale starshade demonstrations at the Princeton Starshade Testbed and we present here the successful completion of a technology milestone focused on the demonstration of high contrast at flight-required levels. We demonstrate 10^{-10} contrast at the inner working angle of a starshade with a flight-like Fresnel number at multiple wavelengths spanning a 10% bandpass. We show that while contrast at the inner working angle is limited by the presence of non-scalar diffraction as light propagates through narrow slits between the starshade petals, high contrast is still achieved over most of the image. Successful completion of this milestone verifies we can design a starshade capable of producing scientifically useful contrast levels.

Keywords: Starshades, High Contrast Imaging, Optical Modeling, Exoplanet Detection

1. INTRODUCTION

Optical testing of sub-scale starshades continues at the Princeton Starshade Testbed and has already provided useful points of validation for diffraction models. Descriptions of the testbed and previous results, including the observance of non-scalar diffraction can be found in Ref. 1 and Ref. 2. Recently, the NASA Exoplanet Exploration Program (ExEP) chartered the Starshade Technology Activity, called S5, to develop starshade technology to Technology Readiness Level (TRL) 5 for a future space mission. S5 is focused on optical, mechanical, and formation flying technologies culminating in a series of milestones to be completed between 2019 and 2023.[3] The first three milestones focus on the demonstration of optical performance at flight-required levels:

Milestone 1A: Small-scale starshade mask in the Princeton Testbed demonstrates 1×10^{-10} instrument contrast at the inner working angle (IWA) in narrow band visible light and Fresnel number ≤ 15.

Milestone 1B: Small-scale starshade mask in the Princeton Testbed demonstrates 1×10^{-10} instrument contrast at the inner working angle at multiple wavelengths spanning $\geq 10\%$ bandpass and Fresnel number ≤ 15 at the longest wavelength.

Milestone 2: Small-scale starshade mask in the Princeton Testbed validates contrast vs. shape model to within 25% accuracy for induced contrast between 10^{-9} and 10^{-8}.

The definition of *contrast* and the related metric *suppression* can be found in the S5 technology development plan.[3] The purpose of Milestones 1A and 1B (the results for which are presented in this paper) is to show we can design a starshade capable of producing scientifically interesting contrast levels. Additional work on Milestone 2, which focuses on the validation of optical models, is underway and will be reported on at a later date.

This paper presents the results supporting the successful completion of Milestones 1A[4] and 1B:[5] the demonstration of 10^{-10} contrast at the inner working angle of a flight-like starshade in broadband light. We start

Email: aharness@princeton.edu

Techniques and Instrumentation for Detection of Exoplanets IX, edited by Stuart B. Shaklan, Proc. of SPIE
Vol. 11117, 111170L · © 2019 SPIE · CCC code: 0277-786X/19/$21 · doi: 10.1117/12.2528445

by detailing upgrades made to the testbed in Section 2. In Section 3 we present the latest experimental data and in Section 4 we describe the analysis used to verify the completion of the milestones. Section 5 provides a quick comparison of the experimental results with our vector diffraction model to help explain the mechanism generating the observed polarization signatures. Finally, we conclude and look to future work in Section 6.

2. TESTBED UPGRADES

The Princeton Starshade Testbed is 80 m long and is capable of testing $1/1000^{\text{th}}$ scale starshades at a flight-like Fresnel number. Shown in the schematic of Figure 1, the diverging beam from a spatially-filtered laser propagates 27.5 m before it diffracts around a starshade mask held in a motorized mask changer (see Figure 2), after which it propagates another 50 m to a camera sitting in the starshade's shadow. The beam line is enclosed in a 1 m diameter tube (which is air-filled) to seal the testbed from stray light and dust and to help stabilize the air inside. Since Ref. 2 was presented, the following hardware upgrades were implemented to support broadband wavelength coverage and to operate the testbed without disturbing the atmosphere inside the tube.

- A lens on a motorized flip mount was added to the camera's optical system to toggle the camera's focus between the light source and the entrance pupil. Focusing on the entrance pupil directly samples the diffraction pattern incident on the camera.
- The masks are now held in a motorized planetary gear that can switch between the starshade mask and a calibration mask (circular aperture) and can position the starshade at various clocking angles.
- A new starshade design was developed to 1) operate at a flight-like Fresnel number (≤ 15), 2) have wider gaps between the petals (16.7 μm vs 7.5 μm previously), and 3) have a thinner optical edge (3 μm vs 7 μm) to reduce "thick screen effects". Parameters for the testbed setup are provided in Table 1.
- The laser now operates at four wavelength channels: 641 nm, 660 nm, 699 nm, and 725 nm.

Figure 1. Layout of testbed showing distances between laser, starshade, and camera.

Figure 2. Motorized planetary gear which holds and rotates the starshade mask as well as a calibration mask.

Starshade Diameter	25.06 mm
Source - starshade separation	50 m
Starshade - camera separation	27.5 m
Aperture diameter	5.0 mm
Fresnel Number (at 641 nm)	13.83

Table 1. Parameters for the testbed geometry for Milestone 1B. The starshade diameter and Fresnel number are calculated to the radius at which the apodization function reaches it's peak value of 0.9. The starshade for Milestone 1A is 3% smaller and operates at a bandpass shifted 50 nm to the blue.

3. EXPERIMENTAL DATA

To support Milestones 1A and 1B (hereafter referred to as M1A and M1B), two similar experiments were run in which high contrast observations were made from within the deep shadow generated by the starshade. In the M1A experiment, we observed the starshade oriented at three clocking angles (0°, 120°, 240°) and at a single wavelength channel (641 nm). Note that the starshade used in this experiment has an identical apodization profile as that used in M1B, but is 3% smaller. The increase in size between M1A and M1B was made in order to shift the starshade's operating bandpass to fall within the laser's wavelength channels; the M1A mask was also made to be 2 μm thick. The contrast maps from this experiment are shown in Figure 3.

Immediately obvious in these images are the bright lobes located at the inner valleys between the petals that are aligned with the polarization direction and remain so when the mask is rotated. As light propagates through the gaps between petals that are 16 μm wide and 2 μm thick, the mask can no longer be considered an infinitely thin screen and interaction of the electric field with the material properties of the mask causes a slight phase and amplitude change. This slightly changes the effect of the apodization profile, which was designed under a scalar diffraction assumption. We refer to this as a "thick screen effect" and the apparent visible polarization signatures are well explained by our optical model that takes this into account (see Section 5). The unbalanced lobes seen in the 120° image can be explained by the camera not being perfectly centered behind the starshade.

In the experiment for M1B, we observed the starshade at a single orientation and at four discrete wavelengths: 641 nm, 660 nm, 699 nm, and 725 nm. The contrast maps from this experiment are shown in Figure 4. The polarization lobes are again visible and equally strong across the wavelengths. The peak contrast at 641 nm is higher than the M1A results, which is consistent with the thicker mask.

At angles much wider than displayed in the contrast maps, we observe light in a pattern of 16 radial spokes

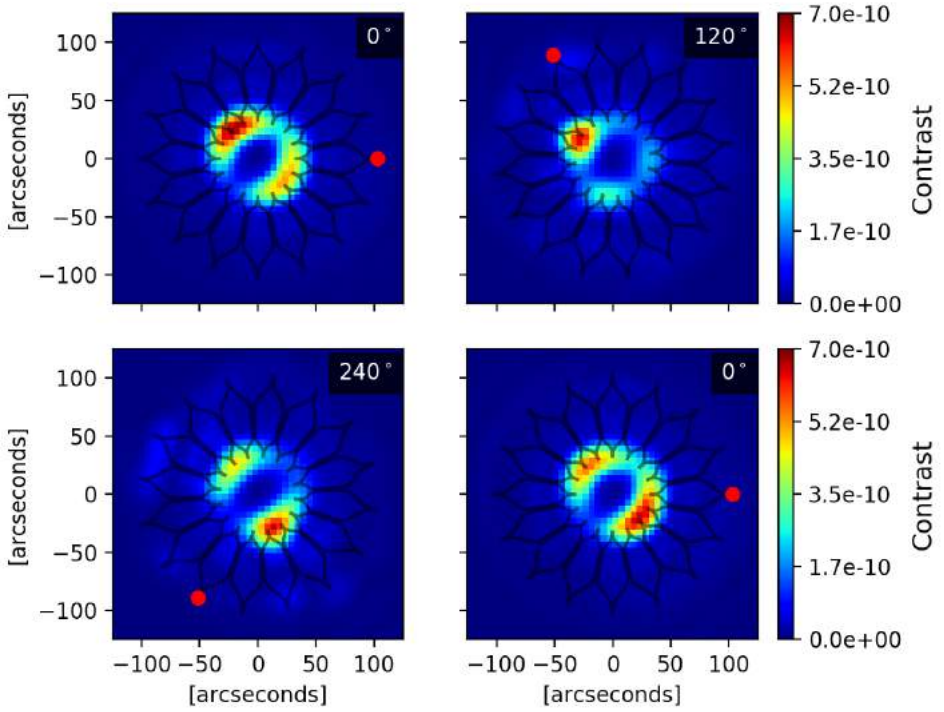

Figure 3. Contrast maps for **M1A** with the mask oriented at three clocking angles. The red dot marks the tip of the first petal. The wavelength is 641 nm.

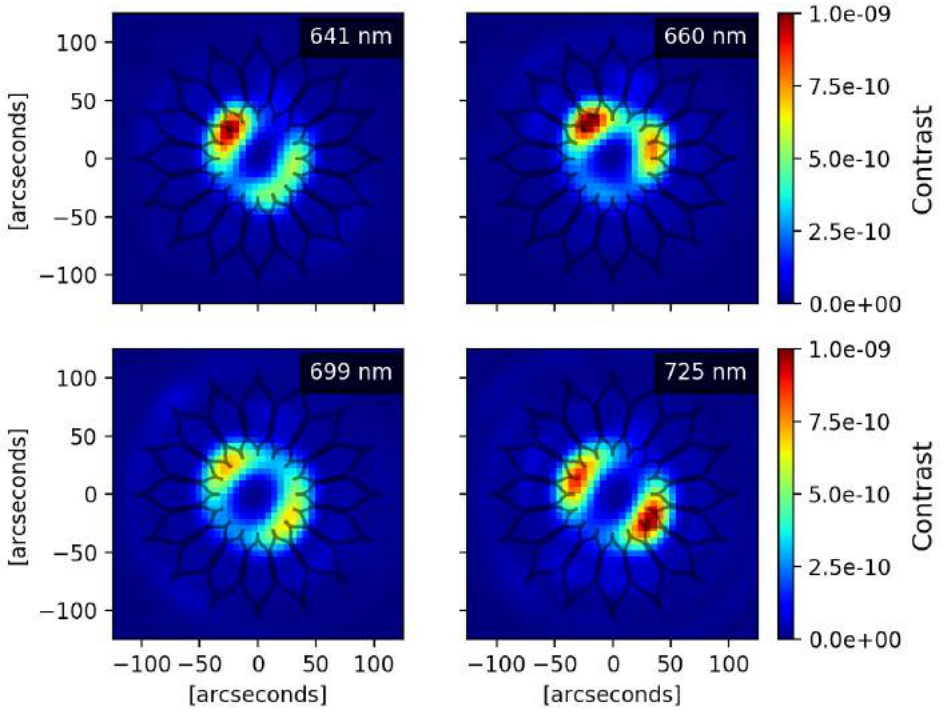

Figure 4. Contrast maps for **M1B** taken at four wavelengths. The orientation of the mask is fixed at 0°.

that extend from the outer working angle (OWA) of the mask to the edge of the camera's field of view. These spokes can be explained by Rayleigh scattering off air molecules in the testbed and in Ref. 6, we present a model that provides excellent quantitative agreement with the experimental data. The contrast contribution from Rayleigh scattering between the IWA and OWA is $< 2 \times 10^{-11}$ and contributes to the contrast floor.

4. FRACTION OF INNER WORKING ANGLE WITH CONTRAST $< 10^{-10}$

The degradation in contrast due to thick screen effects is localized along the polarization vector and high contrast is still achieved in regions of the IWA orthogonal to the polarization. To capture this effect and to stress that the thick screen effects do not corrupt the entire image, we report the fraction over which we meet our milestone contrast of 10^{-10}. To calculate this fraction, we start with the contrast maps of Figure 3 and Figure 4 and for each pixel in the image, we calculate the average contrast within a λ/D wide photometric aperture centered on that pixel. Next, we step outwards in working angle and grab all pixels that fall within a 1 pixel wide annulus. Our fraction is then defined as the number of those pixels that have an average contrast $< 10^{-10}$ divided by the total number of pixels in the annulus.

Mask Orientation	Fraction of IWA with Contrast $< 10^{-10}$	Fraction of Total Search Space
0°	32 ± 8 %	88 ± 2 %
120°	71 ± 8 %	95 ± 1 %
240°	42 ± 8 %	89 ± 2 %
0°	32 ± 6 %	88 ± 3 %
M1A average:	44%	90%

Table 2. For **M1A**: fraction of pixels at the IWA and over the total search space that have average contrast of $< 10^{-10}$.

Wavelength	Fraction of IWA with Contrast $< 10^{-10}$	Fraction of Total Search Space
641 nm	18 ± 4 %	83 ± 4 %
660 nm	34 ± 6 %	77 ± 3 %
699 nm	2 ± 2 %	74 ± 5 %
725 nm	6 ± 2 %	65 ± 5 %
M1B average:	15%	75 %

Table 3. For **M1B**: fraction of pixels at the IWA and over the total search space that have average contrast of $< 10^{-10}$.

The fraction as a function of working angle for M1A is shown in Figure 5 and in Table 2, where on average, 44% of the IWA meets the milestone contrast. We also show that 90% of the *total search space*, which we define as the region between the IWA and OWA, meets the contrast milestone. The fraction quickly rises to 100% past the tips of the starshade and speak to a promising strength of starshades: the sources of instrument contrast are confined to the starshade, and the contrast improves as one looks at radii beyond the starshade tips. The fraction as a function of working angle for M1B is shown in Figure 6 and in Table 3, where a lower average of 15% of the IWA and 75% of the total search space meets the milestone contrast. The lower fraction at the IWA at longer wavelengths is due solely to the broader PSF, which emanate from the inner valleys of the starshade, blending more light into the IWA.

These results verify that despite the presence of non-scalar diffraction, we achieved 10^{-10} contrast at the IWA across the designed bandpass. These results also point to the strength of starshades, where the presence of non-scalar diffraction merely results in a slight reduction in the area in which we can search for planets.

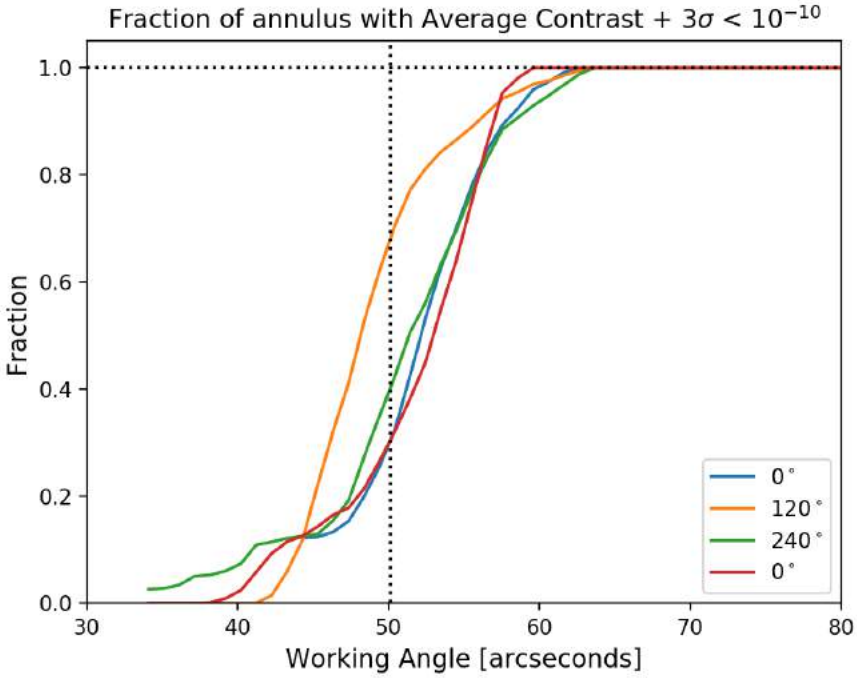

Figure 5. For **M1A**: fraction of pixels in a 1 pixel wide annulus that have average contrast of $< 10^{-10}$. The vertical line marks the IWA.

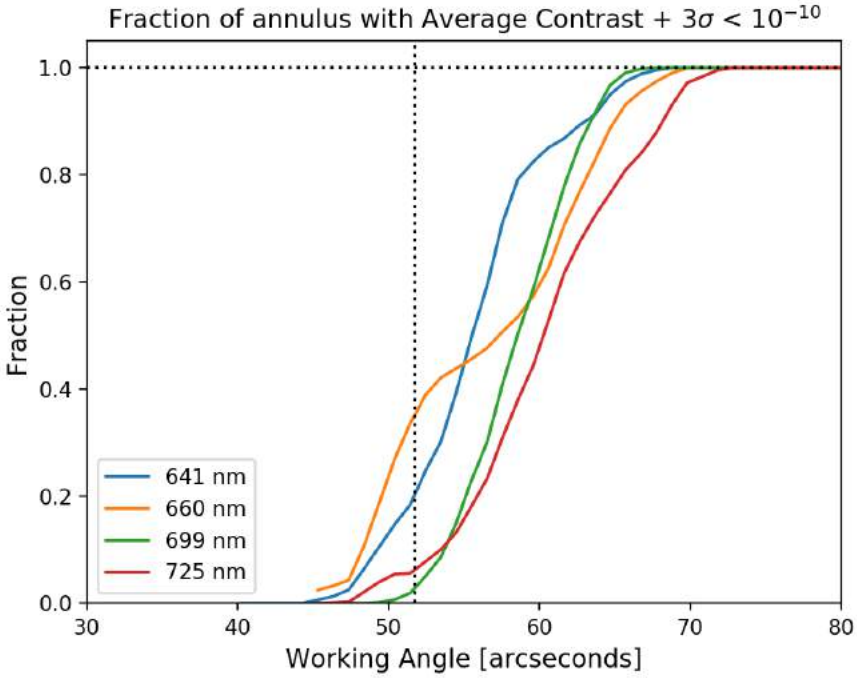

Figure 6. For **M1B**: fraction of pixels in a 1 pixel wide annulus that have average contrast of $< 10^{-10}$. The vertical line marks the IWA.

5. MODEL COMPARISON

A more thorough comparison between models and experimental data is planned for Milestone 2, where model validation is the primary focus. For now, we provide a preliminary comparison to show our implementation of the thick screen effects are able to explain the observed degradation in contrast. The implementation of the thick screen effects into our scalar diffraction model is detailed in Ref. 2. Figure 7 and Figure 8 show the model comparison to the 641 nm and 725 nm M1B data. The model shows good agreement with the data, both in the location and brightness of the polarization lobes. The degradation of contrast at the IWA can easily be explained by phase and amplitude changes that occur as light passes through the thick mask. Reaching perfect agreement between experiment and model is difficult as the vector diffraction model has many more parameters to vary such as thickness, material properties, and vertical profile of the mask. Work to refine the vector diffraction model is ongoing and will be borne out in more detail in Milestone 2.

6. CONCLUSION

The results presented here demonstrate there are no fundamental barriers to designing a starshade capable of producing scientifically useful contrast levels across a wide bandpass. The performance at the IWA is limited by thick screen effects that are due to the gaps between the starshade petals being of size comparable to the wavelength of light. In spite of these effects, we are still able to achieve deep contrast over a significant portion of the IWA and over the entire region beyond the tips of the starshade. Our models suggest that these effects will not be present for the full size starshade, which is 1000× larger. Outside of the IWA, the contrast is limited at 2×10^{-11}, contributed to by thick screen effects and Rayleigh scattering.

The NASA Exoplanet Exploration Program's Technology Assessment Committee (ExoTAC) has deemed Milestones 1A and 1B fulfilled. We have now transitioned to Milestone 2, which is a sensitivity study and model validation experiment to measure the contrast arising from intentionally induced shape errors closely aligned with the errors that comprise the optical performance error budget. These include edge segment displacements, edge segment distortions, single and global petal displacement, and combinations of segment shape and placement errors. Completion of this milestone will leave starshade starlight suppression technology at TRL 5.

ACKNOWLEDGMENTS

Results from this paper are also presented in Ref. 4 and Ref. 5. The authors would like to thank members of the ExoTAC: Alan Boss, Rebecca Oppenheimer, Joe Pitman, Lisa Poyneer, and Stephen Ridgway for reviewing this work and for their many helpful suggestions. This work was performed in part at the Jet Propulsion Laboratory, California Institute of Technology under a contract with the National Aeronautics and Space Administration. Starshade masks were manufactured using the facilities at the Microdevices Lab at JPL.

REFERENCES

[1] Harness, A., Shaklan, S., Dumont, P., Kim, Y., and Kasdin, N. J., "Modeling and performance predictions for the princeton starshade testbed," *Proc. SPIE* **10400**, 20 (2017).

[2] Harness, A., Kasdin, N. J., Shaklan, S., Dumont, P., and Balasubramanian, K., "Modeling non-scalar diffraction in the princeton starshade testbed," *Proc. SPIE* **10698**, 17 (2018).

[3] Willems, P., "Starshade to TRL5 (S5) Technology Development Plan," *Jet Propulsion Laboratory Publications* (2018). https://exoplanets.nasa.gov/internal_resources/1033/.

[4] Harness, A., Shaklan, S., Kasdin, N. J., Balasubramanian, K., White, V., Yee, K., Muller, R., Dumont, P., Vuong, S., Willems, P., and Galvin, M., "Starshade Technology Development Activity Milestone 1A: Demonstration of High Contrast in Monochromatic Light at a Flight-like Fresnel Number," *Jet Propulsion Laboratory Publications* (2019). https://exoplanets.nasa.gov/internal_resources/1210/.

[5] Harness, A., Shaklan, S., Kasdin, N. J., Balasubramanian, K., White, V., Yee, K., Muller, R., Dumont, P., Vuong, S., Willems, P., and Galvin, M., "Starshade Technology Development Activity Milestone 1B: Demonstration of High Contrast in Broadband Light at a Flight-like Fresnel Number," *Jet Propulsion Laboratory Publications* (2019). https://exoplanets.nasa.gov/internal_resources/1211/.

[6] Willems, P. and Harness, A., "Rayleigh scattering in the princeton starshade testbed," *Proc. SPIE* **11117**, 23 (2019).

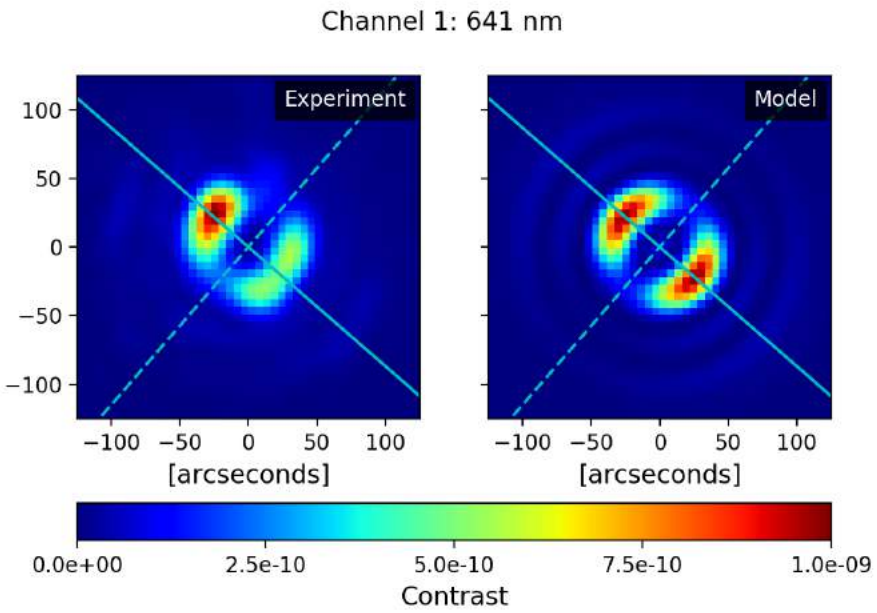

Figure 7. Experimental data (left) and vector diffraction model (right) for the M1B experiment at 641 nm. Solid and dashed lines are parallel and orthogonal to the polarization vector.

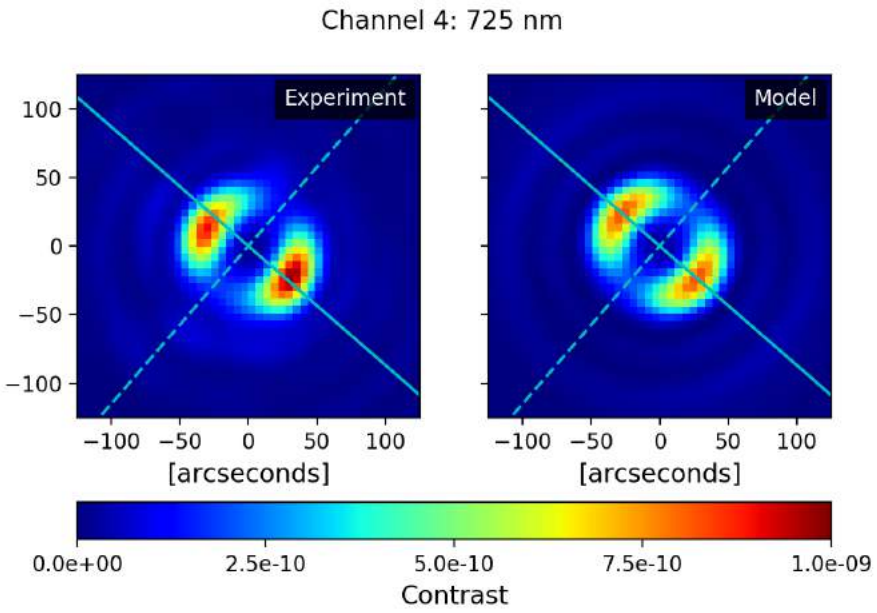

Figure 8. Experimental data (left) and vector diffraction model (right) for the M1B experiment at 725 nm. Solid and dashed lines are parallel and orthogonal to the polarization vector.

Rayleigh scattering in the Princeton starshade testbed

Willems, Phil, Harness, Anthony

Phil Willems, Anthony Harness, "Rayleigh scattering in the Princeton starshade testbed," Proc. SPIE 11117, Techniques and Instrumentation for Detection of Exoplanets IX, 111170M (9 September 2019); doi: 10.1117/12.2528077

SPIE.

Event: SPIE Optical Engineering + Applications, 2019, San Diego, California, United States

Rayleigh Scattering in the Princeton Starshade Testbed

Phil Willems[a] and Anthony Harness[b]

[a]Jet Propulsion Laboratory, California Institute of Technology, 4800 Oak Grove Drive, Pasadena, CA 91109, USA
[b]Department of Mechanical and Aerospace Engineering, Princeton University, Princeton, NJ 08544, USA

ABSTRACT

We present an analysis of the Rayleigh scattering in the Princeton starshade testbed and show that it explains several notable features in the contrast images. The scattering is consistent with that expected due to air molecules and does not require airborne dust to explain. Rayleigh scattering limits the observable contrast at the $\sim 1 \times 10^{-11}$ level at the inner working angle in the contrast images, but it limits the observable suppression at $\sim 10^{-9}$ level. We present a crude estimate of the level of scattering of starlight to be expected in a flight starshade due to zodiacal dust in the solar system and conclude that it is unlikely to be observable. We comment on whether Rayleigh scattering drives longer starshade testbeds to operate in vacuum.

Keywords: starshade, Rayleigh scattering, high contrast imaging, occulter

1. INTRODUCTION

Experiments recently performed at Princeton University have demonstrated contrast performance at 1×10^{-10} and below at the inner working angle.[1,2] These measurements used starshades with flightlike Fresnel numbers, observed at flightlike angular resolution, and so are a major step forward in demonstrating that starshades enable high contrast imaging at a level sufficient for characterization of rocky exoplanets orbiting distant stars.

However, the detailed structure in the contrast images is not consistent with the predictions of scalar diffraction theory. Near the inner working angle of the starshade mask, bright features are seen that exhibit a clear dependence upon the light polarization, and require the more complete vector diffraction theory to explain. Additionally, 'spokes' are seen to extend outward from the mask to very large angles, all the way to the edges of the observing camera's field of view. (See Figure 3.) These spokes can only be produced by light scattering in the testbed between the mask and the camera detector. We will present a detailed analysis to show that this scattering is almost certainly due to air molecules in the testbed, which is not evacuated. However, we first briefly dispense with two alternative explanations for the scatter.

Diffraction spikes are often seen in stellar images. These are generally caused by diffraction in a telescope aperture that is non-circular or that has obscurations like struts. The aperture of the testbed camera is defined by an adjustable iris at the camera's entrance window. Adjustable irises have been known to induce diffraction spikes; however, there are 16 spokes in the contrast images, which is consistent with the 16-fold symmetry of the starshade mask but not consistent with the 10 blades in the camera iris. Diffraction in the camera cannot explain the spokes.

Light scattered off the chamber walls between the mask and camera could also potentially create the observed spokes, but this is extremely unlikely. The spokes are seen to extend outward from the mask across the image of the wall separating the source and camera chambers and then out across the image of the inside of the beam tube. These surfaces can only be significantly illuminated by light passing through the gaps in the mask all the way to the camera wall at the end of the chamber 50 meters away, reflecting off the matte black surface there, and propagating back to the mask wall. The pattern of the gaps would be completely obscured in the illumination pattern at the mask wall after propagating 50 meters from a diffuse reflection.

Further author information: (Send correspondence to P.W.)
P.W.: E-mail: pwillems@jpl.nasa.gov, Telephone: 1 818 354 8019
A.H.: E-mail: anthony.harness@princeton.edu, Telephone: 1 425 268 0547

Techniques and Instrumentation for Detection of Exoplanets IX, edited by Stuart B. Shaklan, Proc. of SPIE
Vol. 11117, 111170M · © 2019 SPIE · CCC code: 0277-786X/19/$21 · doi: 10.1117/12.2528077

2. MODELING OF RAYLEIGH SCATTERING IN THE PRINCETON TESTBED

2.1 Optical Layout

Figure 1 shows the relevant optical layout of the Princeton testbed. Laser light exits a pinhole in the laser station in a diverging gaussian beam that overfills the starshade mask in the mask station 27 m away. The mask consists of a wafer with the inner starshade under test supported at its petal tips by an outer, 'inverted' starshade through a set of sixteen struts, one strut per petal. Figure 2 shows a sample of the masks installed in the testbed, along with the dimensions of one of the gaps between petals in the mask reported in this study- all gaps are nominally identical. Light transmitted through the gaps in the mask propagates through the tube to the camera station a distance of 50 m, illuminating the camera and the camera wall. The mask is set into a wall spanning the mask station, so that light can enter the camera tube only through the mask gaps. The light is observably diffracted upon passage through the starshade; the illumination pattern cast upon the camera wall has roughly the size predicted by geometric optics, but the fine features such as the struts are indistinct. We refer to the tube between the laser and mask stations as the source tube, and that between the mask and camera stations as the camera tube.

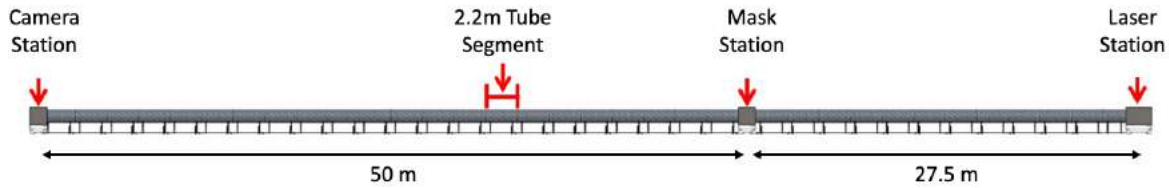

Figure 1. Layout and dimensions of the Princeton starshade testbed.

The light that scatters from the air into the camera can come from the source tube or the camera tube. We treat the light from these two regions differently, and do not consider multiple Rayleigh scattering events. All air molecules within the camera tube will contribute to the scattered light visible in the camera images, so long as they are within the camera's field of view (when measuring contrast images) or its field stop (when measuring suppression images). Our model propagates the diffraction of the laser beam past the mask to determine the intensity illuminating an air molecule at a given location, and then geometrically propagates the scattered beam from the molecule to the camera aperture. The scattering angle was taken as the angle between the lines linking the pinhole to the molecule and the molecule to the center of the camera entrance aperture.

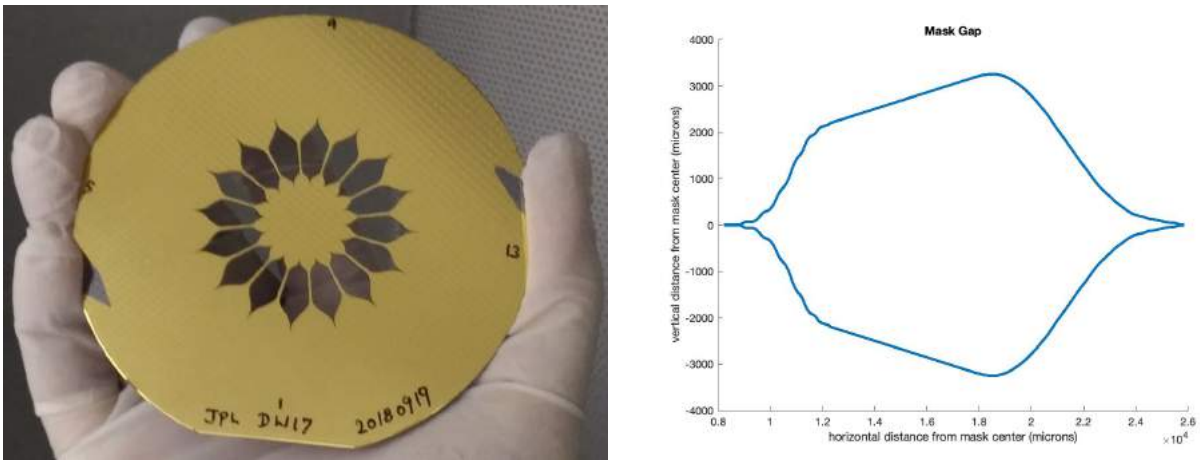

Figure 2. Left: a sample of the masks tested in the Princeton testbed. Right: the dimensions of a gap in the mask used in this study. It is slightly larger than the mask pictured at left but otherwise identical.

All air molecules in the source tube are illuminated by the pinhole, but we treat them as visible to the camera only if the line of sight from the molecule to the center of the camera aperture passes through a gap in the mask. Since the total Rayleigh scattered light illuminating the mask from the source chamber is a resolved, incoherent surface brightness as seen by the camera, we do not model the diffraction by the mask of this scattered light as it propagates to the camera, but instead assume geometric propagation.

2.2 Scattering Power Calculation

The light scattered by an individual air molecule is given by the formula

$$I_{\text{scattered}} = I_{\text{in}} \frac{3\sigma}{8} \left(\frac{1 + \cos^2 \theta}{2} \right), \tag{1}$$

where σ is the Rayleigh scattering cross section, θ is the scattering angle, I_{in} is the incident light intensity in Watts per square meter, and $I_{scattered}$ is the scattered light in Watts per unit solid angle. The cross section σ varies with the light wavelength λ to the inverse fourth power.

Our model is a MATLAB script that subdivides a 16cm x 16cm x 77m volume surrounding the axis of the testbed into 4×10^7 voxels on a three-dimensional Cartesian grid, and determines the amount of power scattered into the camera aperture by the air molecules in each voxel, assuming that they scatter identically to a molecule at the center of the voxel. We treated the scattered illumination at the camera aperture as spatially uniform for each element, and did not consider partial illumination of the aperture for voxels that were partially obscured from the camera by the mask. The volume of the testbed > 8 cm from the axis was either not visible by the camera (in the source tube) or insignificantly illuminated by the source (in the camera tube) and so were not modeled. The MATLAB model exploited the 16-fold symmetry of the mask by calculating the scatter only in one quadrant in the plane tranvserse to the tube axis, and pasting rotated copies of the calculated image into the other three quadrants.

We assume a dry air composition of 79% N_2 and 21% O_2. (About 1% of dry air is Ar, but its electric polarizability is intermediate to those of N_2 and O_2, which are similar to begin with). We use the measured values for σ at 532 nm measured by Sneep and Ubachs[3] of 5.1×10^{-31} m^2 for N_2 and 4.5×10^{-31} m^2 for O_2 and scaled these values to the wavelengths used in the contrast measurements by the familiar λ^{-4} law. As the Princeton testbed is indoors and nearly at sea level, we assume standard temperature of 295 K and pressure of 1 atmosphere to estimate the density of air molecules.

Room air typically contains 0-4% water vapor, and the concentration can vary significantly within that range from day to day. We did not measure the relative humidity within the testbed during these experiments. It would be difficult to estimate the relative humidity from archival weather data, as the testbed is a closed chamber most of the time, and we cannot determine how much fresh air was mixed into it during the relatively brief and infrequent times the various stations were opened to air to install and adjust hardware. Since water molecules have a polarizability only slightly lower than that of O_2 and typically constitute only 1% of air, we did not attempt to model its scattering contribution. Later in this article we will invoke excess scattering by water vapor near its resonant transitions to qualitatively explain a small excess seen in Rayleigh scattering seen at those wavelengths.

The scattering model we use can also account for airborne dust in the testbed if the dust is fine enough to be in the Rayleigh scattering regime. In that case, the Rayleigh scattering formula is

$$I_{\text{scattered}} = I_{\text{in}} \left(\frac{2\pi}{\lambda} \right)^4 \left(\frac{n^2 - 1}{n^2 + 2} \right)^2 \left(\frac{D}{2} \right)^6 \left(\frac{1 + \cos^2 \theta}{2} \right), \tag{2}$$

where n and D are the refractive index and diameter of the dust particle. Such dust can stay airborne a surprisingly long time. The terminal velocity v_t of a spherical particle in air is

$$v_t = \frac{\rho D^2 g}{18\mu}, \tag{3}$$

where ρ is the particle density, g is the gravitational acceleration, and μ is the viscosity of air. For a 0.1 micron silicate particle, this is 0.66 microns per second, and this particle would require about 400 hours to settle to the bottom of the 1 m beam tube. If such dust is introduced into the tubes during a mask installation, it could still be present days later during the measurements. Our data will show that fine dust does not contribute to scatter significantly. Larger dust would tend to scatter light into the forward direction and thus is not well modeled by Rayleigh scatter, but this dust would tend to settle out of the air before the measurements.

2.3 Image Generation

A contrast image is what the testbed camera sees when it is focused through the starshade to the plane of the source pinhole. This is analogous to a telescope imaging a distant star system through a starshade. To create a contrast image, the MATLAB model assigns all the scattered power at the aperture for each voxel to the camera pixel that sees the center of that voxel. The resulting image is then convolved with the point spread function of the camera. The model assumes all voxels to be in focus at the camera. To justify this approximation, we note that the camera PSF is about 91 microns wide, and most of the testbed is within the depth of field if defocal blur at this level is acceptable. The model shows that light scattered near the camera contributes only to the spokes at large angular distance from the mask, and these are intrinsically wide and diffuse, making defocal blur unimportant.

3. RESULTS

3.1 Contrast

Figure 3 shows a side-by-side comparison of a measured contrast image and the result of the Rayleigh scattering model. Note that the measured image has been rotated slightly to facilitate comparison. It is clear that the Rayleigh scattering model qualitatively reproduces the spoke structure seen in the testbed. These spokes are not seen in models of diffraction of light through the starshade mask.

The Rayleigh model also predicts a ring that is brighter than the spokes coinciding with the gaps of the mask in the image. The relative brightness of this ring can be understood by noting that only at this location can Rayleigh scattering from the source chamber be observed. Air molecules in the source chamber are disproportionally bright at the camera because they are close to the source pinhole and therefore are more brightly illuminated. This increased illumination more than compensates for the dimming caused by their greater distance from the camera.

Figure 4 shows plots of the intensity of light in the contrast image from the center of the mask outward along one of the spokes, each plot comparing model to data for a separate wavelength. Note that in all cases the red 'Rayleigh scatter model' curve is generated by the MATLAB model described above with no free parameters. Clearly, the model accurately predicts the quantitative intensity distribution along a spoke at wavelengths below 700 nm, and reproduces the trend of intensity vs. viewing angle at all wavelengths. At angles within 200 arcseconds of the mask center, the measured contrast is generally dominated by the diffraction of light around the mask (the effect these experiments are intended to measure). Even so, the bright ring seen in the Rayleigh scattering model image accounts for most of the measured intensity near 70 arcseconds from the mask center. The brightness at the inner working angle of the mask is of particular interest to high contrast imaging with starshades. At the $\sim$ 50 arcsecond inner working angle for this mask, Rayleigh scattering contributes only $\sim 1 \times 10^{-11}$ to the measured contrast.

At wavelengths $\geq$ 700 nm, the Rayleigh scattering model using only atmospheric nitrogen and oxygen accounts for only about 70% of the intensity seen in the spokes. Nevertheless, the measured angular distribution of the intensity is still consistent with Rayleigh scattering. This suggests that another airborne constituent is scattering light at those wavelengths.

We judge it unlikely that airborne dust is the cause. We can imagine that as airborne dust settles to the bottom of the testbed over time, there will be scatter in excess of that due to to air molecules that also decreases over time. But the measurements at long wavelengths that show excess scatter were made *after* the observations at short wavelength that show no excess. The testbed chamber was kept closed over all the measurements. An increase in dust scatter without an increase in dust over that time is not possible. Likewise, the pressure and/or

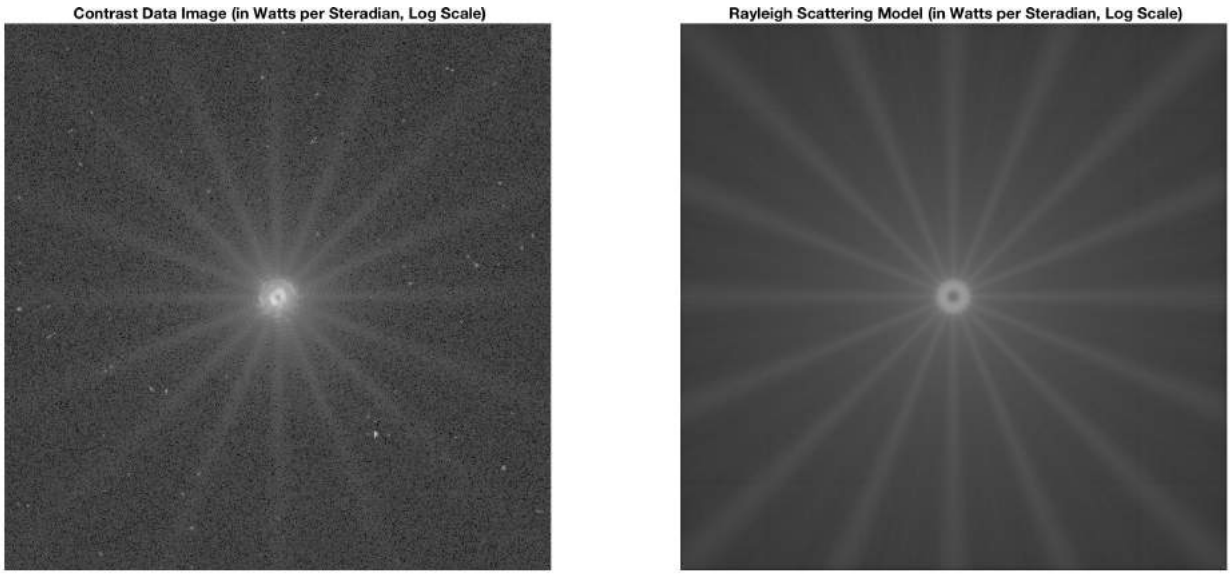

Figure 3. Left: a contrast image collected at 641 nm. Right: the contrast image predicted by the model for Rayleigh scattering by dry air. Both images plot the intensity on the same logarithmic scale.

temperature of the air in the chamber does not change at the 30% level, so fluctuations in the amount of nitrogen and oxygen cannot explain the discrepancy.

We surmise that resonant scattering by atmospheric water vapor is the cause of the excess light at 700 nm and 725 nm. Quantifying the expected level of excess scatter from water vapor resonances is beyond the scope of this article, but it is possible to crudely estimate whether it could be as large as is seen in the data. Water vapor typically accounts for 1% of room air, so in order to contribute to the total scattered light at the $\sim 10\%$ level its scattering cross section must be ~ 10 times that of dry air. The Rayleigh scattering cross section for dry air decreases from 2.2×10^{-31} m^2 at 641 nm to 1.4×10^{-31} m^2 at 725 nm. The *absorption* cross section for a water molecule increases from about 3×10^{-30} m^2 to about 6×10^{-28} m^2 over this same wavelength region.[4] (These figures are averages over the ~ 1 nm bandwidth of the source laser.) The on-resonance *scattering* cross section for a water molecule will generally be less than the on-resonance absorption by a factor of the ratio between the resonance fluorescence decay rate of the molecule's excited state and the decay rate due to all other mechanisms. Water vapor scattering is consistent with the laboratory data if this ratio is of order 1%. In Figure 4, we show both the 'dry air' and 'wet air' Rayleigh scattering predictions for the 700 nm and 725 nm data, where the 'wet air' model increases the scattering cross section enough to be consistent with the intensity seen in the spokes well outside the OWA. In the 'wet air' model, we assume that the moisture content of the air is uniform over the length of the testbed, although in practice the relative humidity could be quite different between the source and camera chambers, depending on the weather conditions when the different stations were opened and closed.

3.2 Suppression

A suppression image is what the camera sees when it is focused to its entrance pupil. It shows the distribution of the light incident upon the camera. Our Rayleigh scattering model makes the assumption that the light scattered by airborne molecules illuminates the aperture uniformly, so it cannot predict intensity distributions, only integrated powers. This approximation of uniform illumination at the aperture is reasonable given the nearly isotropic phase function for Rayleigh scattering, except for air molecules very close to the camera, which inject light outside the camera's field stop.

Figure 5 shows plots of the suppression through the camera aperture at the four measured wavelengths, along with the integrated power at the aperture from the Rayleigh scattering model. While Rayleigh scattering

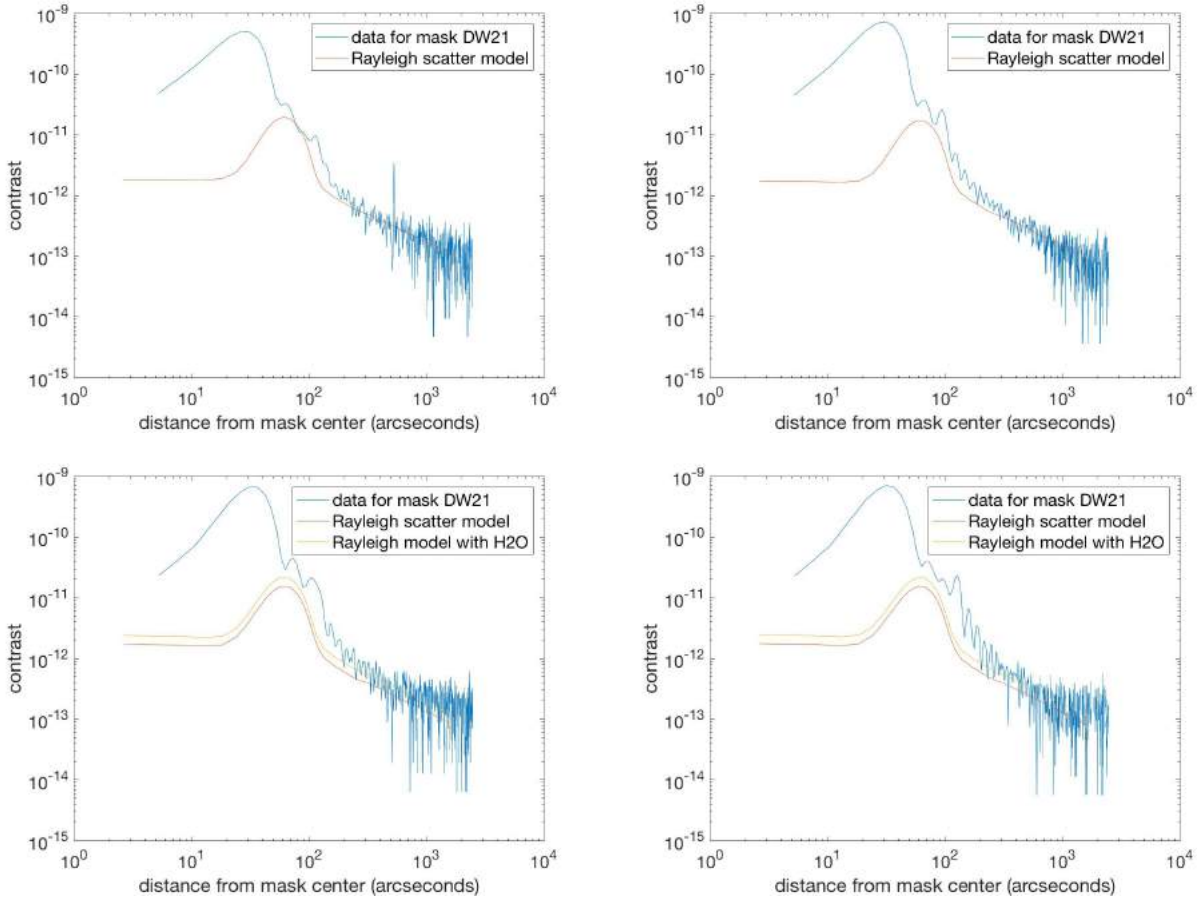

Figure 4. Plots of the contrast along a spoke at four wavelengths. Upper left: 641 nm. Upper right: 660 nm. Lower left: 700 nm. Lower right: 725 nm.

contributes only about 10% of the light intensity at the inner working angle of the mask in the contrast images, it contributes more than half of all the light entering the camera aperture within the camera's field stop. Even though the Rayleigh scattered light has a low surface brightness, it subtends a very large angle as seen by the camera, and so its flux is large. As was the case with the contrast, atmospheric nitrogen and oxygen are sufficient to explain the floor seen in the suppression plots at 641 nm and 660 nm. Likewise, the same level of excess scatter (assumed due to water vapor) that matches the Rayleigh model to the spokes in the contrast images matches the Rayleigh model to the floors in the suppression plots at 700 nm and 725 nm.

4. DISCUSSION

4.1 Implications for Future Starshade Testbeds

The experiments in the Princeton testbed support milestones within NASA's starshade technology development activity that consider contrast to be a key performance parameter, but not suppression. The reason for this is that a contrast requirement can straightforwardly flow down from a mission science traceability matrix, but a suppression requirement cannot.* For this reason, it is acceptable that the Rayleigh scatter dominate in

*There has been a lively debate about whether contrast or suppression is the better metric for judging starshade technology progress, because the contrast relies upon the characteristics of the telescope rather directly in a way that the suppression does not, such that a telescope that does not realistically scale to flight performance can yield artificially good contrast. In the experiments reported here, this concern is addressed by having the number of camera resolution elements spanned by the starshade be the same as expected in flight.

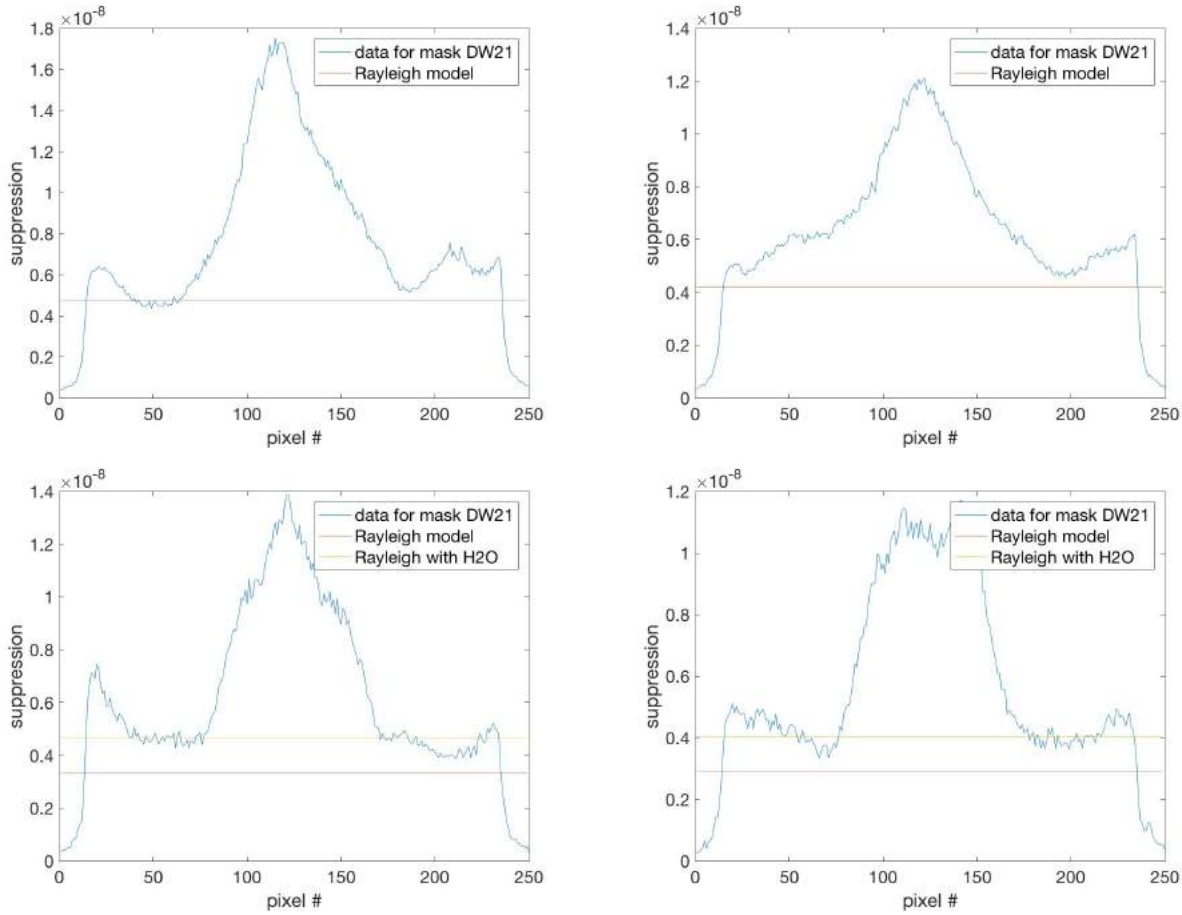

Figure 5. Plots of suppression through the center of the camera aperture at four wavelengths. Upper left: 641 nm. Upper right: 660 nm. Lower left: 700 nm. Lower right: 725 nm.

the suppression plane because it only contributes 10% of the contrast requirement at the inner working angle. Demonstrating the scaling of performance from the Princeton testbed scale to flight scale will require experiments in a testbed of intermediate length. Experiments have already been done over hundreds to thousands of meters baselines, although these have been outdoors, in conditions much less controlled than in the Princeton testbed. It would clearly be convenient that a future testbed be evacuated- this would remove the Rayleigh scattering entirely. But long baseline vacuum enclosures are costly. This raises the question: does Rayleigh scattering make longer baseline starshade testbeds in air impractical?

The answer, surprisingly, is not necessarily. In fact, *the contrast level of Rayleigh scattering at the IWA is independent of the testbed length,* if the testbed and its components are scaled upward in a manner that preserves the Fresnel number and a few other related parameters. Namely, if the size of the starshade mask is scaled up by a factor n, then:

1. the distance from the source to the mask and from the mask to the camera are scaled up by n^2;
2. the size of the camera aperture is scaled up by n;
3. the plate scale of the camera is scaled down by n; and
4. the divergence angle of the source is scaled down by n.

The first condition preserves the Fresnel number, the second and third conditions maintain the number of resolution elements across the starshade, and the fourth condition ensures that the light source overfills the mask by the same relative amount.

Although it may be at first surprising, this result is fairly simple to justify. We divide the testbed into the same number of voxels regardless of the value of n, and consider how the scattered light from a voxel varies as n varies. Given rules 1 and 4 above, which elements are illuminated and which are not is independent of n. The diameter of the illuminating beam at the mask location grows as n like the mask, so the intensity there is reduced as $1/n^2$; the intensity at any voxel will be reduced by the same factor. The solid angle subtended by the camera aperture collecting the light from the scatterer will also be reduced by $1/n^2$. Together, these reduce the light collected from a single molecule by $1/n^4$. However, the volume of the voxel (and therefore the number of scattering molecules) increases like the testbed volume as n^4. The net effect is no change with n in the amount of Rayleigh scattered light collected by the camera. Running the MATLAB model with these scaling relations confirms that the contrast does not change. It therefore does not appear strictly necessary that future starshade optical testbeds need to operate in vacuum, at least as far as Rayleigh scattering is concerned. Should it be desirable that a future testbed not strictly scale from the Princeton testbed in the manner described above, this calculation can be repeated for that specific case. The testbed also need not be filled with air. Helium has only $1/8^{\text{th}}$ the electric polarizability of nitrogen or oxygen, and thus its Rayleigh scattering cross section is 64 times smaller. The Rayleigh scattered light would be completely negligible in a testbed filled with helium at room pressure.

In principle, this analysis suggests that even a testbed that is outdoors and unenclosed would not be limited by Rayleigh scattering, provided that the air is sufficiently dust-free, but this cleanliness appears impossible to guarantee. We acknowledge that other considerations beside Rayleigh scattering can necessitate vacuum, for example the necessity of suppressing turbulent distortions due to heat-driven convection in the air.

4.2 Implications for Starshade Flight Missions

Nearly all proposed missions involving starshades employ space telescopes, and there is no air to scatter starlight into the telescope. There is the zodiacal dust, however. The zodiacal dust creates a fairly uniform foreground brightness of 22 magnitudes per square arcsecond across the sky, due to scattered sunlight. Zodiacal dust grains tend to have sizes of a few microns to a hundred microns, and are thus too large to scatter light with the Rayleigh $1+\cos\theta$ distribution; they will tend to scatter much more of their light in the forward direction and much less at large angles. This implies that the relative dimness of the light scattered by the Sun does not necessarily imply that dust-scattered starlight will be fainter in proportion to the relative apparent magnitudes of the star and the Sun, as the forward-scattered starlight would illuminate the telescope.

Measurements of zodiacal dust reveal that the forward scattering amplitude is about 1,000 times larger than the scattering at right angles, or 7.5 magnitudes.[5] We can therefore crudely estimate that the surface brightness of starlight forward scattered by zodiacal dust for a star of magnitude m will be

$$(22 - 7.5 - m_{Solar} + m)\text{mags/as}^2 = (41.2 + m)\text{mags/as}^2 \tag{4}$$

and so is utterly negligible.

There are also concepts that involve a starshade in space operating jointly with a telescope on Earth.[6] In this case, there is air in the path between the telescope and starshade, but in this case too the scattering due to dust and air is unimportant. The Earth's atmosphere extends upward only tens of kilometers from the Earth's surface, but the starshade is hundreds of thousands of kilometers higher. The starshade's shadow has fully developed when it first impinges upon the atmosphere. Starlight outside the shadow will indeed be scattered by the atmosphere, but the telescope sees this scattering as occurring far outside the working angle of the starshade, and so it can have no impact on the observation of the stellar system.

ACKNOWLEDGMENTS

This work was performed in part at the Jet Propulsion Laboratory, California Institute of Technology under a contract with the National Aeronautics and Space Administration. The authors would like to thank Stefan Martin and Stuart Shaklan for providing helpful comments.

REFERENCES

[1] Harness, A., Kasdin, N. J., Galvin, M., Shaklan, S., Balasubramanian, K., White, V., Yee, K., Muller, R., Dumont, P., Vuong, S., and Willems, P., "Starshade technology development activity milestone 1a: Demonstration of high contrast in monochromatic light at a flight-like fresnel number." https://exoplanets.nasa.gov/internal_resources/1210/ (2019).

[2] Harness, A., Kasdin, N. J., Galvin, M., Shaklan, S., Balasubramanian, K., White, V., Yee, K., Muller, R., Dumont, P., Vuong, S., and Willems, P., "Starshade technology development activity milestone 1b: Demonstration of high contrast in broadband light at a flight-like fresnel number." https://exoplanets.nasa.gov/internal_resources/1211/ (2019).

[3] Sneep, M. and Ubachs, W., "Direct measurement of the rayleigh scattering cross section in various gases," *J Quant. Spect. and Rad. Trans.* **92**, 293–310 (2005).

[4] "Hitran on the web." http://hitran.iao.ru/molecule/simlaunch. (Accessed: 25 March 2019).

[5] Leinert, C., Link, H., Pitz, E., and Giese, R. H., "Interpretation of a rocket photometry of the inner zodiacal light," *Astronomy and Astrophysics* **47**, 221–230 (1976).

[6] Janson, M., "Celestial exoplanet survey occulter: a concept for direct imaging of extrasolar earth-like planets from the ground," *Publications of the Astronomical Society of the Pacific* **19**, 214–227 (2007).